UNIVERSITY OF SOUTHAMPTON

Faculty of Environment and Life Science
School of Ocean and Earth Science

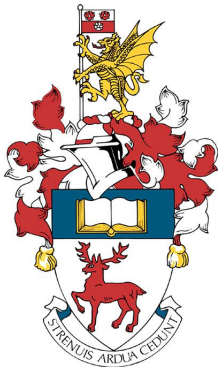


# Advancing Climate-Critical Ocean Carbon Observations Through New Applications of Autonomous Technologies

*by*

**Emily Madison Hammermeister**
BS, BBA
ORCiD: 0000-0002-1739-761X

*A thesis for the degree of*
*Doctor of Philosophy*

January 2026

University of Southampton

Abstract

Faculty of Environment and Life Science
School of Ocean and Earth Science

Doctor of Philosophy

**Advancing Climate-Critical Ocean Carbon Observations Through New Applications of Autonomous Technologies**

by Emily Madison Hammermeister

The ocean is a critical component of the global carbon cycle. As global anthropogenic carbon emissions continue to rise understanding the ocean's role in carbon cycling has become a major focus for scientific observation and intervention. The marine carbonate system underpins the central role of the ocean both in moderating atmospheric $CO_2$ and ocean pH, yet it remains poorly constrained in space and time, particularly in dynamic coastal environments. Traditional ship-based approaches constitute the "gold-standard" data quality but are sparse, seasonally biased, and resource-intensive, highlighting the urgent need for increased high-resolution observational strategies. In this thesis I present new methodological approaches through the use of cutting-edge autonomous technologies to address these gaps and advance the understanding of ocean carbon. Here, I demonstrate that autonomous carbonate observations can approach the quality of traditional methods while delivering unprecedented spatiotemporal coverage at reduced cost and carbon footprint. Lab-on-Chip pH and TA sensors on the Autosub Long Range AUV yielded the first high-resolution carbonate characterisation from autonomous sensors, detecting fine-scale coastal biogeochemical processes with ship-comparable quality. An extended AUV deployment with dual pH sensors resolved carbonate dynamics and air–sea $CO_2$ fluxes while critically assessing sensor corrections and uncertainties. Finally, multi-month autonomous reef observations in the Red Sea—including the first stand-alone TA sensor on a coral reef—captured diel and seasonal variability in different reef environments and provided carbonate chemistry characterisation to an undersampled region. Collectively, this work advances both understanding of ocean carbon dynamics and the capabilities of autonomous observation. I highlight both the scientific insights (ranging from regional carbon cycling to reef metabolic processes) and the methodological advances required for climate-critical ocean carbon observation. By confronting the observational gaps of the marine carbonate system, my doctoral thesis establishes novel autonomous technologies as a defensible strategy to understand, monitor, and respond to ocean chemistry in a changing climate.

# Contents

# List of Figures

# List of Tables

# Declaration of Authorship

I, Emily Madison Hammermeister, declare that this thesis and the work presented in it is my own and has been generated by me as the result of my own original research. I confirm that:

1. This work was done wholly or mainly while in candidature for a research degree at this University;
2. Where any part of this thesis has previously been submitted for a degree or any other qualification at this University or any other institution, this has been clearly stated;
3. Where I have consulted the published work of others, this is always clearly attributed;
4. Where I have quoted from the work of others, the source is always given. With the exception of such quotations, this thesis is entirely my own work;
5. I have acknowledged all main sources of help;
6. Where the thesis is based on work done by myself jointly with others, I have made clear exactly what was done by others and what I have contributed myself;
7. Parts of this work have been published or will be published as:
    - **Emily M Hammermeister**, Stathys Papadimitriou, Martin Arundell, Jake Ludgate, Allison Schaap, Matthew C Mowlem, Sara E Fowell, Edward Chaney, and Socratis Loucaides. New capability in autonomous ocean carbon observations using the autosub long-range auv equipped with novel ph and total alkalinity sensors. *Environmental Science Technology*, 59:7129–7144, 4 2025. ISSN 0013-936X. https://doi.org/10.1021/acs.est.4c10139 doi: 10.1021/acs.est.4c10139.
    - Allison Schaap, Stathys Papadimitriou, Edward Mawji, John Walk, **Emily Hammermeister**, Matthew Mowlem, and Socratis Loucaides. Autonomous sensor for in situ measurements of total alkalinity in the ocean. *ACS Sensors*, 2025 10 (2), 795-803 https://doi.org/10.1021/acssensors.4c02349

- **Emily Madison Hammermeister**, Cathy Wimart-Rousseau, Stathys Papadimitriou, et al. Coastal Marine Carbon and Air-Sea Fluxes Quantified from pH Sensors on an Extended AUV Deployment. *ESS Open Archive* [Preprint]. September, 2025. https://doi.org/10.22541/essoar.175398499.90647984/v2
- **Emily Madison Hammermeister**, Sarah E Cryer, Vincent Saderne, et al. Metabolic Dynamics of an Offshore Coral Reef in the Central Red Sea: Observations from Autonomous Sensors. *ESS Open Archive* [Preprint]. Novemeber, 2025

**Emily Hammermeister**

**January 2026**

# Publications

- **Emily M. Hammermeister**, Stathys Papadimitriou, Martin Arundell, Jake Ludgate, Allison Schaap, Matthew C. Mowlem, Sara E. Fowell, Edward Chaney, and Socratis Loucaides. New capability in autonomous ocean carbon observations using the autosub long-range auv equipped with novel ph and total alkalinity sensors. *Environmental Science and Technology*, 59:7129–7144, 4 2025. ISSN 0013-936X. https://doi.org/10.1021/acs.est.4c10139 doi: 10.1021/acs.est.4c10139.

- **Emily Madison Hammermeister**, Cathy Wimart-Rousseau, Stathys Papadimitriou, et al. Coastal Marine Carbon and Air-Sea Fluxes Quantified from pH Sensors on an Extended AUV Deployment. *ESS Open Archive* [Preprint]. September, 2025. https://doi.org/10.22541/essoar.175398499.90647984/v2 **Under review at JGR Oceans*

- **Emily Madison Hammermeister**, Sarah E Cryer, Vincent Saderne, et al. Metabolic Dynamics of an Offshore Coral Reef in the Central Red Sea: Observations from Autonomous Sensors. *ESS Open Archive* [Preprint]. Novemeber, 2025 **Under review at Global Biogeochemical Cycles*

- Allison Schaap, Stathys Papadimitriou, Edward Mawji, John Walk, **Emily Hammermeister**, Matthew Mowlem, and Socratis Loucaides. Autonomous sensor for in situ measurements of total alkalinity in the ocean. *ACS Sensors*, 2025 10 (2), 795-803 https://doi.org/10.1021/acssensors.4c02349

- Pickup, D. D., Bakker, D. C. E., Heywood, K. J., Glassup, F., **Hammermeister, E. M.**, Stammerjohn, S. E., Lee, G. A., Loucaides, S., Queste, B. Y., Webber, B. G. M., and Yager, P. L.: Cold lenses in the Amundsen Sea: impacts of sea ice formation on subsurface pH and carbon, Ocean Sci., 21, 2727–2741, https://doi.org/10.5194/os-21-2727-2025, 2025.

- Schuback, N., Oxborough, K., Burkitt-Gray, M., López-García, P., Patey, M.D., **Hammermeister, E.**, Wright, A. and Moore, C.M. (2024), Phytoplankton primary productivity: A dual-incubation approach for direct comparison of photosystem II photosynthetic flux ($JVP_{II}$) and $^{14}C$-fixation experiments. *Limnol Oceanogr Methods*, 22: 720-737. https://doi.org/10.1002/lom3.10635

# Acknowledgements

To articulate the gratitude I have for the people, my people, who made this work and experience what it is seems currently impossible. But this is me trying.

First and foremost, they say its not the project that makes or breaks a PhD, but the supervisors. I am fortunate to have genuinely enjoyed my research as much as I did, but it was Socratis, Stathys, and Sara that made this project and this experience one of my proudest achievements. Socratis, thank you for giving me this opportunity and every opportunity. You always built me up and advocated for me and my work. You encouraged and supported all of the workshops, conferences, and fieldwork, and you really allowed me to make the most of it all. So thank you so much for your unwavering encouragement, even on days when it seemed like my imposter syndrome would win. Thank you Stathys, who is the backbone of carbonate chemistry itself, for your countless (and I'm sure repetitive), patient, explanations and guidance. Our laboratory conversations (science-related and not) meant more to me than you realise and I will always cherish your insight on the world and your advice on life. Sara, thank you for being the very first person I met at NOC, with the hours spent talking in the courtyard all those years ago. I look back so grateful knowing we would have many days like that in the years to come. Your mentorship, especially as a young woman in this field has been invaluable. Working with you, I'm so glad I got a lifelong friend too. Thank you Adrian for your steadfast support and guidance. From the beginning you always looked out for me and I appreciate everything you have done.

To the years of 6 Carlton Place and its occupants... How lucky am I to have moved to a country, having never even visited and knowing nobody, and fallen into the hands of my soon-to-be best friends and housemates for the next four years. That simply does not just happen. This group of lifelong friends were at the very core of this experience for me. Anna, Cordelia, Jack, Mark, and Millie, I love you guys so much. Our Carlton family (complete with a certain tailless cat resident), countless kitchen conversations and concerts, belly-aching laughs, PhD commiseration tears, football viewing, Thanksgiving feasts, garden BBQs, and trips to the faraway land of Bedford will have a special place in my heart for the rest of my life. You gave me a family when I was so far from my own, and our lively home and community was everything to me. Thank you for being the best part of the last four years.

To my love, Brandon. You already know. We met months before I moved across the world indefinitely. You supported my dreams before you really even knew me. You crossed an ocean to visit a dozen times and you met me in other corners of the world even if just for a few days together. And right now, you are waiting in OUR kitchen (!!!) to pop a bottle of champagne. These years were so much more than completing a thesis, and a large part of them was about building a life with you that we get to have now, together. I love you. To Wika, I have never been so proud of anyone as I have of you. You are an amazing and inspiring human who sets

the highest standards for what it means to a best friend. Thank you so much Wika, for our forever friendship and sisterhood. Lexie, it's almost as if you moved to Southampton with me. The hours of facetime calls with my longest friend during my commute quite literally fuelled me every day. Thank you for always answering my calls Lex. Dr. Sarah Cryer, my PhD big. From Lima to Eras, I still cannot comprehend just how lucky I was to have you through it all. I aspire one day to impact someone the way you've impacted me. You make me a better friend, scientist, and friendship bracelet crafter. Thank you so much. Molly, you are one of the most thoughtful people I have ever met. I couldn't have asked for a better person to share an office (chatting and procrastinating) with, and I promise to cherish my vandalised periodic table. To Tatjana, your year in London was so iconic for us. Having one of my best friends and a piece of home here was the absolute best. We certainly made the most of it (ask the Welsh), and I will be forever grateful for that special era. To Taylor, our travels overseas are always my favourite. Although I do worry we may never top the week in the French Alps, x-rays and all! Thank you for visiting multiple times, and always being up for fun, food, and crying! Maja, its hard to articulate how glad I am to know you. From masonry to Macedonia, you are such a beautiful best friend for life. The way you and Alex have shown up for me over the years has meant more than you know. Ella, Spencer, Matina, Lewis, Harry, Joe, Beth, Eloise, Isabelle, Will(s), Andres, Tom, and SO MANY MORE. Thank you for being such wonderful friends, for the lively group chat ('Pints?'), and for a bloody good time always. I am so grateful for you. I love you lot.

To my mom and dad, thank you for it all. I dedicate this to you. Your love and support in everything I pursue is the greatest gift, one that I will never take for granted. Thank you for your guidance and thank you for your trust. Poppy, thank you for always being a champion of education and encouraging this effort, I know Grandma is so proud of the both of us. Mimi, I cherish the school pick-ups, conversations, and time together we had when I was a young student. I remember telling you that one day I would get my PhD, and here we are. Thank you for believing in me. Thank you Alyse for loving and supporting me so loudly. You always have and always will be such an incredible role model. And thank you Grampy, for the endless love and compassion, the spirit, and the Hammermeister name.

Finally, to DFA Swift, if only I could put into words what you have put into words for me over the past two decades. Had I been able to refer to articles and single lines from obscure references by memory for my research the way I could for your entire discography, this PhD would have taken half the time. A better woman would have placed easter eggs, numerology, and lyrics throughout this, but I find myself instead sanctimoniously performing a single soliloquy you'll never see. So thank you, not only for showing me it's okay to cry a lot while being so productive, but for the soundtrack to my past, present, and future eras, forevermore. I promise that when the dedicatee(s) of this thesis point to the picture, I'll tell them your name.

What a privilege it is to have so many to thank.

*To my mom and dad*
*who taught me I could do anything I put my mind to*
*and to my future child(ren)*
*for whom I strive to make the world a safer place*

# Chapter 1

# Introduction

## 1.1 The Marine Carbonate System

The marine carbonate system is among one of the most important components of chemical oceanography because of its role in the global carbon cycle and in the regulation of the Earth's temperature. The ocean acts as a major natural reservoir for carbon as it has absorbed over a quarter of atmospheric carbon dioxide ($CO_2$), and is capable of carbon storage on geologic timescales. As $CO_2$ dissolves into the ocean, it reacts with the seawater to form carbonic acid ($H_2CO_3$), which further disassociates into bicarbonate ($HCO_3^-$) and carbonate ($CO_3^{2-}$) ions:

$$H_2O + CO_{2(aq)} \rightleftharpoons H_2CO_3 \overset{H^+}{\rightleftharpoons} HCO_3^- \overset{H^+}{\rightleftharpoons} CO_3^{2-} \tag{1.1}$$

The carbonate speciation described by Equation 1.1 is reflected by pH, which is equal to the negative log of hydrogen ion concentration [$H^+$] (Equation 1.2).

$$pH = -\log[H^+] \tag{1.2}$$

As [$H^+$], which is proportional to the ratio of [$HCO_3^-$] / [$CO_3^{2-}$], increases, it protonates seawater and pH decreases. Seawater pH is commonly reported on varying scales (total, seawater, free, NBS) which differ in their inclusions or exclusions of the interactions of the common conservative anions in seawater sulfate ($SO_4^{2-}$) and fluoride ($F^-$) with $H^+$ (Bates, 1982; Dickson, 1984; Covington et al., 1985; Dickson, 1990, 1993; Carter et al., 2023). This thesis will refer to pH on the total hydrogen ion scale (denoted $pH_T$), which is defined as the sum of the substance contents of $H^+$ and hydrogen sulfate ($HSO_4^-$) concentrations (Equation 1.3).

$$pH_T = -\log([H^+] + [HSO_4^-]) = -\log[H^+]_T \tag{1.3}$$

The global (as of 2019, between 60°N and 60°S) average surface ocean $pH_T$ is 8.07 (Jiang et al., 2019). While dependent on temperature, pressure, and salinity, seawater pH is most accurately determined spectrophotometrically using sulfonephthalein indicator dyes, most commonly m-cresol purple (mCP). Potentiometric glass/reference electrode cells are also commonly used for pH determination when high precision and accuracy is not required (Dickson et al., 2007). Both spectrophotometric and electrochemical modern measurement approaches are calibrated on the total hydrogen ion scale (Carter et al., 2023). pH is one of four key measurable parameters that define the marine carbonate system. The remaining three are dissolved inorganic carbon (DIC), total alkalinity (TA), and partial pressure of $CO_2$ ($pCO_2$). DIC represents the sum of all dissolved inorganic carbon species:

$$DIC = [CO_2] + [HCO_3^-] + [CO_3^{2-}] \tag{1.4}$$

In the ocean, the concentration of DIC is independent of temperature and pressure, and is mainly controlled by the biotic or abiotic production and consumption of inorganic carbon species. DIC is typically measured by acidifying a seawater sample to convert all carbonate species to $CO_2$, which is then detected and quantified coulometrically or spectroscopically in units of $\mu$mol $kg^{-1}$ (Dickson et al., 2007). The TA of seawater is defined as the number of moles of $H^+$ equivalent to the excess of proton acceptors over proton donors (Dickson, 1981). Therefore, TA is related to the charge balance in seawater, and not only reflects the presence of carbon species but also borate, silicate, phosphate, and other organic ions as expressed by Equation 1.5 from Dickson (1981).

$$\begin{aligned} TA = {} & [HCO_3] + 2\,[CO_3] + [B(OH)_4] + [OH] + [HPO_4] + 2\,[PO_4] + [SiO(OH)_3] \\ & + [HS] + 2\,[S] + [NH_3] - [H] - [HSO_4] - [HF] - [H_3PO_4] \end{aligned} \tag{1.5}$$

Like DIC, TA is a conservative quantity, in that it remains unaffected by temperature and pressure (Wolf-Gladrow et al., 2007a; Emerson and Hedges, 2008; Gattuso and Hansson, 2011). TA is mainly driven by the change in the concentration of proton acceptors in solution and their relative proportion with the number of proton donors (Wolf-Gladrow et al., 2007a; Middelburg et al., 2020). The conservative nature of TA and DIC is what makes them the robust, "master" variables of the marine carbonate system that control carbonate speciation. In the laboratory, TA is most commonly determined by open-cell potentiometric titration with hydrochloric acid (HCl). A

least-squares approach is used to identify the titration's equivalence point and determine alkalinity in $\mu$mol kg$^{-1}$ (Dickson et al., 2007).

The fourth measurable key parameter in the marine carbonate system is $pCO_2$, which is related to the concentration of $CO_2$ gas dissolved in seawater (Zeebe and Wolf-Gladrow, 2001). Generally, $pCO_2$ is measured by equilibrating a seawater sample with a known gas phase, followed by determining the $CO_2$ content using a gas chromatograph or infrared detector (Dickson et al., 2007). When at equilibrium with seawater, $pCO_2$ is expressed in simple terms as:

$$pCO_2 = \frac{[CO_2]}{K_H} \tag{1.6}$$

where $K_H$ is Henry's Law coefficient for $CO_2$ (Emerson and Hedges, 2008). Atmospheric $CO_2$ is typically reported as parts per million (ppm), representing the number of $CO_2$ molecules in a given number of dry air molecules (a concentration), whereas $pCO_2$ is expressed in $\mu$atm, which is the gas phase pressure of $CO_2$ (i.e., in the air head space) that would be in equilibrium with the dissolved $CO_2$ (Dickson et al., 2007). Like $pH_T$, $pCO_2$ is non-conservative, and is temperature dependent. Measuring $pCO_2$ provides a direct assessment of the air-sea interface, and whether the ocean is a sink or source of $CO_2$ at a given moment ($CO_2$ fluxes) or over a period of time ($CO_2$ budget). Figure 1.1 summarises the key variables within the marine carbonate system and how they fit into Equation 1.1:

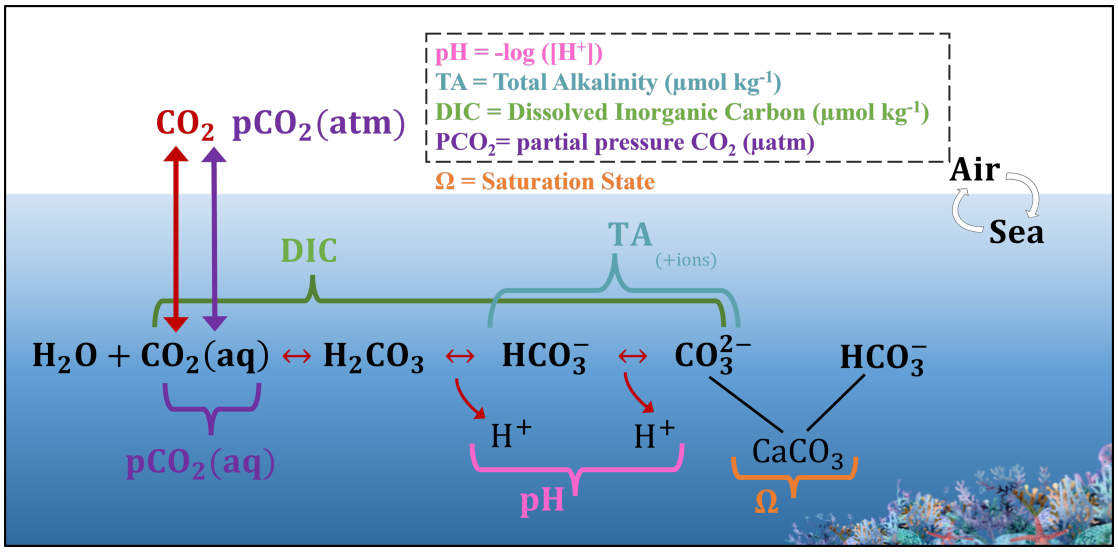


FIGURE 1.1: Visualisation of the Marine Carbonate System, key variables, and their relationships within

Measurements of two of the four key carbonate parameters (pH, DIC, TA, $pCO_2$) can be used to fully constrain the stoichiometry of the marine carbonate system through a system of well-established stoichiometric and thermodynamic equations, and

knowledge of the temperature, salinity, and pressure (Park, 1969; Millero, 1995, 2007). This allows for the determination of carbonate parameters which cannot be measured directly, like the aragonite/calcite saturation state ($\Omega_{arag/calc}$), a key indicator of seawater corrosivity to marine calcifying organisms ($CaCO_3$). The production of $CaCO_3$ by marine calcifying organisms is a fundamental biogeochemical process and form of carbon storage (Berelson et al., 2007) that manifests in a variety of different environments including reef structures built by corals and coralline algae, or as a vital requirement to calcareous plankton (e.g., coccolithophores or foraminifera). The production of $CaCO_3$ (calcification) and the dissolution of $CaCO_3$ can be described by the reaction:

$$CaCO_3(s) + H_2O \rightleftharpoons Ca^{2+} + CO_3^{2-} \tag{1.7}$$

Aragonite is a more-soluble form of biogenic $CaCO_3$, (compared to calcite), and is often used for defining thresholds of marine calcifier health:

$$\Omega_{arag} = \frac{[Ca][CO_3^{2-}]}{K_{sp(arag)}} \tag{1.8}$$

where $K_{sp(arag)}$ is the thermodynamic solubility product. Values of $\Omega_{arag} < 1$ signify undersaturation with respect to aragonite and favourable conditions for mineral dissolution. Conversely, values of $\Omega_{arag} > 1$ signify supersaturation and promote mineral precipitation.

Taken altogether, while any two of the four measurable parameters can be used to constrain the marine carbonate system, the choice of input pair is significant to the quality and associated uncertainty of the calculated parameters. When possible, minimising uncertainty with direct carbonate variable measurements improves the understanding of the process being investigated. For example, direct measurements of DIC are recommended for biological respiration and production studies, measured TA for calcification and $CaCO_3$ dissolution assessments, measured pH for precise monitoring of ocean acidification, and measured $pCO_2$ for air-sea interactions. When measuring parameters directly, only analytical errors involved in the measurement of the variable need to be considered (e.g., instrumentation, laboratory procedure).

When solving for carbonate variables that are not directly measured, the uncertainties associated with the complex seawater acid-base chemistry are introduced and propagated. Fully constraining the marine carbonate system involves resolving several equations describing acid-base reactions in seawater, equilibrium constants, and total contents of acid-base pairs in addition to two measured input variables (Figure 1.2). Each of these components carry with them sources of uncertainty which propagate through to the calculated properties. Additionally, the widely adapted

packages (e.g., CO2SYS, Seacarb, Ocean Data View) that compute marine carbonate chemistry each have associated error that contributes to the final calculate values (Orr et al., 2015). Specifically, the selection of the thermodynamic constants (e.g., $K_1$, $K_2$, $K_S$, $K_F$), for which multiple published parametrisations and values exist and are implemented differently across packages impact carbonate system calculations. Because these constants are empirically derived over specific temperature–salinity (and sometimes pressure) ranges, the chosen constant combination introduces its own (often systematic) distinct uncertainty that should also always be considered.

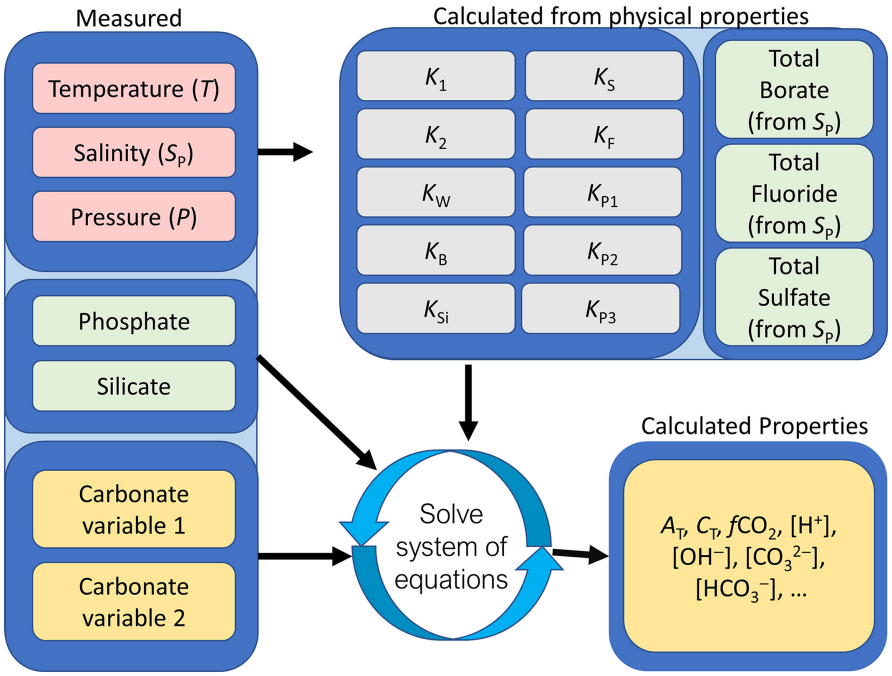


FIGURE 1.2: Schematic taken from Carter et al. (2023) that illustrates the parameters necessary for input to calculate carbonate chemistry variables. Physical measurements are shown with pink-colored backgrounds, total contents of acid-base species are in light green, thermodynamic constants are in gray, and carbonate chemistry variables in yellow.

Each measured input pair combination carries with it uncertainties—separate from their individual analytical uncertainties—when determining the remaining carbonate variable(s). Calculations that use the pH—$pCO_2$ pair are particularly problematic because they rely heavily on highly non-linear, thermodynamic constant-dependent equilibria, yielding large propagated uncertainties (Orr et al., 2018). Calculations that use either TA or DIC paired with either pH or $pCO_2$ are generally best because they pair a robust bulk inventory constraint (TA or DIC) with an independent speciation constraint (pH or $pCO_2$) which reduces sensitivity to thermodynamic constant errors and minimises uncertainty amplification. This is supported by the combined standard uncertainties shown in Table 1.1, which are synthesized from Orr et al. (2018) and are consistent with long-established principles on whether two seawater measurements

provide similar or independent information to constrain the carbonate system (Dickson and Millero, 1987; Millero, 2007; Mclaughlin et al., 2015; Carter et al., 2024).

TABLE 1.1: Propagated percent combined standard uncertainties of output variables based on input pair as synthesised from (Orr et al., 2018)

| Input Pair | pH | DIC | TA | $pCO_2$ | $\Omega_{arag}$ |
|---|---|---|---|---|---|
| **TA – DIC** | 3.0 | — | — | 3.5 | 4.9 |
| **pH – TA** | — | 0.6 | — | 3.5 | 5.6 |
| **pH – DIC** | — | — | 0.6 | 3.2 | 5.9 |
| **$pCO_2$ – pH** | — | 3.7 | 3.8 | — | 7.8 |
| **$pCO_2$ – TA** | 2.3 | 0.5 | — | — | 5.4 |
| **$pCO_2$ – DIC** | 2.5 | — | 0.7 | — | 5.8 |

### 1.1.1 In the Context of Climate Change

Atmospheric $CO_2$ has increased by over 52% since the onset of the anthropocene, with global concentrations reaching 422.45 ppm in 2024, compared to pre-industrial levels of ~278 ppm in 1750 (Figure 1.3; Friedlingstein et al. 2025; Calvin et al. 2023). Total anthropogenic carbon emissions in 2024 exceeded 11.4 GtC $yr^{-1}$, which is 0.3 GtC $yr^{-1}$ higher than in 2023 (Friedlingstein et al., 2025). The human-induced rise in atmospheric $CO_2$ (in addition to other greenhouse gasses) is unequivocally the primary driver of observed global temperature increases, termed global warming, with mean surface temperatures 1.1°C higher than pre-industrial levels (Arias et al., 2021). There is, however, *another $CO_2$ problem* (Doney et al., 2009). It is well-defined that the ocean is a critical component of the global carbon cycle and plays a crucial role in moderating the rise in atmospheric $CO_2$ and accompanying climate changes (e.g., global warming), by absorbing $CO_2$ (Gattuso and Hansson, 2011). The global net uptake of $CO_2$ by the oceans, known as the ocean sink, was $2.9 \pm 0.4$ GtC $yr^{-1}$ in the last decade, accounting for 26% of anthropogenic $CO_2$ annually (Friedlingstein et al., 2025; Quéré et al., 2009a). While atmospheric $CO_2$ continues to rise and the ocean continues to take up more $CO_2$, the ocean's capacity to absorb surplus anthropogenic $CO_2$, or buffer global climate change, has decreased (Feely et al., 2004; Tans, 2009). In fact, recent models suggest the ocean's buffer capacity could continue to decrease as much as 34% by 2100, likely accelerating the response of chemical properties in the ocean (Jiang et al., 2019). Extrapolating from Equations 1.1, 1.2 and Figure 1.1, it is evident that as more $CO_2$ dissolves in the ocean, there is a net addition of $[H^+]$, which decreases the pH of seawater in a process known as ocean acidification (OA) (Caldeira and Wickett, 2003). Figure 1.3, from Lan et al. (2023), clearly presents the *in situ* observations of increasing atmospheric $CO_2$ and seawater $pCO_2$, decreasing seawater pH, and their respective inverse relationships with each other over decadal timescales.

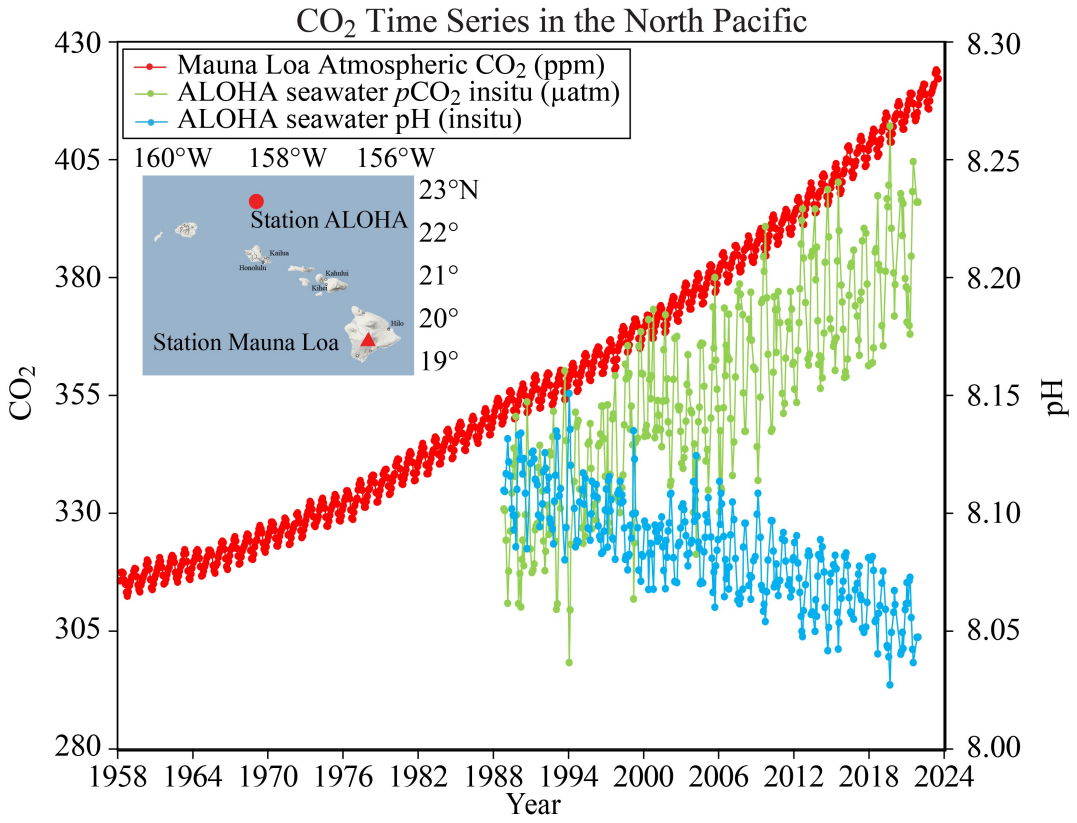


FIGURE 1.3: Long-term atmospheric and oceanic $CO_2$, pH, and $pCO_2$ time series. Red points show atmospheric $CO_2$ (ppm) measured at Mauna Loa Observatory, Hawai'i (Keeling et al., 1976). Blue points show surface seawater $pH_T$ over time. Green points show surface seawater $pCO_2$ ($\mu$atm) over time, both from Station ALOHA, calculated from discrete measurements of DIC and TA collected during Hawaii Ocean Time-series (HOT) cruises. Image from PMEL Carbon Program (2024) with data sources: Mauna Loa Observatory (NOAA Global Monitoring Laboratory, 2025) & Hawai'i Ocean Time Series station ALOHA (HOT, 2025).

Since 1750, the average pH of the global surface ocean has decreased by ~0.11, indicating acidification of 30% (Caldeira and Wickett, 2003; Orr et al., 2005; Jiang et al., 2019). Presently, pH is declining at a rate of ~0.002 $yr^{-1}$ (Jiang et al., 2019; Ma et al., 2023; Feely et al., 2024), but current adopted Shared Socioeconomic Pathways (SSP) models project pH to reach 7.68 by 2100 under high-emission, low-mitigation simulation (SSP-8.5; Kwiatkowski et al., 2020; Jiang et al., 2023). Decreasing pH reflects the shifting equilibria of the marine carbonate system (Equation 1.1) as $CO_2$ increases and

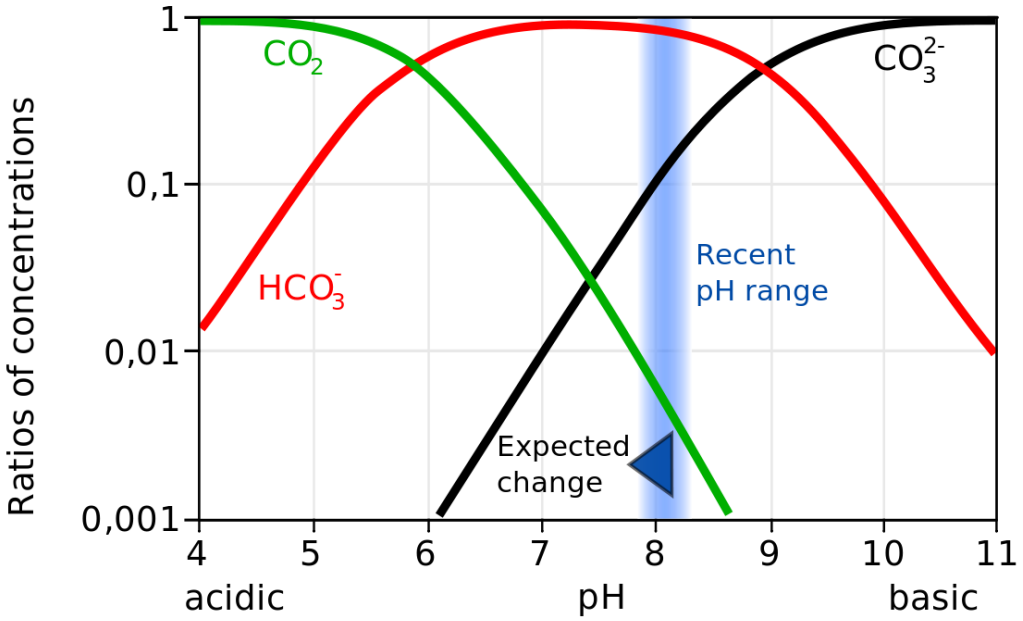


FIGURE 1.4: The Bjerrum plot (Zeebe, 2012; Wolff, 2007) demonstrates the shift in carbonate system speciation as a function of pH.

Ocean carbonation and acidification affect nutrient bioavailability to marine organisms as well as trace element speciation changes (Byrne, 2002). There is also evidence that particle sinking behavior is affected by acid-base equilibria, suggesting that vertical fluxes (e.g., the biological pump) may reduce under OA conditions (Sunda and Hanson, 1987; Millero, 2007). One of the most well-known implications of OA, however, is the threat to calcifying organisms. Definitionally, $CaCO_3$ precipitation is controlled by the concentration of carbonate ions (Equation 1.7, Figures 1.1), which decreases under ocean acidification (Figure 1.4), resulting in water conditions becoming chemically corrosive to aragonite and calcite ($\Omega_{arag/calc} < 1$). Severe decreases in calcification rates and degradation of calcareous structures have been observed in response to ocean acidification and decreasing $[CO_3^{2-}]$ across multiple taxa (Feely et al., 2004; Barton et al., 2012). Calcifying organisms such as corals, pteropods, coccolithophores, and bivalves face reduced capacity to build and maintain their calcium carbonate skeletons and shells, often leading to slower growth, weakened structures, and greater vulnerability to dissolution (Orr et al., 2005; Kroeker et al., 2013). These risks and implications extend beyond individual species, as reef frameworks, planktonic calcifying producers, and shellfish populations all play fundamental roles in supporting biodiversity, biogeochemical regulation, fisheries, and coastal protection. The sensitivity of these processes in the face of changing marine chemistry points to the importance of understanding not only global trends but also local variability of carbon cycling.

### 1.1.2 Coastal Processes

The changing ocean carbonate system is affecting the very basis of the marine food web and biogeochemical balance of the ocean. Consequentially, it is a direct threat not only to ocean health but to human prosperity, by threatening food and economic security. Today, 80% of megacities are coastal, and over 40% of the growing population live within 200 km of the ocean, making human reliance on the ocean's resources ever-increasing (Byrne, 2014). Although coastal regions only represent around 7% of total ocean surface area, they comprise more than 50% of economic value of the ocean's total services (Lønborg et al., 2021; Costanza et al., 2014). Furthermore, as the most biogeochemically active zones in the ocean, coastal systems are disproportionately important in the global carbon cycle (Gattuso et al., 1998). Carbon cycling in coastal waters and along the land-to-ocean transition is complex, dominated by dynamic and intertwined geochemical, physical and biological processes which vary at relatively short temporal and spatial scales. Our understanding of the mechanisms that drive these processes and their role in global carbon cycling is poor and limited by our ability to collect biogeochemical and, more specifically, carbon system data at high spatial and temporal resolution. This thesis provides examples of how autonomous technology can provide the observations needed to better understand carbon cycling and biogeochemical processing, demonstrated in two distinct key coastal systems (Shelf Seas and Coral Reefs).

#### Shelf Seas

Continental margins, defined by shelf seas and nearshore environments, support intense biological production, see strong gradients in temperature, salinity, and nutrients, and act as a major interface for carbon between land, sea, and atmosphere (Borges et al., 2005; Laruelle et al., 2014; Cai, 2011). From their complex physical, biogeochemical, and anthropogenic influences, coastal systems exhibit high variability, which complicates upscaling local observations to global assessments. These highly productive regions— accounting for 15–30% of global oceanic primary production— are characterized by enhanced air-sea $CO_2$ fluxes and are particularly vulnerable to anthropogenic forcings like OA and eutrophication (Gattuso et al., 1999; Duarte et al., 2013; Marrec et al., 2015). Understanding the influence of the coastal ocean is essential for resolving the trajectory of marine carbonate chemistry, yet it remains among some of the most uncertain components of the global carbon budget.

Shelf seas, such as the Celtic Sea, are highly productive transitional zones. The Celtic Sea, situated on the northwest European continental shelf is bounded by Ireland, the UK, and the Bay of Biscay (Figure 1.5). It exhibits strong seasonal cycling and stratification, which drive the development of spring plankton blooms, respiration-dominated bottom waters, and air–sea $CO_2$ exchange (Humphreys et al.,

2019; Cai, 2011). Like many shelf seas, it is estimated to contribute disproportionately to the global ocean sink, with shallow depths and benthic–pelagic coupling driving variability in carbonate chemistry that often exceeds that of the open ocean (Frankignoulle and Borges, 2001; Chen et al., 2013; Laruelle et al., 2018; Mathis et al., 2024). Despite it's ecological and economic significance, carbonate system observations in the Celtic Sea remain sparse and fragmented, historically limited to discrete sampling from research cruises, surface underway measurements, or predictive models (Borges and Frankignoulle, 2003; Hartman et al., 2014; Marrec et al., 2015; Humphreys et al., 2019). Chapters 2 and 3 of this thesis address this gap, by demonstrating and critically evaluating novel autonomous ocean observing technologies, methodologies, and analyses for capturing carbonate and biogeochemical variability across a range of spatial and temporal scales. Chapters 2 and 3 contribute results that help to better constrain the role of the Celtic Sea in regional and global carbon budgets (Figure 1.5).

**Coral Reefs**

Coral reefs are among the most biodiverse and valuable ecosystems on Earth, supporting human livelihoods through fisheries and tourism, while also providing natural coastal protection. They are biogeochemical hotspots for calcification and organic production, where photosynthesis, respiration, calcification, and dissolution often drive strong carbonate and biological diel variability (Gattuso et al., 1998; Cyronak et al., 2018; Cryer et al., 2023). These processes define a reef's metabolism, where net community calcification (NCC) and net community production (NCP) shape reef health and resilience on timescales ranging from hourly to decadal (Kayanne, 2025). Healthy reefs are characterized by sustained NCC exceeding dissolution and erosion, whereas reduced NCC or shifts toward NCP-dominated states often reflect stress or degradation (Andersson and Gledhill, 2013; Smith et al., 2016). Stressed or degraded reefs experience loss of resilience, which can lead to a benthic phase shift from predominantly coral cover to fleshy algae or other opportunistic species (Hughes et al., 2007). Globally, climate change induced stressors including OA and rising sea surface temperatures (SST) are linked to bleaching events, declining NCC, and shifts in reef metabolic balance (Bellwood et al., 2004; Hoegh-Guldberg et al., 2007; Erez et al., 2011; Heron et al., 2016; Davis et al., 2021).

The Red Sea provides a distinctive and understudied setting to investigate these dynamics. Dividing Africa and Asia, the Red Sea is a long, semi-enclosed basin connected to the Indian Ocean via the Bab el Mandeb strait (via the Gulf of Aden), and is among one of the warmest, most saline, and most oligotrophic bodies of water on Earth (Roder et al., 2013). Year-round temperatures range from 25–32°C, even exceeding 37°C in certain reef zones (Roik et al., 2016; Davis et al., 2011; Rich et al., 2022), yet the Red Sea is home to some of the world's most productive, endemic, and

diverse coral ecosystems, with reef frameworks spanning its entire coastline (DiBattista et al., 2016; Fine et al., 2019). Despite its characteristically extreme conditions, the Red Sea is not immune to climate change. Between 1998 and 2015, regional net contribution of hermatypic (reef-building) coral to the $CaCO_3$ budget declined by ∼100%, and calcification rates altogether declined by 26% (Steiner et al., 2018). Even with growing knowledge of Red Sea hydrography and ecology, there are few continuous carbonate system observations, with existing records limited to spatiotemporally infrequent discrete sampling.

Chapter 4 of this thesis presents the first high-resolution autonomous carbonate chemistry observations from a coral reef in the central Red Sea (Figure 1.5). By capturing multi-month variability across sites with different benthic community compositions, this chapter resolves both seasonal and diel cycles of reef metabolism and carbonate dynamics. Critically, this work also demonstrates the first deployment on any coral reef of a standalone autonomous TA sensor. Chapter 4 examines this deployment effort and its observations as a tool for evaluating reef metabolic balance in a region often cited for its apparent resilience, and reinforces the broader need for sustained, high-resolution carbonate measurements in coral reef systems.

Ultimately, improving observational coverage, critical analysis, and mechanistic understanding of coastal systems is required for reducing uncertainties in marine carbon chemistry and the global carbon budget as well as refining climate projections for policy discourse and mitigation efforts.

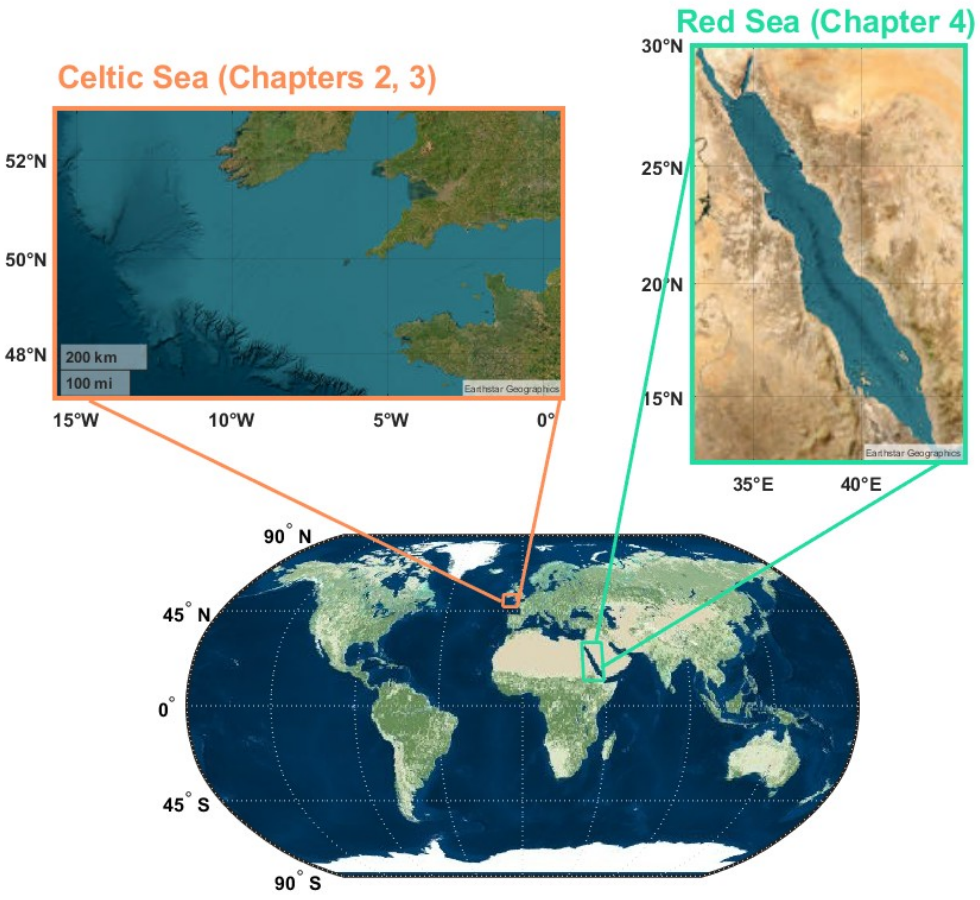


FIGURE 1.5: Map showing the global study regions investigated in this thesis. The Celtic Sea (Chapters 2 and 3) outlined in orange, and the Red Sea (Chapter 4) outlined in green.

## 1.2 Ocean Carbon Observation

The marine carbonate system (inorganic carbon) has been formally designated as an Essential Ocean Variable (EOV) by the Global Ocean Observing System (GOOS) for sustained measurement (IOCCP, 2017). This recognition points to the urgency for better understanding the ocean's role in global carbon cycling. This push calls for reinforcement of the base of the ocean carbon value chain, which links ocean carbon observations to climate models, and ultimately to informed decision-making on emission regulations and mitigation strategies (Tanhua et al., 2019). The utility of the carbon value chain, however, hinges on the quality and availability of the *in situ* observational data. The Global Ocean Acidification Observing Network (GOA-ON) has defined two quality objectives, climate and weather, as criteria for carbonate system observations (Newton et al., 2019). Climate quality observations, intended to resolve long-term climactic trends, require uncertainties of 0.003 in pH (total scale), $\pm 2$ $\mu$mol kg$^{-1}$ for TA and DIC, and $\sim$0.5% for $pCO_2$. Climate quality standards are presently achievable by few laboratories, but rarely achieved using autonomous

instrumentation. Weather quality objectives, by contrast, are designed to capture shorter-term variability and require uncertainties of ∼0.02 in pH, ± 10 $\mu$mol kg$^{-1}$ for TA and DIC, and ∼2.5% for $pCO_2$. Weather quality criteria is expected to be met by most competent laboratories, and high-quality, advanced technology readiness level (TRL) sensors with (Orr et al., 2018; Newton et al., 2019). Together, observations meeting climate and weather quality criteria form complementary tiers of the observing system, with the former providing essential reference baselines and the latter typically enabling sustained, high-resolution coverage.

Ship-based programs such as the Global Ocean Ship-Based Hydrographic Investigations Program (GO-SHIP), the Ships of Opportunity Program (SOOP), and data synthesis networks including the Global Ocean Data Analysis Project (GLODAP) and the Surface Ocean $CO_2$ Atlas (SOCAT) have provided the foundation of our current understanding of the marine carbonate system and subsequent processes (Feely et al., 2010; Bakker et al., 2016; Olsen et al., 2016; Wanninkhof et al., 2020). These coordinated efforts have produced climate-quality datasets that continue to serve as the benchmark for models and inventories of anthropogenic carbon storage. While these programs have provided valuable knowledge for decades, in the face of a rapidly changing climate, data availability is still scarce in time and space, leading to large uncertainties and discrepancies between models and observations (Friedlingstein et al., 2022; Hauck et al., 2023; Friedlingstein et al., 2025). Although ship-based operations provide the highest-quality observations and remain as the ”gold standard” for climate-quality inorganic ocean carbon monitoring, they face several limitations (Table 1.2). Research vessels are expensive to operate, labour-intensive, require long transit times, and often exhibit strong seasonal biases, particularly in polar seas where access is restricted to summer months (Lee et al., 2022b). Ship-based observations also struggle to capture the interannual and sub-seasonal variability that drives much of the spatiotemporal complexity in ocean carbon cycling, especially in coastal regions. Moreover, the global science community seeks to decarbonize oceanographic research and reduce the substantial carbon footprint of research vessels, in line with international governmental consensus (UNESCO-IOC, 2025). Collectively, these challenges highlight the need for complementary observing strategies that can increase spatiotemporal coverage and resolution, and reduce the (environmental and financial) costs of research, while still achieving current scientific and societal objectives.

TABLE 1.2: Comparative matrix of traditional ship-based and autonomous oceanographic observation using SWOT framework.

| | Ship-Based | Autonomous |
|---|---|---|
| **Strengths** | • Climate-quality, "gold-standard" measurements<br>• Tried and tested, trusted methods & QA/QC<br>• On site human expertise and flexibility<br>• Multi-parameter analysis from single discrete sample<br>• Only option for variable determination | • Persistent, high-resolution sampling across space/time<br>• Lower marginal cost per observation<br>• Reduced carbon footprint<br>• Physical access to harsh regions<br>• Remote data transfer<br>• Seasonally flexible<br>• Open access databases |
| **Weaknesses** | • Sparse in time and space<br>• Costly<br>• Seasonal and/or weather-limited<br>• High operational carbon footprint<br>• Labour intensive, human error<br>• Limited coverage between cruises<br>• Ship schedule dependent | • Equipment biofouling<br>• Instrument drift & calibration/QA issues<br>• Energy and communications constraints<br>• Many sensors remain low TRL or unavailable<br>• Barriers to entry include proprietary technology, capital requirements, & learning curves |
| **Opportunities** | • More hybrid efforts: ship–autonomy integration (SOOP)<br>• Fleet decarbonization (routing, alternative fuels)<br>• Cross-calibration/validation of networks and models | • Expanding open access databases<br>• Docking/recharge stations & energy harvesting<br>• Standardized, scalable, modular operations<br>• Maturing legal/policy frameworks<br>• Capture process-scale variability<br>• More data to improve models<br>• Machine learning for adaptive sampling |
| **Threats** | • Budget and emissions policies may reduce sea time<br>• Certified Reference Material production<br>• Persistent gaps if not integrated with autonomy<br>• Specialized personnel capacity | • Regulations (navigation, regional jurisdiction, IP)<br>• Research and development funding<br>• Platform loss, or failure risks without redundancy<br>• Raw materials & parts supply |

### 1.2.1 Autonomous Platforms and Sensors

The emergence and expansion of autonomous observing platforms and instrumentation provide a scalable and sustainable way forward to increased oceanographic sampling and data availability. Profiling floats, underwater gliders, and uncrewed surface vehicles have already transformed global monitoring of oxygen, nutrients, and other properties throughout the water column, and are now increasingly being equipped with carbonate sensors (Martz et al., 2015; Bushinsky et al., 2019; Whitt et al., 2020). These technologies begin to fill critical temporal and spatial gaps needed to constrain all parameters of the ocean carbonate system, processes, and ecological responses, as well as extending observations into regions inaccessible to ships, and provide the resolution required to capture diel-to-seasonal variability (Figure 1.6).

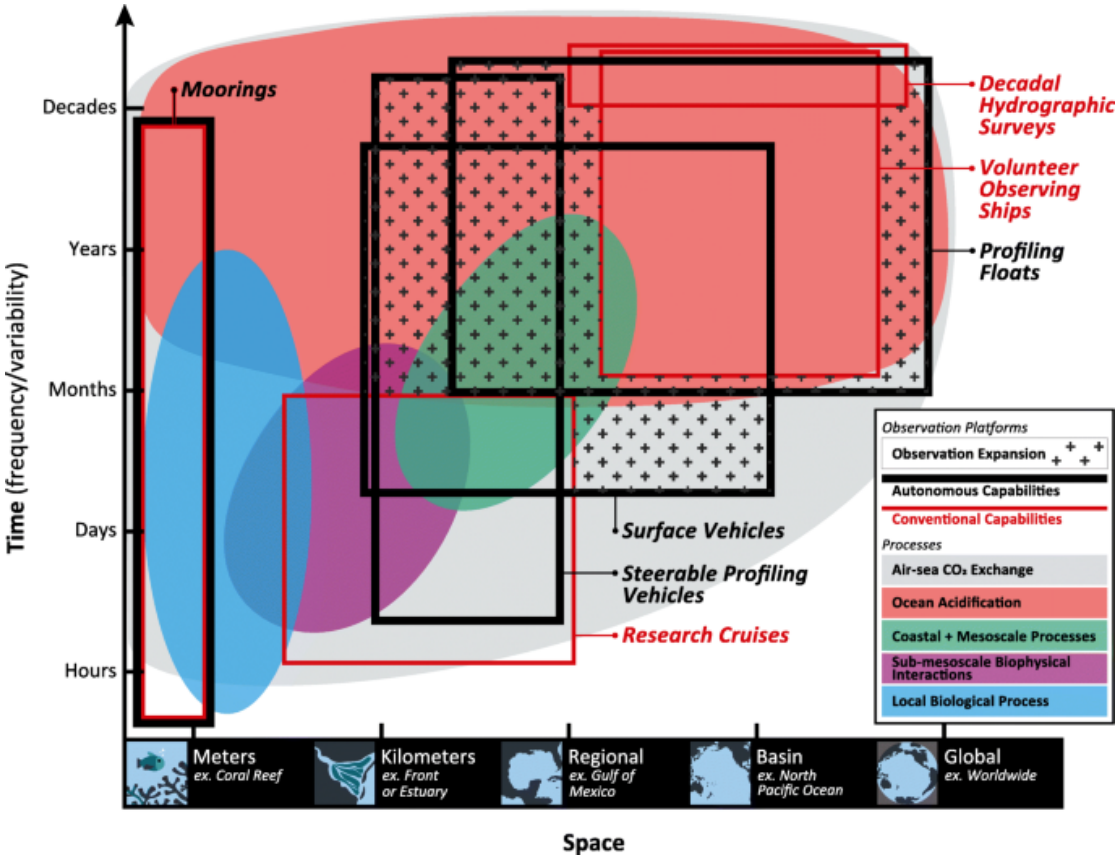


FIGURE 1.6: Illustration of the observational capabilities and gaps as a function of time and space in observing multiple ocean carbonate system processes from Bushinsky et al. (2019). The x-axis represents spatial domains from meters to global scales. The y-axis represents hourly–decadal timescales. Colored shaded regions highlight different ocean processes occurring in space and time. Conventional (ship-based) observing spatiotemporal capabilities are outlined in thin red lines. Autonomous observing spatiotemporal capabilities are outlined in thick black lines. The small black + signs show areas for expansion in observation.

Fixed ocean platforms such as moorings and seabed landers are some of the most robust and mature autonomous measurement platforms and provide long-term, records of physical and biogeochemical parameters including inorganic carbon (mainly $pCO_2$ and pH), vital for understanding seasonal to interannual environmental variability at key locations. The Moored Autonomous $pCO_2$ (MAPCO2 ; https://www.pmel.noaa.gov/) system, for example, operates and maintains global moored buoys that provide climate-quality observations of air-sea $CO_2$ dynamics (Sutton et al., 2014). The Porcupine Abyssal Plain Sustained Observatory (PAP-SO, est. 1989) operates as a multi-disciplinary open-ocean time series site in the NE Atlantic focused on monitoring EOVs such as ocean temperature, salinity, pH, $CO_2$, oxygen, nutrients, benthic ecology, and more from the surface to the seafloor and throughout the water column (Lampitt et al., 2010; Hartman et al., 2021; Gates et al., 2021). Additionally, regional cabled and moored array infrastructure maintained by the Ocean Observatories Initiative (OOI) around the Americas host platforms and sensors tied to fiber optics, which deliver real-time data streams of more than 900 deployed instruments, including measurements of *in situ* $pCO_2$ and pH over multi-year timescales and across the full water column (Kelley et al., 2016; Trowbridge et al., 2019). Chapter 4 of this thesis demonstrates the value of fixed point observations in understanding high-frequency biogeochemical processes in highly dynamic marine environments such as coral reefs.

Profile floats are compact, low-consumption, buoyancy-driven, autonomous platforms that continuously profile the water column, while maintaining drift at depth and periodically surfacing to transmit data. The Biogeochemical Argo Float Program (BGC-Argo) is a global array of autonomous profiling floats equipped with sensors to measure biogeochemical EOVs, and now generate global pH datasets producing more than five times as many pH profiles annually as ship-based measurements (Roemmich et al., 2019; Claustre et al., 2020). Underwater autonomous gliders, propelled by variable-buoyancy systems and wing lift, provide sustained, high-resolution horizontal sections and vertical profiles of pH, $pCO_2$, oxygen, and nutrients across shelf seas and boundary currents. Successful deployments of pH and $pCO_2$ of sensors integrated onto gliders include missions conducted off the United States Northeast coast, (Saba et al., 2019, 2018), the Gulf of Alaska (Hauri et al., 2024), the Labrador Sea (von Oppeln-Bronikowski et al., 2021; Morgan et al., 2025), and within the California Current System (Takeshita et al., 2021).

Uncrewed Surface Vehicles (USVs) offer long-endurance, wind or wave-powered operations that can carry large payloads. Saildrone and Wave Glider USVs have been equipped with systems such as the Autonomous Surface Vehicle $CO_2$ ($ASVCO_2$), enabling basin-scale, high-resolution $CO_2$ air-sea flux quantification in regions previously inaccessible to ships (Sabine et al., 2020; Sutton and Sabine, 2023). Similar pH and $pCO_2$ instrumentation systems have been integrated onto Wave Gliders

including coastal observation deployments by Chavez et al. (2018) and Northcott et al. (2019).

Autonomous Underwater Vehicles (AUVs) are self-contained, untethered vehicles designed to operate underwater without human intervention. AUVs use sensors, onboard computers, and propulsion systems to navigate the ocean and collect data (Bellingham, 2009; van Rein, 2018). They are self-powered, with their energy stored onboard, typically in the form of high-capacity batteries. AUVs are equipped with rugged hardware including pressure vessels that house sensitive electrical components. The AUV's outer shell, or fairing, must be able to withstand harsh conditions of the ocean environment such as biofouling, extreme temperatures, or high wave energy. These vehicles have been increasingly equipped with scientific sensors, yet only few AUV deployments have integrated pH or $pCO_2$ sensors (e.g., Monk et al. 2021). Chapters 2 and 3 of this thesis directly address this gap by presenting and evaluating new capability in ocean carbon observations using novel sensors integrated in state-of-the-art AUVs.

Despite rapid advances in platform technologies during the last decade, available sensor technology still limits our ability to collect high-quality carbon system observations. As clearly showcased above and in Table 1.3, pH and $pCO_2$ are the only carbonate variables that can be measured directly with commercially available sensors suitable for autonomous platforms (Byrne, 2014; Martz et al., 2015; Bushinsky et al., 2019). While these sensors have reached relatively high technology readiness levels, characterising the seawater carbonate system from $pCO_2$ and pH observations propagates uncertainties that are too large for calculating key parameters such as $CO_2$ flux, carbon budgets and saturation states (Table 1.1). As it stands, measurement of DIC and TA are limited to lab-based benchtop instrumentation. This disparity between available technology and measurement needs is illustrated below in Table 1.3, which summarizes the current commercial sensor availability. Significant effort has been invested in the last decade in developing sensors that would fill this gap. This thesis demonstrates the potential of some of these technologies in providing better quality ocean carbon observations and better constraining ocean carbon cycling.

TABLE 1.3: Current commercially available carbonate technology categorized by level of autonomy.
Adapted from Martz et al. (2015); Byrne (2014); Bushinsky et al. (2019)

| | **BENCHTOP** [1] | **UNDERWAY** [2] | **AUTONOMOUS** [3] |
|---|---|---|---|
| **DIC** | VINDTA 3D/3C (Marianda)<br>AIRICA (Marianda)<br>AS-C3 (Apollo SciTech) | | |
| **TA** | OMNIS, Titrando,<br>Ti-Touch (Metrohm)<br>VINDTA 3S/3C (Marianda)<br>AS-ALK2 (Apollo SciTech) | HydroFIA (CONTROS/4H Jena) | |
| **pH** | | AFT-pH (Sunburst Sensors)<br>SP200-SM (SensorLab)<br>FireSting-PRO (PyroScience)<br>Pico-pH (PyroScience)<br>IQ SensorNet 2020 (YSI) | SAMI-pH (Sunburst Sensors)<br>SeaFET (Sea-Bird Scientific)<br>SP101-LB (SensorLab)<br>AquapHOx (PyroScience)<br>Pico-PH-SUB (PyroScience)<br>QC1250 (ANB Sensors)<br>LOC pH Sensor (ClearWater Sensors) |
| **$pCO_2$** | | GO 8060 (General Oceanics)<br>MOG 701 (Kimoto)<br>Super$CO_2$ (Sunburst Sensors)<br>OceanPack (SubCtech)<br>AFT-$CO_2$ (Sunburst Sensors)<br>AS-P2 (Apollo SciTech)<br>SUNDANS (Marianda) | Seaology (Battelle)<br>SAMI-$CO_2$ (Sunburst Sensors)<br>HydroC (Contros)<br>$CO_2$-PRO (Pro-Oceanus)<br>OceanPack (SubCtech)<br>C-Sense (Turner Designs) |

[1] Benchtop auto-assisted instruments for analysis of discrete samples.
[2] Underway systems on ships for semi-autonomous flow-through sampling, externally powered, often non-submersible and fixed onboard.
[3] Autonomous sensors for *in situ* sampling, internally powered.

**Lab-On-Chip Sensors**

Lab-on-Chip (LOC) technology offers miniaturisation of high-performance wet-chemical analyses into low-power, low-reagent autonomous instruments suitable for fixed and mobile platform integration (Manz et al., 1990; Jokerst et al., 2011; Rérolle et al., 2013; Yin et al., 2021). Compared with typical, reagent-based analysers, LOC technology offers integration of fluidic components (e.g., mixers, detectors, valves, etc.) within a microfluidic chip reducing the need for fluidic and electrical connectors and complexity in general and improving robustness and reliability. The integrated nature of this technology also reduces size and power consumption and keeps reagent consumption to a minimum enabling long unattended deployments (e.g., longer than a year). The specialized capabilities of LOC in achieving laboratory-quality *in situ* measurements has made them a valuable tool for environmental monitoring (Campos and Silva, 2013).

LOC based sensors have been in development at the National Oceanography Centre (NOC) for the last two decades. The NOC LOC wet chemical sensor platform is a miniaturised, robust (6000 m depth-rated), autonomous chemical analyser specifically developed for integration on autonomous platforms. The sensor comprises a high-precision pump, miniaturised valves, pressure-tolerant electronics and optics, outer housing for reagent bags, and a microfluidic chip manufactured using patented methodologies (Figures 1.7 and 1.8)

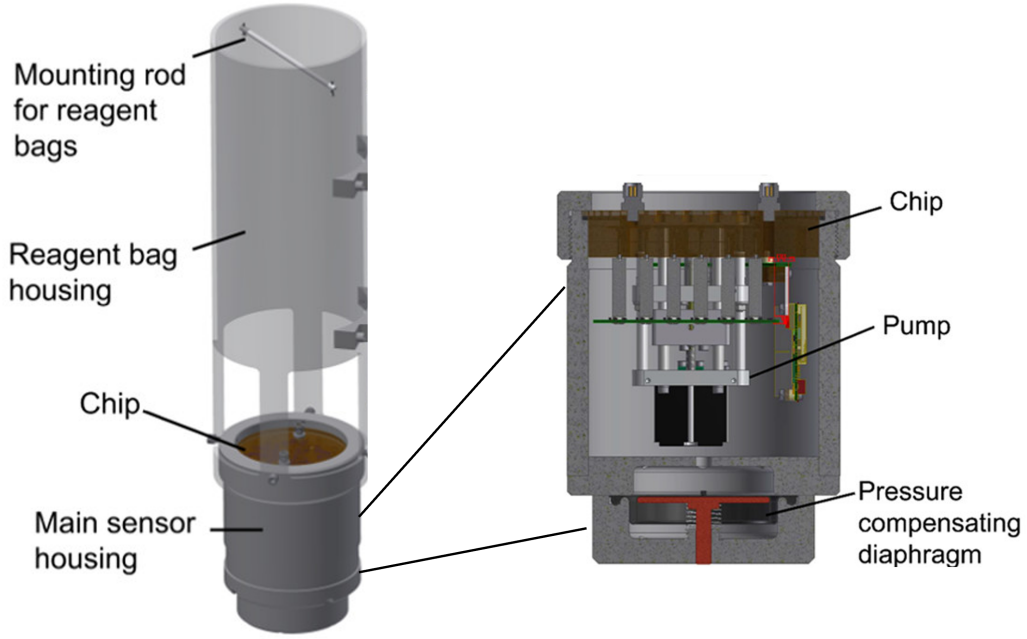


FIGURE 1.7: Schematic of an assembled LOC sensor (left) with reagent bag housing, mounting rod for bags to hang, and main sensor with zoomed inset (right) showing cross-section of main sensor housing, which oil-filled and encapsulates the microfluidic chip and mechanical components of the sensor.

The central component of an LOC platform is a round three-layer dark poly(methyl methacrylate) (PMMA) chip (Figure 1.8 whose microfluidic channels are micro-milled out before each layer is bonded together (Ogilvie et al., 2010; Beaton et al., 2022). The chip also forms the end cap to the underwater housing, allowing it to withdraw *in situ* seawater samples. The outside layer of the chip contains tapped fluidic ports, while the middle layer contains encapsulated nuts that the pump and valves are fixed to. The inside layer contains the milled microfluidic channels, optical cells, light sources, and light detectors (Figure 1.8).

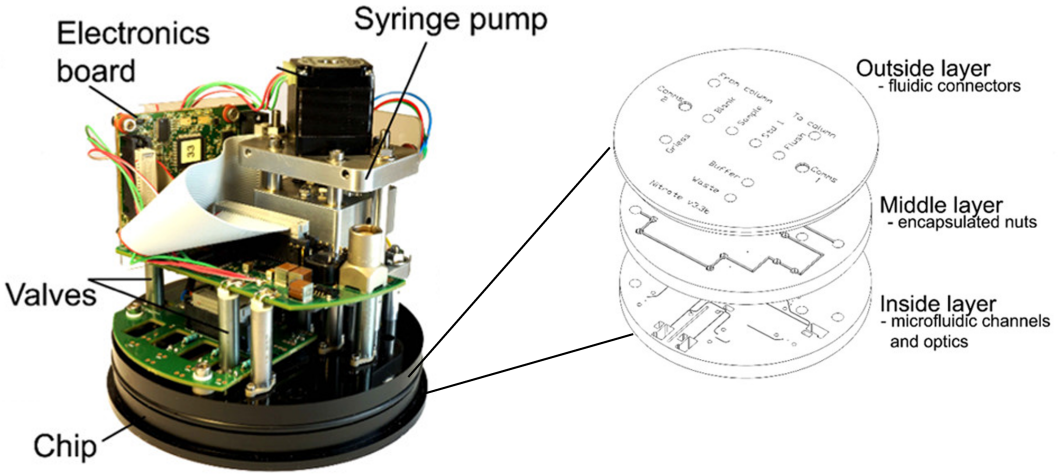


FIGURE 1.8: Close up image (left) of the inside of an LOC sensor showing the microfluidic chip, syringe pump, valves, and electronic board. Zoomed schematic (right) of and example deconstructed three layers of the microfluidic chip shown prior to bonding.

Different fluidic layouts in the microfluidic chip allow for implementation of most reagent-based analytical assays (Figures 1.9a and 1.10a). These assays are all based upon certified or trusted, existing "gold standard" laboratory methods enabling intercomparison with existing datasets and facilitating transition from traditional sample-based measurements. Differences between LOC variants are mostly limited to the fluidic layout, which enables improved robustness and reliability (through more extensive testing and focused design effort), in addition to economies of scale. Low sample requirements for analysis (<1 mL) enables the use of small filter inlets (e.g., 0.45 $\mu$m pore size syringe filters) reducing biofouling during long deployments, while the small volume of analytical waste produced can be stored onboard avoiding potential impacts when deployed within sensitive ecosystems such as coral reefs. Integration on autonomous platforms is enabled by simple mechanical integration and by utilizing the power and communications (RS232) interface provided. For the

latter, a command set enables external control and triggering of pre-programmed states as well as either platform driven (polled) or sensor-initiated transfer of data.

LOC sensors are particularly advantageous for autonomous ocean observing because they make discrete *in situ* measurements by withdrawing a small sample volume of seawater, rather than relying on membrane-based diffusion and/or equilibration processes seen in other sensors. As a result, LOC sensors do not experience a response time, meaning a change in the surrounding environment will be detected immediately during sample intake, and not require multiple measurements to re-equilibrate. Additionally, the long-term stability of the indicator dyes and photometric principle of the measurements, which are independent of changes in detector sensitivity and light source intensity, make LOC sensors far more resistant to drift compared to other optical or electrochemical chemical sensors (Müller and Rehder, 2018; Mosley et al., 2004; Rérolle et al., 2012). The reagent-based nature of LOC sensors also allow for the instruments to carry extra onboard standards and calibration material, which improve quality control efforts and measurement validation (shown in Chapter 4).

Currently, several assays have been implemented on the current version of the LOC platform including nitrate/nitrite, phosphate, silicate, iron and pH, all of which have been commercialised and can be supplied by Clearwater Sensors LTD (CWS; `https://www.clearwatersensors.com/`). These sensors have been deployed by NOC and many end-users globally, integrated on stationary and moving autonomous platforms for diverse applications including nutrient run-off monitoring, ocean biogeochemical monitoring and for detection of $CO_2$ leakage from sub-seabed $CO_2$ storage sites (Beaton et al., 2017; Geißler et al., 2017; Monk et al., 2021; Possenti et al., 2021; Schaap et al., 2021a; Yin et al., 2021; Beaton et al., 2022). Analytical assays for ocean DIC and TA measurements have also been implemented on this LOC platform over the last decade reaching higher TRLs in spring 2022 during the demonstration trial in the Celtic Sea (DY149; Chapter 2). The TA sensor has been demonstrated in several applications including monitoring sub-seabed $CO_2$ storage sites in estuaries (Schaap et al., 2021a) and on autonomous platforms (Chapter2; Hammermeister et al. 2025; Chapter4). In addition, a combined TA/DIC system (TADIC) is currently under development (both TA and DIC measurements from a single LOC platform). The ability to measure two carbonate system variables from a single platform will enable complete carbonate system characterisation by small autonomous platforms such as gliders and profiling floats, which generally have limited payload capacity. The LOC sensors used in this thesis are the pH sensor (Chapters 2, 3, and 4) and the TA sensor (Chapters 2 and 4) developed and operated by NOC.

#### Lab-On Chip pH Sensor

The LOC pH sensor determines pH on the total proton scale photometrically using purified mCP indicator dye (Yin et al., 2021). The sensor operates by using large and

small barrel pumps respectively to withdraw a 700 $\mu$L seawater sample and then inject 3 $\mu$L of indicator dye (Figure 1.9). The sample-indicator solution transfers slowly (57 $\mu$L min$^{-1}$ through the serpentining microfluidic channels, which forces the dispersion and diffusion of the indicator into the sample (Figure 1.9). Light-emitting diodes (LEDs) illuminate the solution within the optical cell at wavelengths ($\lambda$) of the protonated and deprotonated mCP absorbance maxima (434 and 578 nm respectively). Absorbance measurements ($A_\lambda$) are made within the optical cell over time using photo diode (PD; Figure 1.9a) detectors, which yield the Taylor-Aris dispersion curve used to calculate pH (Seidel et al., 2008; Rérolle et al., 2013). Each measurement sequence takes 8 minutes to complete, which includes two sample rinses (for reference absorbance measurement), sample withdrawal, dye injection, absorbance measurements, and sample discharge (Yin et al., 2021). The mCP reagent and waste are stored onboard in flex bags and connected to the sensor using peek tubing.

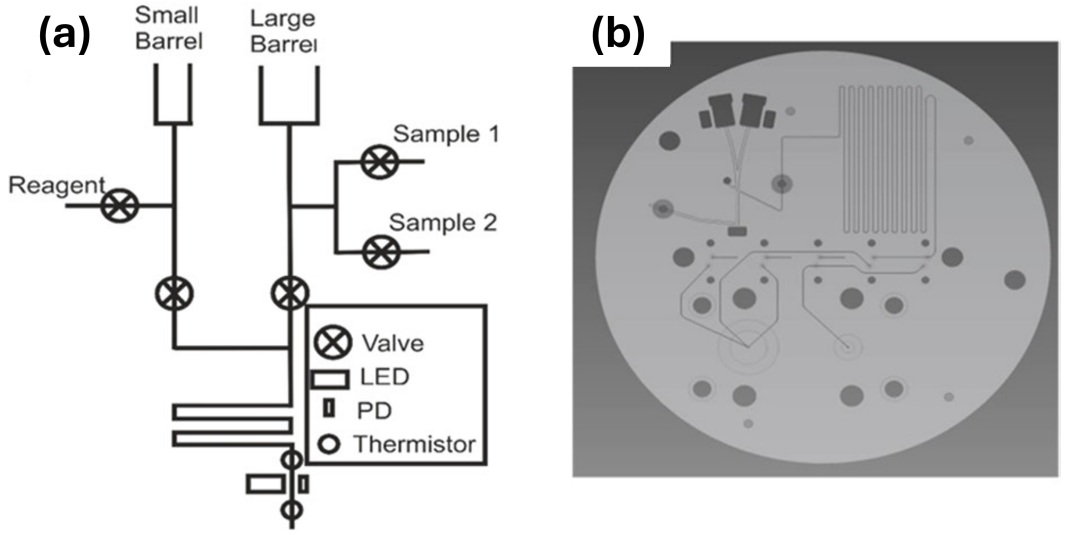


FIGURE 1.9: Lab-On-Chip pH sensor diagram of the (a) microfluidic channel schematic and (b) CAD design of the microflidic channels within the chip. Diagram adapted from Yin et al. (2021).

The sensor measures pH ($pH_{T,m}$) at the temperature within the optical cell ($t_m$) using internal thermistors (Figure 1.9a) and according to equation 1.9:

$$pH_{T,m} = -\log(K_2 e_2) + \log\left(\frac{R - e_1}{1 - R\frac{e_3}{e_2}}\right) \tag{1.9}$$

Where $K_2$ is the second stochiometric (concentration-based) equilibrium dissociation constant of mCP, $e_1$, $e_2$, and $e_3$ are molar extinctions coefficient ratios of mCP, and $R = A_{578}/A_{434}$ is the conventional ratio of absorbances at the absorbance maximum wavelengths 434 and 578 nm (Li et al., 2020; Yin et al., 2021). The *in situ* pH ($pH_T$) is

then derived from $pH_{T,m}$ using the linear temperature factor from Millero (1995):

$$pH_T = pH_{T,m} - 0.01582(T - t_m) \tag{1.10}$$

$K_2$, $e_1$, $e_2$, and $e_3$ used in equation 1.9 are computed from their *in situ* salinity (S) and temperature (T) functions. S and T (used in equation 1.10) are determined independent from the LOC pH sensor, e.g., from a co-deployed CTD (conductivity, temperature, depth) probe for field deployments. The combined standard uncertainty of the sensor $pH_T$ measurements is estimated to be 0.010 pH units (Yin et al., 2021).

**Lab-On-Chip TA Sensor**

The LOC TA sensor measures the alkalinity of a seawater sample using a single-point titration. Seawater is withdrawn into the microfludidic channels inside the sensor using custom syringe pumps (Figures 1.7, 1.8, and 1.10a). The sample is then combined with HCl titrant and (unpurified) Bromophenol Blue (BPB) indicator dye in the microfluidic mixer, where it is acidified to endpoint pH = 3.0–3.5 (Culberson et al., 1970). The acidification of the seawater sample produces $CO_2$, which is removed across a gas-permeable membrane into a recipient solution of sodium hydroxide (NaOH) (Figure 1.10b). The resulting solution is sequentially illuminated in an optical cell by two LEDs with wavelengths ($\lambda_1$ = 435 nm and $\lambda_2$ = 591 nm) determined as the absorption peaks of the pH indicator's protonated and deprotonated forms (Schaap et al., 2025). A photodiode (light detector) at the end of the optical cell then converts the amount of light transmitted into a voltage, which yields measurements of optical absorption (Figure 1.10).

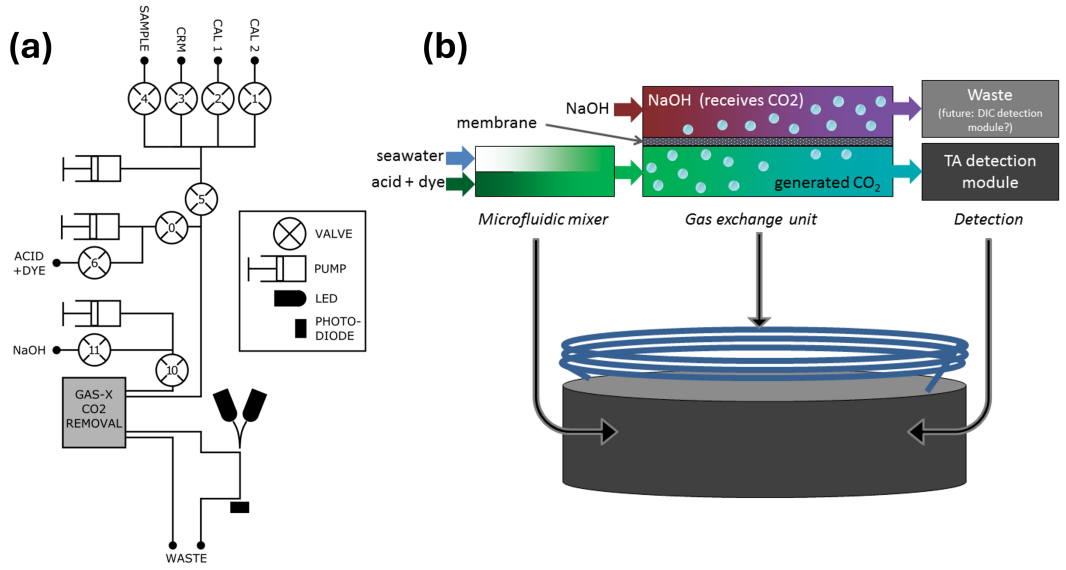


FIGURE 1.10: Lab-On-Chip TA Sensor diagram with (a) microfluidic channel schematic and (b) conceptual diagram of TA system components and measurement process.

The ratio of absorbances (R) is normalised to temperature T=25 °C using a linear coefficient to account for the temperature sensitivity of the pH indicator dye (Breland and Byrne, 1993). The solution pH at the titration endpoint is determined photometrically (Culberson et al., 1970) and is given by the equation:

$$\begin{aligned} \mathrm{pH_{SWS}} &= -\log([\mathrm{H^+}]_{\mathrm{SWS}}) \\ &= c_1\,\mathrm{pK_{a,SWS}} + c_S(35\text{-}S) + \log_{10}\left(\frac{R - e_1}{e_2 - Re_3}\right) \end{aligned} \tag{1.11}$$

which is derived from the equilibrium dissociation reaction of the protonated form of the dye expressed on the seawater proton scale (SWS), with $pK_{a,SWS}$ = -log($K_{a,SWS}$), $K_{a,SWS}$ = stoichiometric equilibrium second dissociation constant (mol/kg), $c_S$ a linear salinity correction factor (Breland and Byrne, 1993), $c_1$ an instrument and environmental-specific calibration factor, and $e_1$, $e_2$, and $e_3$ as ratios of the molar attenuation coefficients of the dye determined at T = 25 °C and S = 35 (Schaap et al., 2025). The endpoint excess proton concentration in the titrated sample in the presence of BPB, i.e., the sum of proton donors (acids) as defined for the zero proton condition for total alkalinity (Dickson, 1981; Wolf-Gladrow et al., 2007a) is then defined as

$$[\mathrm{H^+}]_{\mathrm{excess}} \approx [\mathrm{H^+}]_{\mathrm{SWS}} \tag{1.12}$$

Finally, the sample TA ($\mu$mol kg$^{-1}$) is computed as:

$$TA = 10^{6} \frac{-[H^{+}]_{excess}(m_S + m_A) + c_2 M_A m_A}{m_S} \tag{1.13}$$

where $m_A$ is the titrant mass, $m_s$ is the sample mass, $M_A$ is the titrant acidity (in $\mu$mol kg$^{-1}$) and $c_2$ is an instrument and environmental-specific calibration factor. Titrant and sample masses are replaced by volume ratios defined by the syringe pump geometry, given that the titrant, reference materials, and samples have matching salinity and therefore equal density effects. All associated titrants, reagents, and waste products are stored onboard contained in flex bags and connected to the sensor using peek tubing. The LOC TA sensor has a precision and accuracy better than 5 $\mu$mol kg$^{-1}$ (Schaap et al., 2025).

This thesis showcases these new LOC sensors through a number of field deployments in order to evaluate their potential for expanding and improving global ocean carbon observations. Data and analysis is presented from autonomous deployments of LOC pH and TA sensors integrated on moving and fixed platforms to resolve diel-to-seasonal carbonate system dynamics. In doing so, these chapters demonstrate how LOC carbonate sensors expand the operational envelope of marine carbon observations from both a spatial (shelf seas to coral reefs) and temporal (hours to months) perspective, directly addressing gaps in ocean observing capability.

## 1.3 Thesis Overview

The aim of this doctoral research was to demonstrate and examine the scientific capabilities of novel autonomous instrumentation for ocean carbon observation. A series of applications as three separate deployments informed each science chapter of this thesis and inspired the following central questions:

- How capable is emerging autonomous technology compared to traditional methodology in measuring and characterizing marine carbon? (Chapter 2)
- How will new developments in autonomous sensor and platform technologies help fill gaps in shelf seas carbon observations? (Chapter 3)
- What are the controlling metabolic processes and carbonate dynamics of a coral reef in a unique and understudied region, and can they be resolved from autonomous sensor observations? (Chapter 4)

### 1.3.1 Hypotheses

Chapter 2

- Autonomous pH and TA observations from sensors on an AUV can be of comparable quality to those collected using traditional methods from a ship.
- Challenges in comparing AUV with ship observations in space and time can be adequately resolved using spatial interpolation methods.
- High-resolution observations collected using an AUV can reveal environmental features that traditional surveys can overlook.

Chapter 3

- Characterizing the carbonate system in shallow coastal waters using autonomy and associated computational methods (as per BGC Argo) can lead to significant errors.
- Sensor redundancy can improve data quality by providing a better means for sensor drift correction than traditional computational techniques.
- Total Alkalinity parameterisation using established regional algorithms can be of adequate quality for carbonate system characterization when paired with measured pH from autonomous sensors.

Chapter 4

- High resolution pH, TA, $pCO_2$, and DO observations can help disentangle dominant metabolic processes in a reef system
- TA and pH sensor measurements will reveal the relative contribution of NCP and NCC to the reef's metabolic signal
- High-frequency autonomous observations will capture diel and seasonal variability in reef carbonate chemistry that would be otherwise unresolved by traditional sampling approaches.
- The relative contributions of NCP and NCC to the reef's metabolic signal will be related to the benthic community composition of the reef.

### 1.3.2 Summary

Chapter 2 was originally published in Environmental Science & Technology as Hammermeister et al. (2025) entitled: "New Capability in Autonomous Ocean Carbon Observations Using the Autosub Long-Range AUV Equipped with Novel pH and Total Alkalinity Sensors" (https://doi.org/10.1021/acs.est.4c10139). It presents the first known characterization of the marine carbonate system from an autonomous vehicle based on *in situ* sensor measurements of pH and TA. This chapter examines the intricacies involved in autonomous data collection, analysis, and interpretation, as well as how to validate sensor measurements from a moving platform that are not spatiotemporally synced with discrete "gold standard" co-samples.

Chapter 3 is currently under review for publication in the Journal of Geophysical Research: Oceans as Hammermeister et. al. (2025) entitled: "Coastal Marine Carbon and Air-Sea Fluxes Quantified from pH Sensors on an Extended AUV Deployment". This work showcases the findings from two pH sensors onboard the first fully autonomous long distance scientific mission by the Autosub Long Range AUV, which spanned over five weeks and 2,000 km. The marine carbonate system and air-sea $CO_2$ fluxes are quantified from the novel dataset, revealing seasonal, spatial, and temporal trends and variability. Furthermore, the chapter evaluates the competency of global model estimates and established correction procedures for use with high-resolution pH data, in a dynamic coastal application.

Chapter 4 forms a paper that that is currently undergoing journal submission for publication as an original research article with the following authors: as Hammermeister et. al (2025) entitled: "Metabolic Dynamics of an Offshore Coral Reef in the Red Sea: Observations from Autonomous Sensors". This chapter resolves reef metabolism and carbonate dynamics of a coral reef in the central Red Sea using an extensive, multi-month suite of autonomous, high-resolution sensor observations. To our knowledge, this represented the first-ever deployment of an autonomous stand-alone TA sensor on a coral reef, which provided a unique opportunity for benchmark observations and evaluation of reef carbon cycling in an understudied region.

# Chapter 2

# New capability in autonomous ocean carbon observations using the Autosub Long-Range AUV equipped with novel pH and Total Alkalinity sensors

This chapter forms a paper that has been published in *Environmental Science & Technology* as an original research article:

**Emily M. Hammermeister**, Stathys Papadimitriou, Martin Arundell, Jake Ludgate, Allison Schaap, Matthew C. Mowlem, Sara E. Fowell, Edward Chaney, and Socratis Loucaides. New capability in autonomous ocean carbon observations using the Autosub Long-Range AUV equipped with novel pH and Total Alkalinity sensors. *Environmental Science & Technology* 59:7129–7144, 4 2025. ISSN 0013-936X, https://doi.org/10.1021/acs.est.4c10139, doi: 10.1021/acs.est.4c10139

## Abstract

The development of marine autonomous platforms has improved our capability to gather ocean observations at fine spatial scales and high temporal frequency, which can be used to better measure, characterise, and model ocean carbon. As part of the OCEANIDS programme, novel carbonate sensors were integrated onto the Autosub Long Range (ALR) Autonomous Underwater Vehicle (AUV) and deployed in the Celtic Sea. Autonomous Lab-On-Chip (LOC) sensors measured pH and Total Alkalinity (TA) while onboard the ALR. Using interpolation, the ALR-sensor dataset is compared against CTD co-samples. The average differences between LOC sensor and co-sample pH ranges from -0.011 to -0.015. The TA sensor data agrees with co-samples within 1–2 $\mu$mol kg$^{-1}$ on average. Biogeochemical water properties differing between CTD and ALR observations reveal correlations to carbonate parameter variations. The LOC sensors enabled characterisation of the marine carbonate system from autonomous subsurface measurements for the first time. Sensor pH and TA data were used to calculate Dissolved Inorganic Carbon (DIC), partial pressure of $CO_2$ ($pCO_2$), and aragonite saturation state ($\Omega_{Ar}$) and are compared with CTD co-samples with mean residuals of 4–7 $\mu$mol kg$^{-1}$, 10–17 $\mu$atm, and -0.03 to -0.06, respectively. Future perspectives on sensor deployment and analysis are discussed.

## 2.1 Introduction

It has long been established that carbon dioxide ($CO_2$) levels in the atmosphere are rising. Since the start of the industrial era, total atmospheric $CO_2$ concentration has increased by over 50%, with current anthropogenic emissions surpassing 11 Gt C $yr^{-1}$ (Friedlingstein et al., 2023). The ocean is a natural carbon sink that, in the last decade, has absorbed 2.9 $\pm$0.4 Gt C $yr^{-1}$, equal to 26% of total anthropogenic $CO_2$ emissions (Friedlingstein et al., 2023; Quéré et al., 2009b). As atmospheric $CO_2$ dissolves into the ocean, it reacts with seawater to form carbonic acid, which dissociates into bicarbonate ($HCO_3^-$), carbonate ($CO_3^{2-}$), and hydrogen ($H^+$) ions (Barker and Ridgwell, 2012). The net addition of $H^+$ acidifies the seawater (lowers the pH) in a process known as ocean acidification (Caldeira and Wickett, 2003), and changes the speciation within the carbonate system (Wolf-Gladrow et al., 2007b; Zeebe, 2012). While atmospheric $CO_2$ continues to rise and the ocean continues to take up more $CO_2$, the ocean's capacity to absorb surplus anthropogenic $CO_2$, or buffer global climate change, has decreased (Feely et al., 2004; Tans, 2009). In fact, recent models suggest the ocean's buffer capacity could decrease as much as 34% by 2100, likely accelerating ocean acidification (Jiang et al., 2019).

Ocean acidification and the changing ocean carbonate system is affecting the basis of the marine food web and marine biogeochemical cycles. It is not only a threat to marine health, but to human prosperity by threatening food and economic security (Whitt et al., 2020). Over 40% of the growing human population live in coastal regions, making our dependence on the ocean's resources ever-increasing (Byrne, 2014).

Reflecting the urgency and importance of understanding the changes to the ocean carbon system, the Global Ocean Observing System (GOOS) has deemed inorganic carbon (ocean carbonate system) as an Essential Ocean Variable (EOV) to measure. Ocean carbon observations are essential for assessments of the ocean carbon budget and quantification of fluxes which, through the ocean carbon value chain, are used to inform policymakers and stakeholders on managing emissions and climate change mitigation strategies (Tanhua et al., 2019). However, the quality of these assessments are a function of the quality and availability of carbon data observations that have come from ship-based programs (e.g., GO-SHIP, SOOP, etc). While these programs have provided critical insights into the ocean carbon cycle, data availability is scarce in time and space, leading to large uncertainties and discrepancies between models and observations (Friedlingstein et al., 2022; Hauck et al., 2023) that hinder policymaking progress and climate resolution.

Although offering the highest quality observations required to track climate-scale changes in the ocean's carbon system, traditional ship-based observing strategies have several limitations including high operating costs, long transit times, and practical seasonal biases—especially in polar regions (Lee et al., 2022a). Ship-based

observations often fail to capture interannual variability and the dynamic spatiotemporal variability in coastal oceans. Additionally, the carbon footprint of ship-based operations is facing increasing scrutiny as the world strives to achieve net-zero carbon emissions (e.g., Future Marine Research Infrastructure (`https://fmri.ac.uk`). Efficient and sustainable ocean observing strategies are therefore needed to increase measurement resolution in space and time, complementing ship-based methods in an effort to decarbonise marine research and meet current scientific and societal needs.

The emergence and expansion of autonomy in ocean observations, specifically platforms such as profiling floats, underwater gliders, and surface vehicles equipped with scientific sensors, offer a scalable, sustainable, and complementary solution to the current observational needs. Even so, the lack of autonomous sensors for direct characterisation of the ocean carbonate system remains as the limiting factor to wide-scale and high-resolution ocean carbon observations.

To quantify and characterise the marine carbonate system, there are four measurable key variables to consider: Dissolved Inorganic Carbon (DIC), Total Alkalinity (TA), pH, and partial pressure of $CO_2$ ($pCO_2$) (Byrne, 2010). The carbonate system can be constrained by a system of stoichiometric equations so that any pair of these four parameters can be used (alongside salinity, temperature, and pressure) to calculate the remaining two (Millero, 2007). Currently, only sensors measuring pH and $pCO_2$ are available commercially and capable of autonomous observations. However, because of the covariance of these two parameters in the environment, their choice as input parameters is less desirable since it leads to large uncertainties in the characterisation of the carbonate system (Orr et al., 2018; Sutton and Sabine, 2023). In the absence of commercial, integrable sensors capable of directly measuring TA or DIC *in situ*, characterisations of the carbonate system based on autonomous platform observations (e.g., BGC-Argo and SOCCOM programs) rely on TA estimated from empirical algorithms using salinity, oxygen and nutrients as input parameters (Carter et al., 2018; Juranek et al., 2011). Although this approach provides a good alternative to direct observations, its applicability and reliability varies.

There has been recent work to integrate carbonate sensors onto autonomous platforms including Autonomous Surface Vehicles (ASVs) and gliders. For example, the Saildrone and Wave Glider ASVs have been equipped with $pCO_2$ ($ASVCO_2$) systems (Sabine et al., 2020; Sutton et al., 2021), and proved to be a valuable tool for $CO_2$ flux quantification, especially in hard-to-reach environments. Additionally, the first ever integration of a Lab-On-Chip (LOC) pH sensor onto a glider, by Possenti et al. (2021), provided valuable insights into biogeochemical interactions and processes in the North Sea. Similar to BGC-Argo floats, Possenti was able to derive carbonate variables using autonomous pH data paired with salinity-derived TA estimations. Despite these advancements, autonomous instrumentation falls short of fully matching the

comprehensive carbonate data collection capabilities of traditional ship-based methods.

In this article, we introduce novel state-of-the-art autonomous observing technologies capable, for the first time, of direct seawater carbonate system characterisation along predefined oceanographic transects. The system comprises a long-range Autonomous Underwater Vehicle (AUV) newly loaded with LOC sensors for the measurement of seawater pH, TA and DIC. We evaluate the performance of these new technologies—including quality of observations and ability to constrain the carbonate system—relative to the traditional ship-based approach.

## 2.2 Methods

### 2.2.1 Study site

The study site was located in the Celtic Sea, between the Celtic Shelf and Deep Celtic Basin in ocean waters ranging 100 to 3000 m deep. This region was chosen due to its proximity to the UK and the presence of biogeochemical gradients across the continental shelf break. The study took place between March 19–30, 2022 supported by the Royal Research Ship, *RRS Discovery*, during expedition DY149.

### 2.2.2 Autonomous platform and sensors

The Autosub Long Range (ALR) is a family of large flight-style AUVs (3.6 m long, nominally weighing 750 kg) developed and operated by the National Oceanography Centre (NOC) with a depth rating of 1500 m (ALR1500) or 6000 m (ALR6000). The ALR-2 (ALR6000) was used for this deployment and is hereafter referred to as the ALR. The ALR has flooded payload bays that sit forward and aft, and can be configured with a wide range of oceanographic sensors. Long endurance is achieved using lithium batteries combined with low transport costs from modest travel speeds, passive buoyancy control, and optimised power consumption of onboard systems (Roper et al., 2021). A propeller, magnetically coupled to an electric motor and gearbox enables speeds between 0.45–0.8 m $s^{-1}$ through water. Large aerofoil section dive wings provide downward force and control surfaces at the aft that manage pitch and heading. Typical dive rates of 0.1–0.3 m $s^{-1}$ are achieved with downward pitch of 10–30°. The ALR navigates using Doppler Velocity Log (DVL) aided dead reckoning, achieving navigational accuracy <1% of distance travelled when in range of the seabed (Roper et al., 2021; Phillips et al., 2023).

For this deployment, the ALR was fitted with three additional major sensor suites: carbonate chemistry LOC sensors (pH, TA, and DIC), nutrient LOC sensors

(Nitrate/nitrite, phosphate, silicate, and iron), and a Single Turnover Active Fluorescence (STAF) phytoplankton sensor. As a part of its standard payload, the ALR was equipped with a pumped CTD (SBE 52-MP) sensor, and for this work, an SBE 43F dissolved oxygen (DO) sensor was added to the CTD. All three carbonate LOC sensors are rated to 6000 m (Yin et al., 2021; Schaap et al., 2025; Monk, 2020), however the maximum depth rating for this deployment was reduced from 6000 m to 600 m due to the limited pressure rating of the STAF sensor. The hotel load (systems and science payload) in this configuration was 60 W giving an expected endurance of 10 days and range of 550 km at a speed of 0.6 m $s^{-1}$.

In this work we focus on the CTD, DO, pH, TA, and DIC sensors and their capability within the autonomous system to characterise the ocean carbonate system. The pH LOC sensor determines pH on the total proton scale ($pH_T$) photometrically using purified meta-Cresol Purple (mCP) as the indicator dye, with $< 0.001$ precision, 0.003 $\pm 0.022$ accuracy relative to validation seawater samples, and $\pm 0.010$ combined standard measurement uncertainty (Yin et al., 2021). The pH LOC sensor has been widely demonstrated in remote operated vehicles (ROVs), seabed landings, and gliders (Cryer et al., 2023; Monk et al., 2021; Possenti et al., 2021; Schaap et al., 2021a) and is now commercially available (`https://www.clearwatersensors.com/`). The TA LOC sensor determinations are based on single-point acid titration to endpoint pH = 3.0–3.5 that is determined photometrically using (unpurified) Bromophenol Blue (BPB) as the indicator in the hydrochloric acid (HCl) titrant (Culberson et al., 1970). The TA sensor has a precision and accuracy better than 5 $\mu$mol $kg^{-1}$ (Schaap et al., 2025), and the TA measurement uncertainty is estimated to be $\pm 7$ $\mu$mol $kg^{-1}$ in this deployment. Full details of the calibration and validation procedures of the pH and TA LOC sensors are outlined in Yin et al. (2021) and Schaap et al. (2025). While the temperature and optical calibrations of these sensors are performed once post-manufacturing, validation is typically performed with standardized (e.g., 'tris' buffer, validation co-samples (Yin et al., 2021)) or certified materials pre-deployment, during deployment with onboard materials, and post-deployment (TA sensor only).

The DIC LOC sensor is based on the conductimetric method in Hall and Aller (1992), which involves extraction of DIC as $CO_2$ from a seawater sample by acidification with 10% phosphoric acid, $CO_2$ transfer into a 0.007 M sodium hydroxide (NaOH) solution across a gas permeable membrane, and determination of the conductivity change in the NaOH solution from its reaction with $CO_2$ to $CO_3^{2-}$ (Sayles and Eck, 2009)[]. The calibration procedure of the conductimetric DIC LOC sensor is based on that outlined in Sayles and Eck (2009). The DIC sensor used for this deployment was an early, now retired, prototype which featured an external detector with relatively high measurement uncertainty (estimated at $\pm 38$ $\mu$mol $kg^{-1}$) (Monk, 2020).

The carbonate sensors were integrated in the aft payload bay of the ALR (Figure 2.1). Integration of the carbonate sensors with the ALR was performed using a

communications sensor hub.

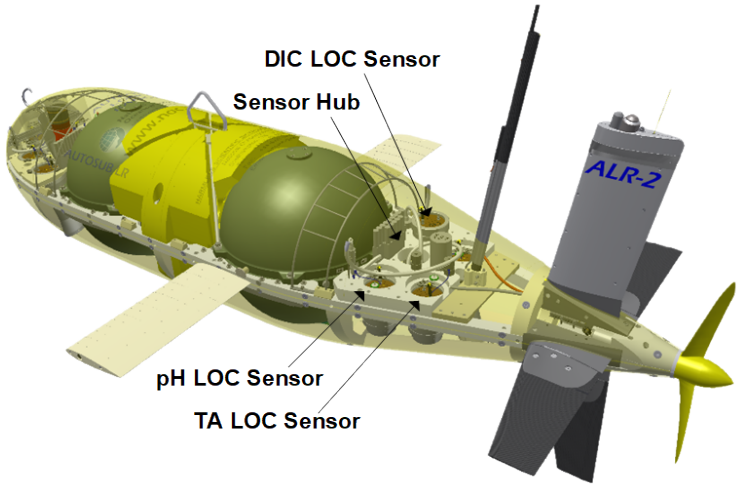


FIGURE 2.1: Diagram of the ALR with carbonate LOC sensor and sensor hub integration in the aft payload bay. Reagent bags not shown.

The sensor hub was developed specifically to simplify the integration of multiple sensors on autonomous platforms. It primarily operates as a port expander, providing a power and serial communications interface between a vehicle and multiple sensors. The hub is fully programmable, allowing it to perform any degree of protocol translation or other 'smart' functions. In this application, the sensor hub managed the operation of the individual carbonate sensors and presented the ALR with an interface to a single "virtual carbonate sensor" which could start, stop, and poll for samples. Performance of the system was improved further by making real-time supplementary CTD and DO data available to the LOC sensors via a 1 Hz stream from the SBE 52-MP CTD sensor onboard the ALR which enabled real-time calculation of carbonate system parameters at *in situ* salinity (S), temperature (T), and pressure (P). The LOC and CTD-DO sensors sampled seawater from a shared flow-though system that pumped seawater from an intake tube outside of the ALR's housing.

### 2.2.3 Autonomous missions

Carbonate system observations were conducted through a series of ALR missions along two main transects: The Shelf Transect (ST) and the Deep Transect (DT) (Figure 2.2). During the ST missions, the ALR travelled in a south-westerly direction across the continental shelf over a period of five days (March 24–29, 2022).

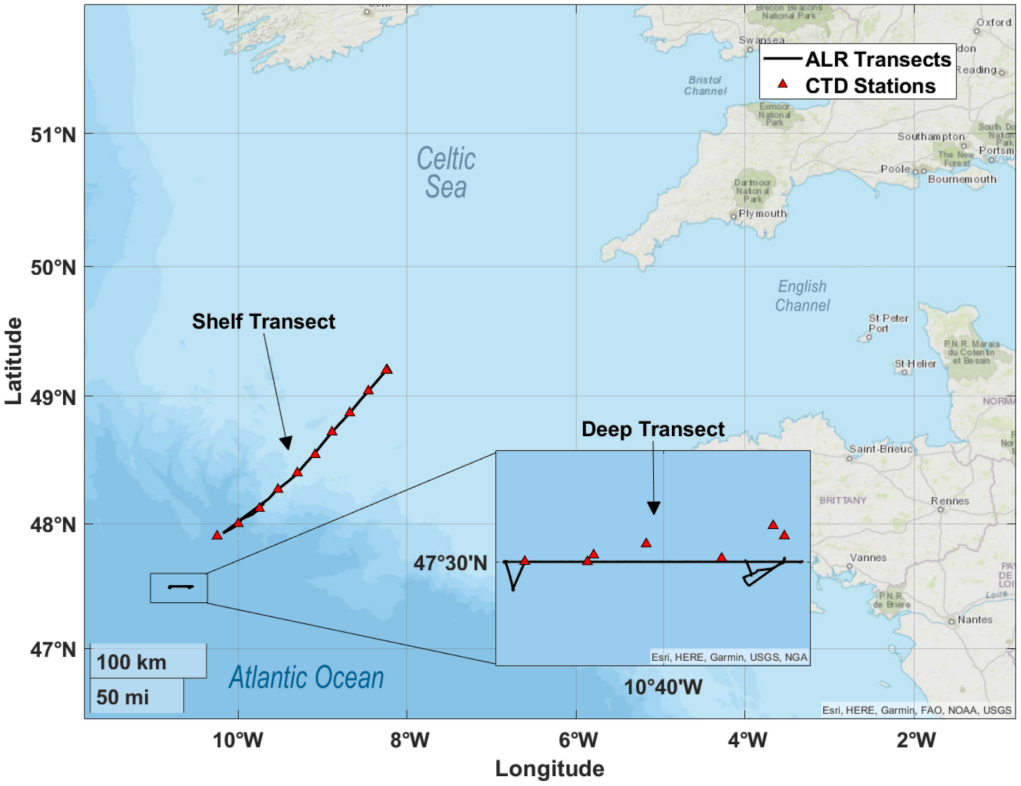


FIGURE 2.2: Sampling sites located Southeast off the coast of England in the Celtic Sea and off the Celtic Shelf in open ocean (Atlantic) waters.

The ALR followed a "staircase" survey pattern, reaching depths up to 250 m along a total distance of over 200 km (Figure 2.3). The DT mission took place just off the continental shelf over a period of three days (March 20–22, 2022). The ALR travelled along three 25 km stacked transects at 20 m, 250 m, and 600 m depth (Figure 2.4).

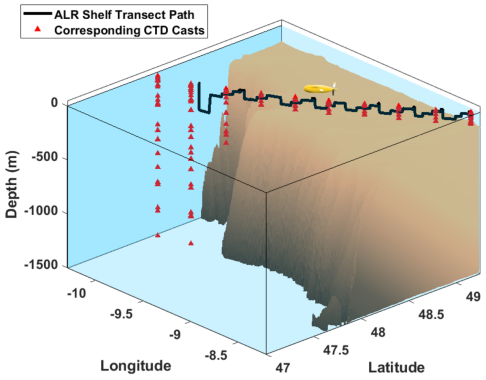


FIGURE 2.3: Visualisation of ST ALR path (black line) and corresponding CTD casts (red triangles). ALR vehicle transit across the continental shelf edge at various depths in a diagonal trajectory with respect to latitude and longitude (denoted here in decimal degrees).

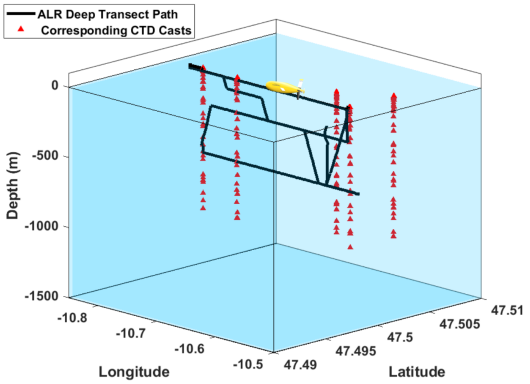


FIGURE 2.4: Visualisation of DT ALR path (black line) and corresponding CTD casts (red triangles). Latitude and longitude are denoted here in decimal degrees. ALR vehicle transit path is along 47.5 N at various depths. Seafloor is at 3500 m.

### 2.2.4 Autonomous data processing

The carbonate LOC sensors were switched on by the ALR at the start of each dive sequence and measured at each of their maximum sampling frequencies as outlined in Table 2.1. Each LOC sensor measurements were time-matched with the CTD-DO measurements by the hub and compiled within a single data file. The *in situ* S, T, and P were used to determine $pH_T$ and TA as described by Yin et al. (2021) and Schaap et al. (2025).

TABLE 2.1: Sampling rates of sensors onboard the ALR. The LOC sensors were powered off after every mission when the ALR was at the surface transmitting data and powered back on at the beginning of the next mission. The LOC sensors were set to measure at their highest possible frequency to ensure maximum data collection and prove ability rather than achieve measurement synchronization. *During deployment, onboard Reference Materials (RMs) were analysed periodically for both the TA and DIC sensor.

| **Sensor on ALR** | **Sampling Rate** |
|---|---|
| pH Lab-On-Chip (NOC) | 1 measurement per 7.5 minutes |
| TA Lab-On-Chip (NOC) | 1 measurement per 10 minutes<br>RMs every 3 measurements* |
| DIC Lab-On-Chip (NOC) | 1 measurement per 15 minutes<br>RM every 12 measurements* |
| SBE 52 CTD (Sea-Bird Scientific) | 1 Hz (1 measurement / second) |
| SBE 43F Dissolved Oxygen (Sea-Bird Scientific) | 1 Hz (1 measurement / second) |

The use of "CO2-in-seawater Reference Materials" (RMs), certified for TA and DIC, is a standard practice in marine carbonate system measurements. These RMs are also a reliable tool for field sensor calibration and verification because they are stable for long periods of time and unaffected by changes in temperature and pressure (Dickson and Dickson, 2010; Sharp and Byrne, 2021). The TA sensor seawater measurements were determined relative to data collected periodically during deployment from the onboard RM and in-house prepared standard (seawater that has been filtered, poisoned with mercuric chloride, and standardized against RM and certified titrant, both from Scripps Institution of Oceanography, USA), as described in Schaap et al. (2025). The TA LOC sensor carried two onboard RMs, RM1 (certified, Scripps Batch 189) with TA = 2205.26 $\mu$mol kg$^{-1}$ and RM2 (in-house standardized seawater with TA = 2340.8 $\mu$mol kg$^{-1}$, which were each measured once every 3 external seawater measurements (Table 2.1). The DIC sensor used one onboard RM (certified, Scripps Batch 193) with DIC = 2048.36 $\mu$mol kg$^{-1}$, which was measured in triplicate every 12 external seawater measurements during deployment (Table 2.1).

### 2.2.5 Discrete bottled co-samples

Discrete seawater co-samples were collected during ALR missions (Figures 2.2–2.4) using the ship's CTD rosette sampler, equipped with 24 Niskin bottles (20 L each), a Sea-Bird SBE 911 plus CTD, a Sea-Bird SBE 43 dissolved oxygen sensor, and an Aquatracka MKIII fluorometer (Chelsea Technologies Group). For each CTD cast, seawater was collected from various depths, including the depth of the ALR track.

Sample collection, preservation and storage for carbonate analysis was conducted according to standard procedures described in Dickson et al. (2007). The bottled co-samples were analysed in the laboratory, with a subset ($n$=47) analysed for $pH_T$, DIC, TA, at NOC and the remaining samples ($n$=109) analysed for DIC and TA at the Bermuda Institute in Ocean Science (BIOS). All discrete carbonate samples were analysed within seven months of collection. Seawater $pH_T$ (NOC) was determined on a Cary 60 UV-vis (Agilent Technologies) spectrophotometer using purified mCP indicator at 20°C (Dickson et al., 2007), with an estimated uncertainty of 0.005 (Yin et al., 2021) (SI. Table A.1). The reported *in situ* $pH_T$ for bottled co-samples that were analysed at NOC was computed from the laboratory measured $pH_T$, measurement temperature, DIC and nutrient concentrations at *in situ* S, T, P using CO2SYS (see Carbonate system calculations section below). The *in situ* $pH_T$ reported here for the remainder of bottled co-samples was computed from the DIC and TA measured at BIOS at *in situ* S, T, P using CO2SYS. Seawater DIC (NOC) was determined by infrared (IR) gas analysis following acidification with 10% phosphoric acid and stripping of the generated $CO_2$ with pure nitrogen gas on an AIRICA® DIC Analyser (Marianda, Kiel, Germany) coupled with a LICOR 840A IR $CO_2/H_2O$ Analyser (O'Sullivan and Millero, 1998; Goyet and Snover, 1993; Call et al., 2017). The analytical system was calibrated daily with RMs (Scripps Institution of Oceanography, USA). The DIC concentration was determined from two repeat measurements from the same discrete sample bottle, each measurement consisting of integrated $CO_2$ peaks from four repeat injections of 1.2 mL of sample each, with a precision better than 6 $\mu$mol kg$^{-1}$, and an average precision of 3 $\mu$mol kg$^{-1}$ ($1\sigma$ = 2 $\mu$mol kg$^{-1}$). The same DIC determination method was used at BIOS, coupled with $CO_2$ determination by coulometric titration on a VINDTA 3C (Versatile INstrument for the Determination of Total Alkalinity; Marianda, Kiel) with accuracy and precision of 2 $\mu$mol kg$^{-1}$. For all co-sample DIC determinations, $\pm$6 $\mu$mol kg$^{-1}$ is used here as a maximum estimate of measurement uncertainty (SI. Table A.1). Seawater TA (NOC) was determined potentiometrically with an open cell multi-point titration between pH 3.5 and 3.0 (Dickson et al., 2007) using a Metrohm Ti-Touch 916 automated titrator (Metrohm, 2022), with a precision better than 0.1% and a combined standard measurement uncertainty of $\pm$3 $\mu$mol kg$^{-1}$. At BIOS, the TA was determined using the potentiometric semi-closed titration system (Dickson et al., 2007) on the VINDTA 3S, with a precision better than 0.1%. For all discrete co-sample TA determinations $\pm$3 $\mu$mol kg$^{-1}$ is used here as an estimate of measurement uncertainty (SI. Table A.1). In addition, all discrete co-samples ($n$=156) were analysed for concentrations of dissolved inorganic phosphorous (hereafter phosphate) and silicic acid (hereafter silicate) at NOC following standard continuous flow analysis methods (Becker et al., 2020) on a QuAAtro39 AutoAnalyzer (SEAL Analytical), with estimated uncertainties of 3.7% and 2.4% respectively (Birchill et al., 2019) (SI. Table A.1). Finally, all discrete co-samples were analysed for DO on the day of collection using the Winkler method (Winkler, 1888) following Carpenter (1965) and

Langdon (2010), on a Metrohm 794 Basic Titrino system with an estimated measurement uncertainty of 0.06% (Langdon, 2010).

### 2.2.6 Sensor measurement validation

To validate the performance of the sensors onboard the ALR, sensor measurements were compared with the water samples collected from the ship that were analysed using the "gold standard" laboratory techniques described above. Proximity between sensor measurements and discrete samples unavoidably varied in frequency, space, and time, making direct comparisons impossible and interpolation (a common practice when dealing with oceanographic data (McIntosh, 1990; Ledoux et al., 2005)) necessary. To enable effective and meaningful comparisons between sensor measurements and validation samples, the biogeochemical parameters (pH, TA, DIC, DO, S, T) measured in the discrete samples were spatially gridded using natural neighbour interpolation without extrapolation in MATLAB (Amidror 2002; Sibson 1981 ;The Mathworks Inc., 2024). The discrete data were interpolated rather than the sensor data to provide the most accurate representation of the water column given its trusted methodology and more consistent sampling coverage versus the ALR track. Nonetheless, the natural neighbour interpolation method was chosen because it performs well with the irregularly distributed data typically associated with oceanographic sampling (Ledoux et al., 2005; Sambridge et al., 1995). All parameters were regarded in *density space*, that is, they were interpolated based on their relationship to seawater density (calculated from S, T, P; (McDougall and Barker, 2011)) rather than water depth. When parameters are compared in density space, the variability caused by vertical displacement is minimised since the ocean primarily mixes on isopycnals (density gradients) and therefore provides a clearer understanding of parameter ($x$) in question within a given water mass (Gomis et al., 1997; Lozier et al., 1994; Ridgway et al., 2002).

Direct spatial comparison was achieved by extracting values from the discrete co-sample interpolant product $x_{i-CTD}$ at the vertical (density) and lateral (location along track) coordinates corresponding to each ALR sensor measurement $x_{ALR}$. Residuals $r(x)$ between the two measurement methods were then calculated using Equation 2.1.

$$r(x) = x_{i-CTD} - x_{ALR} \tag{2.1}$$

Finally, the mixed layer depth in the DT was determined using the Threshold Method with criterion $\Delta\sigma_\theta$=0.125 kg m$^{-3}$ where $\sigma_\theta$ represents potential density (Monterey and Levitus, 1997; Levitus, 1982; de Boyer Montégut et al., 2004a).

### 2.2.7 Carbonate system calculations

The speciation of the carbonate system was characterised from the discrete co-sample dataset obtained from the CTD casts using the CO2SYS MATLAB package (Lewis and Wallace 1998; Sharp et al. 2023a; van Heuven et al. 2011b; The Mathworks Inc., 2024) with TA, DIC, and nutrient (phosphate and silicate) concentrations as input parameters, as well as S, T, and P from the CTD sensor on the ship's rosette sampler. These computations yielded CTD-based pCO2 and the aragonite saturation state ($\Omega_{ar}$).

The speciation of the carbonate system was also characterised from the LOC sensor data on the ALR. These data were interpolated and gridded spatially, as outlined above, to account for the differing measurement frequencies and resulting spatial and temporal mismatch between LOC sensors. The interpolated sensor TA and $pH_T$ values from the generated spatial grids were used with corresponding gridded S, T, and P from the CTD onboard the ALR for carbonate system characterisation using CO2SYS. All CO2SYS computations used the dissociation constants of carbonic acid ($K_1$ and $K_2$) from Lueker et al. (2000), $K_{SO_4}$ from Dickson (1990), KF from Perez and Fraga (1987), and total Boron concentration from Lee et al. (2010). These computations produced grids of calculated carbonate system parameters ($pCO_2$, DIC, and aragonite saturation state ($\Omega_{ar}$)) from the sensor data.

The derived carbonate parameters from bottle samples ($x_{CTD}$) were compared with those from the ALR sensor-derived interpolant values ($x_{i-ALR}$) based on corresponding vertical (density) and lateral (location along a transect) coordinates (SI. Figure A.1). The resulting carbonate parameter residuals $r_{carb}(x)$ were calculated using Equation 2.2.

$$r_{carb}(x) = x_{CTD} - x_{i-ALR} \tag{2.2}$$

The combined standard uncertainty $u_C(y)$ of $r(x)$ was calculated as the positive square root of the combined variances using Equation 2.3, and based on the uncertainties of sensor measurement and equivalent laboratory method (SI. Table A.1) (JCGM et al., 2008).

$$u_c^2(y) = \sum_{i=1}^{N} u_i^2(y) \tag{2.3}$$

The combined standard uncertainty of the calculated carbonate parameters was determined by error propagation using the CO2SYS function *errors.m* with the routine's default standard errors for dissociation constant inputs (Orr et al., 2018) and individual parameter uncertainty values from SI. Table A.1. The resulting propagated error associated with each calculated carbonate parameter (for both discrete and sensor data) was used to derive $u_C(y)$ of $r_{carb}(x)$ using Equation 2.3 and values from SI. Table A.1.

## 2.3 Results and discussion

### 2.3.1 Autonomous Data Collection

During March 20–29, 2022, the ALR successfully completed over 10 dive missions that formed the Shelf Transect (ST) and the Deep Transect (DT). The pH, TA, and DIC Lab-On-Chip (LOC) sensors onboard the ALR made 947, 423, and 251 *in situ* measurements respectively. Data taken from the ALR LOC sensors for $pH_T$ ($pH_{T-ALR}$) and TA ($TA_{ALR}$) are used in this study. Due to unreliable performance of the LOC DIC sensor (outlined below), DIC sensor data is not used in this study. During the same period, 156 discrete water samples were taken from the water column and analysed for TA ($TA_{CTD}$) and DIC ($DIC_{CTD}$), 47 of which were also analysed directly for $pH_T$ ($pH_{T-CTD}$). The CTD-DO sensors on the ALR and ship-based CTD rosette sampler recorded continuous (1 Hz) measurements for salinity ($S_{ALR}$ and $S_{CTD}$), temperature ($T_{ALR}$ and $T_{CTD}$), pressure ($P_{ALR}$ and $P_{CTD}$), and dissolved oxygen ($DO_{ALR}$ and $DO_{CTD}$). Values of $pH_T$, TA, DIC, S, and T collected from sensors and bottle samples fell within expected ranges for the region and generally agreed with each other (Table 2.2).

TABLE 2.2: Summary of observed and historical parameter values. [a] Kitidis et al. (2012) Western English Channel (Stations E1 & L4 Feb–April). [b] Marrec et al. (2013) Western English Channel (Stations E1 & L4 Spring). *Indicating surface water measurements only

| **Parameter** | **ALR Transects** | **CTD Casts** | **Regional Data[a]** | **Regional Data[b]** |
|---|---|---|---|---|
| $pH_T$ | 7.97–8.09 | 7.94–8.06 | 8.1–8.2 | n/a |
| TA ($\mu$mol $kg^{-1}$) | 2302–2370 | 2314–2357 | 2310–2360 | 2326–2345* |
| DIC ($\mu$mol $kg^{-1}$) | 2107–2182 | 2117–2217 | 2050–2150 | 2074–2135* |
| Salinity (PSU) | 35.34–35.61 | 35.34–35.60 | 34.4–n/a | 35.04–35.47 |
| Temperature °C | 10.56–12.29 | 10.32–12.36 | 7.5–12.5 | 8.8–13.9 |

The prototype DIC sensor operated throughout the majority of the deployment and produced measurements within expected ranges (Table 2.2). However, DIC observations did not follow expected trends (i.e increase with depth due to carbon mineralisation) and rather showed random variability over the deployments. Investigation post-deployment pointed towards failure of the gas exchange unit and calibration error, therefore sensor DIC data were flagged as unreliable and will not be discussed further. Since the deployments described here, a new version of the DIC LOC sensor has been developed and is undergoing field trials.

### 2.3.2 Comparison between ship-based and autonomous observations

#### General hydrography and biogeochemistry

One of the primary objectives of this study was to evaluate whether an autonomous observing system such as the one described here could provide comparable information to that of traditional shipside collection along oceanographic transects. The observational plan was therefore designed to enable meaningful comparisons between ALR and ship observations. Validation bottle sample collection was planned along the programmed ALR path and (where possible) at a time when the ALR was in proximity but at a safe distance so to avoid collision with the CTD rosette. Time between ALR sensor measurements and bottle sample collection in the same proximity ranged between 1 minute and 15 hours ($\mu$ = 6 hours) for the ST and between 5 minutes and 85 hours ($\mu$ = 40 hours) for the DT.

Co-location of sensor measurements and validation samples is more critical in shallow waters (within the mixed photic zone) due to light-driven diel biogeochemical variability, irregularity in phytoplankton abundance, and strong mixing from tidal currents that also affect biogeochemical variables. Most observations collected along the ST by the ALR were either within the vertically homogeneous (mixed) waters above the continental shelf or within the $\sim$ 320 m surface mixed layer off the shelf. Both ALR and ship-based observations show similar trends along the ST. There is a lateral gradient of increasing salinity (35.35–35.55 PSU) and temperature (11–12.5 °C) as the transect moves away from the continental shelf (SI. Figure A.2). This trend is consistent with freshwater influence from the coast and the existence of a warmer mixed layer offshore. Dissolved oxygen decreased with depth (260–220 $\mu$mol kg$^{-1}$), with peaks (275 $\mu$mol kg$^{-1}$) near the surface (60–100 km along the track) where elevated fluorescence concentrations (1.1 $\mu$g L$^{-1}$) were detected consistent with primary productivity (SI. Figure A.2).

There was closer agreement between ship and ALR observations along the DT where vertical stratification was present. The mixed layer depth averaged 345 m calculated from ship CTD observations which is similar to that calculated using the ALR observations (338 m). Seawater salinity ranged from 35.45–35.6 PSU, the temperature ranged from 10.5–12.4 °C, and the DO ranged from 180–245 $\mu$mol kg$^{-1}$ (SI. Figure A.3). It is important to note that because of the sampling spatiotemporal differences between the ALR and CTD, their water mass properties are not identical. While it is evident that each of the ALR and CTD salinity, temperature, dissolved oxygen, and density observations show the same general trends and ranges in each of the sampling transects, there are still subtle differences that are reflected in and propagated through their respective carbonate measurements and comparison residuals.

**pH**

The $pH_{T-ALR}$ data show good agreement with interpolated $pH_{T-CTD}$ across both transects (Figure 2.5 and Figure 2.7). During the ST, $pH_T$ values ranged 0.094 pH units from 7.991 to 8.085 throughout the water column. Generally, pH decreased with

depth, with the highest values recorded in regions of high fluorescence and oxygen concentrations (Figure 2.5a, SI. Figure A.2). A strong positive correlation (n=950, $R^2$ = 0.87, SI. Figure A.4) between $pH_T$ and DO throughout the deployment implies a primarily biological control (photosynthesis–respiration) on pH variability within the surface mixed layer.

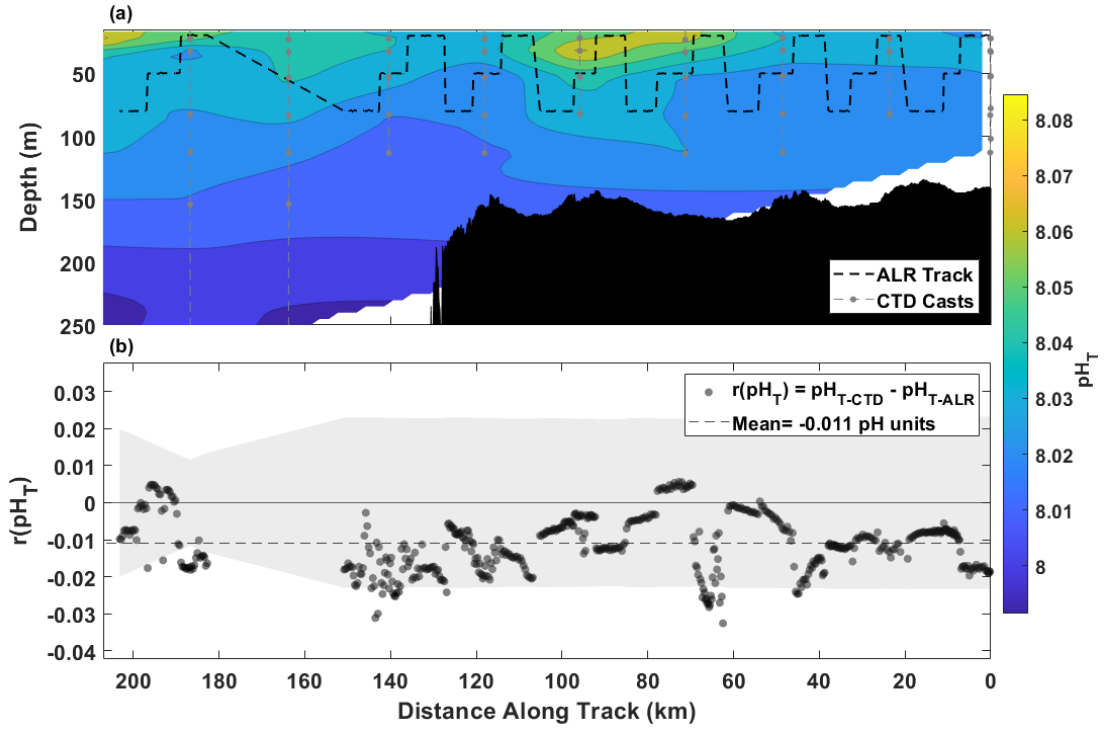


FIGURE 2.5: Shelf Transect $pH_T$ and intercomparison. The shared x-axis is plotted from right to left to better represent geographic location and direction of travel (away from the continental shelf). (a) Contour map from interpolated $pH_{T-CTD}$ with contours denoted by colour with respect to depth (m) on the y-axis and distance (km) on the x-axis. (b) Residuals of $pH_{T-CTD}$ - $pH_{T-ALR}$ plotted where $pH_{T-CTD}$ is an interpolated value at the density and distance where $pH_{T-ALR}$ measured. Running combined standard uncertainty (mean = $\pm$0.022) is shaded in grey.

The mean residual between interpolated $pH_T$ from bottle measurements and $pH_{T-ALR}$ ($r(pH_T)$) in density space along the ST was -0.011 ($\sigma$=0.008, n=560). $r(pH_T)$ varied from -0.033 to 0.006 with 94% of $r(pH_T)$ within the mean combined standard uncertainty ($\pm$0.022) of the sensor and lab-based pH analysis (Figure 2.5b). The negative bias in $r(pH_T)$ reflects the consistently higher $pH_{T-ALR}$ values than $pH_{T-CTD}$. The source of this systematic bias is likely the ALR pH sensor measurements as it would be highly improbable for calculated $pH_{T-CTD}$ and directly measured $pH_{T-CTD}$ analysis to carry the same bias. Further investigation into the pH sensor's raw data revealed no signs to suggest that its performance was compromised. The pH sensor's thermistors and optics were functioning correctly, indicating that the observed bias was not due to equipment limitations, but rather likely a

deployment-related reason. This points to another notable challenge when comparing ocean observation methodologies and necessitates further research.

To help interpret the $r(\mathrm{pH}_T)$ in the ST, residuals from other observed parameters such as DO, S, and T were also evaluated in density space along the transect (Figure 2.6). For residuals of DO ($r$(DO)), S ($r$(S)), and T ($r$(T)) evaluated along the ST, the larger deviations from $r(x) = 0$ (where $x_{i-CTD} = x_{ALR}$), coincided in space with larger $r(\mathrm{pH}_T)$ as illustrated clearly between $\sim$ 40–80 km along the ST track (Figure 2.6a–c). In fact, $r(\mathrm{pH}_T)$ correlated positively with $r$(DO), $r$(S), and $r$(T) [ $r$(DO) / $r(\mathrm{pH}_T)$ ($R^2$=0.60, $p<0.001$), $r$(S) / $r(\mathrm{pH}_T)$ ($R^2$=0.25, $p<0.001$, and $r$(T) / $r(\mathrm{pH}_T)$ ($R^2$=0.66, $p<0.001$)] in density space, along the entire transect as shown in Figure 2.6d–f.

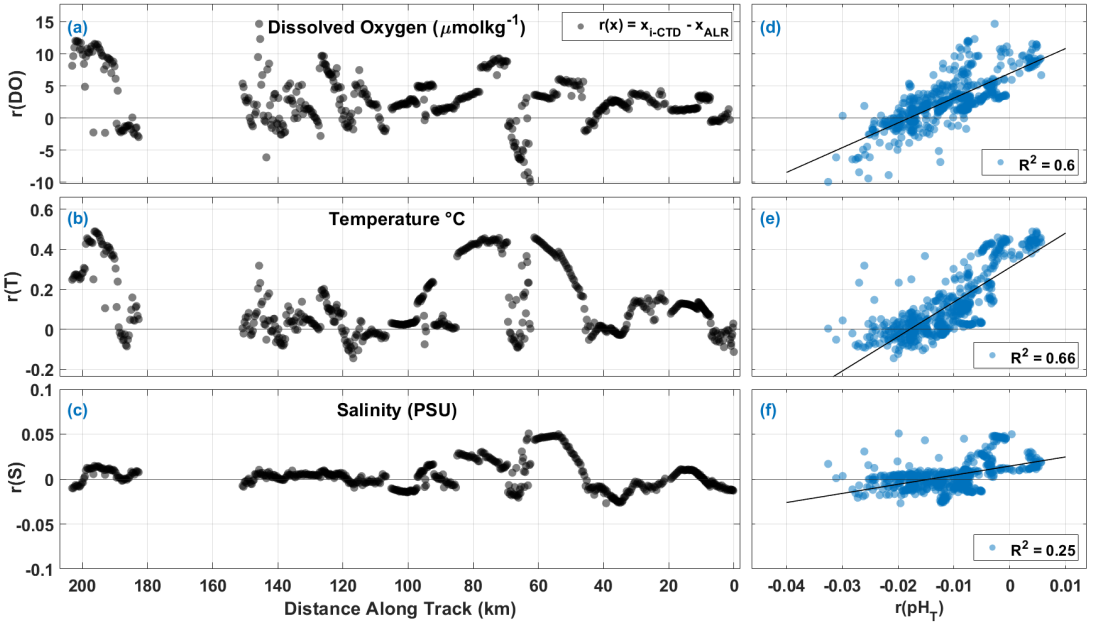


FIGURE 2.6: Comparison of residuals from measurements of dissolved oxygen, temperature, and salinity with respect to distance (km) along transect (a–c) and $r(\mathrm{pH}_T)$ (a–f). (a) Residuals of dissolved oxygen $r$(DO) in $\mu$mol kg$^{-1}$ along distance. Grey circles represent residuals calculated as $r(x) = x_{i-CTD} - x_{ALR}$. (b) Residuals of temperature $r$(T) in °C and (c) residuals of salinity $r$(S) in PSU along distance, with the same legend as in (a). (d) $r$(DO) as a function of $\mathrm{pH}_T$ residuals $r(\mathrm{pH}_T)$. (e) $r$(T) as a function of $r(\mathrm{pH}_T)$. (f) $r$(S) as a function of $r(\mathrm{pH}_T)$.

Similar comparisons between $r(\mathrm{pH}_T)$ and depth as well as $r(\mathrm{pH}_T)$ and hours between sample collection versus sensor measurement ($r$(Time)) show weak yet significant correlation ($p<0.001$, SI. Figure A.5). The highest $r(\mathrm{pH}_T)$ values correspond to the highest $r$(time) (5–15 hours), and especially where (at $\sim$ 60–80 km along ST track) fluorescence was highest (areas of high primary productivity)(SI. Figure A.2). This implies that in highly productive waters, such as the shelf region of the Celtic Sea on the cusp of spring, spatiotemporal variability in biogeochemistry makes measurement comparisons between platforms and sensor measurement validation challenging.

Therefore, sensor measurement validation should be avoided in shallow productive waters or special care must be taken to minimise the spatiotemporal mismatch between sensor measurements and validation samples.

Along the DT, observed $pH_T$ values ranged between 7.931 in deep waters (1000 m) and 8.063 close to the surface (Figure 2.7a). The observed $pH_T$ decreased uniformly with depth, reflecting the shift from net photosynthesis to net respiration with diminishing light availability.

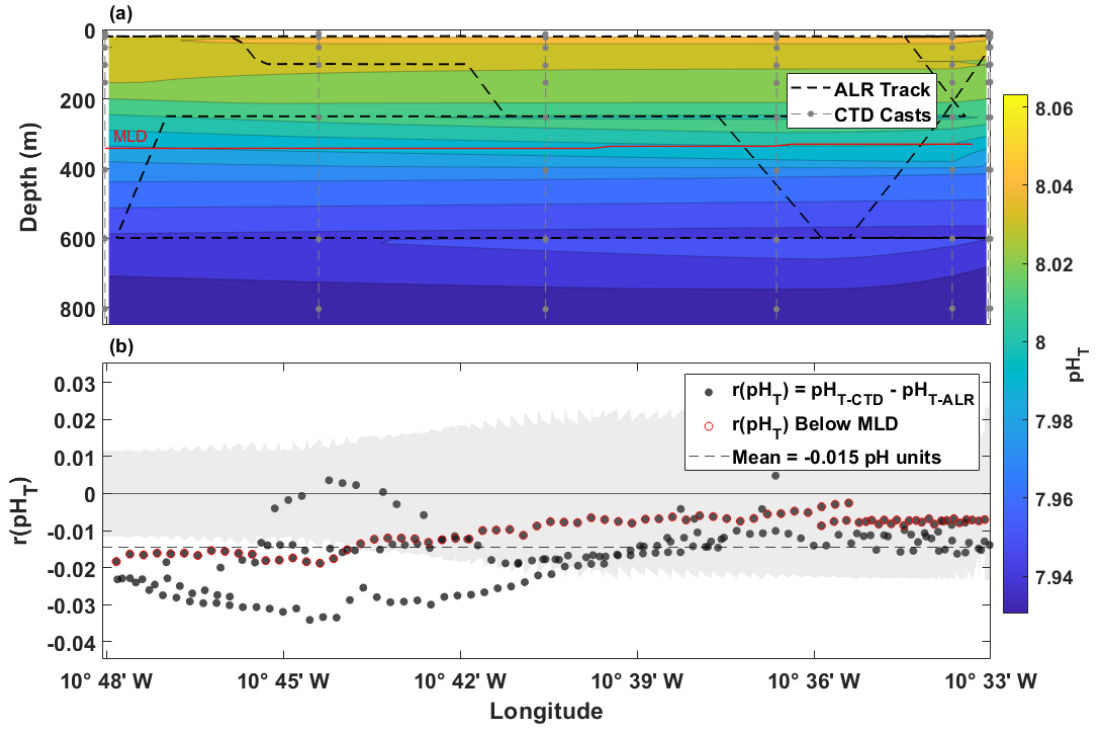


FIGURE 2.7: Deep Transect $pH_T$ data and intercomparison. Shared x-axis represents longitudinal position on transect. (a) Contour map created from interpolated $pH_{T-CTD}$, and contours denoted by colour with respect to depth (m) on the y-axis and longitude on the x-axis. (b) Residuals of $pH_{T-CTD}$ - $pH_{T-ALR}$ plotted where $pH_{T-CTD}$ is an interpolated value at the density and longitude where $pH_{T-ALR}$ was measured. The r($pH_T$) calculated from observations below the average mixed layer depth (MLD) of 345 m are outlined in red. Running combined standard uncertainty (mean = ±0.018) is shaded in grey.

The mean $r(pH_T)$ in the DT was -0.015 ($\sigma$=0.008, n=234) with a similar negative bias as seen in the ST. Values of $r(pH_T)$ varied from -0.034 to 0.005 with 77% of $r(pH_T)$ within the mean combined standard uncertainty (±0.018) of the sensor and lab-based pH analysis (Figure 2.7b).

Along longitude in the DT, particularly between, 10°42′ W and 10°45′ W, there are notable differences between the ALR and CTD DO, S, and T that mimic the larger spread of $pH_T$ residuals at the same location (Figure 2.8a–c). The $r(pH_T)$ values correlated positively with $r$(DO) ($R^2$=0.31, p<0.001) and $r$(T) ($R^2$=0.11, p<0.001),

although not with $r$(S) (Figure 2.8). There was no significant relationship between $r$(Time) and $r(\mathrm{pH}_T)$ (SI. Figure A.6). Interestingly, depth correlated positively with $r(\mathrm{pH}_T)$ in the DT ($R^2$=0.30), showing more $\mathrm{pH}_T$ variability closer to the surface rather than at depth (SI. Figure A.1d). Unlike pressure effects commonly seen with oceanographic instrumentation use, the trend seen here comes from mismatch near the surface and within the MLD. As seen in Figure 2.7b and Figure 2.8a–c, data points that are below the MLD (outlined in red) showed slightly more stability than those above the MLD. This reflects the challenge in comparing biogeochemical observations made in heterogeneous waters such as productive regions or across physical boundaries such as nutriclines and fronts.

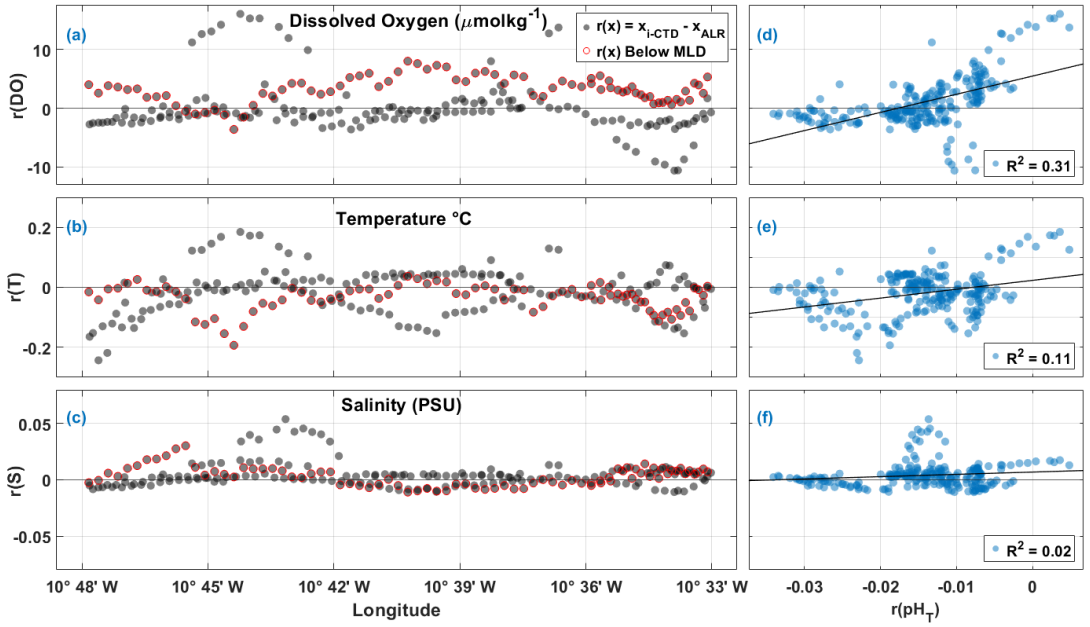


FIGURE 2.8: Comparison of residuals from measurements of dissolved oxygen, temperature, and salinity with respect to longitude (a–c) and $r\mathrm{pH}_T$ (d–f) in the DT. (a) Residuals of dissolved oxygen $r$(DO) in $\mu$mol kg$^{-1}$ along longitude. Grey circles represent residuals calculated as $r(x) = x_{i-CTD} - x_{ALR}$, of those residuals, outlined in red are below the average mixed layer depth (MLD) of 345 m. (b) Residuals of temperature $r$(T) in °C and (c) Residuals of salinity $r$(S) in PSU as along longitude, with the same legend as in (a). (d) $r$(DO) as a function of $r(\mathrm{pH}_T)$. (e) $r$(T) as a function of $r(\mathrm{pH}_T)$. (f) $r$(S) as a function of $r(\mathrm{pH}_T)$.

Similar to the ST pH intercomparison, there is evidence here that the ALR was operating in biogeochemically different water than the CTD casts at times, which then led to pH disagreement. However, the negative bias of the pH residuals is likely not a coincidence and may point to other operational and systematic insights, as described earlier about the ST.

In both transects, the pH LOC sensor measurements showed overall good agreement with the $\mathrm{pH}_T$ of the CTD discrete samples with maximum $r(\mathrm{pH}_T)$ in the order of 0.035

which are twice as large as previously reported for this device (-0.013 by Yin et al. (2021); 0.015 by Nehir et al. (2022)) in shallow coastal water deployments. The largest discrepancy between $pH_{T-ALR}$ and $pH_{T-CTD}$ reported here likely reflects the temporal and spatial mismatch between the sensor measurements and CTD sample collection. The pH LOC sensor has previously been integrated on a seaglider and deployed in the North Sea for a duration of 10 days. During the deployment, four samples were taken using the ship's CTD alongside the glider and analysed for TA and DIC. Calculated $pH_T$ was within 0.005 from the sensors $pH_T$ measurements. However, examples of pH observations from AUVs are very limited and are still at the "experimental" stage (Hemming et al., 2017; Saba et al., 2019). This is mainly because, unlike the pH LOC sensor, no other technology is readily integrable on small platforms (such as gliders) with most requiring bespoke electronics and housings. More recently the "Deep-Sea DuraFET" pH sensor (based on Honeywell's Durafet ISFET technology (Johnson et al., 2016)) has been integrated and demonstrated on a Spray glider with promising results (Takeshita et al., 2021). Mean difference between sensor $pH_T$ measurements and $pH_T$ measured in CTD samples using spectrophotometry was in the order of 0.006 $\pm$0.021 (n=155). The only commercially available stand-alone Deep-Sea DuraFET sensor (SeaFET/SeapHOx, Seabird Scientific) however, is designed mainly for moored application. Both spectrophotometric and ISFET-based technologies show promise for ocean carbon observations (Yin et al., 2021; Rérolle et al., 2016), yet more work is needed to improve analytical performance in order to meet GOOS requirements and enable easy integration by end-users on autonomous platforms.

**TA**

Total Alkalinity measured *in situ* by the TA sensor onboard the ALR ($TA_{ALR}$) agreed very well in density space with the TA measured in the bottle samples collected from the ship's CTD ($TA_{CTD}$) along both the ST and DT. Along the ST, the observed TA values ranged between 2314 and 2357 $\mu$mol kg$^{-1}$ throughout the 250 m water column (Figure 2.9a). There was a horizontal gradient of increasing TA away from the UK coast as with salinity (SI. Figure A.2b), consistent with the influence of low-TA freshwater inputs from land (Hartman et al., 2014). The mean $r$(TA) was 1 $\mu$mol kg$^{-1}$ ($\sigma$=4, n=191), ranging between -9 and 14 $\mu$mol kg$^{-1}$ with no observed bias. Of the TA residuals along ST, 91% fall within the mean combined uncertainty ($\pm$8 $\mu$mol kg$^{-1}$) of the sensor and lab-based TA analysis (Figure 2.9b).

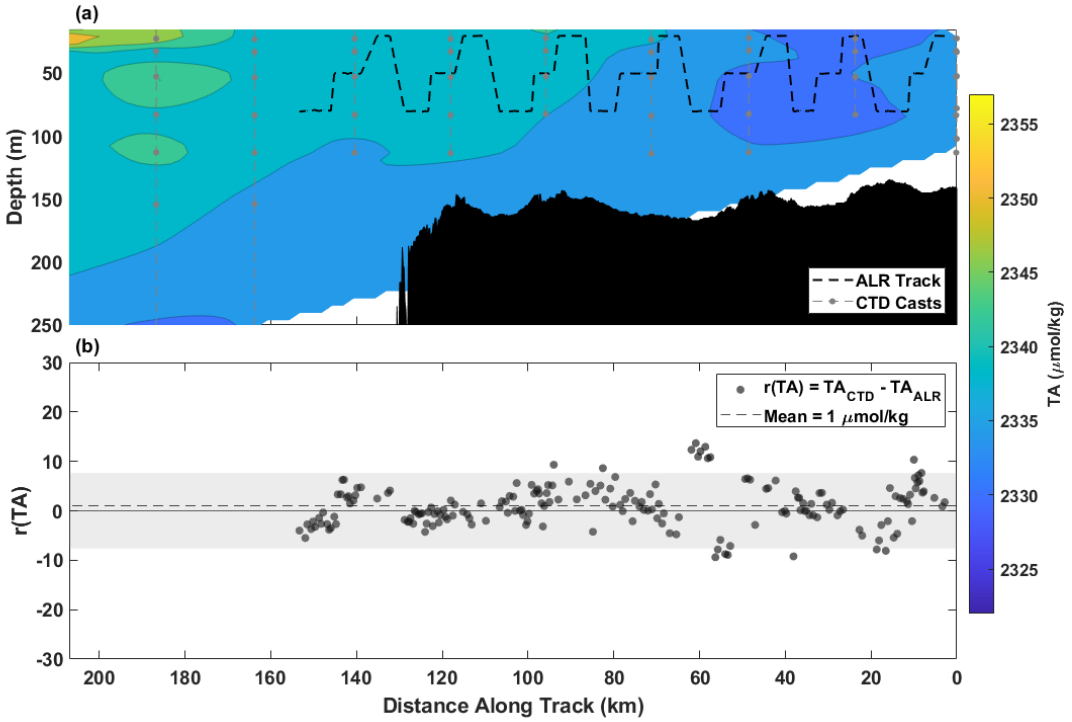


FIGURE 2.9: Shelf Transect TA and intercomparison. The shared x-axis is plotted from right to left to better represent geographic location and direction of travel (away from the continental shelf). (a) Contour map created from interpolated $TA_{CTD}$ and contours denoted by colour with respect to depth (m) on the y-axis and distance (km) on the x-axis. (b) Residuals of $TA_{CTD}$ - $TA_{ALR}$ plotted where $TA_{CTD}$ is an interpolated value at the density and distance where $TA_{ALR}$ measured. Running combined standard uncertainty (mean = $\pm 8$ $\mu$mol kg$^{-1}$) is shaded in grey.

Along the DT, the observed TA ranged between 2325 and 2352 $\mu$mol kg$^{-1}$ throughout the 600 m of sampled water column (Figure 2.10a). The mean $r$(TA) was 2 $\mu$mol kg$^{-1}$ ($\sigma$=5, n=129), and ranged between -9 and 13 $\mu$mol kg$^{-1}$ with no observed bias. 87% of $r$(TA) fall within the bounds of the mean combined uncertainty ($\pm 8$ $\mu$mol kg$^{-1}$) of the sensor and lab-based TA analysis (Figure 2.10b). The good agreement between $TA_{ALR}$ and $TA_{CTD}$ also reflects the spatial and temporal homogeneity with respect to TA which exhibits a largely conservative distribution in the open ocean and is not significantly affected by biological processes.

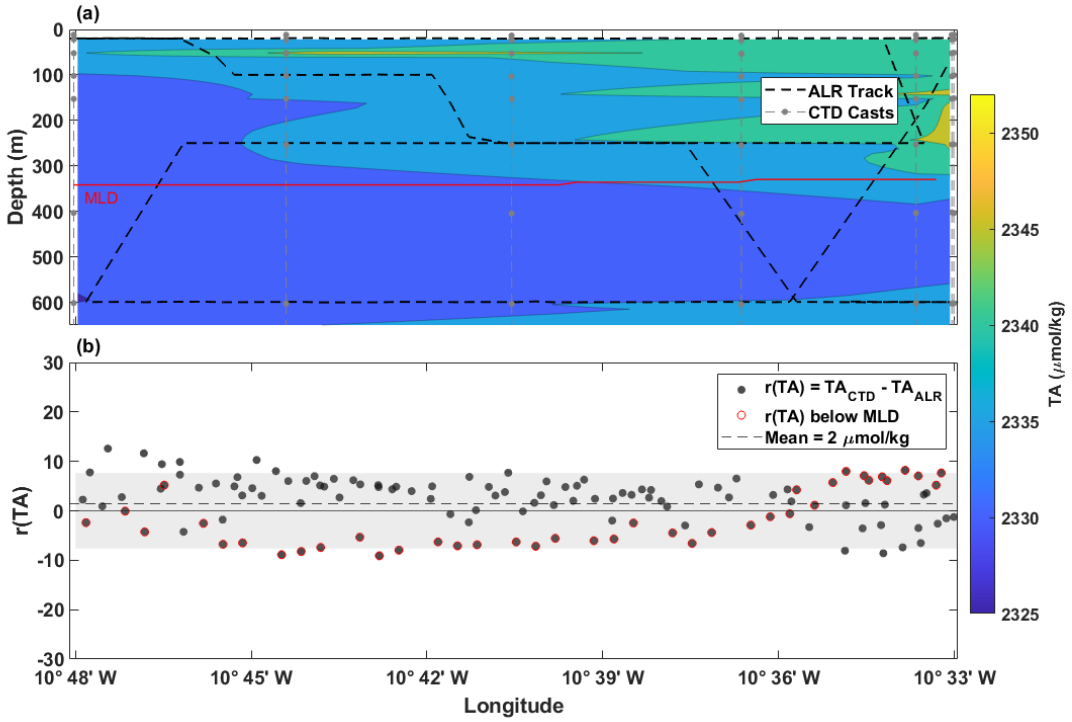


FIGURE 2.10: Deep Transect TA data and intercomparison. (a) Contour map created from interpolated $TA_{CTD}$ and contours denoted by colour with respect to depth (m) on the y-axis and longitude on the x-axis. (b) Residuals of $TA_{CTD}$ - $TA_{ALR}$ plotted where $TA_{CTD}$ is an interpolated value at the density and longitude where $TA_{ALR}$ measured. The r(TA) calculated from observations below the mean mixed layer depth (MLD) of 345 m are outlined in red. Running combined standard uncertainty (mean = $\pm 8$ $\mu$mol $kg^{-1}$) is shaded in grey.

According to current research, this is the first demonstration of a TA sensor on an autonomous vehicle. Other autonomous TA sensors based on similar spectrophotometric technology are reported in the literature, however, they are currently limited to shallow moored applications (Sonnichsen et al., 2023; Qiu et al., 2023). The NOC LOC platform, which the TA LOC sensor is based on (as is the pH and DIC LOC), is specifically designed for integration versatility on stationary and small moving platforms. Although TA can be estimated with certain confidence in large parts of the ocean (Carter et al., 2018), direct measurements are necessary to accurately constrain TA and the seawater carbonate system in regions with high calcification or riverine inputs (Spaulding et al., 2014; Cai et al., 2010). Additionally, TA sensors will be a key tool in quantifying TA generation and dynamics at Ocean Alkalinity Enhancement (OAE) application sites.

### 2.3.3 Constraining the marine carbonate system autonomously

To our knowledge, this work presents the first *in situ* characterisation of the marine carbonate system from an autonomous vehicle based on direct sensor measurements

of $pH_T$ and TA. The challenge so far in achieving such has been the lack of *in situ* sensors (mainly for TA and DIC) capable of autonomous observations onboard moving platforms such as AUVs, ASVs and floats. For this reason, autonomous characterisation of the carbonate system (e.g., BGC Argo and SOCCOM programs) currently relies on measured pH and modelled TA, which carries uncertainties. Although in principle the carbonate system can be measured and constrained using commercially available pH and $pCO_2$ sensors (such as the PMEL mooring based observing network (Cronin et al., 2023)), this approach uses the least desirable combination of input variables due to large errors propagated in the calculated carbonate system parameters (Orr et al., 2018; Sutton and Sabine, 2023). Additionally, $pCO_2$ sensors are much less practical on moving platforms due to technical limitations including slow response times, integrability, and high power requirements (Clarke et al., 2017).

In the following sections, we present carbonate system parameters calculated from $pH_{T-ALR}$ and $TA_{ALR}$, including dissolved inorganic carbon ($DIC_{ALR}$) in $\mu$mol kg$^{-1}$, partial pressure of carbon dioxide ($pCO_{2-ALR}$) in $\mu$atm, and aragonite saturation state ($\Omega_{ar-ALR}$) which is unitless. We then compare these parameters against those calculated from measured $TA_{CTD}$ and $DIC_{CTD}$ ($pCO_{2-CTD}$ and $\Omega_{CTD}$) in order to evaluate the capability of the ALR-sensor system to constrain the seawater carbonate system.

**Shelf Transect**

The sample area for constraining the carbonate system on the shelf is a subset of the ST used in the above analysis, dictated by where both $pH_{T-ALR}$ and $TA_{ALR}$ measurements were available. It spans 0–140 km along the transect and is from 20–80 m in the water column (SI. Figure A.5). Calculated $DIC_{ALR}$ ranged from 2121 to 2150 $\mu$mol kg$^{-1}$ and $pCO_{2-ALR}$ ranged from 366 to 431 $\mu$atm with higher values for both at depth. Calculated $\Omega_{ar-ALR}$ ranged from 2.4 near the surface to 2.0 at depth (Figure 2.11a–c). The variability observed in measured $pH_{T-ALR}$ close to the surface (likely caused by primary productivity) has propagated into the calculated $DIC_{ALR}$, $pCO_{2-ALR}$, and $\Omega_{ar-ALR}$.

When compared in density space, the directly measured $DIC_{CTD}$ and the calculated $DIC_{ALR}$ show very good agreement with a mean $r$(DIC) of 4 $\mu$mol kg$^{-1}$ ($\sigma$=4, n=16), and 100% of the residuals within the mean combined uncertainty of $\pm$11 $\mu$mol kg$^{-1}$ (Figure 2.11a, d). Similarly, there is also good agreement between calculated $pCO_{2-CTD}$ and $pCO_{2-ALR}$. The mean $r(pCO_2)$ is 10 $\mu$atm ($\sigma$=9, n=16), where 94% of the residuals lie within the mean combined analytical uncertainty of $\pm$ 23 $\mu$atm (Figure 2.11b, e).

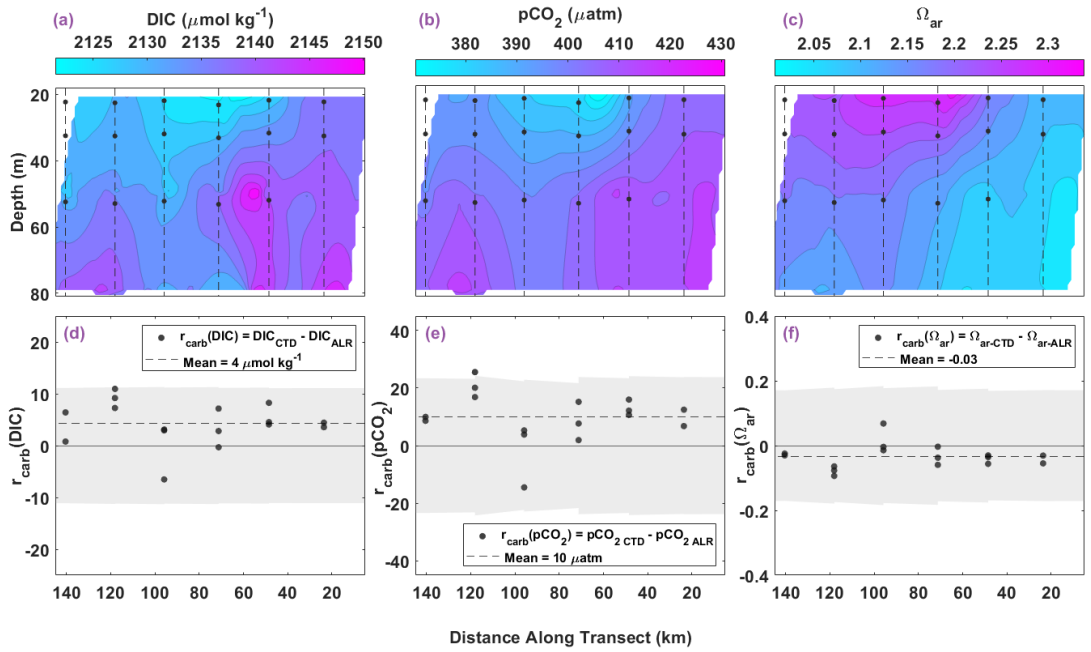


FIGURE 2.11: Vertical contoured distribution of calculated carbonate system parameters from ALR sensor data in the ST (a–c), paired with comparison measured and calculated bottle sample carbonate parameters (d–f). (a) Contour of $DIC_{ALR}$ ($\mu$mol/kg) in ST water column along the transect distance. Black circles connected by dashed lines represent bottle sample locations from CTD casts.(b) Contour of $pCO2_{-ALR}$ ($\mu$atm) and (c) contour of $\Omega_{ar-ALR}$ with the same format as in (a). Residuals show variability between CTD and ALR measurements along ST, where $x_{i-ALR}$ is an interpolated value at the density and distance where $x_{CTD}$ was collected, to produce residual $r_{carb}(x)$. (d) Residuals of DIC ($r$(DIC), $\mu$mol/kg) along transect distance (km). Black circles represent residuals calculated as $r$(DIC) = $DIC_{CTD}$ - $DIC_{ALR}$. The dashed line indicates the mean residual (4 $\mu$mol/kg). (e) Residuals of $pCO_2$ ($r(pCO_2)$, $\mu$atm) along track distance with mean residual of 10 $\mu$atm, and (f) residuals of $\Omega_{ar}$ ($r(\Omega_{ar})$) as a function of longitude with mean residual of -0.03, both with the same legend as in (d) for respective parameters. Grey shaded regions in plots (d)–(f) represent running combined standard uncertainty, including error propagation, with means of (d) $\pm$11 $\mu$mol, (e) $\pm$23 $\mu$atm, and (f) $\pm$0.18.

The mean $r(\Omega_{ar})$ is -0.03 ($\sigma$=0.04, n=16) with 100% of the residuals within mean combined uncertainty of $\pm$0.18 (Figure 13c, f). The positive bias in the ST DIC and $pCO_2$ residuals and the negative bias in $\Omega_{ar}$ residuals reflect the bias in $pH_{T-ALR}$ propagated through the carbonate system calculations as mentioned earlier.

### Deep Transect

The interpolated grid for carbonate calculations of the DT uses the entire same sample area as the previous section. Along the DT, measured and calculated DIC ranged from 2123–2190 $\mu$mol kg$^{-1}$, calculated $pCO_2$ ranged from 388–551 $\mu$atm, and calculated $\Omega_{ar}$ ranged from 1.5–2.3. Similar to the shelf region, $\Omega_{ar}$ decreases with depth as a consequence of the higher DIC and $pCO_2$ concentrations in deeper waters.

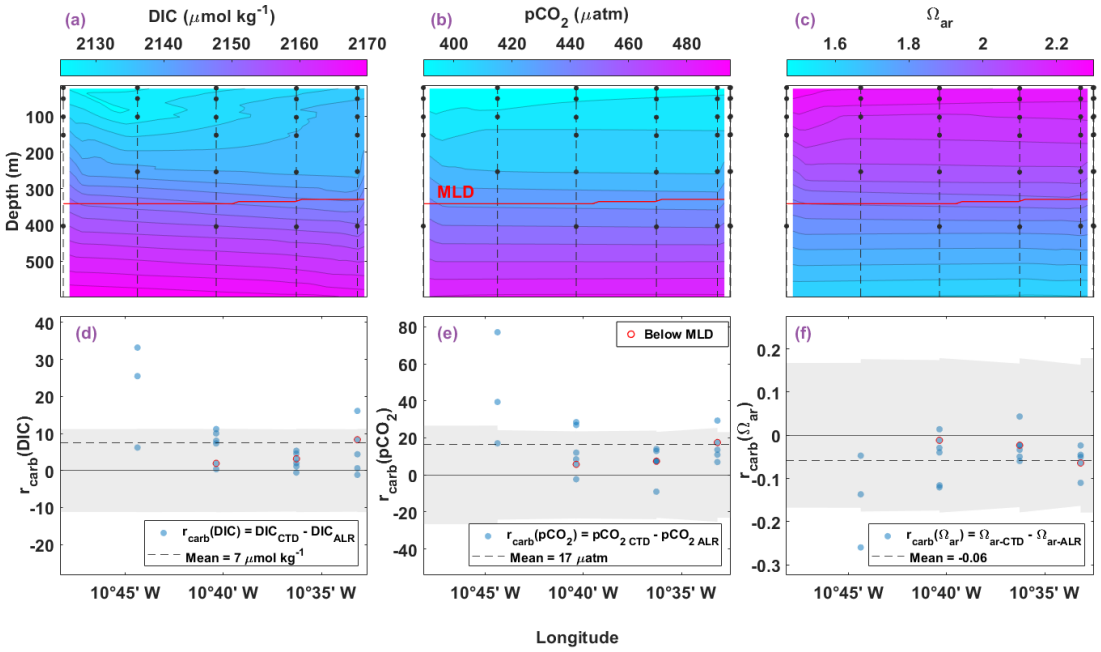


FIGURE 2.12: Vertical contoured distribution of calculated carbonate system parameters from ALR sensor data in the DT (a–c), paired with comparison of measured and calculated bottle sample carbonate parameters (d–f). (a) Contour of DIC$_{ALR}$ ($\mu$mol/kg) in DT water column along the longitudinal transect. Black circles connected by dashed vertical lines represent bottle sample locations from CTD casts. Red horizontal line indicates the average MLD at 345 m. (b) Contour of pCO$_{2-ALR}$ ($\mu$atm) and (c) contour of $\Omega_{ar-ALR}$ with the same format as in (a). Residuals show variability between CTD and ALR measurements along DT, where $x_{i-ALR}$ is an interpolated value at the density and longitude where $x_{CTD}$ was collected, to produce residual $r_{carb}(x)$. (d) Residuals of DIC ($r_{carb}$(DIC), $\mu$mol/kg) along longitude. Black circles represent residuals calculated as $r_{carb}$(DIC) = DIC$_{CTD}$ - DIC$_{ALR}$. Circles outlined in red represent residuals below the MLD. The dashed line indicates the mean residual (7 $\mu$mol/kg). (e) Residuals of pCO$_2$ ($r_{carb}$(pCO$_2$), $\mu$atm) along longitude with mean residual of 17 $\mu$atm, and (f) residuals of $\Omega_{ar}$ ($r_{carb}(\Omega_{ar})$) along longitude with mean residual of -0.06, both with the same legend as in (d) for respective parameters. Grey shaded regions in bottom plots represent running combined standard uncertainty, including error propagation, with means of (d) $\pm$11 $\mu$mol, (e) $\pm$24 $\mu$atm, and (f) $\pm$0.17.

For calculated carbonate system evaluation in the DT, the median ($\tilde{x}$) residual is also reported because the mean residual is skewed from comparisons near 10°45′ W (Figure 2.12d–f). Compared in density space, the measured DIC$_{CTD}$ and the calculated DIC$_{ALR}$ in the DT result in a mean residual of 7 $\mu$mol kg$^{-1}$ ($\sigma$=9 n=20, $\tilde{x}$=5). 85% of $r_{carb}$(DIC) lie within the mean combined uncertainty of $\pm$11 $\mu$mol kg$^{-1}$ (Figure 2.12d). Between calculated pCO$_2$ from both the ALR and CTDs, mean $r_{carb}$(pCO$_2$) is 17 $\mu$atm ($\sigma$=18, n=20, $\tilde{x}$=13) where 75% of the residuals lie within the uncertainty region of $\pm$24 $\mu$atm (Figure 2.12e). Finally, the mean $r_{carb}(\Omega_{ar})$ is -0.06 ($\sigma$=0.06, n=20, $\tilde{x}$=-0.05). Of the $\Omega_{ar}$ residuals in the DT, 95% are within the combined standard uncertainty region spanning on average $\pm$0.17 (Figure 2.12f). As mentioned previously, there are large disparities between the ALR and CTD carbonate parameters along the DT near 10°45′ W that were likely amplified as they propagated through the carbonate calculations. Divergences in $r$(S), $r$(T), $r$(DO), and $r$(pH$_T$) are in the same location (10°45′ W) of the

DT (Figure 2.7b, Figure 2.8a–c). This shows each input parameter—and their differences—contribute to calculated carbonate variable final values. For all residuals of calculated carbonate variable comparisons within the DT, those that lie below the MLD (outlined in red in Figure 2.12d–f) are the smallest, reflecting the higher biogeochemical homogeneity at depths where biological processes are less dominant.

Overall, carbonate system parameters calculated using ALR-sensor pH and TA are comparable to those calculated from the CTD sample measurements with most residuals within the expected combined analytical uncertainty. This does not only add confidence to the quality of the sensor measurements, but also to the data treatment used (i.e. spatial interpolation) to enable carbonate system characterisation. It is important to note that the residuals calculated from comparisons between ALR and CTD observations reflect not only the analytical uncertainty of the sensor and laboratory measurements, but also the spatiotemporal mismatch between the two. Measurements uncertainties of $pH_T$ and TA from both sensors and discrete bottled samples met GOA-ON's weather quality objective (0.02 for $pH_T$, 10 $\mu$mol kg$^{-1}$ for TA) but not the climate quality objective (0.003, 2 $\mu$mol kg$^{-1}$) (Newton et al., 2019). Similarly, the uncertainty in DIC measurements—both directly from bottled samples and as propagated error from CO2SYS—met the weather quality objective (10 $\mu$mol kg$^{-1}$) but fell short of the climate quality standard (2 $\mu$mol kg$^{-1}$) (Newton et al., 2019). The presented work suggests that the autonomous technology described here can provide viable carbonate system information along transects as it has been traditionally done so far from ships. However, further work is necessary to improve the analytical performance of the autonomous sensors, in order to match the measurement quality that can be achieved through laboratory analysis, and satisfy EOV quality objective requirements such as GOA-ON's.

Considerations must also be paid to sensor operation and specifically to measurement synchronisation. The carbonate sensors on the ALR were configured to make measurements at their maximum measurement frequency as illustrated in Table 2.1. A 2.5 minute difference between the pH LOC and TA LOC measurements may seem small but it translates into a spatial mismatch in the order of around 100 m. Traditionally, the carbonate system is characterised from measurements (usually TA and DIC) of the same sample. In the case of the ALR observations, the mismatch was addressed by gridding the $TA_{ALR}$ and $pH_{T-ALR}$ data and using the resulting compatible arrays for the carbonate system calculations. Although this is a valid approach in accounting for this issue (McIntosh, 1990; Ledoux et al., 2005; Sambridge et al., 1995), special care must be taken when applying this treatment in waters with high spatial biogeochemical variability such as productive surface waters, fronts, and sharp vertical gradients. Our data demonstrates that comparisons between ALR and CTD measurements can be challenging in productive surface waters when there is a sample measurement mismatch in space and time. Inevitably, carbonate system

parameters calculated from interpolated values will carry uncertainty that will be difficult to quantify. To avoid this issue, it is, therefore, recommended that sensors are configured so that measurements coincide as much as possible, especially when monitoring in biogeochemically heterogeneous waters.

### 2.3.4 Future perspectives

To this day, ship-based hydrography remains the only method for obtaining high quality carbonate system data over the full ocean column. Global hydrographic surveys have been carried out across defined transects (e.g., GO-SHIP (Sloyan et al., 2019)) approximately every decade since the 1970s, and they are the primary source of information on the status and changes to the ocean carbon system. The advancement of AUVs equipped with carbonate sensors presents a new breakthrough in dynamic observing, monitoring, and characterising the marine carbonate system at high spatiotemporal resolutions. This high-resolution data is necessary to understand fine-scale processes and localised high-frequency changes in pH and $CO_2$ fluxes. The work presented here demonstrates that autonomous ocean observing technology is reaching a readiness level where it can generate carbon observations currently only possible using ships. As it stands, AUV endurance cannot cover the longest of the GO-SHIP repeat transects (in the order of 10,000 km), while sensor analytical performance also needs to be improved. The LOC sensors are designed to be integrated onto other platforms. The key consideration for integration is the availability of supplementary data (S, T, P) required for parameter determination by the sensor. Following this, the primary limiting factor for LOC sensors in these types of autonomous deployments is power demand, whereas in systems with continuous power (e.g., underway ship systems or cabled arrays), reagent supply and occasional mechanical or electronic failures become more critical limitations. Optimal sensor performance requires balancing sampling frequency with deployment duration, site conditions, power availability, and spatial constraints to effectively manage reagent storage, waste disposal, mechanical wear, and biofouling limitations, particularly on long-duration or high-frequency missions. Nevertheless, future advancements in battery technology and improvement in sensor performance could see AUV-based carbon observations meet the requirements of the observing community while increasing data resolution and reducing carbon footprint. By leveraging autonomous technology to observe and constrain the marine carbonate system, today's scientists can better study critical climate issues while ensuring not to contribute to the very problem we seek to understand and mitigate.

## Acknowledgements

The authors would like to thank the captain and crew of the *RRS Discovery*, and all participating scientists during DY149 expedition. In particular, the authors would like to acknowledge the Marine Autonomous Robotic Systems (MARS) team for sensor integration help and most importantly keeping the ALR safe and on track. The authors thank Dr Patricia López-García and Dr Matthew D. Patey for discrete nutrient analysis, and Prof Mark Moore for fantastic cruise leadership. Thank you to the folks at BIOS for their part in the discrete co-sample TA and DIC analysis. We acknowledge funding through Natural Environment Research Council (NERC) grant NE/P02081X/1 (CarCASS project) and NE/P020798/1 (AutoNutS project) which is part of the NERC Oceanids Programme funded by UK Government through the Industrial Strategy Challenge Fund (ISCF) and through the INSPIRE DTP. Finally, the authors thank Swift (D.F.A), Director B. Leyert, Donna, Tim, and of course Ruthie B.

## Supporting Information

The Supporting Information is available free of charge:

- Simplified diagram visualising the carbonate calculation interpolation method. Sensor and bench-top determination uncertainties used to derived combined uncertainties used in the main text.
- Additional data on water column temperature, salinity, dissolved oxygen, density, and fluorescence measured by CTD and ALR during the ST and DT deployments. Relationship between pH and dissolved oxygen deployment-wide, and relationships between depth, time, and density versus pH residuals in the ST and DT.

# Chapter 3

# Coastal Marine Carbon and Air-Sea Fluxes Quantified from pH Sensors on an Extended AUV Deployment

This chapter forms a paper that that is currently under peer review in *The Journal of Geophysical Research: Oceans* as an original research article with the following authors:

**Emily M. Hammermeister**, Cathy Wimart-Rousseau, Stathys Papadimitriou, Pablo Trucco-Pignata, Edward Chaney, Robert Templeton, Alexander B. Phillips, and Socratis Loucaides. Coastal Marine Carbon and Air-Sea Fluxes Quantified from pH Sensors on an Extended AUV Deployment.*ESS Open Archive* [Preprint]. September, 2025. DOI: https://doi.org/10.22541/essoar.175398499.90647984/v2

## Keypoints

- Autonomous observations reveal fine-scale spatiotemporal variability and seasonal processes in carbonate chemistry and air-sea $CO_2$ fluxes/.
- The Celtic Sea acts primarily as a $CO_2$ sink in May–June; shown by one of the region's most detailed continuous carbonate datasets collected.
- Small pH differences can reverse $CO_2$ flux direction under high winds

## Abstract

For the first time, the Autosub Long Range (ALR) completed a fully-autonomous, long-distance (2000 km) scientific mission, delivering new insight into coastal carbonate dynamics and air-sea $CO_2$ fluxes. Equipped with a suite of oceanographic sensors—including a Lab-on-Chip (LOC) pH sensor, a SeaBird SeaFET pH sensor, a conductivity-temperature-depth sensor (CTD), and a dissolved oxygen sensor—the mission generated nearly 50000 high-resolution pH measurements, providing one of the most detailed continuous coastal carbonate datasets collected to date in this region. We evaluated sensor performance and adjustment of the SeaFET k0 parameter using various reference pH inputs, including neural network estimates. The LOC and SeaFET pH sensors showed close agreement ($\Delta pH_T = 0.013 \pm 0.009$), which improved further after k0 adjustment ($\Delta pH_T = 0.00004 \pm 0.007$), while both diverged from model estimates, underscoring the inability of models to resolve fine-scale coastal variability. Total alkalinity (TA) was derived from salinity-based relationships and model predictions, and paired with pH (raw, corrected, and modelled) to estimate the partial pressure of $CO_2$ ($pCO_2$), which ranged 263–598 $\mu$atm. Resulting air-sea $CO_2$ fluxes ranged –17.0–7.1 mmol $m^{-2}d^{-1}$, with the Celtic Margin acting as a net $CO_2$ sink in May–June. Flux direction proved highly sensitive to subtle pH differences under high winds, but far less to TA estimates. Our findings demonstrate the critical role of high-resolution how high-resolution autonomous observations in quantifying coastal carbonate dynamics and $CO_2$ fluxes, capturing processes and variability that are largely unresolved by ship-based surveys or global models.

## Plain Language Summary

For the first time, the Autosub Long Range (ALR), a robotic underwater vehicle, completed a long-distance (2,000 km) scientific mission without ship support. During the mission, the ALR collected ocean data using sensors that measured water temperature, oxygen, and seawater acidity (pH). The mission generated nearly 50000 high-resolution pH measurements, providing one of the most detailed continuous coastal carbonate datasets collected to date in this region. We evaluated how well two onboard pH sensors agreed with each other, as well as with model-based estimates, and we tested the efficacy of an applied correction method. After correction, the sensors closely agreed, showing that autonomous platforms can gather high-quality chemical measurements used to quantify and evaluate marine carbon dynamics. We used the pH data, along with estimates of total alkalinity, to calculate the amount of carbon dioxide ($CO_2$) exchanged between the ocean and atmosphere, finding that the region operates primarily as a sink for carbon in May–June. Our calculations were strongly influenced by the choice of pH input but much less by alkalinity, highlighting the importance of accurate pH observations. This study shows that autonomous sensors can improve monitoring of carbon cycling in coastal waters, which are dynamic, understudied regions that play a key role in the global carbon system.

## 3.1 Introduction

Carbon dioxide ($CO_2$) levels in the atmosphere have increased by nearly 52% since the onset of the Anthropocene, with 2024 emissions exceeding 11.4 GtC $yr^{-1}$, which is 0.3 GtC $yr^{-1}$ higher than in 2023 (Friedlingstein et al., 2025). It is well defined that the ocean is a critical component of the global carbon cycle and plays a crucial role in moderating the rise in atmospheric $CO_2$. The global net uptake of $CO_2$ by the oceans, known as the ocean sink, was $2.9 \pm 0.4$ GtC $yr^{-1}$ in the last decade, accounting for 26% of anthropogenic $CO_2$ annually (Friedlingstein et al., 2025; Quéré et al., 2009a). Yet, the dissolution of $CO_2$ into seawater affects its chemical equilibria, driving ocean acidification (OA) and altering the marine carbonate system— with lasting impacts that ripple across ecosystems, food webs, and global climate processes (Caldeira and Wickett, 2003; Feely et al., 2004; Barker and Ridgwell, 2012; Wolff, 2007). As atmospheric $CO_2$ continues to rise, the ocean's capacity to buffer global climate change diminishes (Tans, 2009). Models now project a buffer capacity decline by up to 34% by 2100, likely accelerating OA and related biogeochemical perturbations (Jiang et al., 2014). Inorganic carbon (the ocean carbonate system) has been deemed an essential ocean variable (EOV) by the Global Ocean Observing System (GOOS); highlighting to the criticality of ocean carbon observations for the assessment of the ocean carbon budget and the quantification of carbon transfer between the atmosphere and ocean (air-sea $CO_2$ fluxes) (Tanhua et al., 2019).

Over the past decades, high quality ship-based ocean carbon observations— driven by programs like GO-SHIP and Ships of Opportunity (SOOP), and data synthesis efforts such as the Global Ocean Data Analysis Project (GLODAP), and the Surface Ocean $CO_2$ Atlas (SOCAT)— have substantially advanced our understanding of ocean carbon cycling. These coordinated initiatives have provided extensive, quality-controlled datasets for global climate models quantifying air–sea $CO_2$ exchange and ocean carbon budgets (McKinley et al., 2016; Schuster et al., 2013; Khatiwala et al., 2013; Wanninkhof et al., 2013). However, ocean carbon data remain sparse in space and time especially in coastal regions and along continental margins where carbon cycling is poorly understood (Marrec et al., 2015; Roobaert et al., 2019; Regnier et al., 2013). Coastal areas exhibit high variability due to complex physical, biogeochemical, and anthropogenic influences, complicating efforts to scale localised observations to the global level. These highly productive regions— accounting for 15–30% of global oceanic primary production— are characterised by enhanced air-sea $CO_2$ fluxes and are particularly vulnerable to anthropogenic forcings such as OA and eutrophication (Gattuso et al., 1999; Duarte et al., 2013; Marrec et al., 2015). Improving observational coverage and mechanistic understanding of coastal systems is critical for reducing uncertainties in the global carbon budget and refining climate projections and mitigation efforts.

Autonomous observing platforms have expanded high-resolution observations of key physical and biogeochemical observations. For example, the Biogeochemical Argo (BGC-Argo) Float Program is a global array of autonomous profiling floats equipped with sensors to measure key biogeochemical variables such as oxygen, pH, nitrate, chlorophyll, and particulate matter (Claustre et al., 2020; Roemmich et al., 2019). BGC-Argo has become a key tool, critical for tracking ocean carbon cycling, improving biogeochemical models, and supporting global carbon budget assessments. Efforts to integrate carbonate sensors onto other autonomous platforms such as Uncrewed Surface Vehicles (USVs), Autonomous Underwater Vehicles (AUVs), and gliders are also well underway. For example, Saildrones and Wave Glider USVs have been equipped with the partial pressure of $CO_2$ ($pCO_2$) systems ($USVpCO_2$), enabling $CO_2$ flux quantification (Sutton and Sabine, 2023; Sabine et al., 2020). Sensors for pH and $pCO_2$ have been integrated on gliders (e.g Saba et al. 2019; Hauri et al. 2024) including Lab-On-Chip (LOC) pH sensor for quantification of sea-atmosphere $CO_2$ fluxes in the North Sea and carbonate system dynamics by the Dodson ice shelf (Possenti et al., 2021; Pickup et al., 2025). More recently, LOC sensor prototypes measuring total alkalinity (TA) and pH enabled complete carbonate system characterisation from a Long Range AUV (Hammermeister et al., 2025), marking the first time this was achieved using direct autonomous observations.

The marine carbonate system is defined by four key variables: dissolved inorganic carbon (DIC), TA, pH, and $pCO_2$. Any two of these variables, combined with temperature, salinity, and pressure, can be used to calculate the remaining two variables through a well-established system of stoichiometric equations (Park, 1969; Millero, 1995, 2007). Currently, only pH and $pCO_2$ sensors are commercially available and widely used for autonomous subsurface deployment (Martz et al., 2015). However, the environmental covariance of pH and $pCO_2$ makes them the least desirable combination to constrain the carbonate system, as it leads to large uncertainty in the derived variables (Orr et al., 2018; Raimondi et al., 2019; Sutton and Sabine, 2023). Currently, carbonate system characterisation from autonomous platforms (e.g., BGC Argo floats) relies heavily on algorithm-derived or estimates of TA paired with measurements of either pH or $pCO_2$). As a conservative parameter in ocean chemistry, TA exhibits a strong linear relationship with salinity in the surface waters of the open ocean, allowing the development of salinity-based algorithms to predict TA where direct measurements are unavailable (Takahashi et al., 2014; Cai et al., 2010; Lee et al., 2006; Millero et al., 1998). The global coverage of the BGC Argo network has helped refine and validate more advanced models that incorporate temperature, oxygen, and other biogeochemical variables to estimate TA across a wide range of oceanic environments. These estimates are used with measured pH to calculate $pCO_2$ and its exchange with the atmosphere (Williams et al., 2017). The quality of these calculations is proportional to the uncertainty of both the TA estimation and the pH sensor measurements which can be a challenge to quantify

over extended autonomous deployments. On BGC-Argo floats, pH sensor stability and accuracy is managed through frequent in situ recalibration: when the float is in deep (below 1000 m) waters where pH is stable and well constrained (Maurer et al., 2021). However, this approach cannot be applied in shallower and more dynamic coastal environments, where pH variability and complex biogeochemical processes render model-based reference values less accurate. Consequently, monitoring pH sensor performance on autonomous platforms in coastal areas remains a significant challenge.

Without reliable recalibration and validation methods in coastal zones, changes in pH sensor performance compromises the quality of derived carbonate system variables and reduces confidence in autonomous air–sea $CO_2$ flux estimates—especially in under-observed, highly variable environments where precise monitoring is most critical.

The work presented here addresses this challenge by investigating the use of a low-frequency (1 hr) photometric pH sensor as an onboard reference for periodic recalibration of high-frequency (1 min) electrochemical pH sensors, commonly used on profiling floats and other fast moving platforms. This approach was tested during the first shore-launched and recovered, long-range scientific mission of the Autosub Long Range (ALR) AUV. We evaluate the environmental data collected by the onboard sensors during the 35-day mission and conduct an intercomparison of the two onboard pH sensors against community-adopted correction protocols and model estimated pH. Our analysis assesses the feasibility of sensor cross-validation for recalibration in coastal settings, examines the role of TA derivation and methodological choices, explores fine-scale spatiotemporal variability in carbonate chemistry, and evaluates the implications for determining $pCO_2$ and air-sea $CO_2$ fluxes. This work aims to demonstrate the new capabilities enabled by novel autonomous technology and represents a step towards improving the reliability and scientific value of carbonate system observations in previously under-sampled, highly dynamic coastal regions.

## 3.2 Materials and Methods

### 3.2.1 The Autosub Long-Range Autonomous Underwater Vehicle

Autosub Long Range (ALR) is a family of large, flight style AUVs (3.6 m length, 750 kg dry mass) developed and operated by the National Oceanography Centre (NOC) with depth ratings of either 1500 m (ALR-1500) or 6000 m (ALR-6000) (Roper et al., 2021). They fitted with a default baseline suite of sensors used for both navigation and science, that include GPS, Doppler Velocity Logs (DVL)/Acoustic Doppler Current

Profilers (ADCPs), and a conductivty-temperature-depth sensor (CTD). Underwater, these vehicles navigate using DVL aided dead reckoning, achieving navigational accuracy <1% of distance travelled in a straight line when in DVL bottom lock range of the seabed. The ALR uses Wi-Fi, acoustic, and Iridium Short Burst Data (SBD®) channels for communication with Iridium SBD serving as the primary communication channel for remote operations. High energy-density lithium primary cells or lithium-ion secondary cells, combined with modest travel speeds, passive buoyancy control, and optimised power consumption of all onboard systems provide long endurance capabilities. Large airfoil section dive wings provide downward force, and control surfaces at the aft that allow for pitch and heading control. Typical dive rates of 0.1–0.3 m $s^{-1}$ are achieved with at a nose down pitch angle of 10–30 degrees. Efficient propulsion is provided by a 600 mm diameter propeller, magnetically coupled to an electric motor and gearbox that enable travel speeds through water between 0.45–0.8 m $s^{-1}$. The propeller enhances modes of operation in the vertical plane, such as being able to profile or maintain a constant depth/altitude from the seabed. ALR-4, an ALR-1500, was used for this deployment, and is hereafter referred to in this text as the ALR.

### 3.2.2 Autonomous Mission

As a part of the ALR's extensive development program, the Long-Distance Proving Trial (LDPT) was defined to demonstrate the endurance capabilities of the ALR, particularly in a scientific capacity. From the 10th of May to the 13th of June 2022, the ALR transited independently in a south-west direction from Plymouth's coastal waters, past the continental shelf into open ocean (Atlantic), and back (Figure 3.1A). The deployment consisted of dives lasting roughly 4 to 24 hours; after each dive the ALR telemetered back decimated data and received piloting instructions for the next dive. Following 5 weeks of operation at sea without topside vessel support, the ALR returned to Plymouth under its own power, marking its longest and furthest deployment to date (as of March, 2022). Throughout the deployment, the ALR performed various sampling patterns at different depths and profiling frequencies (Figure 3.1. B) and tested its ability to follow mission instruction dependent on sampling needs (Phillips et al., 2023). The total expected power consumption in this configuration was 32 W giving an expected maximum endurance of 100 days and range of 4750 km at a speed of 0.55 m $s^{-1}$.

#### Sensors and Equipment

The ALR has flooded payload bays that sit forward and aft of its main pressure hull and can be configured with a wide range of oceanographic sensors in addition to its standard sensor payload. As a part of its standard payload, the ALR was equipped

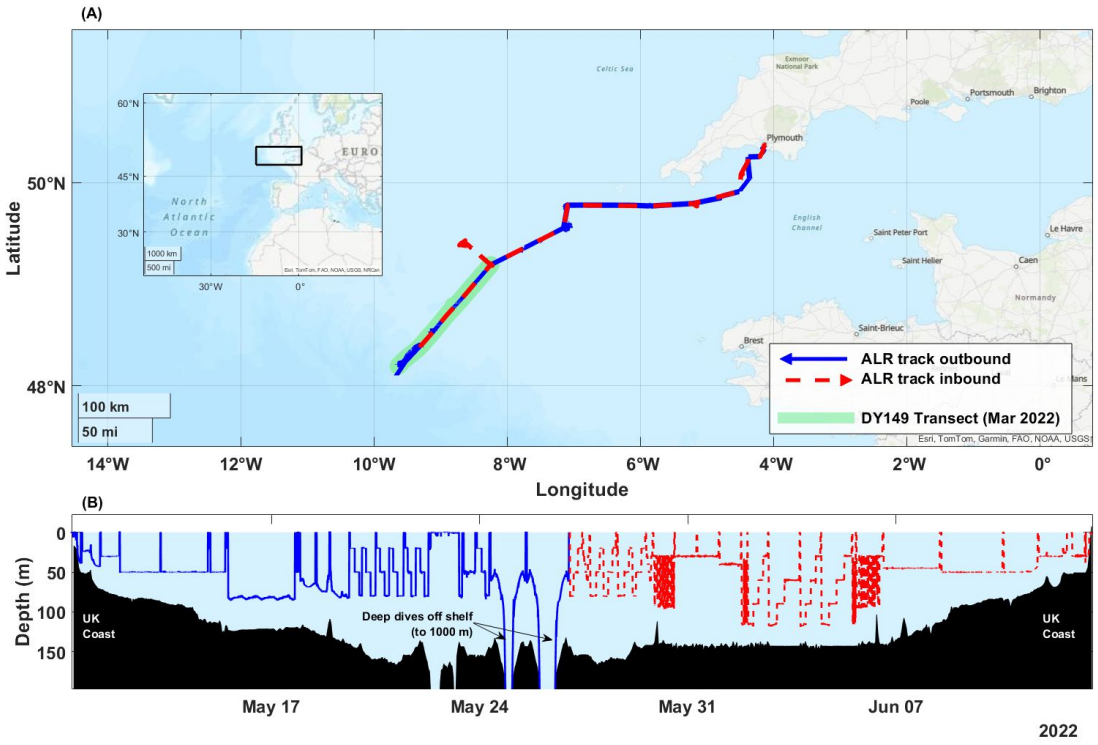


FIGURE 3.1: Long-Distance Proving Trial (LDPT) study site located Southeast off the coast of England in the Celtic Sea and continental margin. (A) Map of the entire deployment track of the Autosub Long Range (ALR) departing from and returning to Plymouth, UK. The green shaded area represents the DY149 ship-supported ALR transect conducted in March 2022 with ALR-2. (B) ALR transect and dive profiles plotted as depth (m) over time (mid-May to early June 2022), with seafloor bathymetry (black shading). For both (A) and (B) the outbound track of the ALR is shown as a solid blue line and the inbound track is shown as a dashed red line.

with a pumped CTD (SBE 52-MP) sensor, which for this mission, was equipped with an auxiliary SBE 43F dissolved oxygen (DO) sensor. The CTD-DO operated at a frequency ($f$) of 1 Hz (1 measurement per second) and provided measurements of in situ temperature (T), salinity (S), pressure (P), and dissolved oxygen (DO). The forward bay of the ALR was fitted with an Lab-On-Chip pH (LOC; NOC) sensor, and a Deep SeaFET V2 (SeaFET; SeaBird Scientifc) electrochemical pH sensor (Figure 3.2 and Table 3.1).

The LOC pH sensor determines pH on the total proton scale ($pH_T$) photometrically using purified meta-Cresol Purple (mCP) as the indicator dye. It achieves a precision of 0.001 pH units associated with a $0.003 \pm 0.022$ accuracy relative to validation seawater samples and a combined standard measurment uncertainty of $\pm$ 0.010 pH units (Yin et al., 2021). The SeaFET uses a solid-state ion-sensitive field-effect transistor (ISFET) sensor to measure pH by detecting hydrogen ion concentration in seawater (based on Honeywell's Durafet ISFET technology; Johnson et al. 2016). The SeaFET sensor has a reported pH accuracy of 0.05 pH units on the total scale and is therefore

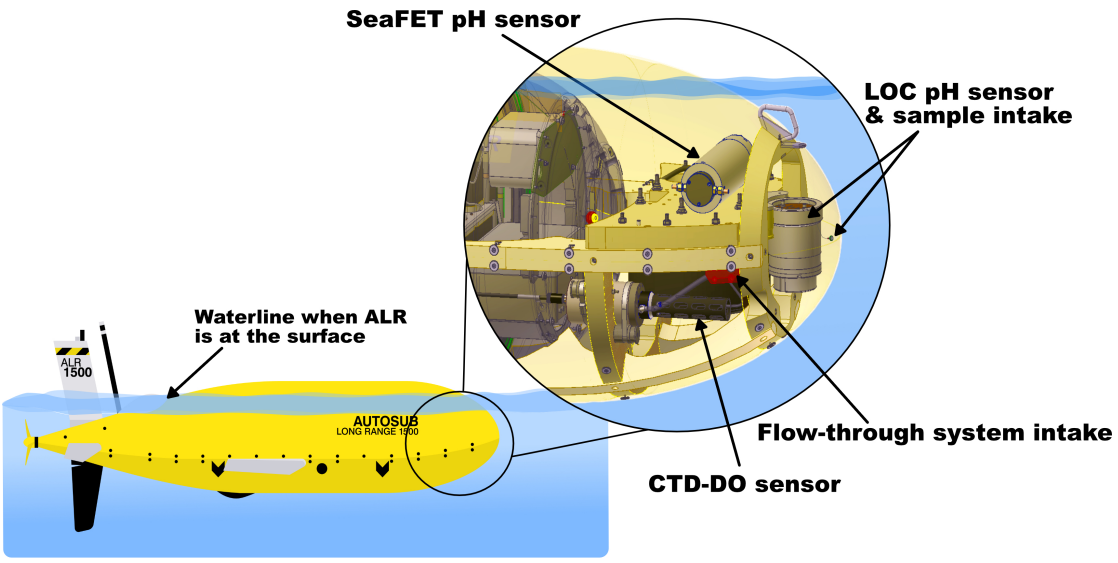


FIGURE 3.2: Schematic of Autosub Long Range 1500 (ALR) equipped with scientific instrumentation for the Long-Distance Proving Trial deployment. A zoomed view into the front bay of the ALR shows how the CTD-DO, each pH sensor, and sample intake systems, were situated. When positively buoyant at the surface, the ALR sits mostly submerged, with the sensor intakes approximately 0.4 m below the waterline.

TABLE 3.1: Summary of pH sensors used for deployment

| pH Sensor | Determination Method | Measurement Uncertainty | Measurement f (LDPT Deployment) | Depth Rating |
|---|---|---|---|---|
| Lab-On-Chip<br><br>NOC (Southampton, UK) | Photometric, mCP reagent | 0.01 pH | 1 measurement / hour | 6000 m |
| SeaFET<br><br>Sea-Bird Scientific (Seattle, WA, US) | Electrochemical, ISFET | 0.05 pH | 1 measurement / min | 2000 m |

used here as a first-order estimate of the SeaFET pH measurement uncertainty (Sea-Bird Scientific, 2024, 2025). A summary of the two pH sensors used in this deployment can be found in Table 3.1.

The LOC pH sensor drew power from an isolated 25.2 V 152 AH Lithium Thionyl Chloride battery pack, 1 of 30 total fitted to power the ALR. A DC-DC converter provided 12 VDC required by the sensor. The SeaFET was independently powered by its 12 D-cell alkaline internal batteries. The SeaFET sensor was fitted with a flow-cell cap and plumbed into the flow-through system shared by the CTD-DO sensors. Seawater was continuously pumped from an intake outside the ALR's fairing, 43 mm below the centreline of the vehicle (Figure 3.2). The LOC pH sensor sampled seawater through a 0.7 mm PEEK tube and filter (0.45 $\mu$m pore size and 2.5 cm diameter) perturbing the ALR's front fairing, 30 mm below its centreline (Figure 3.2). All sensors

operated continuously (See Table 3.1) from the ALR's deployment until its recovery without interruption and although the ALR surfaced frequently for data transfer and navigation updates, sensor water intakes remained submerged approximately 400 mm below the sea surface, depending on sea state (Figure 3.2).

### 3.2.3 Sensor Data Processing

In situ T, S, and P measurements from the CTD-DO sensor were time-matched with pH sensor measurements manually post-recovery and were used to determine in situ $pH_T$ as described in (Yin et al., 2021) for the LOC pH sensor and manufacturer's instruction (AN-99; (Sea-Bird Scientific, 2024)) for the SeaFET pH sensor. More details on the calculations and calibrations of each sensor are provided in the Supporting Information (e.g., Table B.1). The mixed layer depth (MLD) was determined using the threshold method with criterion $\Delta\sigma_\theta = 0.125$ kg m$^{-3}$ where $\sigma_\theta$ represents potential density (Monterey and Levitus, 1997; Levitus, 1982; de Boyer Montégut et al., 2004b).

#### Correction of $pH_{SeaFET}$ Data

Although SeaFET sensors have demonstrated good measurement stability over time relative to other electrochemical and optical sensors (e.g., Bittig et al. 2018; Johnson et al. 2016), signal drifts over long autonomous deployments are unavoidable and hard to quantify. In comparison, spectrophotometric pH measurements are resistant to drift due to long-term stability of the indicator dye and principle of the measurement which is independent of changes in detector sensitivity and light source intensity (Müller and Rehder, 2018; Mosley et al., 2004; Rérolle et al., 2012, 2016). The SeaFET sensor measures in situ $pH_T$ ($pH_{SeaFET}$) by detecting the voltage difference between the ISFET source and the reference electrode, which is directly exposed to seawater and sets the reference potential (k0) using the salinity-dependent conservative concentration of chloride ions in seawater (Johnson et al., 2016; Sea-Bird Scientific, 2024; Dickson et al., 2007). This measured potential is then transformed into $pH_T$ through calibration coefficients. Despite careful calibration practices in the laboratory before deployment, k0 shifts may occur in response to environment temperature changes because the Nernst slope (which transforms sensor potential into pH) is temperature-dependent (Johnson et al., 2017, 2016). To combat the resulting sensor drift and reach accuracy levels required for global $CO_2$ system studies (Newton et al., 2015), $pH_{SeaFET}$ data from Argo profiling floats are corrected by adjusting the sensor's k0 based on established calibration procedures (Johnson et al., 2016).

The correction procedure developed for Argo float pH data (Maurer et al., 2021) assesses the changes in k0 by comparing in situ pH values measured against a reference ($pH_{ref}$) to calculate an at-depth (typically around 1500 dbar for Argo floats) pH anomaly. This approach was used in this study to drift-correct the $pH_{SeaFET}$

observations using a reference depth of 500 m adapted to account for the shallower ALR mission. As with the Argo float pH corrections, $pH_{ref}$ was calculated based on Empirical Seawater Property Estimation Routines from neural networks (ESPER-NN) (Carter et al., 2021). ESPER's Locally Interpolated Regression (ESPER-LIR) routine was also used to generate $pH_T$ values for comparison but not used as a reference pH due to its similarity to the more rigorous ESPER-NN output. The ESPER-NN and ESPER-LIR routines produced $pH_T$ estimates, hereafter labeled as $pH_{NN}$ and $pH_{LIR}$ respectively. For this work, ESPER was the chosen routine for estimating pH given the following reasons:

1. ESPER's inclusion of new data from GLODAPv2.2020 data product.
2. Algorithm imitates the design of the widely regarded "Carbonate system and Nutrients concentration from hydrological properties and Oxygen using a Neural-network version B" (CANYON-B) algorithms by (Bittig et al., 2018; Sauzède et al., 2017).
3. Use of a new first-principles-based approach to estimate anthropogenic impacts on $pH_T$ as updated from the OA adjustment presented with the locally interpolated pH regression (LIPHR) product by (Carter et al., 2018).
4. Quantifiable uncertainty estimation is returned by the routines.
5. Robust assessments, particularly in the North Atlantic region.

Estimates calculated through both ESPER products used inputs T, S, DO, depth and GPS coordinates measured by the CTD-DO and ALR systems, with the estimate date set to 2022. For comparison, we evaluate the use of two different $pH_{ref}$ for the $pH_{SeaFET}$ adjustments. Since the LOC pH sensor measurements ($pH_{LOC}$) had spatiotemporal crossovers occurring every $\sim$ 60th SeaFET measurement, it was used as the second $pH_{ref}$ alongside $pH_{NN}$. By correcting the high frequency $pH_{SeaFET}$ measurements to the stable and accurate $pH_{LOC}$ measurements, we maximise the strengths of each sensor, resulting in a high-resolution and reliable dataset. The $pH_{SeaFET}$ k0-adjusted using $pH_{LOC}$ will henceforth be referred to as $pH_{k0–LOC}$ and the $pH_{SeaFET}$ k0-adjusted using $pH_{NN}$ will henceforth be referred to as $pH_{k0–NN}$.

To determine the adjustment and overcome the offsets and drift calibration jumps that often occur during the sensor's life, the pH anomaly time series was divided into separate segments bound by breakpoint nodes determined by a cost function (Killick et al., 2012). The MATLAB function *ischange* (The Mathworks Inc., 2024), was used to perform the binary splitting that separated the segments to find the optimal location of an increasing number of breakpoints which is constrained by a threshold value on the mean residual. The threshold value— most commonly set to 0.005 pH units by the Argo community(Maurer et al., 2021)— specifies the sensitivity of change detection

and is driven by the target accuracy of the sensor. If the threshold value is omitted or set too low, an excessive number of breakpoints will be detected and is equivalent to assuming no inherent noise (points with a few changes will be detected), which is inconsistent with known sensor behavior (Maurer et al., 2021). Next, a linear least squares fit was applied to each anomaly data series between each node, determining offset and drift values for each section (see Figure 3.5). Since the k0 adjustment using $pH_{LOC}$ was derived from observation-based $pH_T$ with less measurements than $pH_{SeaFET}$, each linear rate of change segment was applied across the $pH_{SeaFET}$ data set based on breakpoint nodes timestamps.

Conceptually, the linear rate of change should be applied to the k0, assuming that the reference potential is drifting over time. Hence, a temperature-relation correction (TCOR) term is then applied to the determined correction value by normalizing the adjustment along the section to the temperature at which the adjustment was derived. Temperature-normalised changes in pH are calculated by multiplying the change in pH computed at depth by the ratio of the absolute temperature of the sample to the absolute temperature at reference depth. The constant at-depth reference temperature value of 10 °C is used as determined by the mean temperature recorded by the ALR below 500 m.

#### Comparison of $pH_T$ Data

The differences between $pH_T$ values ($\Delta pH_T$) measured by sensors and estimated from ESPER are calculated to evaluate the agreement between methods and variance within each method. Additionally, combined standard uncertainty ,$u_c$, was calculated when comparing $pH_T$ values. It was calculated as the positive square root of the combined variances using Equation 3.1 and based on the documented uncertainties of the sensors and estimate routines (JCGM et al., 2008).

$$u_c^2(y) = \sum_{i=1}^{N} u_i^2(y) \tag{3.1}$$

### 3.2.4 Carbonate System and Flux Calculations

#### Total Alkalinity Derivation

To constrain the marine carbonate system and consequently calculate $CO_2$ flux, another measurable carbonate input parameter is needed. We use four different methods to derive total alkalinity ($TA_n$) to compare the impact of each method on calculated $pCO_2$ and $CO_2$ flux. $TA_1$ was determined from salinity based on the relationship of Takahashi et al. (2014) and $TA_2$ was determined from salinity and temperature based on Lee et al. (2006). Other algorithms exist for TA estimation (e.g.,

Cai et al. 2010; Millero et al. 1998), however, the Takahashi et al. and Lee et al. relationships are best suited for the North Atlantic. $TA_3$ and $TA_4$ were determined by implementing ESPER-LIR and ESPER-NN (Carter et al., 2021) estimations respectively, using inputs T, S, DO and GPS coordinates measured by the CTD-DO and ALR systems, with the estimate date set to 2022 (Table 3.2).

#### Calculation of $pCO_2$ (pH, TA)

The speciation of the carbonate system was characterised using the MATLAB (version v3.1.1; The Mathworks Inc., 2024) CO2SYS package (Sharp et al., 2023b; Orr et al., 2018; van Heuven et al., 2011a; Lewis and Wallace, 1998) with measured $pH_T$ and derived TA concentrations as the carbonate input parameters as well as T, S, and P from the CTD on board the ALR. Following the recommendations from (Dickson et al., 2007), CO2SYS computations used the dissociation constants of carbonic acid ($K_1$ and $K_2$) from (Lueker et al., 2000), $K_{SO4}$ from (Dickson, 1990), KF from (Perez and Fraga, 1987), and total boron concentration from (Lee et al., 2010). Similar to TA, different $pH_T$ measurements (both uncorrected and corrected) were evaluated to assess their impacts on the final $pCO_2$ values. Therefore, several combinations of $pH_T$ and $TA_n$ were used to derive seawater $pCO_2$ (Table 3.2).

TABLE 3.2: Input combinations of pH and TA used to calculate $pCO_2$

| Label | pH input | TA input | pH Correction |
|---|---|---|---|
| **$pH_1TA_1$** | $pH_{SeaFET}$ | Takahashi et al. (2014)[a] | n/a |
| **$pH_1TA_2$** | $pH_{SeaFET}$ | Lee et al. (2006)[b] | n/a |
| **$pH_1TA_3$** | $pH_{SeaFET}$ | ESPER-LIR | n/a |
| **$pH_1TA_4$** | $pH_{SeaFET}$ | ESPER-NN | n/a |
| **$pH_2TA_1$** | $pH_{k0\text{-}LOC}$ | Takahashi et al. (2014) | $pH_{SeaFET}$ k0-adjusted using $pH_{LOC}$ |
| **$pH_2TA_2$** | $pH_{k0\text{-}LOC}$ | Lee et al. (2006) | $pH_{SeaFET}$ k0-adjusted using $pH_{LOC}$ |
| **$pH_2TA_3$** | $pH_{k0\text{-}LOC}$ | ESPER-LIR | $pH_{SeaFET}$ k0-adjusted using $pH_{LOC}$ |
| **$pH_2TA_4$** | $pH_{k0\text{-}LOC}$ | ESPER-NN | $pH_{SeaFET}$ k0-adjusted using $pH_{LOC}$ |
| **$pH_3TA_1$** | $pH_{k0\text{-}NN}$ | Takahashi et al. (2014) | $pH_{SeaFET}$ k0-adjusted using $pH_{NN}$ |
| **$pH_3TA_2$** | $pH_{k0\text{-}NN}$ | Lee et al. (2006) | $pH_{SeaFET}$ k0-adjusted using $pH_{NN}$ |
| **$pH_3TA_3$** | $pH_{k0\text{-}NN}$ | ESPER-LIR | $pH_{SeaFET}$ k0-adjusted using $pH_{NN}$ |
| **$pH_3TA_4$** | $pH_{k0\text{-}NN}$ | ESPER-NN | $pH_{SeaFET}$ k0-adjusted using $pH_{NN}$ |

[a] $TA = 45.30(S) + 733.00$; Location range: 40°N–55°N, 60°W–10°E

[b] $TA = 2305 + 53.97(SSS - 35) + 2.74(SSS - 35)^2 - 1.16(SST - 20) - 0.040(SST - 20)^2$, Location range: Mid Atlantic Drift, 30°N–80°N

### $CO_2$ Flux Calculations

To estimate the air-sea $CO_2$ fluxes from data collected by the ALR we use the bulk flux formulation:

$$CO_2\ flux = k_w \times K_0 \times \Delta pCO_2 \tag{3.2}$$

where $CO_2$ flux is the net $CO_2$ transfer (positive from ocean to atmosphere), $k_w$ is the gas transfer velocity (m $s^{-1}$), $K_0$ is the solubility of $CO_2$ in seawater (mol $m^{-3}$), and $\Delta pCO_2 = pCO_{2,ocean} - pCO_{2,atm}$ is the air-sea difference in partial pressure of $CO_2(\mu atm)$. As described in Section 3.2.4, $xCO_2$ (the mole fraction of $CO_2$ in dry air

assuming 1 atm total pressure) was calculated using CO2SYS and filtered to include only values from when the ALR was at the surface—meaning all recorded values measured at the fixed sensor intake depth ($\sim$ 0.04 m below the water line). To get $pCO_{2,ocean}$ needed for flux calculations, the $xCO_2$ was then adjusted to be at equilibrium with surface waters in accordance with ocean $CO_2$ standard operating procedures (Dickson et al., 2007) using the following:

$$pCO_{2,ocean} = (P_{atm} - P_{H20}) \times xCO_2 \tag{3.3}$$

where $P_{atm}$ = ambient atmospheric pressure (atm) and $P_{H20}$ = vapour pressure (atm) over seawater at a given sea surface temperature (SST) and salinity (SSS), and $xCO_2$ = atmospheric $CO_2$ as mole fraction (ppm). The $xCO_2$ was obtained from the Penlee Point Atmospheric Observatory (PPAO;Plymouth Marine Laboratory and Yang 2017; Yang et al. 2019; Archibald et al. 2025), part of the Western Channel Observatory (WCO), and was converted to $pCO_{2,atm}$ ($\mu$atm) according to Equation 3.4:

$$pCO_{2,atm} = \left[(P_T - (\frac{RH}{100}) \times P_{H20})\right] \times [xCO_2] \tag{3.4}$$

where $P_T$ = total atmospheric pressure (in atm), RH = relative air humidity (percent), and $P_{H20}$ = vapor pressure of water at ambient temperature (Dickson et al., 2007). The PPAO dataset had a 15-minute resolution which was linearly interpolated to match the 1-minute resolution $pCO_{2,ocean}$ obtained by the sensors onboard the ALR (Figure B.1). The solubility $K_0$ was computed using the T and S dependent formulation by (Weiss, 1974). The gas transfer velocity kw was parameterised following (Wanninkhof, 2014), which is defined as:

$$k_w = 0.251 \times (U_{10})^2 \times (\frac{Sc}{660})^{-0.5} \tag{3.5}$$

here $U_{10}$ = wind speed at 10 m height (m $s^{-1}$), extracted from ERA5 reanalysis product (Hersbach et al., 2020), and Sc = Schmidt number. Specifically for $U_{10}$, the eastward and northward components of the 10 m wind were retrieved from the Climate Data Store (`https://cds.climate.copernicus.eu/`) at a 0.25 $\times$ 0.25 spatial resolution and hourly temporal resolution. To ensure temporal consistency, the wind time series was linearly interpolated to 1-minute resolution (Figure B.2) and time-matched to ALR surface measurements, enabling accurate flux estimations. The Schmidt number was calculated as a function of temperature in (°C) using:

$$Sc = 2116.8 - 136.25 \times T + 4.7353 \times T^2 - 0.092307 \times T^3 + 0.0007555 \times T^4 \tag{3.6}$$

## 3.3 Results

### 3.3.1 Autonomous Data Collection

Following five weeks of autonomous operation, the ALR was recovered at 13:40 on the 13th of June just south of the Plymouth breakwater. In total, the ALR travelled approximately 2000 km, which spanned 54 separate programmed missions and over 800 hours of continuous data collection. The ALR reached depths up to 1000 m when travelling off the continental shelf but spent most of the deployment in the top 100 m of the water column in coastal waters.

#### Biogeochemical Water Properties

Figure 3.3 shows the temporal and spatial trends in T, S, and DO across the deployment. The full range of T (9.1 – 16.5 °C), S (33.2 – 35.9 psu), and DO (174 – 317 $\mu$mol kg$^{-1}$) is seen in Figure 3.3A,D,G. However, because the ALR spent 90% of the deployment within the top 100 m of the water column, a magnified view of T, S, and DO in the water column over time is presented in Figure 3.3B,E,H, revealing the MLD varying between 4 and 52 m over the five-week mission. Surface conditions (top 20 m), shown in Figure 3.3C,F,I indicate a steady T increase and DO decline over time. Salinity peaked when the ALR moved off the shelf and dropped near the coast at the mission's start and end, likely due to freshwater inputs (Figure 3.3 D–F).

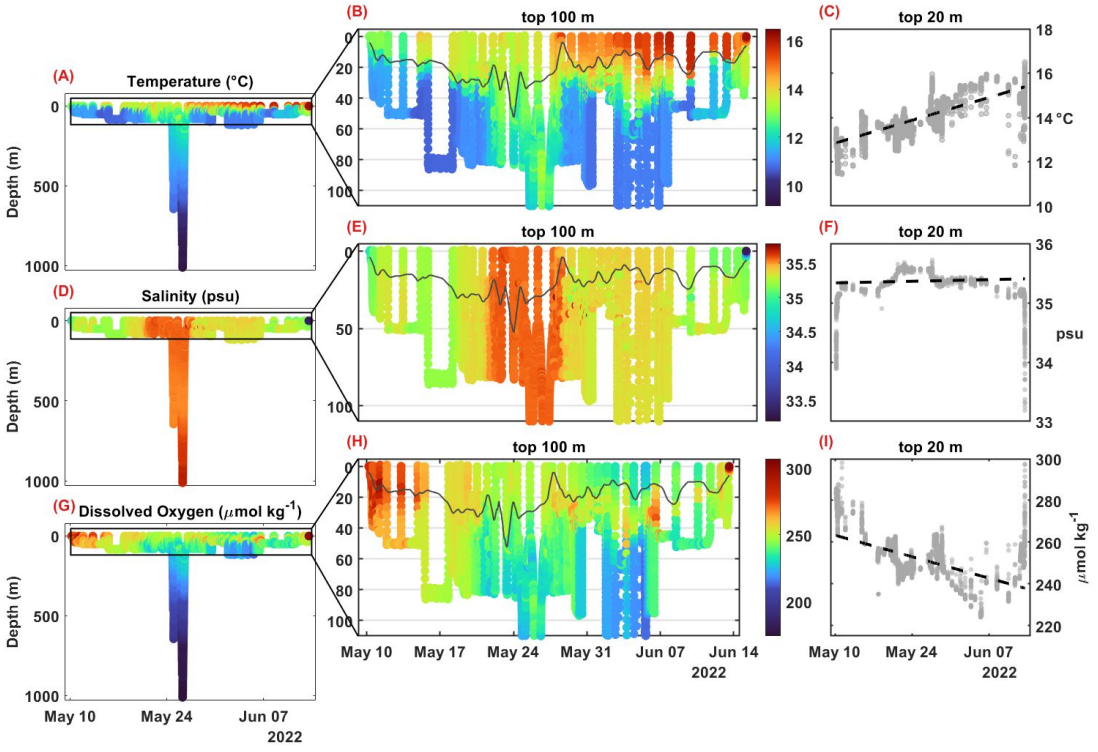


FIGURE 3.3: Autonomous high-resolution observations of temperature (°C), salinity (psu), and dissolved oxygen ($\mu$mol kg$^{-1}$) collected by sensons onboard the ALR during the five-week LDPT deployment (May–June 2022). Panels (A), (D), and (G) show full-depth profiles (to $\sim$ 1000 m) for temperature, salinity, and dissolved oxygen (represented by colour), respectively throughout the deployment. Panels (B), (E), and (H) present a magnified view of the top 100 m, capturing most of the ALR's observational period. The black line in panels (B), (E), and (H) indicates the estimated mixed layer depth over time. Panels (C), (F), and (I) display conditions in the upper 20 m of the water column over time showing surface temporal trends over the course of the deployment.

### pH Data

The pH sensors onboard the ALR operated the entirety of the LDPT, with neither showing evidence of hardware, software, or power malfunction. The LOC pH sensor made 858 $pH_T$ measurements, and the SeaFET pH sensor made 49,184 $pH_T$ measurements. Prior to any $pH_{SeaFET}$ corrections, combined sensor $pH_T$ measurements ranged 7.898–8.187 ($1\sigma$ = 0.380, n = 50042), with generally good agreement between the two sensors (Figure 3.4A). The mean uncorrected pH difference between the two sensors ($\Delta pH_{T-uncorrected}$) was 0.013 $\pm$ 0.009 pH units ($1\sigma$, n = 858) with 99% of $\Delta pH_{T-uncorrected}$ falling within the combined measurement uncertainty (of $\pm$ 0.051 pH units) (Figure 3.4B). The $pH_{SeaFET}$ required approximately 10 days to stabilise, exhibiting reduced drift and improved consistency with $pH_{LOC}$ measurements (Figure 3.4A,B). This behaviour, known as "electrode conditioning", is a well-documented characteristic of ISFET technology (Martz et al., 2010; Bresnahan et al., 2014).

After correcting $pH_{SeaFET}$ with the k0 adjustment using $pH_{LOC}$ as the reference pH (see

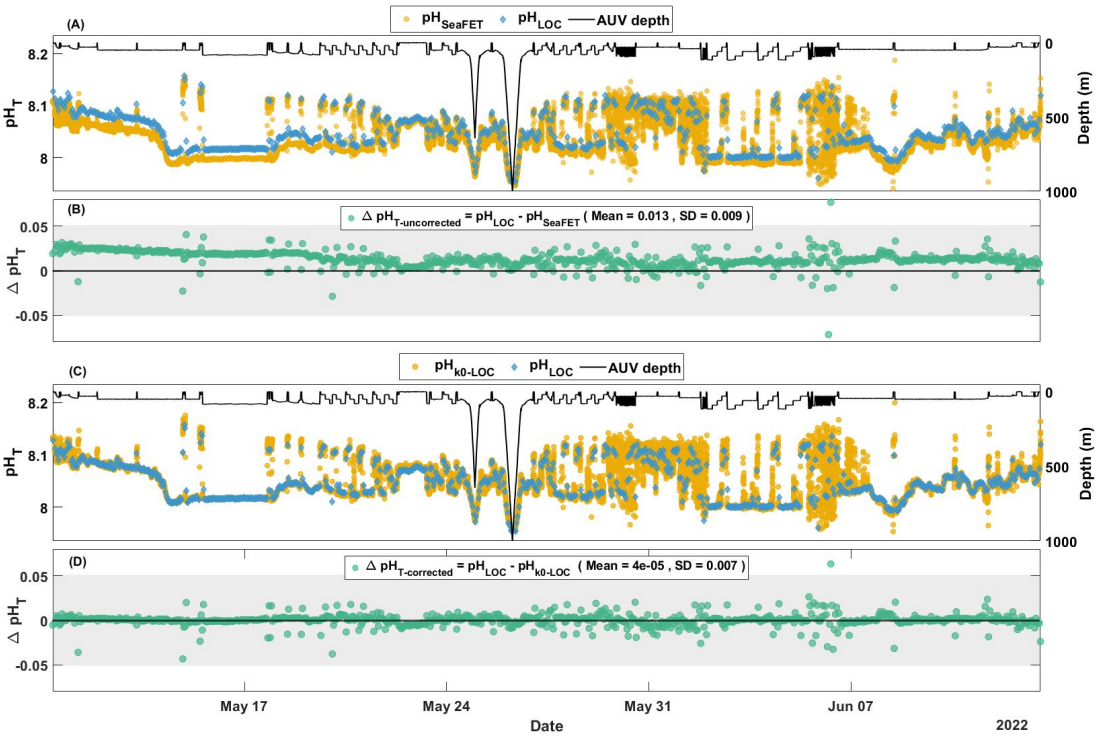


FIGURE 3.4: Time series comparison of pH measurements and offsets between SeaFET pH sensor and LOC pH sensor before and after k0 adjustment (see section 3.2.3). (A) In situ uncorrected $pH_T$ data from the SeaFET sensor (yellow) and $pH_{LOC}$ measurements (blue diamonds) shown alongside the transiting depth of the ALR (black line). (B) Uncorrected pH difference ($\Delta pH_{T\text{–uncorrected}} = pH_{LOC} - pH_{SeaFET}$), with a mean offset of 0.013 pH units and standard deviation of 0.009 pH units. (C) SeaFET sensor pH referenced to LOC sensor pH via the k0 adjustment (yellow), and $pH_{LOC}$ (blue diamonds). (D) ($\Delta pH_{T\text{–corrected}} = pH_{LOC} - pH_{k0\text{–}LOC}$), with mean offset of $4 \times 10^{-5}$ pH units and reduced standard deviation of 0.007 pH units. Shaded gray regions in (B) and (D) span $\pm$ 0.051 pH units, representing combined sensor uncertainty $u_c$.

section 3.2.3 above and Figure 3.5 below), all $pH_T$ measurements from both pH sensors ranged from 7.911–8.200 (average $\pm$ 1$\sigma$ = 0.038 $\pm$ 0.038, n=50042 ). As expected, the two sensors showed near-perfect agreement, with the SeaFET's electrode conditioning period effectively removed (Figure 3.4C). The average $\Delta pH_{T\text{–corrected}}$ approached zero and the standard deviation was improved (1$\sigma$ = 0.007), with 99% of $\Delta pH_{T\text{–corrected}}$ values falling within the combined measurement uncertainty ($\pm$ 0.051 pH units) of the sensors (Figure 3.4D). The time series comparison before and after correction using $pH_{NN}$ as the reference $pH_T$ is not shown here due to its less effective performance and noisier appearance, but can be found in Supporting Information Figure B.3.

Figure 3.5 illustrates the adjustment process by exhibiting the pH anomaly changes ($\Delta pH_T$) throughout each dataset (n sample) comparing $pH_{SeaFET}$ values against $pH_{LOC}$ measurements (Figure 3.5A) and $pH_{NN}$ outputs (Figure 3.5B). Breakpoint nodes were identified using respective threshold values to segment the data and calculate linear rate of changes. Each threshold value was modified to preclude the determination of

unrealistic breakpoint nodes. A threshold of 0.00500 was used for the $pH_{LOC}$ dataset that yielded two clear breakpoints and three segmented correction rates to be applied (Figure 3.5A). Given the particularly noisy anomaly series using $pH_{NN}$, a higher threshold value of 0.10000 was used, producing 20 breakpoints and corresponding segments (Figure 3.5B). Threshold values are regarded in pH units. The $pH_{LOC}$-based k0 adjustment was derived from n = 858 observational $pH_T$ values, while the $pH_{NN}$-based k0 adjustment used n = 49184 neural network $pH_T$ estimates that were aligned $pH_{SeaFET}$ timestamps (n = 49184).

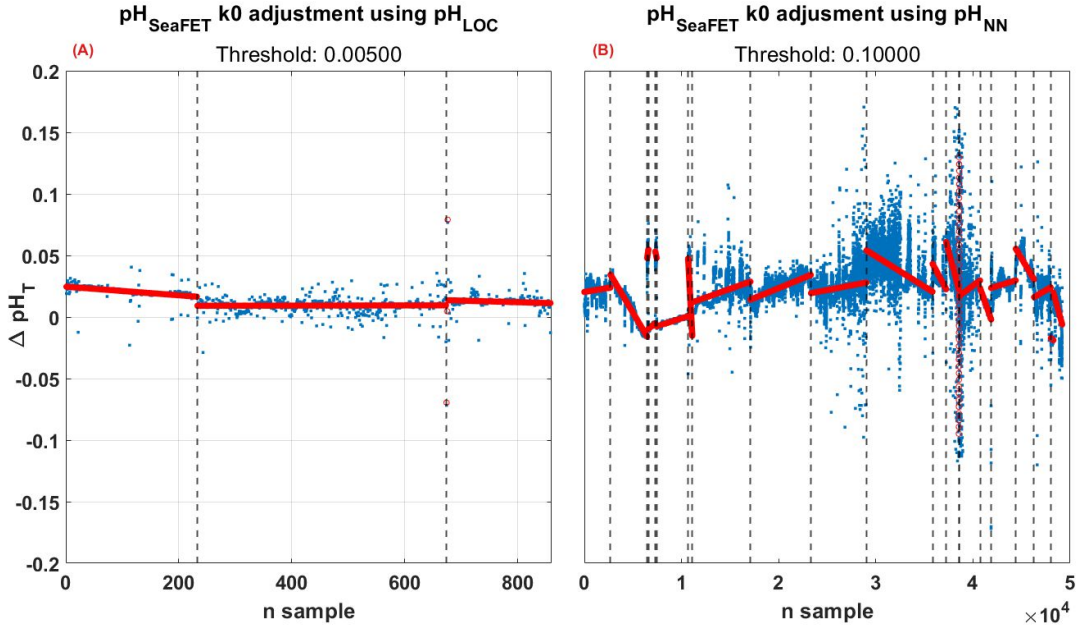


FIGURE 3.5: Correction of $pH_{SeaFET}$ values with k0 adjustment method using (A) $pH_{LOC}$ and (B) $pH_{NN}$ as the pHref. The plots represent the pH difference ($\Delta pH_T$ on y-axis) between each $pH_{ref}$ and $pH_{SeaFET}$ for each measurement taken (n sample on x-axis) represented by blue dots. The vertical dashed black lines indicate each instance where a breakpoint node was identified based on the defined threshold criteria (A: 0.00500, B: 0.10000). Red lines show each segmented linear correction rate to be applied between each breakpoint. The local calibration method (A) shows tighter agreement and lower variance compared to the neural network adjustment (B).

Results from this section provide strong evidence that $pH_{k0\text{–}LOC}$ quantitively represents the most reliable pH determination with the least associated uncertainty, and will henceforth be regarded as such. In the following sections, downstream products calculated from $pH_{k0\text{–}LOC}$ (or $pH_2$) are emboldened (green) in figures comparing observation methods, and serve as the primary dataset for scientific interpretations.

### 3.3.2 $pCO_2$ Data

Using various combinations of three different $pH_T$ datasets and four different derived TA datasets, oceanic $pCO_2$ values were calculated during the LDPT, and ranged from 263–598 $\mu$atm (n = 590208, all combinations). Figure 3.6 shows the distribution of $pCO_2$ generated by each dataset combination. The $pCO_2$ results highlight a noticeable pH input dependency, the extent of which is further supported by the matrix analysis found in the Supporting Information (Figure B.5). Notably, the highest $pCO_2$ values (up to 598 $\mu$atm) were predominately associated with the $pH_3$ ($pH_{k0–NN}$) input, while the lowest values were associated with the $pH_2$ ($pH_{k0–LOC}$) combination.

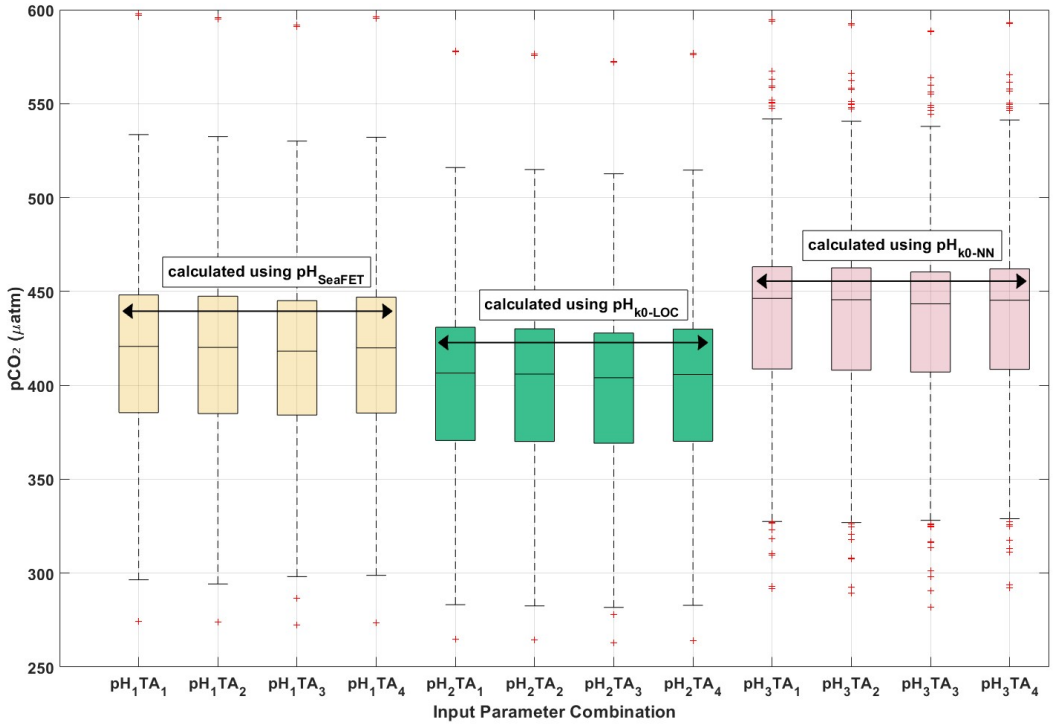


FIGURE 3.6: Comparison of calculated seawater partial pressure of $CO_2$ in $\mu$atm ($pCO_2$, y-axis) using different input pH and total alkalinity (TA) combinations (See Table 3.2). Box plots show $pCO_2$ distributions grouped by pH input (1) uncorrected SeaFET sensor pH measurements (yellow), (2) k0-adjusted pH using $pH_{LOC}$ ($pH_{k0–LOC}$, emboldened green), and (3) k0-adjusted pH using neural network-derived estimations ($pH_{k0–NN}$, red). For each method, four TA values ($TA_1$–$TA_4$) were paired with corresponding pH inputs to assess sensitivity. The central line in each box indicates the median value of each $pCO_2$ distribution, the box bounds correspond to interquartile ranges, whiskers extend to data within 1.5 times the interquartile range, and red crosses indicate outliers.

The $pCO_2$ results can be grouped according to the input $pH_T$ used in the carbonate calculation. When calculated using $pH_{SeaFET}$ ($pH_1$), the average $pCO_2$ seen is 413 $\pm$ 39 $\mu$atm (1$\sigma$, n = 196736) across the deployment. In comparison, $pCO_2$ calculated using $pH_{k0–LOC}$ ($pH_2$) yielded a lower mean value of 399 $\pm$ 39 $\mu$atm, while calculations

using $pH_{k0–NN}$ ($pH_3$) produced a higher average of 438 $\pm$ 38 $\mu$atm and showed a greater number of outlying values (Figure 3.6). When plotted against time (Figure 3.7), the $pCO_2$ values from each group track broadly similar temporal patterns, responding coherently to environmental changes and vehicle depth during the deployment. However, consistent offsets persist between the different pH input types. The black trace, representing ALR depth, revelas that the largest $pCO_2$ values and sensor divergences often coincide with periods of vertical profiling or rapid depth change, a potential indication into when sensor calibrations or correction becomes most impactful. Notably, $pH_{k0–NN}$-based $pCO_2$ values remain persistently higher throughout the mission, amplified during deeper dives, while $pH_{k0–LOC}$-based values are tend to be lower (Figure 3.7). These offsets, while systematic, also appear to diverge slightly at certain timescales, suggesting both sensor-specific differences and variable sensitivity to environmental conditions.

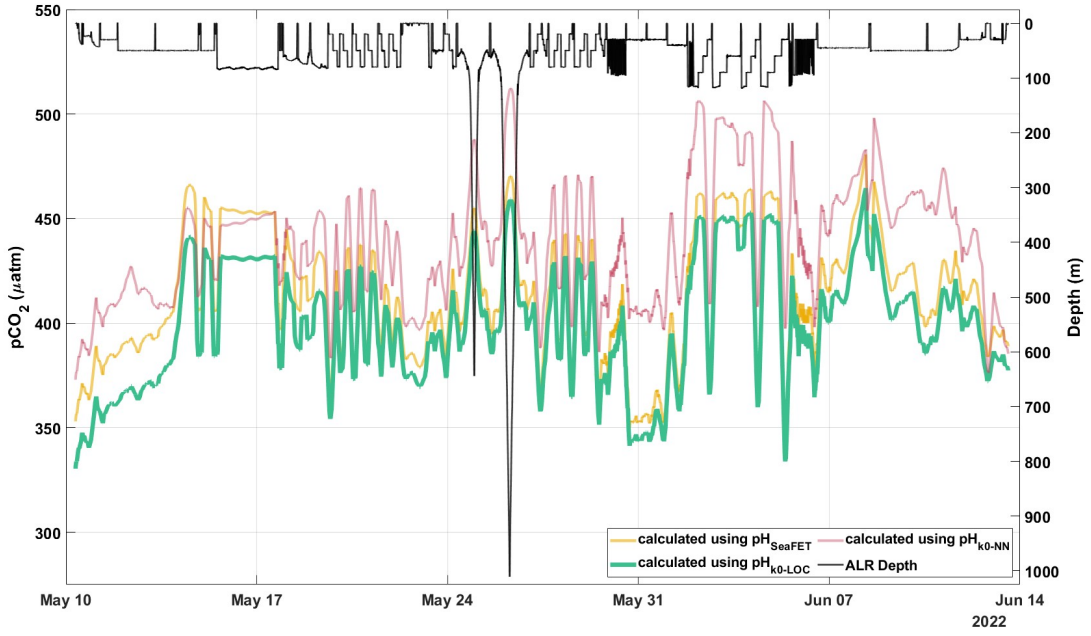


FIGURE 3.7: Time series of partial pressure of $CO_2$ in $\mu$atm ($pCO_2$, left y-axis) grouped by pH input used in carbonate calculations: $pH_{SeaFET}$ (yellow), LOC k0-corrected ($pH_{k0–LOC}$, emboldened green), and neural network k0 corrected pH ($pH_{k0–NN}$, red). All $pCO_2$ shown here were calculated using $TA_1$ as the other carbonate input parameter. The ALR transect depth (black, right y-axis) is overlaid.

A matrix analysis that compared the mean $pCO_2$ differences across various input combinations revealed that TA input choice has marginal contribution to derived $pCO_2$, while pH input choice has a larger impact on final derived $pCO_2$ values. When the $pH_T$ is held constant for calculating $pCO_2$, results vary by a maximum of 3 $\mu$atm. In contrast, holding TA constant while varying $pH_T$ leads to $pCO_2$ differences up to 42 $\mu$atm (Figure B.5).

Figure 3.8 shows the temporal and spatial trends of $pH_{k0–LOC}$ and $pCO_2$ calculated using $pH_{k0–LOC}$ and $TA_1$ (Lee et al., 2006). The full range of $pH_{k0–LOC}$ (7.911–8.200) and $pCO_2$ (265–578 $\mu$atm)is seen in Figure 3.8A,D, and a magnified (top 100 m) view of $pH_{k0–LOC}$ and $pCO_2$ is seen in 3.8B,E. Throughout the water column, as depth increases $pH_T$ decreases and $pCO_2$ increases. Surface values (top 20 m), shown in Figure 3.8C,F for both parameters are variable but indicate a slight decrease in $pH_T$ and increase $pCO_2$ over time. Notably, there is a drop in surface $pH_T$ and peak in surface $pCO_2$ around May 24, 2022, which coincides with the deepest MLD, when the ALR is furthest from shore and crossing continental shelf break (Figures 3.8 and 3.1).

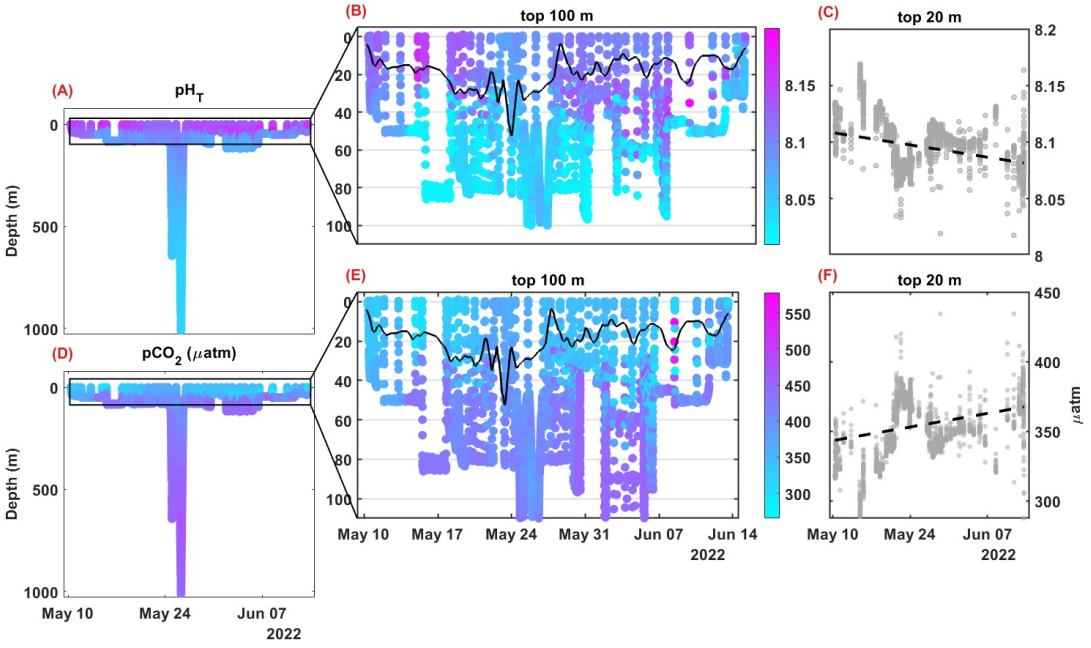


FIGURE 3.8: Autonomous high-resolution observations of $pH_T$ and $pCO_2$ ($\mu$atm) during the five-week LDPT deployment (May–June 2022). Plotted $pH_T$ measurements (panels A–C) are from the SeaFET pH sensor k0-corrected to the LOC pH sensor ($pH_{k0–LOC}$). Plotted $pCO_2$ values (panels D–E) are calculated using $pH_{k0–LOC}$ and $TA_1$ as input parameters. Panels (A) and (D) show full-depth profiles (to $\sim$ 1000 m) of $pH_T$ and $pCO_2$ respectively (represented by colour), throughout the deployment. Panels (B) and (E) present magnified views of the top 100 m. The black line in panels (B) and (E) indicates the estimated mixed layer depth over time. Panels (C) and (F) display parameter values in the upper 20 m of the water column over time.

### 3.3.3 $CO_2$ Flux

Building on the $pCO_2$ estimates, $CO_2$ fluxes were calculated to evaluate air–sea dynamics during the LDPT. Given these flux calculations are derived directly from surface $pCO_2$ values, they exhibit similar dependencies on input parameter

combinations. During the LDPT, $CO_2$ fluxes ranged from -17.0 to 7.1 mmol $m^{-2}$ $d^{-1}$ (n = 43152, all combinations), depending on $pH_T$ and TA datasets used. By convention, negative fluxes indicate uptake of $CO_2$ by the ocean (i.e., the ocean is a carbon sink), while positive fluxes indicate $CO_2$ outgassing from the ocean to the atmosphere. Figure 3.9 shows the distribution of air-sea $CO_2$ fluxes determined using various $pCO_2$-derived input combinations. Consistent with the $pCO_2$ results, flux estimates cluster primarily according to the $pH_T$ dataset used. When using $pH_1$ (SeaFET), the mean flux was -3.5 mmol $m^{-2}$ $d^{-1}$ ($1\sigma$ = 3.6 , n = 3596). Using $pH_2$ (k0-LOC), resulted in a more negative mean flux of -4.3 mmol $m^{-2}$ $d^{-1}$ ($1\sigma$ = 4.3), while $pH_3$ (k0-NN), produced a less negative mean of -2.4 mmol $m^{-2}$ $d^{-1}$ ($1\sigma$ = 2.9). Across all methods, the mean air-sea $CO_2$ fluxes were negative, indicating that the region acted as a net $CO_2$ sink during the deployment period. While we present method-specific ranges, we do not propagate uncertainty from the input variables (pH, TA, wind speed, atmospheric $CO_2$ into the final flux estimates. As such, the variability across methods should be considered a minimum bound of potential uncertainty in calculated air-sea $CO_2$ flux.

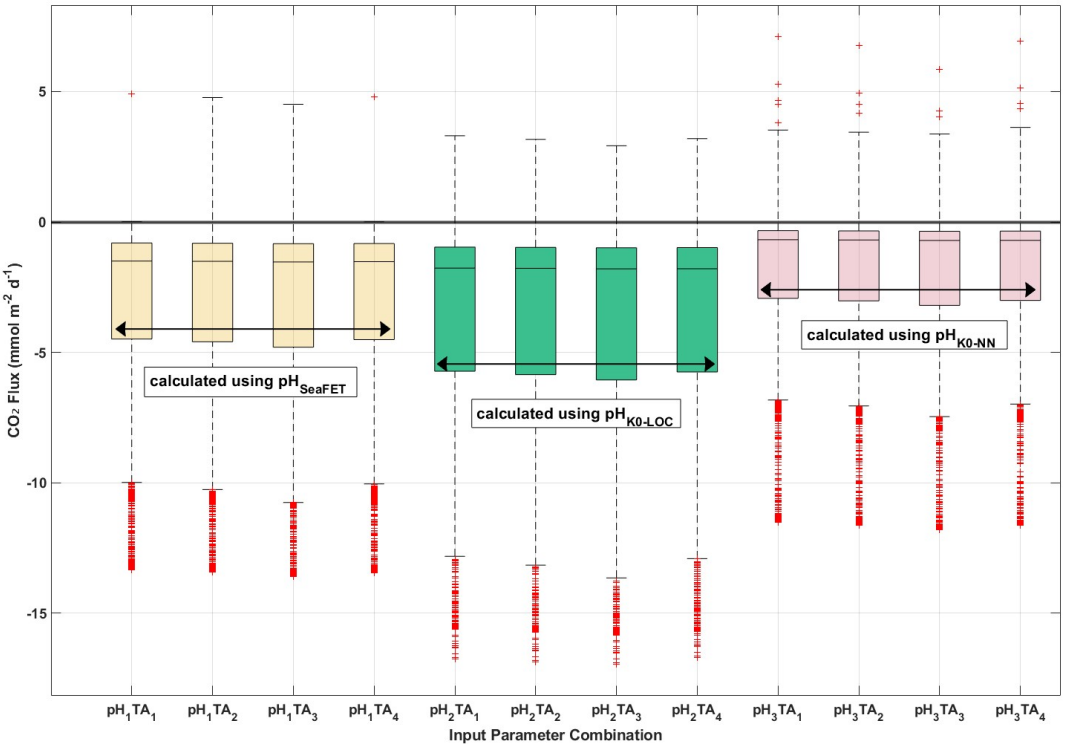


FIGURE 3.9: Comparison of calculated air-sea $CO_2$ flux (mmol $m^{-2}$ $d^{-1}$, y-axis) using different input pH and total alkalinity (TA) combinations. Box plots show $CO_2$ flux distributions grouped by pH input (1) uncorrected SeaFET sensor pH measurements (yellow), (2) k0-adjusted pH using $pH_{LOC}$ ($pH_{k0–LOC}$, emboldened green), and (3) k0-adjusted pH using neural network-derived estimations ($pH_{k0–NN}$, red). For each method, four TA values ($TA_1$–$TA_4$; defined in Table 3.2) inputs were paired with corresponding pH inputs to assess sensitivity. The central line in each box indicates the median value of the distribution, boxes represent interquartile ranges, whiskers extend to data within 1.5 times the interquartile range, and red crosses indicate outliers. All flux calculations were done using only measurements from when the ALR was at the surface (water intake 0.4 m below the waterline).

When the different flux estimates—grouped by pH input as defined in Figure 3.9 above—are plotted over time alongside wind speed, variability stemming from differences in input parameters and environmental factors such as wind can be observed. While wind does not directly cause divergence between methods, it modulates the magnitude of the flux response and can highlight where methodological differences become most impactful. Figure 3.10 illustrates the noticeable impact of high wind speed period on air-sea $CO_2$ fluxes variability, with periods of elevated wind speed often coinciding with amplified discrepancies between flux estimates (Figure 3.10). In some cases, flux calculated using $pH_{SeaFET}$ and $pH_{k0–LOC}$ show different responses to increased wind than flux calculated using $pH_{k0–NN}$. Notably, during the week of June 07– June 14, fluxes derived from $pH_{SeaFET}$ and $pH_{k0–LOC}$ exhibit different responses to wind variability compared to those based on $pH_{k0–NN}$, including a marked divergence in flux direction, underscoring the sensitivity of flux calculations to both sensor corrections and external forcing.

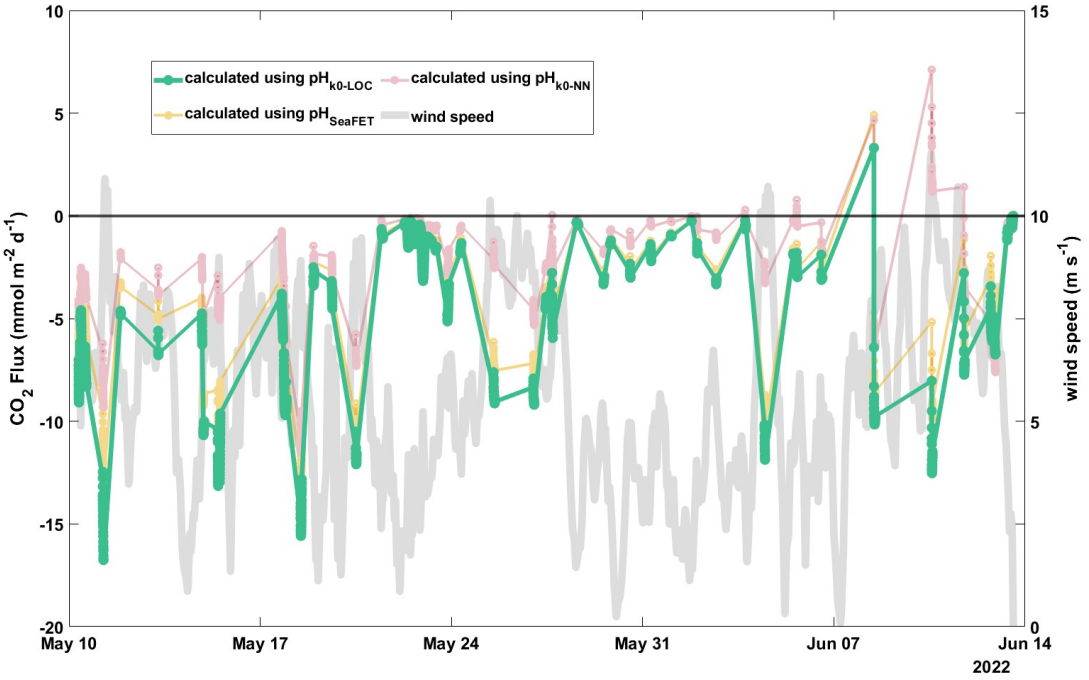


FIGURE 3.10: Time series of air–sea $CO_2$ fluxes (mmol $m^{-2}$ $d^{-1}$, left y-axis) grouped by pH input to calculations: $pH_{SeaFET}$ (yellow), LOC k0-corrected ($pH_{k0–LOC}$, emboldened green), and neural network k0 corrected pH ($pH_{k0–NN}$, red). All $CO_2$ fluxes shown here used $TA_1$ as the other carbonate input parameter when calculated. All flux calculations were done using only measurements from when the ALR was at the surface (water intake 0.4 m below the waterline). Wind speed in $ms^{-1}$ (gray line, right y-axis) is overlaid.

Given the high variability and wide range of values in the flux data, the performed matrix analysis compared the median fluxes (instead of mean) from each input combination in order to mitigate the influence of extreme values on the overall interpretation (Figures 3.10 and B.6). When pH is held constant across different TA inputs, median flux differences within $\sim$ 0.04 mmol $m^{-2}$ $d^{-1}$ are observed. Conversely, keeping TA constant, while varying pH input induces differences that can exceed 1.11 mmol $m^{-2}$ $d^{-1}$ (Figure B.6). This difference represents $\sim$ 25% of the average flux magnitude. While this difference may appear modest in absolute terms, it could meaningfully alter seasonal or annual budget estimates when extrapolated over time and space. These results, consistent with the $pCO_2$ analysis, underscore the implications of selecting and validating input sources in carbonate chemistry, but particularly with pH in $CO_2$ flux calculations.

## 3.4 Discussion

### 3.4.1 Autonomous Coastal Observations

The LDPT deployment demonstrates not only the robust endurance of the ALR and onboard sensors to sample seawater properties across coastal and open ocean waters, but more critically, its ability to autonomously monitor the marine carbonate system with built-in quality control. This represents a key step toward increasing availability of comprehensive carbonate measurements of coastal regions, building on and complementing ongoing monitoring efforts. While remote human oversight is still needed for mission programming and ALR position monitoring, this approach also substantially reduces the carbon footprint and operational costs compared to traditional ship-based surveys (Phillips et al., 2023).

Over the five-week deployment, continuous high-resolution profiles and transects of temperature, salinity, dissolved oxygen, and pH throughout the water column were successfully recorded. These measurements revealed distinct seasonal and spatial patterns across the Celtic continental margin as this deployment occurred during a season of heightened coastal productivity, when biogeochemical conditions shift rapidly over short timescales and small spatial scales. For instance, surface-layer DO declined steadily as temperature increased, suggesting biological consumption likely linked to the waning spring bloom (Figure 3.3I). Spatial salinity trends highlighted the transition between coastal and offshore domains, with a shift from the fresher coastal waters to saltier offshore conditions, though no evident temporal salinity trends were detected (Figure 3.3D,E,F). Added temporal resolution is especially important when placed in the context of traditional ship-based surveys. Between March 19 and 30, 2022 (two months prior to the LDPT deployment), the ALR6000 and CTD sampling surveyed the same transect (Figure 3.1) on the Celtic shelf margin supported by the Royal Research Ship, *RRS Discovery*, during expedition DY149.

Within the upper 40 meters of the water column, total alkalinity (TA) values from the LDPT closely align with those from the DY149, with all TA estimates falling with the DY149 range of 2325–2345 $\mu$mol kg$^{-1}$ (Hammermeister et al., 2025). This agreement reinforces the conservative behaviour of TA in this region (Hartman et al., 2014). In contrast, the $pH_T$ and $pCO_2$ values observed during LDPT, although calculated using various methodologies, span broader distributions that extend beyond the DY149 ranges (8.03–8.08 for $pH_T$ and 375–415 $\mu$atm for $pCO_2$). Such divergence is expected, given the high temporal variability of these non-conservative parameters, which are subject to pronounced seasonal variability. The LDPT deployment took place during late May—a period typically characterised by increasing primary production, stratification, and warming—factors that contribute to elevated pH and decreased $pCO_2$ that we see in Figure 3.8. The LDPT pH and $pCO_2$ observations are consistent

with prior studies from the Celtic margin (Kitidis et al., 2012; Hartman et al., 2014; Joint et al., 2001; Seguro et al., 2019), indicating that the LDPT values reflect expected natural seasonal shifts rather than sensor bias or error when compared to the DY149 values.

Beyond seasonal trajectories, diel signals could also be resolved from our dataset. Figure 3.11 shows mean DO, $pH_T$ ($pH_{k0–LOC}$), and $pCO_2$ (from $pH_{k0–LOC}$ and $TA_1$; Lee et al. 2006) in the upper 100 m of the water column binned by hour of the day, for the entire LDPT deployment. During the day, DO and $pH_T$ peak, while $pCO_2$ drops, indicating biological control though photosynthesis and respiration, supported by previous reports during the Celtic Sea spring bloom (Seguro et al., 2019). The error bars in Figure 3.11 represent one standard deviation of each mean, revealing the wide variability amongst all three parameters. This is an unsurprising reflection of the variation seen from aggregated data across the entire deployment's spatial domain (2,000 km), where we see other seasonal and spatial trends take place over the 35 days of observation. Impressively, a diel signal still emerges through that variability, reinforcing the presence of biological and/or physical forcing in the top 100 m of the Celtic Margin. In other words, this underscores how daily cycles can still drive short-term carbonate dynamics, even when spatial and temporal-scale variability is high. This is a signal uniquely captured by this type of autonomous, high-frequency deployment, as ship-based surveys and models would have likely not resolved it at this scale.

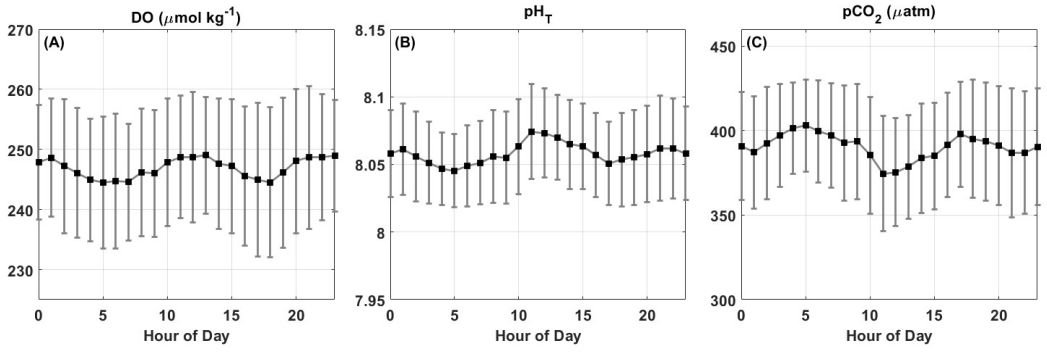


FIGURE 3.11: Diel cycling of (A) DO ($\mu$mol $kg^{-1}$), (B) $pH_T$, and (C) $pCO_2$ ($\mu$atm) in the upper 100 m of the water column across the five-week LDPT deployment. Each panel shows mean values binned by hour of the day, with the error bars representing one standard deviation. $pH_T$ is $pH_{k0–LOC}$, and $pCO_2$ is calculated from $pH_{k0–LOC}$ and $TA_1$

.

These results provide rare, high-resolution evidence of how seasonal and short-term productivity transitions modulate carbonate chemistry in shelf seas, resolving processes at timescales inaccessible to ships. By extending beyond the static ship-based snapshot of March, the ALR revealed the onset of late-spring carbonate changes, underscoring the importance of autonomous observations to close seasonal

gaps in carbon cycle assessments. Short-term AUV observations capture the natural seasonal trajectory beyond ship-based "snapshots," which often miss the dynamics between expeditions. This speaks directly to the importance of autonomous deployments to constrain seasonal carbon budgets in continental margins for better understanding of the tightly coupled biological and physical processes that drive coastal carbonate variability.

### 3.4.2 Dual pH Sensors for Coastal Monitoring

The presence of two distinct pH sensors (LOC and SeaFET) onboard the ALR proved highly valuable, not only by providing data redundancy, but also by enabling mutual validation in the absence of traditional discrete water samples. This deployment offered a rare opportunity to cross-validate sensor performance during long-haul seagoing conditions, something particularly important for autonomous platforms where ship-based validation is not possible, or where global models may underperform. Despite operating on fundamentally different measurement principles, the two pH sensors showed stronger agreement with each other than with model-based pH estimates. Such pre-correction consistency across sensor types is particularly noteworthy given the highly variable conditions of shallow shelf areas, and highlights both the growing advancement of autonomous pH sensing technologies and the crucial need of redundancy when feasible.

Model-derived pH outputs ($pH_{LIR}$, $pH_{NN}$) were also assessed as alternatives to co-sensor calibration, particularly in scenarios where only a single sensor is available. However, while these models can effectively mitigate sensor drift, they remain constrained by their underlying assumptions and training data. Moreover, their performances tend to be better under the stable conditions typically found in the deep ocean, where platforms like the BGC-Argo array regularly recalibrate against "known" deep water chemistry. In contrast, the heterogeneous and rapidly changing biogeochemical gradients of shallow shelf seas, which were mostly sampled during this mission, pose significant challenges to these models, often limiting their predictive skill and transferability. Coastal waters lack the quasi-conservative behaviour seen in deep open ocean waters, and the input-output relationships captured by neural networks and linear regressions trained on deep datasets may not hold in these regimes. That two (fundamentally) different pH sensors converged more closely with each other than with model estimates is not only a case for redundancy, but also gives clear evidence that carbonate variability in shelf seas exceeds the resolving capacity of current models. This highlights the central role of in situ sensing in capturing carbonate dynamics in margin areas. Additionally, the pH estimate routines used in this work relied heavily on dissolved oxygen as a key input parameter, making their output inherently sensitive to the accuracy and calibration of the oxygen optode itself.

**pH Comparisons**

To quantify and asses the impact of the k0 adjustment procedure, comparisons were made between sensor-measured $pH_T$, corrected $pH_T$, and model-estimated $pH_T$. Figure 3.12 represents the distribution of average $\Delta pH_T \pm$ first standard deviation ($1\sigma$) for each comparison. Both before and after correction, the two onboard pH sensors showed the best agreement and lowest variability relative to ESPER estimates (LIR and NN). Interestingly, the uncorrected $pH_{SeaFET}$ aligned more closely with both $pH_{LIR}$ and $pH_{NN}$ (both $\mu$ = -0.023) than $pH_{LOC}$ did (both $\mu$ = 0.035), but this came with the highest variation of all comparisons ($1\sigma$ = 0.020/0.018 versus $1\sigma$ = 0.018/0.017 for $pH_{LIR}$ and $pH_{NN}$ respectively) (Figure 3.12). The two ESPER-derived $pH_T$ estimate datasets were nearly identical to each other, yielding indistinguishable mean results when compared to the same pH sensor measurement, although $pH_{LIR}$ comparisons consistently showed a slightly greater variability of 0.002 higher standard deviation compared to $pH_N$N. Correction routines applied using both $pH_{LOC}$ and $pH_{NN}$ successfully adjusted the $pH_{SeaFET}$ resulting in corrected values ($pH_{LOC}$ and $pH_{NN}$) with rounded mean $\Delta pH_T$ values of 0. Notably, the distribution of the $pH_{k0–NN}$ comparison has more variability ($1\sigma$ = 0.011 ) than the $pH_{k0–LOC}$ comparison ($1\sigma$ = 0.007). The closer agreement between $pH_{LOC}$ and $pH_{SeaFET}$ compared to either versus the model-derived values reinforces that unresolved short-term and fine-scale processes dominate carbonate dynamics in coastal waters. These dynamics are poorly represented in models, which helps explain why shelf carbonate systems remain one of the least constrained components of the global carbon budget.

Across all comparisons, $\Delta pH_T$ indicated that the LOC sensor consistently measured a higher $pH_T$ than the SeaFET and the ESPER estimates, and the SeaFET sensor, in turn, reported higher $pH_T$ values than the ESPER models (Figure 3.12). These observations reinforce the value of in situ sensors, which captured fine-scale spatiotemporal pH variations more accurately than model-based estimates. Micro-scale pH patterns were detected by the onboard sensors but less reflected by model estimates, evident by the much better agreement between the two sensors than either sensor with the models. This divergence highlights a key limitation of data-driven models in dynamic environments and speaks to the importance of direct, high-frequency measurements, especially in coastal monitoring or, when interpreting related parameters such as $pCO_2$ and $CO_2$ flux. Together, these comparisons demonstrate that autonomous dual-sensor observations do more than provide redundancy: they reveal heterogeneous and dynamic shelf carbonate systems, and demonstrate why models alone cannot yet deliver reliable constraints on coastal carbon fluxes.

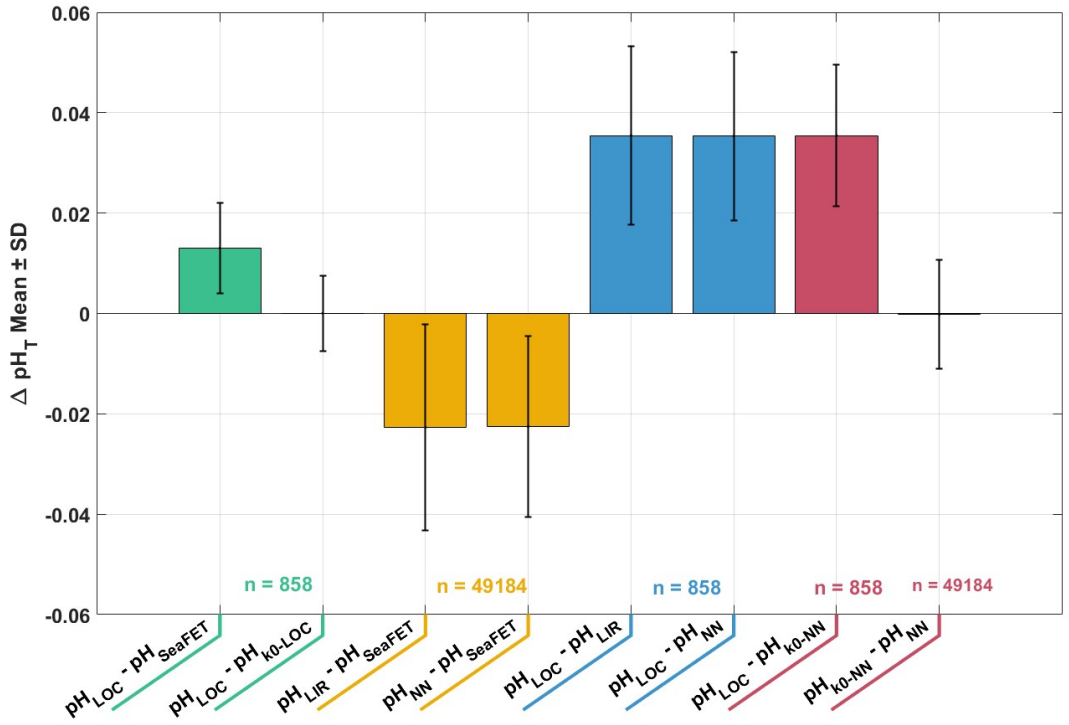


FIGURE 3.12: Bar chart with error bars of mean difference (± standard deviation) of $pH_T$ ($\Delta pH_T$) between different measurement methods and/or model estimations. Grouped by colours based on comparison parameters: between the two onboard sensors before and after k0 correction based on LOC as $pH_{ref}$ (green), original $pH_{SeaFET}$ values compared to both output model estimates (yellow), $pH_{LOC}$ values compared to both output model estimates (blue) and comparison of $pH_{k0–NN}$ to $pH_{LOC}$ and to $pH_{NN}$ which was used as $pH_{ref}$ to get $pH_{k0–NN}$ (red). Sample size (n) for each comparison is shown. Error bars represent 1 standard deviation.

### Efficacy of the k0 Correction Approach

A central aspect of this study was the adaptation and implementation of the k0 correction to adjust the SeaFET pH sensor measurements using either a co-sensor (LOC pH sensor) or neural network-derived estimates (ESPER-NN). The correction method effectively addressed both the initial electrode conditioning period typically experienced by the SeaFET sensors, and brought its measurements into near-perfect alignment with each respective $pH_{ref}$. However, comparisons also revealed that k0-corrected SeaFET data based on $pH_{NN}$ exhibited greater variability ($1\sigma$ = 0.011) than corrections based on $pH_{LOC}$ ($1\sigma$ = 0.007). This difference stems from the noise and uncertainty associated with model-generated pH estimates, particularly in a shallow coastal setting. The k0 correction was originally designed for deep-ocean profiling floats equipped with ISFET pH sensors, and using model estimates for $pH_{ref}$, thus benefiting from stable environmental conditions and better model performances at depth. Our work, however, shows this correction approach can be successfully

applied to monitoring marine carbon in the coastal ocean when adapted to a co-sensor who's performance is more reliable than model output in such a setting.

Although $pH_{LOC}$ had far fewer data points than $pH_{SeaFET}$, this did not inhibit the correction's performance. The k0 approach leveraged the complementary strengths of both onboard sensors by using the more power-intensive, high-precision measurements from the LOC sensor intermittently as "stabilizers" to the more frequent, lower-power measurements from the SeaFET. Beyond improving individual measurements, the k0 correction enabled nearly 50000 reliable pH observations throughout the full deployment, providing one of the most detailed continuous coastal carbonate records collected to date in this region. The resulting dataset captures fine-scale spatiotemporal variability in pH, offering unprecedented opportunities to resolve the processes driving carbonate dynamics on short timescales but also potentially on biologically mediated processes, given the direct links between pH, marine carbon chemistry, and ecosystem function. This reinforces the advantage of co-deploying sensors for deriving corrections, while also demonstrating that neural network estimates can substitute for a second sensor when needed, albeit with slightly reduced precision. Taken together, this combination of dual sensors and k0 adjustment of one sensor to the companion sensor output represents a step-change in observational capacity for coastal carbonate system research, particularly in dynamic shelf-sea environments where traditional ship-based monitoring cannot resolve rapid biogeochemical changes.

### 3.4.3 Air-Sea $CO_2$ Fluxes

Air-sea $CO_2$ flux estimates from the LDPT autonomous deployment indicate that during late spring the Celtic Sea acted predominately as a net sink of atmospheric $CO_2$ into the ocean (Figure 3.10). These findings are consistent with previous studies also reporting the Celtic Sea as a net sink for atmospheric $CO_2$ (Marrec et al., 2015), which is common for this type of marginal sea (Laruelle et al., 2014; Mathis et al., 2024). Notably, the spike in $pCO_2$ just before May 24 in Figure 3.8D–F, coincident with the ALR's transition off the continental shelf (Figure 3.1), corresponds to a period of near air-sea equilibrium ($CO_2$ flux approaching zero) shown in Figure 3.10. This strongly corroborates the findings of Humphreys et al. (2019) who found the Celtic Margin to exhibit greater net air-sea $CO_2$ flux than the open ocean, aligning with the increasing strength of biogeochemical stratification that we also clearly observe in Figures 3.3 and 3.8 as our observations move away from the open ocean. Direct observational data of the carbonate system in the Celtic Sea remains scarce, with most prior flux estimates derived from models or algorithms (Hammermeister et al., 2025; Humphreys et al., 2019; Marrec et al., 2015; Wakelin et al., 2012). High-resolution datasets like the one

presented here help fill this capability gap and anchor modelled flux magnitudes to direct *in situ* evidence, which is shown to be crucial for coastal carbon budget models.

Air-sea flux calculations are inherently sensitive to the accuracy of input carbonate chemistry parameters, particularly surface $pCO_2$, which depends strongly on the quality of pH data used to derive it when not measured directly. Despite robust correction strategies and convergence of pH datasets, calculated $CO_2$ fluxes still showed variability. Importantly, this variability sometimes even resulted in fundamental disagreements in flux direction, altering interpretation of the ocean as a $CO_2$ source or sink. As shown in Figure 3.9, flux values segregate more by pH dataset than by TA, underscoring the critical role of pH observations for flux interpretation. Further complicating matters is the influence of wind speed in modulating air–sea exchange. A critical aspect of this sensitivity lies in the non-linear nature of carbonate system thermodynamics. $CO_2$ flux is computed from the gradient between surface water $pCO_2$ and atmospheric $pCO_2$, scaled by wind speed–dependent transfer velocity. Because this transfer velocity is multiplicative, even modest differences in calculated $pCO_2$ ($\pm$ 0.01–0.02 pH units) can result in disproportionately large changes in calculated flux, especially under high wind conditions. Shown in Figure 3.10, the clearest example of the amplifying role of the wind occurs between June 7–14, when wind speeds reach up to $\sim$ 12 m $s^{-1}$. During this period, the flux estimates diverge substantially: fluxes based on $pH_{k0–LOC}$ suggest the ocean remains a sink, absorbing nearly 15 mmol $m^{-2}$ $d^{-1}$ whereas those based on $pH_{k0–NN}$ suggest the ocean a source of nearly 8 mmol $m^{-2}$ $d^{-1}$. Such a reversal in flux direction has major implications, such as altering the interpretation of ocean–atmosphere carbon exchange during this period, when the ocean switches from a net sink to a net source under high wind conditions. This finding is fundamentally important for interpreting both regional and global flux estimates, as it suggests that some existing flux products may systematically misclassify the carbon budget, particularly in coastal and shelf environments.

An additional factor influencing $CO_2$ flux determination is the actual depth at which ”surface” carbonate parameters are measured. While this deployment sampled at just 0.4 m below the surface, many instrumented platforms contributing to SOCAT, such as SOOP, measure $pCO_2$ from depths of $\sim$ 4–5 m. However, near-surface vertical gradients in $pCO_2$ and $pH_T$ can develop rapidly due to stratification, diurnal heating, and biological activity, particularly in coastal or shallow systems such as the site in this study. As highlighted by Morgan et al. (2025) and Ho and Schanze (2020), significant differences in $pCO_2$ have been observed between the surface and 5 m below the surface. These depth-dependent discrepancies can introduce systematic offsets in calculated air–sea $CO_2$ fluxes, with downstream implications for global flux products and model estimates. The near-surface sampling (0.4 m) in this study therefore may help explain some of the variability when comparing to model-derived

estimates while highlighting the importance of vertical gradients in pH and $pCO_2$. Even a few meters difference in sampling depth can substantially alter flux estimates, challenging assumptions used in current global climatologies.

Therefore, in autonomous deployments, where real-time corrections and discrete validation samples may be absent, the selection and validation of pH input becomes paramount. Conservative interpretation of flux results, particularly during high wind intervals, should account for these interactions. As Figure 3.10 shows, agreement among methods is best preserved during lower wind periods, suggesting that high-frequency wind monitoring is an essential co-variable in assessing confidence levels of derived flux products. As highlighted by Gandoin and Garza (2024) and Nickford et al. (2024), discrepancies between in situ wind observations and reanalysis products like ERA5 (used in this work) can introduce substantial uncertainty in air-sea $CO_2$ flux estimates, particularly in coastal and upwelling regions. Their study found that ERA5 tends to underestimate the highest wind speed events ($> 10$ m $s^{-1}$), leading to systematic underestimations of $CO_2$ flux magnitude. These biases likely contribute to the amplified flux differences observed in our data under high-wind conditions. If ERA5 is already underestimating high wind, the true extent of these discrepancies in flux calculations could be even more pronounced and thus warrant thoughtful consideration, leading to mischaracterisations of air-sea carbon exchange dynamics.

The broader implication is that pH uncertainty cannot be considered in isolation when interpreting $CO_2$ flux. Instead it acts as a non-linear driver whose influence is modulated and amplified by environmental factors such as wind speed or fine-scale surface gradients which can transform small sensor or model disagreements into large differences in flux magnitude, and even direction. This dynamic interplay complicates efforts to identify sink/source transitions and may lead to contradictory assessments of the ocean's role in short-term carbon exchange, particularly in regions with variable weather and shallow bathymetry where mixed-layer dynamics respond quickly to physical forcing. Taken together, these findings underscore why high-resolution autonomous carbonate observations are essential for robust quantification of air–sea $CO_2$ fluxes and downstream products like $pCO_2$, especially in dynamic coastal seas that remain a major source of uncertainty in the global carbon cycle. By capturing fine-scale temporal and vertical variability, autonomous platforms provide critical insight into processes that ship-based surveys and coarse models cannot resolve.

## 3.5 Conclusion

This mission is a first of its kind deployment. The LDPT is the first fully autonomous deployment of the ALR equipped with scientific biogeochemical sensors— including dual pH instrumentation— to perform continuous, long-duration, and long-distance

carbonate system monitoring. The deployment achieved the longest autonomous pH acquisition to date by the ALR and generated nearly 50000 reliable pH observations, providing one of the most detailed coastal carbonate datasets collected in this region. Crucially, the deployment demonstrated the success of dual sensor operation, which not only improved data quality but enabled high-frequency capture of fine-scale spatiotemporal variability. These data reveal how tightly coupled biological and physical processes drive carbonate chemistry in shelf seas, capturing seasonal transitions and vertical gradients that are typically missed by ship-based surveys. Small differences in pH were shown to significantly affect calculated $CO_2$ fluxes, including reversals in flux direction under high wind conditions, emphasizing that coarse models may misclassify source or sink status in dynamic coastal systems.

All together, this confirms the value of our approach as a powerful tool for determining air-sea gas fluxes, with clear potential applications beyond $CO_2$. Overall, this mission highlights the central role of autonomous, high-resolution observations in constraining short-term carbon dynamics, air–sea gas fluxes, and broader coastal carbon cycle processes. This study paves the way for future high-resolution biogeochemical monitoring as well as for long-endurance deployments to fill critical observational gaps, improving our understanding of ocean acidification, carbon cycling, and air-sea exchange, and providing essential data to support climate modelling that contribute to scientific policy making and mitigation efforts.

## Acknowledgments

The authors would like to thank the Marine Autonomous Robotic Systems (MARS) team and others that made the Long Distance Proving Trial (LDPT) possible with their tireless commitment to a successful shore vehicle launch and recovery, mission piloting, and any and all engineering, mechanical, or software needs.The development and LDPT of the ALR1500 was supported by the Industrial Strategy Challenge Fund / Natural Environment Research Council's (ISCF/NERC's) Oceanids Programme and NERC National Underpinning Autonomy Capability funding and through the INSPIRE DTP. We would also like to thank Dr. Mingxi Yang and the Penlee Point Atmospheric Observatory at Plymouth Marine Laboratory for providing atmospheric $CO_2$ data which were supported by the NERC ACSIS (grant no. NE/N018044/1) and MOYA (grant no. NE/N015932/1) projects. Finally, as always, the authors thank Swift (D.F.A), Director B. Leyert, Donna, Tim, Ruthie B, and Wika.

## Open Research Section

All sensor data are available from The University of Southampton Data Repository via [DOI TBD].

# Chapter 4

# Metabolic Dynamics of an Offshore Coral Reef in the Red Sea: Observations from Autonomous Sensors

This chapter forms a paper that that is currently undergoing journal submission for publication as an original research article with the following authors:

**Emily M. Hammermeister**, Sarah E. Cryer, Vincent Saderne, Chiara Pisapia, Stathys Papadimitriou, Sara E. Fowell, Jake Ludgate, Allison Schaap Socratis Loucaides and Maggie D. Johnson. Metabolic Dynamics of an Offshore Coral Reef in the Red Sea: Observations from Autonomous Sensors.

*Author Contributions*:
**E. Hammermeister**: Conceptualisation, Methodology, Formal analysis, Investigation, Resources, Data Curation, Writing - Original Draft, Writing - Review and Editing, Visualization
S. E. Cryer: Conceptualisation, Resources, Writing - Original Draft, Writing - Review and Editing
V. Saderne: Methodology, Resources, Writing - Review and Editing
C. Pisapia: Methodology, Formal analysis, Resources, Writing - Review and Editing
S. Papadimitriou: Methodology, Formal analysis, Resources, Writing - Review and Editing, Supervision
S. E. Fowell: Conceptualisation, Writing - Review and Editing, Supervision
J. Ludgate: Methodology, Resources, Writing - Review and Editing
A. Schaap: Methodology, Formal Analysis, Resources, Writing - Review and Editing
S. Loucaides: Conceptualisation, Funding Acquisition, Methodology, Writing - Review and Editing, Supervision
M.D. Johnson: Funding Acquisition, Methodology, Resources, Writing - Review and Editing, Supervision

## Keypoints

- Quantified biogeochemical and carbonate system dynamics using autonomous sensors in an understudied region.
- Autonomous pH-DO observations concluded the reef was net autotrophic, and combined with autonomous TA sensor the reef has net community production of 87%.
- Turf algae likely drove the metabolic signal in the lagoon while hard coral drove the signal in the fore reef.

## Abstract

Coral reefs are under increasing threat from local and global stressors which alters the composition and health of reefs. Traditional methods of monitoring reefs through visual analysis are time-intensive and provide only a snapshot of reef condition. Recent efforts now aim to monitor reefs by measuring and determining their metabolism, or the balance of net community production (NCP) and net community calcification (NCC). While physical benthos is a key (albeit at times misleading) indicator of reef health, reefs are considered "healthy" when they are actively growing and accreting calcium carbonate ($CaCO_3$), a metric requiring comprehensive biogeochemical measurements over time. Using autonomous sensors can transform reef monitoring from occasional snapshots into a high-frequency observing system. While pH and partial pressure of $CO_2$ ($pCO_2$) sensors are widely available for autonomous in situ observation, their strong covariance make them sub-optimal for NCP and NCC calculations. This work reports the first multi-month deployment of a high-resolution, autonomous total alkalinity (TA) sensor on a coral reef, alongside pH, $pCO_2$, and dissolved oxygen (DO) sensors. Simultaneous observations were conducted at lagoon and fore reef sites within Cement Wreck Reef, a central Red Sea offshore reef, and their contrasting benthic compositions were linked to biogeochemical dynamics. Both sites experienced strong diel cycling, with $pH_T$ and DO ranging 7.80–8.30 and 24–432 $\mu$mol kg$^{-1}$ respectively. The lagoon pH–DO relationship closely matched a Redfield-based photosynthesis:respiration model ($R^2 = 0.943$), while the fore-reef relationship was weaker ($R^2 = 0.145$). The inclusion of sub-hourly TA observations in the lagoon allowed over determination of carbonate chemistry, with TA–DIC stoichiometry yielding a slope of 0.26, indicating NCP dominance of 87% over NCC. This study contributes a baseline understanding of Red Sea reef metabolism, a location lacking carbonate observations, and suggest that despite environmental extremes unique to the Red Sea, these reefs metabolically behave in ways consistent with coral reef ecosystems around the world.

## Plain Language Summary

Globally, coral reefs are threatened due to rising temperatures, changes in seawater chemistry, pollution and overfishing. Traditionally the health of a reef was monitored by reef composition through visual analysis. Recent work has shown that reef health can be more accurately monitored by changes in surrounding seawater chemistry. Deploying autonomous sensors allows the collection of high-resolution data on the seawater chemistry, illustrating daily cycles and changes over time. In this study we deploy, for the first time on a reef, a total alkalinity sensor, which alongside commercially available pH and oxygen sensors allows us to determine whether a reef is actively growing (through calcification) and the dominant processes occurring on the reef. Deploying sensors provides far higher resolution dataset than could be collected through discrete water sampling, saving both time and money while providing more data points. This study contributes a baseline understanding of Red Sea reef metabolism, a location lacking in high-resolution observations, and suggest that despite environmental extremes unique to the Red Sea, these reefs metabolically behave in ways consistent with coral reef ecosystems around the world.

## 4.1 Introduction

Coral reef ecosystems are among the most biodiverse and valuable ecosystems in the world, supporting human livelihood through fisheries and tourism, while also providing coastal protection (Moberg and Folke, 1999; Bruckner, 2002). Reefs are biogeochemical hotspots where metabolic processes such as photosynthesis respiration and calcification recycle carbon and nutrients across a range of timescales (Wagner et al., 2020; Reaka-Kudla, 1997). (Smith, 1973; Gattuso et al., 1998; Cyronak et al., 2018). Organic carbon is fixed via photosynthesis by symbiotic algae (zooxanthellae) and other primary producers, while inorganic carbon is precipitated through biogenic calcium carbonate ($CaCO_3$) production (calcification) as aragonite forming the skeletons of corals and as calcite by calcifying algae which together construct and maintain the structural foundation of reefs (Pilcher, 2001; Erez et al., 2011). During the day, coral reefs sequester $CO_2$ and produce oxygen ($O_2$) through photosynthesis, while simultaneously releasing $CO_2$ through calcification and respiration. Calcification rates decrease at night (Moya et al., 2006) making respiration the dominant metabolic process and increasing seawater $CO_2$ at night. The cyclic succession of photosynthesis and respiration drives pronounced diel signals in oxygen and $CO_2$ (and consequently pH) (Suzuki et al., 1995; Cryer et al., 2023), with magnitudes determined by the relative balance of net community production (gross primary production minus respiration; NCP) and net community calcification (gross calcification minus dissolution; NCC). This balance of NCP and NCC is indicative of whether a reef is a net source or sink of $CO_2$ to the atmosphere at any given time and is often considered as a vital signal of reef health (Kayanne, 2025).

Reef health is defined by both benthic characterisation and biogeochemical function. For a coral reef to maintain its structure and support the diverse ecosystem it depends on, calcification rates must exceed those of dissolution, erosion (Andersson and Gledhill, 2013; Erez et al., 2011; Kleypas et al., 1999) and sea level rise (Perry et al., 2018) combined. Reefs with high coverage of hard coral and crustose coralline algae (CCA) are often NCC-driven, while algal-dominated reefs are NCP-driven (Smith et al., 2016). Additionally, reduced NCC often reflects a stressed or degraded reef that may be undergoing a phase shift to macroalgal dominance (Hughes et al., 2007). Still, a healthy reef is not only one with high coral cover at a given point in time, but one with active net reef growth and accretion over time (Andersson and Gledhill, 2013). So while its logical that reefs with a greater abundance of reef-builders (hard corals, CCA) will be healthier, reef condition is best understood as a trajectory.

Reductions in calcification are increasingly linked to anthropogenic-induced environmental stressors including ocean acidification (OA) and rising sea surface temperatures (SST) (Hoegh-Guldberg et al., 2007; Erez et al., 2011). Rising SST often results in coral bleaching, the process in which corals expel their zooxanthellae

symbiomes, which reduces their ability to calcify (Hughes et al., 2017; Heron et al., 2016). As ocean pH decreases, through the continuous absorption of anthropogenic $CO_2$ (Doney et al., 2009), saturation states of calcite and aragonite decline, making calcification energetically expensive for corals and dissolution more likely, especially at night (Eyre et al., 2018; Hoegh-Guldberg et al., 2007; Erez et al., 2011). Additionally, during stress events (e.g., heat waves), corals tend to maximise their chances of survival by temporarily reducing calcification (Schoepf et al., 2015; D'Olivo and McCulloch, 2017), showing that even without a net loss of benthic calcifiers, these events impact metabolic processes. Globally, coral reef ecosystems are now exhibiting declining NCC and increasing NCP (Davis et al., 2021). Specifically, net contribution of hermatypic coral to the $CaCO_3$ budget of the Red Sea has declined by ∼100% between 1998 and 2015, and calcification rates in the Red Sea altogether have declined by 26% (Steiner et al., 2018).

In a reef system, metabolic processes drive changes in the seawater's carbonate chemistry. NCP mainly effects dissolved inorganic carbon (DIC) concentration through photosynthesis and respiration while NCC changes both DIC and total alkalinity (TA) in a 2:1 ratio (Gattuso et al., 1998; Cyronak et al., 2018). Constraining the seawater's carbonate system within a coral reef environment at a high temporal resolution can therefore shed light into the dominant metabolic processes and their rates. Characterizing the seawater carbonate system requires knowledge of two of the four measurable carbonate system variables (DIC, TA, pH, and the partial pressure of carbon dioxide ($pCO_2$)) along with temperature, salinity, and pressure (Park, 1969; Millero, 1995, 2007). Currently, only pH and $pCO_2$ sensors are widely available for autonomous *in situ* observation (Martz et al., 2015), but the environmental covariance of pH and $pCO_2$ makes them the least desirable combination, and propagating large uncertainties in derived TA and DIC are sub-optimal for NCP and NCC calculations (Orr et al., 2018; Raimondi et al., 2019; Sutton and Sabine, 2023). In the open ocean, TA can often be estimated from its conservative relationship with salinity (Millero et al., 1998; Lee et al., 2006; Cai et al., 2010; Takahashi et al., 2014), but such approaches are unreliable in coastal reef environments where mixing, riverine input, and strong metabolic activity decouple TA from salinity. Therefore, direct *in situ* observations of TA or DIC alongside pH or $pCO_2$ are essential for characterizing reef metabolism.

The ability to monitor the biogeochemical processes occurring on coral reefs provides crucial insights into ecosystem function by capturing the natural variability, as well as establishing baselines for detecting long-term changes or climactic effects. Visual indicators, such as the reef benthic composition, often show threshold responses to environmental stressors, whereas shifts in seawater biogeochemistry provide a more reliable early detection of reef health (Hughes et al., 2010). This is particularly important because global calcification rates are decreasing at a faster rate than concurrent decline in calcifier cover (Davis et al., 2021). Yet, high-resolution

observations from coral reefs remain scarce. In addition, complex reef geomorphology and shallow bathymetry (Blanchon, 2011) hinder high-resolution data via traditional discrete sampling, but advances in autonomous sensors offer improved capability, including providing sustained, fine-scale measurements (Takeshita et al., 2018; Hammermeister et al., 2025; Yin et al., 2021; Schaap et al., 2025; Cryer et al., 2020). While sensor technologies have continued to come online over the past several years and expanded high-frequency reef pH data (e.g., Cyronak et al. 2020; McMahon et al. 2018; Saderne et al. 2019; Cryer et al. 2023) autonomous carbonate measurements and parameter-relationship records from coral reef observations are still limited, particularly in the Red Sea, whose carbonate system remains understudied.

In this work, we investigate reef metabolism and carbonate dynamics at an offshore Red Sea reef using novel autonomous sensors. By collecting a continuous high-resolution multi-month dateset, we capture seasonal trends, resolve diel variability, and examine biogeochemical relationships between two different sites and their benthic compositions within the reef system. We are able to fully constrain the carbonate system of the reef's lagoon and quantify it's metabolic balance. Here we report the first-ever deployment of an autonomous stand-alone TA sensor on a coral reef, providing a unique benchmark for evaluating reef carbon cycling under extreme thermal and saline conditions, and offering new insights into coral reef responses to ongoing ocean and climate change.

## 4.2 Materials and Methods

### 4.2.1 Study Site

Sensor mooring observations were conducted at Cement Wreck Reef, located approximately 20 km off the coast of Saudi Arabia in the Central Red Sea (Figure 4.1). The Red Sea extends 2270 km from 30°N to 12°N dividing Africa and Asia, and offers a natural test site for reef carbonate cycling under extreme conditions. It is characterised by its high seawater temperature and salinity, and is home to some of the world's most productive, endemic, and diverse coral ecosystems, with reef frameworks spanning its coastline (DiBattista et al., 2016; Fine et al., 2019). In the central Red Sea, year-around temperatures for an offshore reef range from 25–32°C, but can exceed 37°C in certain reef zones such the reef flat or lagoon (Roik et al., 2016; Davis et al., 2011; Rich et al., 2022).

Cement Wreck (22°23′ N, 38°51′ E) is an offshore coral reef that is part of the Shib Nazar reef system, which spans approximately 10 km in the North–South direction (Rich et al., 2022; Roik et al., 2018). Cement Wreck was chosen as the study site for this work because of it's protected, shallow ($\sim$ 1.5 m) lagoon, and its exposure to offshore

seawater exchange. The reef flats, or lagoons, within the Shib Nazar system are dominated by hermatypic (reef-building) *Stylophora pistillata* and are the sole branching coral species in the Cement Wreck lagoon (Rich et al., 2022).

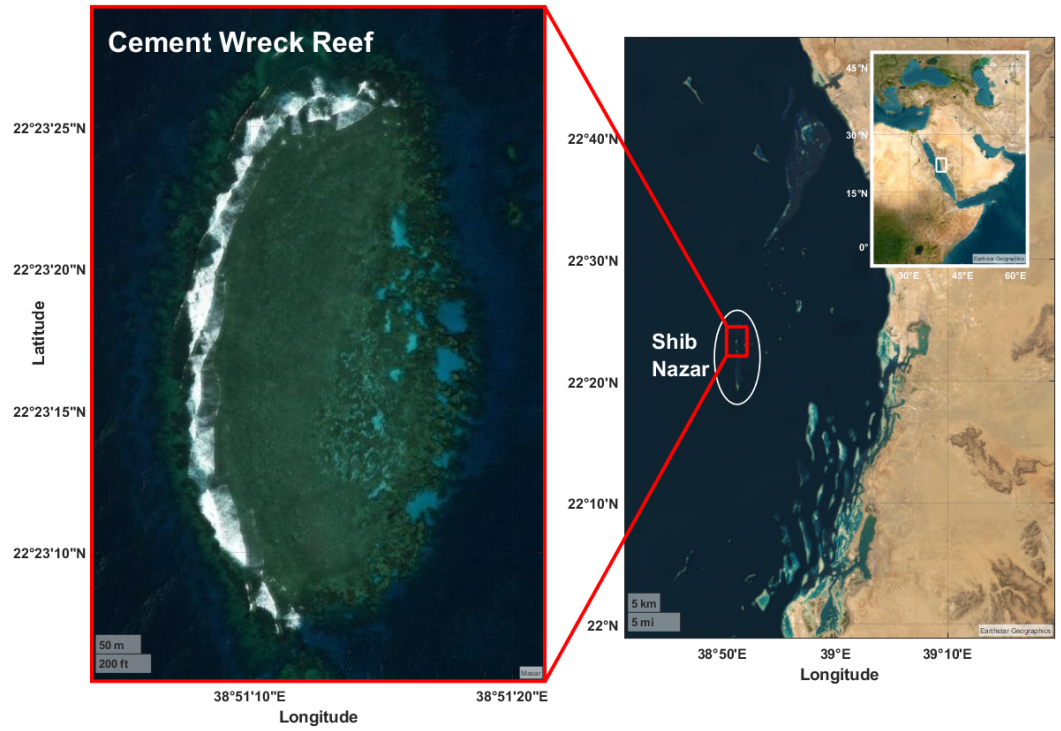


FIGURE 4.1: Location of Cement Wreck Reef (left) in the Central Red Sea (right), part of the Shib Nazar reef system (circled in white, right).

### 4.2.2 Autonomous Sensor Mooring

Two fixed-point sensor moorings were deployed on Cement Wreck reef. The primary mooring was deployed in the lagoon from October 19–December 12, 2023, and the secondary mooring was deployed on the fore reef slope of Cement Wreck from October 26–November 30, 2023 (Figure 4.2).

The primary sensor mooring was a custom-built steel frame fixed-point observing platform originally developed by the National Oceanography Centre (NOC) for the Commonwealth Marine Economies Program `https://cmeprogramme.org/`). Without instrumentation, the frame weighs 20 kg, is 0.75 m in height, and has a base footprint spanning 0.5 m in width. The frame was fitted with several oceanographic sensors including a Lab-On-Chip (LOC) pH sensor (NOC), a LOC TA sensor (NOC), SAMI-CO2 sensor (`http://www.sunburstsensors.com`), a SBE 37 SMP-ODO MicroCAT Conductivity-Temperature-Depth / Dissolved Oxygen sensor (CTD-DO; SeaBird Scientific), and an ECO Triplet-w chlorophyll sensor (SeaBird Scientific) and deployed at a depth of $\sim$ 1.5 m (Figure 4.2).

The LOC pH sensor measures pH on the total proton scale ($pH_T$) with a precision of 0.001 pH units using photometric determination with the purified indicator dye meta-Cresol Purple (mCP). Relative to validation seawater samples, the LOC pH sensor has 0.003 $\pm$ 0.022 accuracy and a combined standard measurement uncertainty of $\pm$ 0.010 pH units (Yin et al., 2021). The LOC TA sensor methodology is based on single-point acid titration to a photometrically determined endpoint pH = 3.0–3.5. The titration is done using hydrochloric acid (HCl) titrant containing unpurified Bromophenol Blue (BPB) indicator dye. The titrant consisted of 0.03 M HCl and 0.00015 M BPB in 0.6 M NaCl, formulated to a salinity of 41.52 psu, aligning with the high-salinity conditions of the Red Sea. The TA sensor has a precision and accuracy better than 5 $\mu$mol $kg^{-1}$ in ideal conditions (Schaap et al., 2025). Here, we present the first deployment of the TA sensor in an environment with such high salinity and temperatures ($>$ 38 psu, $>$ 30°C). The LOC pH and TA sampled every hour, except for November 30–December 04, 2023, when the TA sensor made measurements every 30 minutes (Table 4.1).

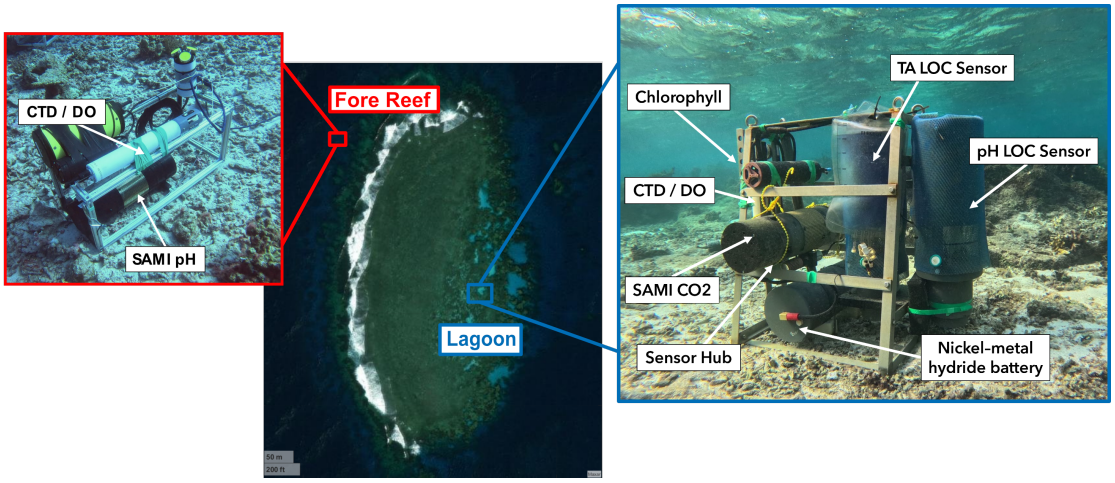


FIGURE 4.2: Sensor mooring frames deployed at Cement Wreck Reef. The primary sensor mooring (zoomed inset image right, outlined in blue) is situated in the lagoon at $\sim$ 1.5 m depth, and secondary sensor mooring (zoomed inset image left, outlined in red) on the fore reef slope at $\sim$ 15 m depth, both with labeled oceanographic sensors integrated.

The CTD-DO on the primary sensor mooring measured *in situ* temperature (T), salinity (S), and dissolved oxygen (DO) every two minutes (Table 4.1), and was independently powered by 12 lithium AA batteries. Corresponding *in situ* T and S data from the CTD-DO were made available to the LOC pH and TA sensors when they made a measurement via a 1 Hz stream facilitated by the Sensor Hub. The Sensor Hub was developed by NOC specifically to simplify the integration of multiple sensors on autonomous platforms, and is fully programmable, allowing it to poll for samples from the CTD-DO. Power was provided to the LOC pH sensor, LOC TA sensor, and

Sensor Hub by a custom-made rechargeable nickel-metal hydride (Ni-MH) battery pack enclosed within polyvinyl chloride (PVC) housing rated to 100 m depth.

The SAMI-CO2 is a commercially available sensor that measures the partial pressure of $CO_2$ ($pCO_2$) using the colorimetric reagent method (DeGrandpre et al., 1995), and made measurements every 30 minutes. The SAMI-CO2 was powered from a self-contained 8 alkaline D-cell battery pack and has an accuracy and precision of $\pm$ 2 $\mu$atm and $<$1 $\mu$atm respectively (DeGrandpre et al., 1995; Lai et al., 2018). The ECO Triplet-w recorded measurements every two minutes as the average from a burst of five 1 Hz optical fluorescence signals. Chlorophyll concentration was then derived using the calibrated coefficients and scale factor specific to the instrument provided by the manufacturer (Scientific, 2023).

The secondary sensor mooring comprised of a SAMI-pH Sensor and a CTD-DO situated at $\sim$ 15 m water depth (Figure 4.2). The SAMI-pH sensor is a commercially available sensor that measures $pH_T$ based on the spectrophotometric method in which a diprotic sulfonephthalein pH indicator is used (Lai et al., 2018). The SAMI-pH sensor has a reported accuracy and precision of $\pm$ 0.003 and $<$0.001 pH units respectively (Sunburst Sensors, LLC, Shangguan et al. 2022; Seidel et al. 2008) and for this work, made measurements every hour on the fore reef. The Idronaut CTD-DO sensor in the forereef took measurements of T, S, DO (polarographic), and pressure (P) every five minutes. An overview of each sensor's reef location, deployment duration, and frequency can be found in Table 4.1.

TABLE 4.1: Overview of sensor deployments at Cement Wreck Reef lagoon and fore reef slope. Listed are sensor type, manufacturer, deployment start and end dates, duration, and measurement frequency.

| Location | Sensor | Start Date | End Date | Duration (days) | Frequency *f* |
|---|---|---|---|---|---|
| **Lagoon** | Lab-On-Chip pH (National Oceanography Center) | 19/10/2023 | 12/12/2023 | 54 | 1 hr |
| | Lab-On-Chip TA (National Oceanography Center) | 02/11/2023 | 04/12/2023 | 32 | 1 hr / 30 min |
| | cTD-DO (SeaBird Scientific) | 19/10/2023 | 12/12/2023 | 54 | 2 min / 5 min |
| | chlorophyll (SeaBird Scientific) | 26/10/2023 | 02/11/2023 | 39 | 2 min |
| | Sami-CO2 (Suburst Sensors LLC) | 02/11/2023 | 09/11/2023 | 27 | 30 min |
| **Fore Reef** | cTD-DO (Idronaut) | 26/10/2023 | 30/11/2023 | 35 | 5 min |
| | Sami-pH (Sunburst Sensors LLC) | 26/10/2023 | 30/11/2023 | 35 | 1 hr |

### 4.2.3 Data Processing

In the lagoon, corresponding *in situ* T and S measurements from the CTD-DO polled by the sensor hub were used by the LOC pH and TA sensors to determine $pH_T$ and TA as described by Yin et al. (2021) and Schaap et al. (2025) respectively. For marine carbonate system measurements, it is standard practice to use "CO2-in-seawater Reference Materials" (RMs). RMs have certified values for TA and DIC and are stable for long periods of time and unaffected by temperature. The TA sensor seawater measurements were determined relative to periodic calibration measurements (Schaap et al., 2025) from two different onboard certified RMs (Dickson Lab).

Oxygen saturation, [O2]%, was calculated as a ratio (percent) of measured dissolved oxygen concentration (DOsensor) of the seawater to the dissolved oxygen concentration of water at equilibrium with atmosphere based on potential temperature and salinity (DOeq) using Equation 4.1 and following the international thermodynamic equations of seawater (TEOS-10) by IOC et al. (2010) and McDougall and Barker (2011).

$$[O_2]\% = \frac{DO_{sensor}}{DO_{eq}} \times 100 \tag{4.1}$$

The operation and data processing for the remaining sensors (SBE CTD-DO, ECO Triplet-w, SAMI-CO2, Idronaut CTD-DO, and SAMI-pH) were in accordance with the standard operating procedures and software provided by the manufacturers. Outliers were detected and removed from all data using the Hampel Filter with a 1-hour rolling window (Hampel 1974; The Mathworks Inc., 2024). The Hampel Filter was chosen based on the time series nature of the dataset and the high diel cycles seen throughout (Roos-Hoefgeest Toribio et al., 2025; Liu et al., 2004)

#### 4.2.3.1 Carbonate System Calculations

The speciation of the marine carbonate system in the Cement Wreck lagoon was constrained using the MATLAB (version v3.1.1) CO2SYS package (Sharp and Byrne 2021; Orr et al. 2018; Lewis and Wallace 1998; The Mathworks Inc., 2024) with sensor obtained *in situ* TA, $pH_T$, S, T, and set P = 1.5 dbar as input parameters. Nutrient (phosphate and silicate) concentrations were not measured during this deployment and were therefore set to 0 for computation. In accordance with the recommendations from Dickson et al. (2007), CO2SYS computations used the the dissociation constants of carbonic acid (K1 and K2) from Lueker et al. (2000), KSO4 from Dickson (1990), KF from Perez and Fraga (1987), and total boron concentration from Lee et al. (2010) to derive DIC, aragonite saturation state ($\Omega_{arag}$), and partial pressure of $CO_2$ ($pCO_2$) in the lagoon of Cement Wreck.

#### 4.2.3.2 Sensor Validation Efforts

During the final week of the deployment, two vacant inlets of the TA sensor were plumbed to RMs (one high alkalinity and one low alkalinity). The sensor measuring the RMs as routine samples, and both inlet measurements had good agreement with the RMs. This check confirmed that the observed diel TA behaviour in the lagoon and the TA–DIC slopes are not artifacts. Both the LOC pH sensor (deployed in the lagoon) and the SAMI-pH sensor (deployed in the fore reef) were simultaneously verified against the same certified TRIS buffer post-deployment. Each instrument reported pH values that matched the known TRIS value within stated uncertainty and no systematic bias relative to one another. The remaining sensors (e.g., CTD, DO) are community-accepted as routine mooring instrumentation without regular co-samples validation. Each of these sensors were factory-calibrated (or calibrated to manufacturer specifications) prior to deployment.

### 4.2.4 Metabolic Analysis

For periods with overlapping measurements, time series of $pH_T$ and DO from the lagoon and fore reef were each synchronised and analysed using linear least squares regression (The Mathworks Inc., 2024). Following the method outlined by Cryer et al. (2023) and Frieder et al. (2012), the co-variation between $pH_T$ and DO was further compared against a theoretical Photosynthesis: Respiration (P:R) model. The P:R model uses the Redfield Ratio (Equation 4.2; Anderson 1995) and the change in TA based on proton production / removal during respiration / photosynthesis (Equation 4.3; Frieder et al. 2012; Stumm and Morgan 1996) to predict the pH for a given DO under the assumption that photosynthesis and respiration are the only processes occurring.

$$\Delta CO_2 = \frac{\Delta O_2}{-150/106} \tag{4.2}$$

$$\Delta TA = \frac{\Delta CO_2}{-18/106} \tag{4.3}$$

The P:R model assumes that if there is calcification or carbonate dissolution present, then it would be observed through pH change without mirrored oxygen change, and that there is limited carbon contribution from air-sea fluxes. Lagoon median TA and DIC values (alongside *in situ* T,S,P, and density) were input to the P:R model for pH / DO predictions in the lagoon. The fore reef site, which did not have TA measurements, used lagoon median TA and DIC derived from fore reef pH and lagoon TA as inputs for the P:R model's pH / DO predictions. For comparison to observed pH and DO relationships at each site, a subset of the P:R model, based on site-specific variable range, was fitted to a curve using linear least squares regression.

Derived DIC and observed TA measurements in the lagoon over the course of the deployment were analysed using linear least squares regression. The relative% influence of NCP on changes in DIC was calculated according to Equation 4.4 (Cyronak et al., 2018);

$$\%NCP = (1 - \frac{m_{TA-DIC}}{2} \times 100) \tag{4.4}$$

where mTA-DIC is the slope of the TA-DIC regressions. For all calculations, TA and DIC data were not normalised to salinity because our site was an offshore reef with minimal salinity variability in a region without major river (freshwater) input or heavy precipitation. In addition, the absence of a well-defined region-specific oceanic or freshwater end-member and linear TA-S relationship could introduce data artifacts or unnecessary error into our results (Courtney et al., 2022; Jiang et al., 2014).

### 4.2.5 Benthos Characterisation

In the lagoon, benthic cover was quantified from an averaged quadrat image analysis (0.5 × 0.5 m, n = 5) collected within 5 m of the sensor frame using a GoPro HERO12 Black (https://gopro.com/). Each image was analysed using CoralNet (https://coralnet.ucsd.edu/), where 25 stratified random points per image were manually classified according to sub-functional groups: Hard coral, soft coral, sponge,other invertebrates, calcifying algae, CCA, macroalgae, dead coral, rubble, rock, and sand. Benthos characterisation on the fore reef used still image frames taken from video survey within 5 m of the sensor site (using a GoPRO HERO12 Black). The images were taken from where the camera's frame represented an estimated 0.5 m × 0.5 m quadrat, and analysed using CoralNet with the same routine as used for the lagoon analysis (n = 5).

## 4.3 Results

The two sensor moorings captured high-resolution biogeochemical and carbonate observations across the lagoon and fore reef zones of Cement Wreck Reef (Figures 1 & 2). These data reveal distinct environmental processes, diel variability, and spatial contrasts linked to benthic compositions. A complete summary of the physical, biogeochemical, and carbonate properties recorded at both sites is provided in Table 4.2.

TABLE 4.2: Summary of physical, biogeochemical, and carbonate chemistry observations at Cement Wreck Reef from the lagoon and fore reef sensor moorings. For each parameter, minimum–maximum (range), mean ± standard deviation (SD), and number of observations (n) are reported.

| Location | Variable | Min–Max (Range) | Mean ± SD | n |
|---|---|---|---|---|
| **Lagoon** | Temperature (°C) | 28.71–33.37 (4.66) | 30.60 ± 0.73 | 38559 |
| | Salinity (psu) | 38.67–39.76 (1.09) | 39.37 ± 0.10 | 38495 |
| | DO (µmol/kg) | 55–288 (408.51) | 173.13 ± 53.46 | 38556 |
| | [O2]% | 13–243 (230) | 94 ± 30 | 38572 |
| | Chlorophyll (µg/L) | 0.01–0.44 (0.43) | 0.13 ± 0.06 | 16897 |
| | pH | 7.80–8.30 (0.50) | 7.98 ±0.07 | 1183 |
| | TA (µmol/kg) | 2406–2565 (159) | 2522.60 ± 26 | 871 |
| | $pCO_2$ ($\mu$atm) | 214–1743 (1529) | 537 ± 148 | 1479 |
| | Derived $pCO_2$ ($\mu$atm) | 228–825 (598) | 516 ± 103 | 755 |
| | Derived DIC (µmol/kg) | 1871–2297 (426) | 2156 ± 66 | 755 |
| | Derived $\Omega_{arag}$ | 2.90–6.15 (3.24) | 4.07 ± 0.53 | 755 |
| **Fore Reef** | Temperature (°C) | 29.89–31.58 (1.68) | 30.91 ± 0.31 | 8007 |
| | Salinity (psu) | 39.1–39.52 (0.40) | 39.38 ± 0.04 | 7933 |
| | DO (µmol/kg) | 81–370 (290) | 172 ± 25 | 7844 |
| | [O2]% | 44–203 (159) | 94 ± 14 | 8025 |
| | pH | 7.91–8.11 (0.20) | 8.05 ± 0.02 | 899 |

### 4.3.1 Physical Setting and Biogeochemical Conditions

In the lagoon, temperatures ranged from 28.71 to 33.37°C (mean 30.60 ± 0.73°C), with clear short-term, diurnal variability and a broader seasonal decrease in temperature over the deployment (Figure 4.3a). Salinity varied between 38.90 and 39.64 psu (mean 39.37 ± 0.10 psu) with short-term decreases likely coinciding with heavy rainfall events (Figure 4.3b). Fore reef temperatures experienced a smaller diel cycle than the lagoon, ranging 29.80–31.58°C (mean 30.91 ± 0.31°C; n = 8,007; Figure 4.3a) and exhibited a narrower salinity range of 39.10–39.52 psu (mean 39.38 ± 0.04; Figure 4.3b). Salinity was the only parameter observed that did not have any diel signal. Dissolved oxygen (DO) concentrations differed in both range and variability between the Cement Wreck mooring sites. Lagoon DO spanned 24–432 $\mu$mol $kg^{-1}$ (mean 173 ± 53 $\mu$mol $kg^{-1}$), corresponding to oxygen saturation of 13–243% (mean 94% ± 30; Figure 4.3 c, Table 4.1). The fore reef exhibited a similar mean DO (172 ± 25 $\mu$mol $kg^{-1}$) but a narrower range of 81–370 $\mu$mol $kg^{-1}$, with saturation levels ranging 44–203% (mean

94% ± 14; Figure 4.3 c, Table 4.2). At both sites, DO experienced daily peaks, with their highest values during daylight, and did not exhibit clear seasonal trends over the course of the deployment (like temperature). In the lagoon, chlorophyll concentrations were low, ranging from 0.01–0.44 $\mu$g $L^{-1}$ (mean 0.13 ± 0.06 $\mu$g $L^{-1}$) but experienced daily fluctuation (Figure 4.3d).

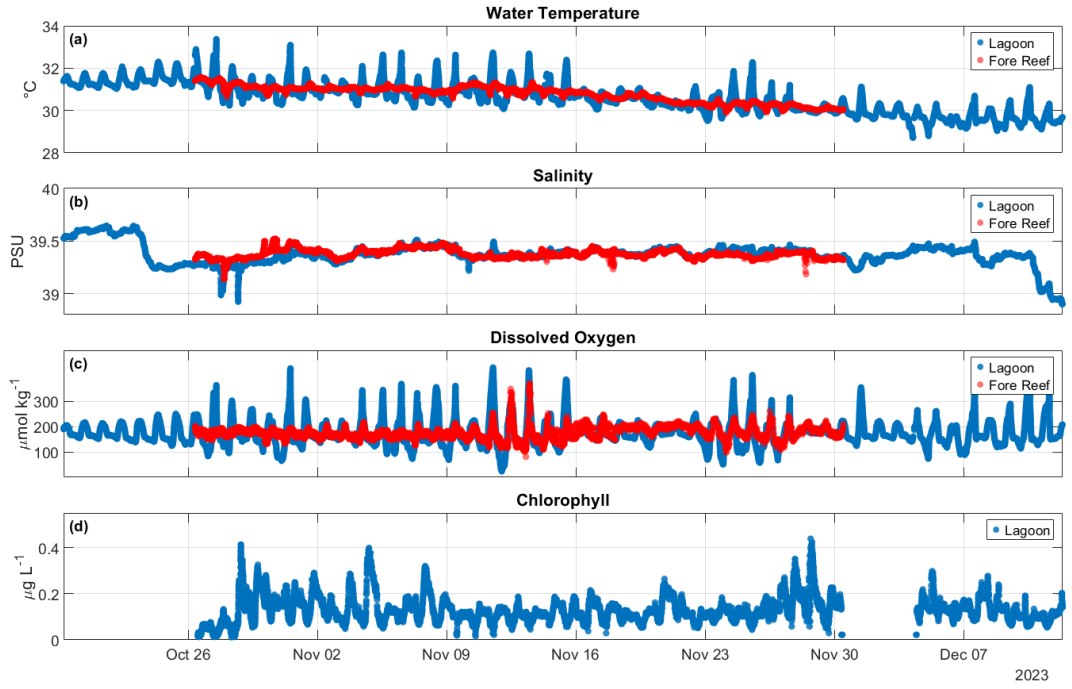


FIGURE 4.3: Time series of physical and biogeochemical parameters at Cement Wreck Reef lagoon (blue) and fore reef (red) sites. (a) Temperature in°C , (b) salinity in psu, (c) DO concentration in $\mu$mol $kg^{-1}$, and (d) chlorophyll concentration in $\mu$g $L^{-1}$ (lagoon only) are plotted from October 19–December 12, 2023.

#### 4.3.1.1 pH across the reef

Throughout the deployment, $pH_T$ in the lagoon ($pH_{T–Lagoon}$) was observed to be more variable than in the fore reef ($pH_{T–FR}$). Ranging 7.80–8.30, $pH_{T–Lagoon}$ not only had a wider range, but a lower mean (7.98 ± 0.07) than that of $pH_{T–FR}$ which ranged 7.91–8.11 and averaged 8.05 ± 0.02 (Figure 4.4). Both sites displayed strong diel cycles. The pH discrepancy between sites ($pH_{T–FR} - pH_{T–Lagoon}$) ranged from -0.27 to 0.28 (mean = 0.08 ± 0.07) and persisted the extent of the deployment.

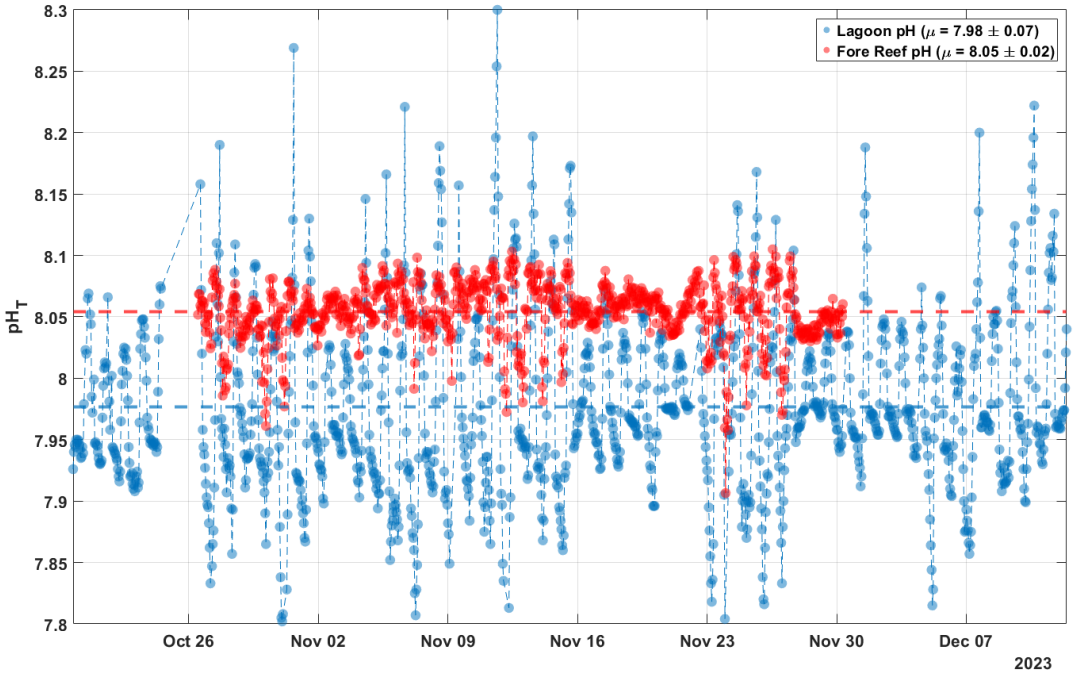


FIGURE 4.4: Time series of $pH_T$ at Cement Wreck Reef lagoon (blue) and fore reef (red) sites. Dashed blue line ($pH_T$ = 7.976) and dashed red line ($pH_T$ = 8.054) represent the mean $pH_T$ in the lagoon from October 19–December 12, 2023 and in the fore reef from October 26–November 30, 2023 respectively.

#### 4.3.1.2 Lagoon Carbonate Observations

Carbonate chemistry measurements in the lagoon further demonstrated the observed lagoon pH variability described above. TA ranged 2414–2570 $\mu$mol kg$^{-1}$ with a mean of 2523 $\pm$ 24 $\mu$mol kg$^{-1}$ (Figure 4.5a). Measured $pCO_2$ exhibited wide fluctuations ranging from 213–1743 $\mu$atm with mean 537 $\pm$ 148 $\mu$atm, and derived $pCO_2$ (from TA/pH LOC sensor measurements) closely tracked sensor $pCO_2$, with a milder range of 228–825 $\mu$atm and mean 516 $\pm$ 103 $\mu$atm (Figure 4.5b). The mean and median difference between (time-matched) measured and derived $pCO_2$ in the lagoon was 18 $\mu$atm, and 6 $\mu$atm respectively ($1\sigma$ = 64 $\mu$atm, n = 748). The only significant disagreement between measured and derived $pCO_2$ can be seen the week of November 23 (Figure 4.5), when the SAMI-CO2 sensor measured $pCO_2$ up to 1743 $\mu$atm (November 24 at 02:00 AST) while the derived $pCO_2$ peaked at 817 $\mu$atm (November 23 at 23:00 AST). The median difference between the two is much lower than the mean difference because of this event.

DIC, which was calculated from sensor measured TA and $pH_T$, ranged 1868–2298 $\mu$mol kg$^{-1}$ with mean 2157 $\pm$ 67 $\mu$mol kg$^{-1}$ (Figure 4.5c) and often tracked $pCO_2$ changes in relative magnitude and timing. Unlike $pH_T$, the TA and $pCO_2$ sensors were deployed for a shorter duration beginning October 26, 2023 and ending on November

30, 2023 with non-operational performance gaps spanning November 9–14, 2023 for TA and $pCO_2$ sensors and Nov 18–22, 2023 for only the TA sensor. Subsequently, there are gaps in the DIC time series during these dates because of it's reliance on TA for derivation (Figure 4.5). The aragonite saturation state ($\Omega_{arag}$) ranged from 2.90–6.15 with mean 4.07 $\pm$ 0.53.

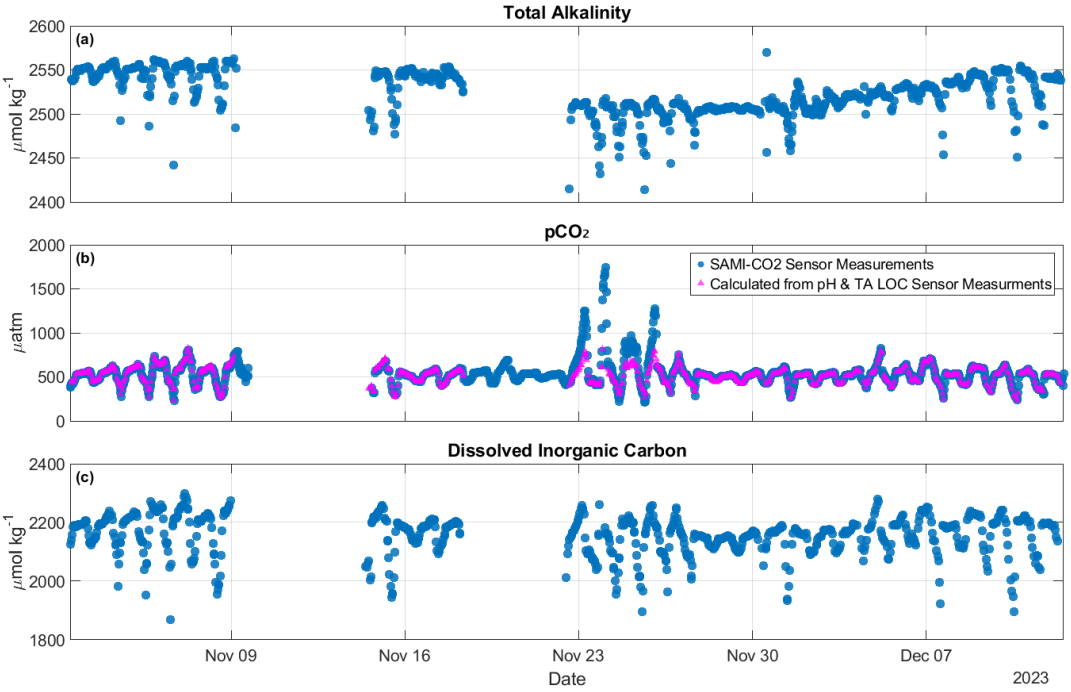


FIGURE 4.5: Time series of carbonate system observations in the Cement Wreck lagoon. (a) TA in $\mu$mol kg$^{-1}$, (b) $pCO_2$ (in $\mu$atm) measured by the SAMI-CO2 sensor (blue) and $pCO_2$ derived from pH and TA LOC sensor measurements (pink) (c) derived DIC in $\mu$mol kg$^{-1}$ are plotted from November 02–December 12, 2023. Gaps in time series reflect sensor downtime (a–b) and therefore corresponding missing derived DIC (c) and derived $pCO_2$ (b).

### 4.3.2 Metabolic Signals

Pronounced diel cycles were observed in several parameters at both sites, with greater amplitudes in the lagoon than on the fore reef (Figure 4.6). In the lagoon, water temperatures increased during daylight hours (daylight hours defined as between 06:00 and 18:00 AST), producing daily ranges over 1.5°C, with highest temperatures between 13:00 and 14:00 AST and lowest temperatures between 05:00 and 06:00 AST (Figure 4.6a). The fore reef experienced daily high and low temperatures at the same time as the lagoon but exhibited much smaller daily temperature changes, generally less than 0.25°C (Figure 4.6a). Salinity experienced minimal to no diel variability at both sites with daily ranges less than 0.02 PSU (Figure 4.6b). DO concentrations in the lagoon peaked during late afternoon (14:00–15:00 AST) and reached minima in the

early hours of each morning (02:00–04:00 AST), with daily amplitudes frequently exceeding 120 $\mu$mol kg$^{-1}$ (Figure 4.6c). Unlike the lagoon, the fore reef DO reached minima later in the morning (around 05:00–06:00 AST) and consistently peaked earlier in the afternoon (11:00–12:00 AST), with much smaller daily changes than the lagoon, typically less than 60 $\mu$mol kg$^{-1}$ (Figure 4.6c). Observed $pH_T$ mirrored DO in its diel cycle. $pH_{T-Lagoon}$ values peaked around 15:00 AST and nighttime minima between 04:00 and 06:00 AST, with average daily ranges of 0.14 (Figure 4.6d). Like DO in the fore reef, $pH_{T-FR}$ peaked earlier in the day (11:00–12:00 AST) but reached minima an hour before DO, between 03:00 and 04:00 AST. Diel amplitudes of $pH_{T-FR}$ were comparatively much smaller than $pH_{T-Lagoon}$, averaging 0.04 pH units (Figure 4.6d). Overall, $pH_{T-FR}$ values were much less variable than $pH_{T-Lagoon}$, and were consistently higher, except for during the $pH_{T-Lagoon}$ daily maxima when the upper $\pm$ 1 standard deviation reaches up to 8.12 at 16:00 AST.

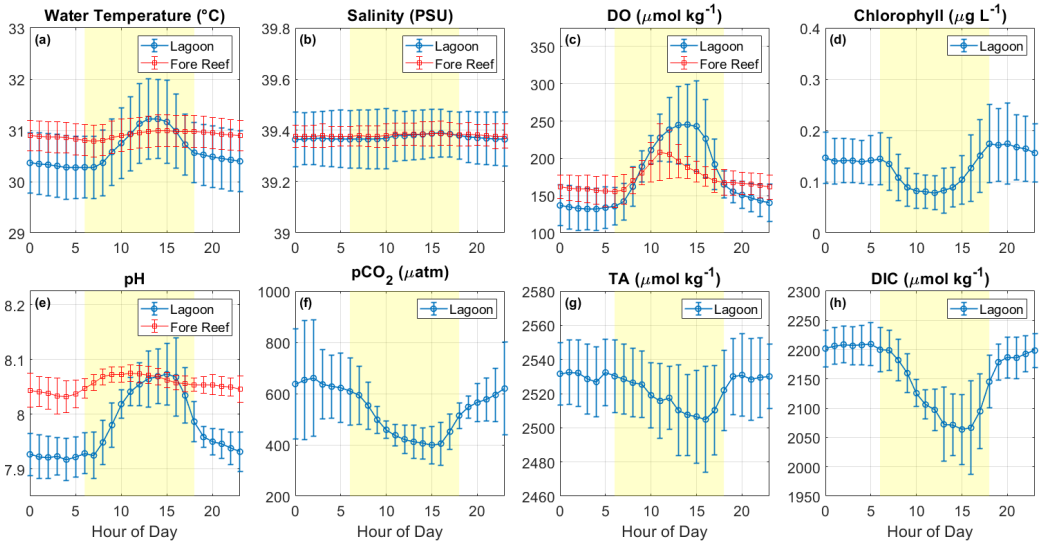


FIGURE 4.6: Diel cycles of environmental and carbonate parameters in the lagoon (blue) and fore reef (red) sites of Cement Wreck Reef. (a) Temperature in °C from both sites, (b) salinity in psu from both sites, (c) DO in $\mu$mol kg$^{-1}$ from both sites, (d) chlorophyll in $\mu$g L$^{-1}$ from the lagoon, (e) $pH_T$ from both sites (f) $pCO_2$ in $\mu$atm from the lagoon, (g) TA in $\mu$mol kg$^{-1}$ from the lagoon, and (h) derived DIC in $\mu$mol kg$^{-1}$ from the lagoon are all plotted representing the average value of each parameter per hour of day over the duration of the deployment, with error bars representing $\pm$ 1 standard deviation. Yellow highlighted areas (a–h) depict daytime hours from 06:00–18:00 Arabian Standard Time (AST).

Chlorophyll, $pCO_2$, TA, and derived DIC exhibited inverse diel cycling. These parameters were only observed in the lagoon, and they reveal a daily nighttime maxima and daytime minima. Chlorophyll concentrations in the lagoon show a clear dip in middle of the day around 12:00–13:00 AST, followed by a sharp increase still during daylight but peaking just after sunset around 18:00–20:00 AST. The daily change in chlorophyll averaged 0.1 $\mu$g L$^{-1}$. In the lagoon, highest $pCO_2$ values occur at

02:00 AST and lowest values later in the day between 15:00 and 16:00 AST (Figure 4.6f). Daily $pCO_2$ maxima commonly exceeded 600 $\mu$atm, with minima at 400 $\mu$atm (atmospheric equilibrium), and typical daily changes averaging 300 $\mu$atm. TA in the lagoon exhibited a shallower diel curve due to its higher variability throughout the deployment. TA was relatively steady during the nighttime, averaging 2529 $\mu$mol kg$^{-1}$ from the hours of 19:00–06:00 AST. However, TA would decrease daily at around 15:00–1600 AST and often drop below 2500 $\mu$mol kg$^{-1}$ (Figure 4.6g). The amplitude of change in TA during the day ranged from 4–108 $\mu$mol kg$^{-1}$ (Figure 4.4a & 4.5g), meaning that during some 24-hour periods, there was very limited change in TA (e.g., Nov 28–29). DIC followed a similar pattern to $pCO_2$, with afternoon minima (between 15:00 16:00 AST) ranging from 1987–2124 $\mu$mol kg$^{-1}$, and nighttime maxima (between 04:00 and 05:00 AST) ranging from 2174–2246 $\mu$mol kg$^{-1}$, resulting in average diel cycle of 146 $\mu$mol kg$^{-1}$.

The relationship between measured $pH_T$ and DO were compared to the theoretical relationship (pH:DO) based on Redfield Ratio (Figure 4.7). pH and DO correlated positively at both sites, however, the relationship between pH and DO varied.

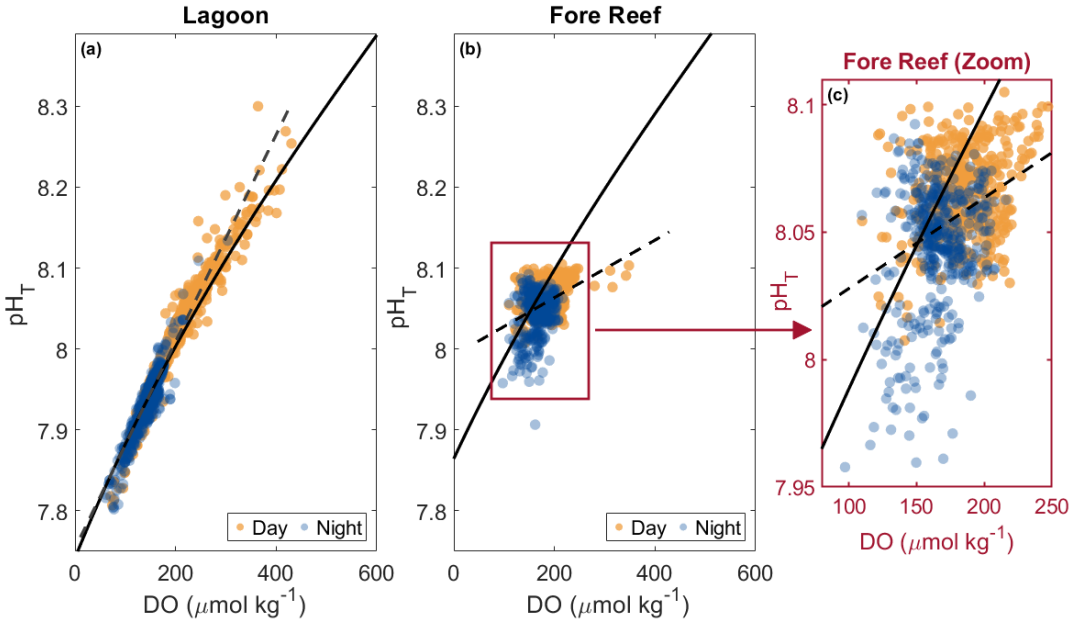


FIGURE 4.7: Relationship between DO and $pH_T$ at (a) lagoon and (b) fore reef sites of Cement Wreck Reef. A zoomed view of the fore reef pH:DO relationship is shown in (c). Both relationships are compared with theoretical Redfield-based Photosynthesis:Respiration (P:R) model shown as a solid black line in (a), (b), and (c). Best fit line between pH and DO as determined by the linear least squares regression (dashed black line) in (a), (b), and (c).

In the lagoon, the pH:DO relationship was highly correlated ($R^2$ = 0.943) and the slope of its best-fit line closely followed that of the theoretical relationship subset of 0.0013 and 0.0011 respectively (Table 4.3, Figure 4.7a). In the fore reef, the $pH_T$ values are

lower than expected based on DO range, and the pH:DO relationship is weak ($R^2$ = 0.145). When fit to a linear regression, the fore reef observed pH:DO relationship has a slope of 0.0004, which differs from the P:R model subset slope of 0.0011 (Table 4.3, Figure 4.7 b,c). On both sites, we observe a pH:DO nighttime slope 0.0002 higher than the respective daytime slope (Table 4.3).

TABLE 4.3: Linear regression equations describing the relationship between DO and $pH_T$ at lagoon and fore reef sites of Cement Wreck Reef, separated by diel periods (all, day, night). The P:R Model subset for each site is included (red). Best-fit equations, coefficient of determination ($R^2$), root mean squared error (RMSE), and number of observations (n) are reported for each.

| Location | Diel Cycle | Equation of best fit line | $R^2$ | RMSE | n |
|---|---|---|---|---|---|
| **Lagoon** | All | y = 0.0013x + 7.75 | 0.943 | 0.017 | 1280 |
| | Day | y = 0.0012x + 7.77 | 0.934 | 0.018 | 629 |
| | Night | y = 0.0014x + 7.7266 | 0.886 | 0.013 | 651 |
| | P:R Model | y = 0.0011x + 7.7812 | 0.996 | 0.009 | n/a |
| **Fore Reef** | All | y = 0.0004x + 7.9923 | 0.145 | 0.022 | 854 |
| | Day | y = 0.0002x + 8.0347 | 0.070 | 0.017 | 440 |
| | Night | y = 0.0004x + 7.9844 | 0.074 | 0.025 | 414 |
| | P:R Model | y = 0.0011x + 7.8823 | 0.998 | 0.004 | n/a |

### 4.3.3 Benthic Habitat

Benthic habitat quadrat surveys at the lagoon site found that the substrate was dominated by rock (46%), followed by rubble (15%), macroalgae (13%), and hard coral cover (10%) (Figure 4.8). Smaller contributions included sand (5%), CCA (5%), dead coral (3%), and calcifying macroalgae (2%). In the fore reef, estimated quadrat surveys revealed benthic composition comprised of higher coverage of hard coral (21%) and rubble (30%), followed by sand (15%), CCA (14%), and rock (13%). While not found in the lagoon, soft coral (3%), other invertebrates (2%) and sponges (1%), contributed minimal percent coverage in the fore reef. There was less dead coral found in the fore reef (1%) than the lagoon (3%). Unlike the lagoon, macroalgae and calcifying algae were not found in the fore reef benthic survey.

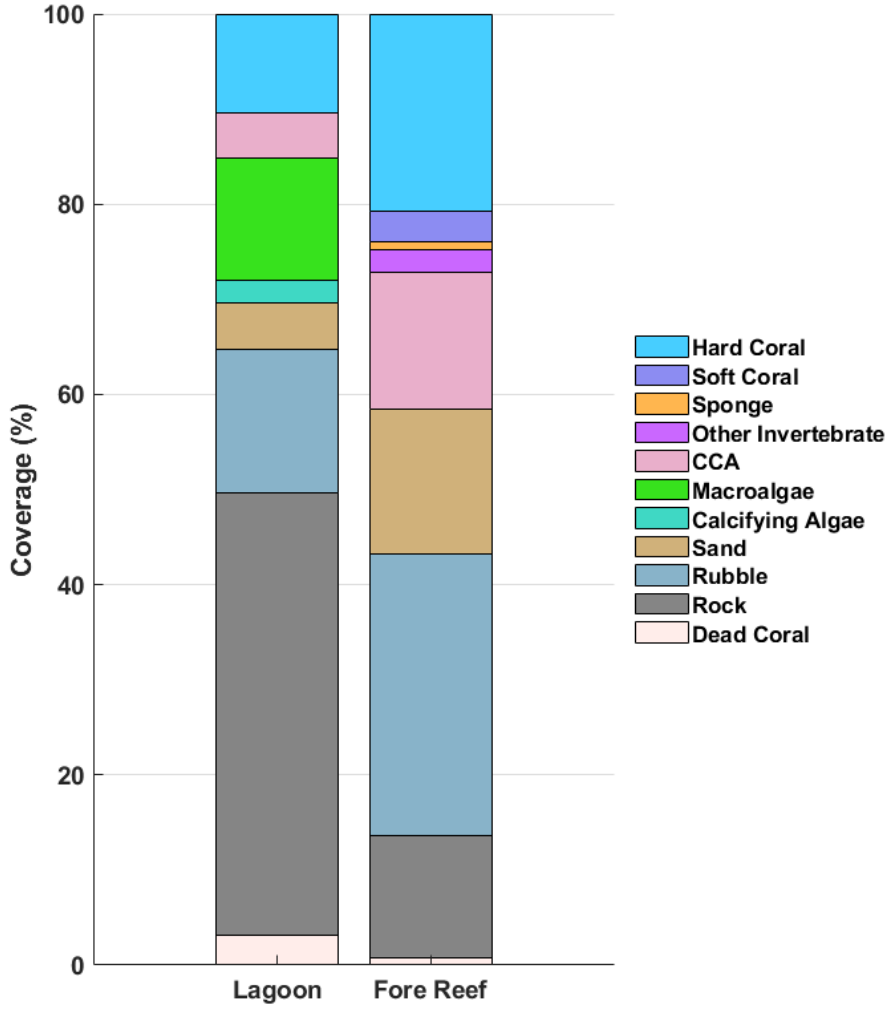


FIGURE 4.8: Lagoon (left) and Fore Reef (right) benthic habitat composition based on quadrat analysis, showing proportions of major functional groups

## 4.4 Discussion

### 4.4.1 Drivers of Temporal Variability

High-resolution sensor observations revealed pronounced diel variability in temperature, $pH_T$, and DO on the Cement Wreck Reef. At both sites, daily cycles followed the expected pattern of oxygen production and $CO_2$ uptake driven by photosynthesis during the day (0600–1800 AST), and respiration with oxygen drawdown and $CO_2$ release at night (18:00–06:00 AST). The magnitude and range of these cycles was much higher in the lagoon compared to the fore reef (Figure 4.6 a, c, e). This observation is consistent with previous studies reporting reefs that experienced greater diel temperature variability also exhibit greater diel pH variability, and that these ranges are tightly linked to reef depth (Cyronak et al., 2020; Òscar Guadayol et al., 2014). In particular, diel variability of temperature and pH was

found to diminish significantly at depths greater than $\sim$ 6 m (Cyronak et al., 2020), a finding we observed on the fore reef (sensor mooring at 15 m depth). While residence times, or the duration a water parcel remains within a reef, are not reported for Cement Wreck Reef, it is important to note that longer residence times are often expected to amplify diel ranges by allowing greater seawater modification (Zhang et al., 2013; Lowe et al., 2016). However, rapid diel oscillations in parameters like those measured in this study (temperature, DO, pH) dominate short-term variability from biological forcing whereas residence time will play a greater role in determining mean reef conditions over longer time periods (Takeshita et al., 2018; Falter et al., 2013; Zhang et al., 2013; Cyronak et al., 2020).

Chlorophyll concentrations in the lagoon exhibited unique diel variability, with minima measured at midday followed by an increases toward late afternoon and evening. The same chlorophyll concentration dynamics in the Red Sea have been previously reported by Wang et al. (2025) who found this diel phenomena to be predominately controlled by irradiance rather than nutrient availability. High midday irradiance, as found in the Red Sea (Overmans and Agustí, 2019), induces photoinhibition in phytoplankton, reducing chlorophyll density, and limiting primary production (Wang et al., 2009). These responses are consistent with photoacclimation observed in the dominant coral of Cement Wreck, *Stylophora pistillata*. The success of hermatypic corals such as *S. pistillata* in oliogotrophic waters is underpinned by their symbiosis with photosynthesising microalgae, zooxanthellae (Rowan, 1998). To sustain this relationship, *S. pistillata* is known to dynamically adjust chlorophyll concentration in response to irradiance levels (photoacclimation) in the Red Sea (Winters et al., 2009; Titlyanov et al., 2001). Alongside Winters et al. (2009), Mass et al. (2007) found *S. pistillata* corals in the Red Sea to decrease their chlorophyll concentration per symbiont cell under high light, and displayed strong depth-driven photoacclimation. This offers an explanation as to why lagoon DO and pH, linked to photosynthesis rates, peaked later in the day compared to the fore reef, where greater depth buffered irradiance levels. This finding alongside that of Wang et al. (2017) could indicate that although chlorophyll was not measured on the fore reef, it is reasonable to assume that chlorophyll concentrations were likely higher and peaked earlier in the day at that site. Finally, Mass et al. (2007) showed that *S. pistillata* and other calcifiers in the Red Sea maintain higher calcification rates under high irradiance despite reducing chlorophyll per symbiont cell. This supports our observation of afternoon decreases in lagoon TA (Figure 4.6g), which likely reflect calcification even under high irradiance levels.

### 4.4.2 Cement Wreck Reef Metabolic Processes

The strong diel co-variation, and large diel range of pH and DO observed in the lagoon (Figure 4.6c and e) is indicative of biological activity dominated by photosynthesis and respiration. The close match between the slope of the lagoon pH-DO relationship and the slope of the theoretical Redfield Ratio P:R model (Figure 4.7a; Table 4.3), supports this interpretation (Cryer et al., 2023). The fore reef exhibited a weaker pH–DO correlation that did not align as well with the P:R model, which suggests that the additional processes, such as calcification and/or dissolution are likely occurring. This difference can be explained by the benthic composition, the lagoon site is dominated in the living fraction by turf algae and has low calcifying coral cover and CCA, while the fore reef has a more than double percentage cover of hard coral and no macroalgae present. A reef with greater hard coral cover will alter the pH-DO further from the theoretical P:R Model due to the influence of calcification on pH.

Analysis of lagoon TA and DIC stoichiometric dynamics provides further confirmation of the metabolic controls we see in the Cement Wreck Reef. The overall TA–DIC slope ($\Delta$TA:$\Delta$DIC= 0.26, $R^2$ = 0.510 , $p < 0.001$, Figure 4.9, Table 4.4) is characteristic of organic metabolism, falling nearer the ratio for photosynthesis/respiration (slope = 0.2), than the calcification dissolution ratio (slope = 2) line (Ho and Schanze, 2020; Yeakel et al., 2015; Cyronak et al., 2018).

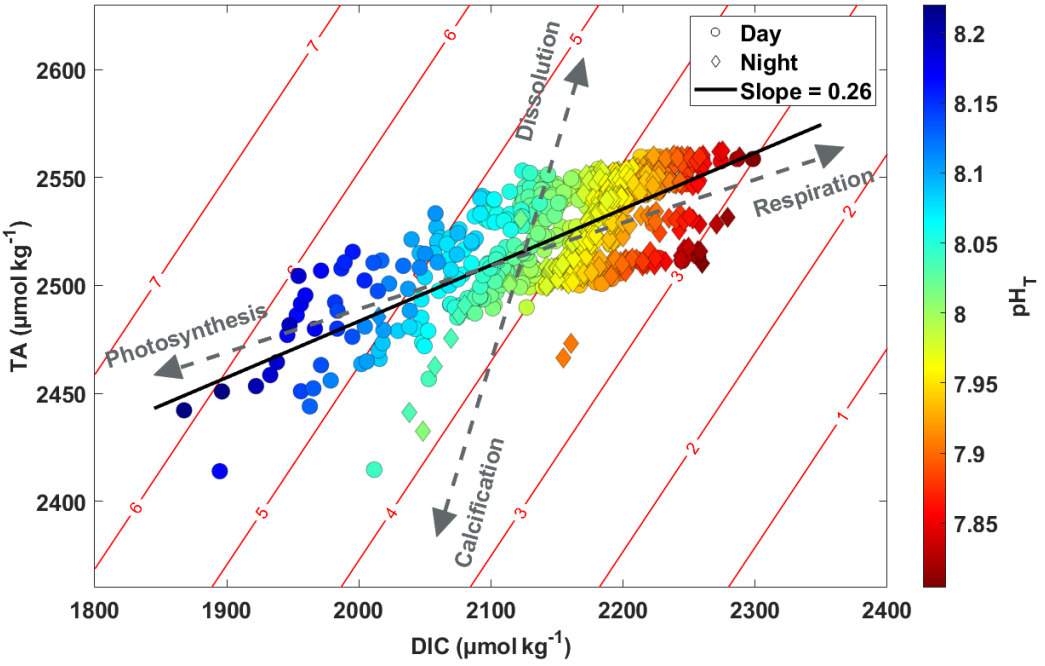


FIGURE 4.9: Relationship between DIC and TA in the lagoon. Colour represents $pH_T$ with circle markers at daytime and diamond markers at nighttime. Aragonite saturation state ($\Omega_{arag}$) levels are drawn in red diagonal contour lines. The DIC to TA known ratios for calcification / dissolution (-2/2) and photosynthesis/respiration (-0.2/0.2) are depicted by gray dashed lines. The best fit line between DIC and TA as determined by the linear least squares regression (slope = 0.26) is the solid black line. It should be noted that the intersection of the known ratios (gray dashed lines) have been centred on the scattered data distribution and are not intended to imply where each process begins and ends, but rather illustrate the expected trajectories of these processes in DIC-TA space.

NCP accounted for ~87% of observed variability in DIC and TA. Since photosynthesis-respiration primarily modulate DIC with comparatively small, nutrient-linked changes in TA, a low TA-DIC slope is expected when NCP is the predominant metabolic driver, therefore corroborating that diel changes in carbonate chemistry in the Cement Wreck lagoon were largely governed by organic carbon processes rather than NCC (Shamberger et al., 2011; Yeakel et al., 2015; Cyronak et al., 2018). Algae/turf communities tend to exhibit higher NCP but comparatively low NCC compared to coral-dominated communities which show higher NCC for a given amount of production (Roth et al., 2020, 2021). Thus, a turf-heavy community alongside lesser coral/CCA cover (Figure 4.8) provides an explanation for the NCP-dominated TA–DIC slope (0.26; Table 4.4) and the large diel ranges of pH–DO in the lagoon (Figures 4.6e and 4.7a).

TABLE 4.4: Linear regression equations for the relationship between DIC and TA in the lagoon at Cement Wreck Reef, separated by diel periods (all, day, night). Equation of best fit line, coefficient of determination ($R^2$), root mean square error (RMSE), and number of observations (n) for each are reported. Each relationship was found to be statistically significant with all p-values<0.001.

| Location | Diel Cycle | Equation of best fit line | $R^2$ | RMSE | n |
|---|---|---|---|---|---|
| **Lagoon** | All | y = 0.2602x + 1963 | 0.510 | 17.2 | 755 |
| | Day | y = 0.2654 + 1955 | 0.533 | 17.4 | 369 |
| | Night | y = 0.4011 + 1651 | 0.473 | 15.7 | 368 |

When placed in a global context, contribution of NCP (87%) and the TA-DIC slope (0.26) at Cement Wreck falls at the uppermost end of NCP and the lower end of TA-DIC slope of the global reef ranges (32–88%, 1.36–0.24 respectively; Cyronak et al. 2018). Reefs with a large NCP contribution are particularly effective at driving pH, because organic metabolism produces stronger proton fluxes per unit change in DIC compared to calcification/dissolution. This can be visualised in TA-DIC space where pH isolines typically have a slope close to 1. When the TA-DIC relationship yields a slope <1 (as seen with dominant NCP), it crosses more isolines of pH, resulting in larger pH variability (Cyronak et al., 2018). This is demonstrated in Figure 4.9 as our data points cover pH range 7.85–8.22 (pH represented by color, crossing $\Omega_{arag}$ contours depicted by red contour lines) and DIC range 1871–2297 within the TA-DIC space. Visualizing this concept from another perspective, Figure 4.6 panels c, e, g, h depict a large drawdown of daytime DIC with a concurrent large uptake of oxygen and increase in pH, yet a modest change in TA. Regional comparisons from the northern Red Sea reveal near-identical TA-DIC slopes of 0.29, 0.26, and 0.25 NCP of 85%, 87%, and 87% reported in years 1997, 1998, and 2013 respectively (Silverman et al., 2007; Cyronak et al., 2018). This suggests that while reefs around the world have seemingly shifted towards NCP, reefs like Cement Wreck within the Red Sea have been dominated by primary production for the last 25 years and may be stable in this state.

Day-night contrasts in Table 4.4 add important nuance to our interpretations. The daytime TA-DIC slope (0.265) remains firmly in the NCP-dominated regime, while at the night the slope steepens (0.401), indicating a larger NCC contribution in addition to respiration. This is consistent with enhanced $CaCO_3$ dissolution seen by reef frameworks under low pH and low $\Omega_{arag}$ nighttime conditions—an effect shown to intensify under ocean acidification (Stoltenberg et al., 2021; Kwiatkowski et al., 2016; Cyronak and Eyre, 2016). For example, long-term observations from the Eilat Nature Reserve (Northern Red Sea) documented substantially higher nighttime $CaCO_3$ dissolution in 2015–2016 compared to 2000–2002 (Moav-Barzel et al., 2023). Our pH-coloured data plotted across $\Omega_{arag}$ contours in Figure 4.9 align with this archetype of lower pH, lower $\Omega_{arag}$ at night (denoted by diamond markers), with modest TA

repletion, likely by dissolution. Taken together, these results highlight how the balance between organic and inorganic metabolism varies not only across global reef settings but also within single reef systems over a diel periods. Abiotic dissolution of aragonite should not occur as the seawater is supersaturated with respect to aragonite ($\Omega_{arag} > 2.5$; Figure 4.9), however dissolution has been identified on reefs where seawater $\Omega_{arag} > 2.5$ due to micro environment effects (de Orte et al., 2021; Islam et al., 2016). Furthermore, substantial substrate (rock, rubble, sand) coverage in the lagoon (Figure 4.8) could possibly imply that there are permeable sediments where pore water advection may enhance the nighttime dissolution signal we see, offering insight into the steeper slope of the TA-DIC at night (0.401), but remains to be investigated further (Cyronak et al., 2013; Rao et al., 2012; Precht and Huettel, 2003; Moav-Barzel et al., 2023).

## 4.5 Conclusion and Broader Implications

The central novelty of this work was the use of co-located, autonomous, high-resolution sensors including *in situ* TA for multi-month observations on a coral reef. Autonomous sensors transform reef biogeochemistry from occasional snapshots into a high-frequency observing system. Critically, this deployment demonstrated the feasibility and scientific value of continuous *in situ* TA alongside pH and DO on a reef. The inclusion of high-resolution autonomous TA observations allowed for an ideal input parameter pairing to constrain the carbonate system, highlight direct alkalinity short-term trends, and corroborated interpretations of reef metabolic control based on pH/DO observations. By sustaining sub-hourly measurements, our sensor moorings detected synoptic variability that drives reef metabolic processes, and captured short-lived transitions between net production and net dissolution that conventional sampling surveys may miss. Furthermore, the sheer quantity of observations tightens regressions and reaffirms processes seen across diel cycles.

By characterizing diel variability and quantifying the dominance of NCP over NCC at Cement Wreck Reef, this study contributes a baseline understanding of Red Sea reef metabolism. Our results suggest that despite environmental extremes unique to the Red Sea, these reefs metabolically behave in ways consistent with coral reef ecosystems around the world, and in a climate where reefs are constantly under threat there is evidence of stability in NPP and TA-DIC slope over the last 25 years. As reefs continue to face global and local stressors the ability to monitor reefs is imperative and we demonstrate how by deploying pH, DO and TA sensors we are able to fully constrain (and overdetermine) the carbonate chemistry of the reefs and identify metabolic process more efficiently than traditional discrete measurements. Scaling up autonomous deployments like this one and integrating them into comprehensive

observing networks could more effectively predict how future warming and acidification will alter coral reef carbonate budgets and metabolic balances globally.

## Open Research Section

All sensor data are available from The University of Southampton Data Repository via https://doi.org/10.5258/SOTON/D3691.

# Chapter 5

# Conclusions

## 5.1 Summary and Key Results

The global ocean plays a central role in regulating Earth's climate, absorbing anthropogenic carbon dioxide ($CO_2$) emissions and regulating temperature (Gruber et al., 2023; Friedlingstein et al., 2025). Yet, the increased flux of $CO_2$ into surface oceans is reducing seawater pH, and consequently ocean carbonate ion availability (Zeebe and Wolf-Gladrow, 2001; Doney et al., 2009; Jiang et al., 2019). Ocean acidification, alongside increasing sea surface temperature, have profound consequences for global marine ecosystems, carbon storage, and biogeochemical cycling, that threaten ocean resources relied on by the majority of the human population (Doney et al., 2020; Falkenberg et al., 2020; Maslin et al., 2025). Established ship-based monitoring approaches, while precise, are limited in temporal and spatial coverage, and leave many coastal, shelf, and reef environments under-sampled and poorly constrained (Bushinsky et al., 2019). As high-quality, high-resolution autonomous carbon system observing technologies emerge, a greater emphasis has been placed on honing and harnessing their capabilities. We've reached a defining moment for our planet and civilization's health alike, and sustained, scientific investigation and intervention is **incontrovertibly required**.

The work in this thesis set out to expand the scientific capabilities for autonomous observing of the marine carbonate system, whilst targeting dynamic environments where traditional ship-based approaches may overlook significant variability. Across three distinct scientific applications and deployments, novel autonomous technology is demonstrated as a tool for high-quality carbonate measurements at resolutions that resolve fine-scale processes and improve our understanding and interpretation carbon cycling, air–sea $CO_2$ exchange, and ecosystem metabolism.

**Chapter 2** showcases the first successful use of an autonomous vehicle to characterise the carbonate system from direct *in situ* measurement by pH and TA. Lab-On-Chip

(LOC) sensors integrated onto the Autosub Long Range (ALR) collected measurements with uncertainties meeting weather-quality criteria ($\pm$0.02 for pH and $\pm$10 $\mu$mol kg for TA), and aligned closely to the "gold standard" discrete bottle samples collected from coincident ship operations. Residual analysis revealed environmental properties from observation spatiotemporal mismatch that explained pH disparities observed between ALR sensing and ship-based CTD discrete sampling (Hammermeister et al., 2025).

**Chapter 3** extended capabilities of the autonomy demonstrated in Chapter 2 in both spatial and temporal scales while unsupported by ship operations, undertaking the first fully autonomous long-distance ALR mission with scientific sensors onboard (Phillips et al., 2023). With both a SeaFET pH and LOC pH sensor measuring continuously throughout, the ALR traveled over $\sim$2000 km in the course of five weeks, transiting the Celtic Sea continental shelf. Sensor redundancy was proven as a robust tool for drift and accuracy corrections for the coastal pH measurements, outperforming established global models and neural networks. Importantly, the mission yielded unprecedented high-resolution air–sea $CO_2$ flux estimates, uncovering process-scale variability missed by climatologies and flux sensitivity to pH measurement, amplified by wind conditions.

**Chapter 4** used the same Lab on Chip / sensor hub technology from Chapters 2 and 3 to observe the unique yet poorly understood biogeochemical dynamics of reef systems in the Red Sea, during a multi-month autonomous sensor mooring deployment. Chapter 4 documents the first record of autonomous standalone TA sensor measurements on a coral reef, alongside extended high-resolution observations of pH, $pCO_2$, derived DIC, dissolved oxygen, temperature, salinity, and chlorophyll. Differing benthic community characterisations contextualized the metabolic dynamics seen between the two sub-sites (fore reef and lagoon) within the reef. The reef experienced pronounced diel cycling, with the lagoon exhibiting higher fluctuation and pH-DO coupling than the fore reef. The inclusion of high-resolution TA measurements in the lagoon enabled over determination of the carbonate system, and resolved a TA-DIC relationship (slope = 0.26) indicating net community production accounted for $\sim$87% of the metabolic dynamics on the reef; remarkably matching decade-old studies by Silverman et al. (2007).

## 5.2 Discussion

The chapters of this thesis examine how autonomous technologies can be used to better our understanding of the marine carbonate system across distinct ecological and hydrographic settings. Each demonstrated application (chapter) resolves a different question in ocean carbon cycling (biogeochemical gradients across a

temperate shelf sea in Chapter 2, flux variability from a coastal transect in Chapter 3, and metabolic forcings on a coral reef in Chapter 4) all while working to demonstrate, analyse, and validate high-frequency autonomous novel instrumentation for high-quality oceanographic research. The LOC sensor technology used throughout this thesis has proven capable of achieving weather-quality carbonate system observations in both moving and fixed platform settings. This work establishes a methodological basis for autonomy as a strong scientific tool at scales otherwise unattainable, and as logical complement or substitute to ship-based observations.

The progression across chapters in this thesis also highlights how observing strategy design is important in addressing key questions most effectively. Temperate shelf seas, like the Celtic Sea, exhibit strong hydrographic and seasonal variability that influence carbonate chemistry, but have been difficult to constrain with limited resolution of ship-based surveys (Humphreys et al., 2019; Laruelle et al., 2014). Therefore, resolving gradients and carbon cycling throughout the water column and across continental margins requires high-resolution measurements, best achieved from moving platforms capable of covering broad domains in space and time (Chapters 2 and 3), complementary to the lower coverage of repeat research cruises (e.g., GO-SHIP; Sloyan et al. 2019). In coral reef systems, driving metabolic processes are better defined using fixed-point observatories to capture the fast-changing chemistry driven by often shallow hydrography and benthic ecosystem composition (Chapter 4.

Similarly, the choice of measured parameters will have a big impact on the uncertainty of the calculated carbonate system parameters and the quality of the overall study results . Chapters 2 and 4 used pH–TA as input variables to characterise and over-determine the marine carbonate system. As outlined in Table 1.1, pH–TA is a more desirable input pair for minimizing propagated error (Dickson and Riley, 1978; Orr et al., 2018). Comparisons to ”gold standard” discrete ship-based measurements in Chapter 2 and cross-sensor agreement (e.g., ISFET pH vs LOC pH) in both Chapters 2 and 4, support this choice for accurate carbonate system characterisation (Figures 2.11,2.12, and4.5b). In Chapter 3, redundancy between spectrophotometric LOC pH and electrochemical SeaFET pH provided a means of onboard corrections, and improved reliability for interpreting pH and quantifying air-sea $CO_2$ exchange. While Chapter 3 deployment incorporated modeled TA to close the system, sensitivity analysis confirmed that TA uncertainty contributed only marginally to $pCO_2$ and flux estimates, whereas small differences in pH had a much larger impact. This finding reconciles the use of parameterised TA in Chapter 3 with the broader conclusion that accurate direct pH measurements are the most critical factor in reducing error for flux determinations.

By positioning these results to address community capability gaps, and validating them against discrete sampling, literature, and system over-determination, this thesis contributes to efforts to expand high-resolution, autonomous carbonate monitoring

into dynamic coastal and reef systems that remain undersampled relative to the open ocean (Bushinsky et al., 2019; Tilbrook et al., 2019). The demonstrated consistency of methodological principles, optimal use of input selection, sensor redundancy, and cross-validation across very different environments throughout this suggests that autonomous observations can provide scientifically sound determinations and evaluations of the marine carbonate system.

### 5.2.1 Limitations

Autonomous deployments with advanced technology inherently involve instrument and platform limitations. LOC analysers require power, reagents, and co-located S, T, P from a CTD for in-situ corrections (Yin et al., 2021; Schaap et al., 2021b). In Chapters 2 and 4 LOC carbonate sensors were connected to CTD/DO data stream, managed by the sensor-hub interface. These design choices enable real-time *insitu* calculations but rely on vehicle compatibility and CTD availability. Moreover, despite strong performance, sensor measurements generally met GOA-ON weather-quality (and not climate-quality) criteria, leaving room for improvement of uncertainty reduction, and continued technological development.

The primary challenge faced by Chapter 2 was working to validate sensor performance by comparing a moving platform dataset to discrete bottle samples that are mismatched in space and time. To enable comparison, discrete results (chosen for their uniform spatial sampling and ”gold standard” determination) of pH, TA, DIC, dissolved oxygen, salinity, and temperature were interpolated in density space using natural neighbour techniques and sampled at ALR measurement coordinates. While methodologically defensible, this step introduces uncertainty that is difficult to quantify, particularly in heterogeneous coastal waters. Additionally, the pH and TA LOC sensors were not temporally synchronized, and because they were on a moving platform this also made them not spatially synchronized. Therefore, gridding (via natural neighbour interpolation) pH, TA, salinity, and temperature collected from the ALR to produce compatible arrays was required for carbonate calculations. Again, while this enabled high-quality derivations, and arguably extended observational coverage in time and space, another source of error was added to the results.

Because Chapters 2 and 2 were both based on ALR operations, several vehicle-induced limitations were shared. The LOC sampling intervals (pH $\approx$ 7.5 min, TA $\approx$ 10 min) made the spatial representation of data sensitive to ALR ascent/ descent rates across vertical biogeochemical gradients. When the ALR moves quickly through the water column, the LOC intake is not sampling consistent water masses, which degrades the quality of measurement and the ability to compare it to coincident discrete samples, and ultimately resulted in omission of data. Additionally, vehicle sampling pattern (e.g., lawn mower, staircase) affect the spatial resolution of sensor

measurements any subsequent interpolation. Categorised as operational errors, rather than analytical or technical, they are an increasing consideration for autonomous vehicle sampling operations. Spatial coverage needs to be ensured without costly redundancy and energy consumption, while obtaining an accurate estimate of the underlying scalar fields of interest (Ho and Saripalli, 2011). Ideally, deployment of the autonomous vehicle with sensors onboard need to adapt to data processing needs and desired outcome from the data. Chapter 2's Deep Sampling Transect followed a strict latitudinal line (Figure 2.4), simplifying analysis, but only sampled a few constant depths across a wide depth range. This can cause inaccurate interpolation, especially in mixed layers. Meanwhile, the diagonal path of the Shelf Sampling Transect (2.3) prevented fitting data to latitude or longitude, so a 'total distance' transect was calculated from GPS coordinates. This creates convoluted analysis if there is overlap during transect, like the one in Chapter 3, because it eliminates the independent variable as a "total distance traveled" and becomes an arbitrary distance along track. Analyses in Chapter 3 did not require spatial interpolation, so this limitation was avoided by focusing on the dataset as a time series.

While using fixed-point observatories can solve some spatial and operational limitations involved with moving platforms, new limitations, such as biofouling, arise. The sensor mooring in Chapter 3 required weekly servicing for reagent management, battery swaps, and anti-bioufouling, which as it stands, would considerably constrain practical deployment duration. A major limitation of Chapter 4 however, was the lack of discrete sampling, especially for TA on the fore reef. Unlike Chapter 4, algorithm-derived TA was not feasible due to the absence of a well-defined region-specific oceanic or freshwater end-member and linear TA-S relationship. Futhuremore, despite having a TA sensor, we could not calculate net community calcification (NCC) rates using the TA-anomaly technique at the reef scale, an approach that requires paired upstream–downstream TA (or reef vs offshore) and flow/transport to convert concentration differences into rates (Eulerian or Lagrangian approaches) typically supported by water current measurements (e.g., ADCP) (Gattuso et al., 1999; Shaw et al., 2014; Pisapia et al., 2019). Reviews and intercomparisons highlight that TA-anomaly NCC estimates depend critically on flow path definition and hydrodynamic residence time; without defined separate TA measurement sites and known seawater flow, community-scale rates cannot be resolved, even when high-frequency TA is available (Cyronak et al., 2018; Gazeau et al., 2015; Cohen et al., 2017). Chapter 4's deployment, (one TA site; no ADCP), chemical variability and stoichiometric inferences (e.g., TA–DIC slopes) were made instead of integrated NCC rates.

### 5.2.2 Future Perspectives

The results presented in this thesis demonstrate that autonomous carbonate system observations can deliver weather-quality measurements across a range of dynamic environments. Building on these advances, future development should focus on improving analytical stability, extending deployment endurance, and continuing to expand autonomous operations. Future recommendations specific to LOC technology and LOC-based deployments suggest lowering reagent and power requirements, synchronizing multi-sensor measurements, and pushing toward climate-quality precision criteria. These developments would better enable long-term climate trend detection in addition to process-scale investigations. Continued efforts to complement ship-based surveys and fixed observatories will remain important for global model improvements, data accessibility, and advancement of multi-platform observing networks.

A particularly pressing application of these technologies is in the emerging need for measurement, reporting, and verification (MRV) to support rapidly-growing marine carbon dioxide removal (mCDR) efforts. Specific methods of mCDR include ocean alkalinity enhancement (OAE), blue carbon enhancement (blueCDR), and off-shore geological carbon storage (mCS) (Yao et al., 2025). Current best-practice frameworks for mCDR emphasize the importance of direct measurements of pH, TA, DIC, and $pCO_2$ to attribute and quantify net carbon removal, with explicit uncertainty budgets (National Academies of Sciences and Medicine, 2022; Ho et al., 2023). The use of LOC TA and pH sensors in this thesis directly address these requirements by reducing propagated error in derived variables and providing high-frequency records of the marine carbonate system. Embedding such sensors into OAE, blueCDR, and mCS pilot studies would allow the effects of alkalinity addition to be tracked against natural variability, providing data that are both scientifically rigorous and verifiable against international standards such as the GOA-ON quality objectives (Tilbrook et al., 2019; Newton et al., 2019). Similarly, autonomous carbonate observations also have potential for the continued monitoring of offshore carbon capture and storage (CCS) projects, like the work by Schaap et al. (2021a), who demonstrated an approach for LOC sensors to detect and quantify a subsea release of $CO_2$ that imitated a leak from a subsea $CO_2$ reservoir. Ultimately, the methodological advances demonstrated in this thesis, including sensor validation, sensor redundancy, and spatiotemporal analysis strategies offer transferable templates for MRV of CCS and OAE efforts alike. These perspectives highlight how autonomous technology is positioned not only to advance scientific understanding of ocean carbon cycling, but also to support the applied monitoring needs for credible climate mitigation.

## 5.3 Hypotheses Revisited

This thesis successfully undertook the main aims of this work (Chapter 1, Section 1.3) to:

- demonstrate emerging autonomous technology capabilities and compare them to traditional methodology when measuring and characterising marine carbon (Chapter 2)
- investigate new developments in autonomous sensor and platform technologies to help fill gaps in shelf seas carbon observations (Chapter 3)
- resolve the controlling metabolic processes and carbonate dynamics of a coral reef in a unique and understudied region from autonomous sensor observations (Chapter 4)

Below the hypotheses defined in Chapter 1 Section 1.3.1 are evaluated:

Chapter 2

- *Autonomous pH and TA observations from sensors on an AUV can be of comparable quality to those collected using traditional methods from a ship.*
  - Sensors achieved weather-quality uncertainty thresholds, and agreed with discrete bottle samples within combined uncertainties. Differences largely reflected spatiotemporal mismatch rather than analytical bias.
- *Challenges in comparing AUV with ship observations in space and time can be adequately resolved using spatial interpolation methods.*
  - Spatial interpolation methods successfully (and numerically) compared AUV transect sensor measurements with ship-based discrete observations, which provided meaningful insights between the two methodologies. However, this approach likely introduced additional error that is difficult to quantify, which highlighted an inherent limitation when comparing and validating moving autonomous platform observations against discrete sampling.
- *High-resolution observations collected using an AUV can reveal environmental features that traditional surveys can overlook.*
  - Sensor measurements from ALR transects captured small-scale gradients and variability across shelf boundaries that were not apparent from coincident CTD discrete sampling alone, highlighting the added value of continuous autonomous observations.

Chapter 3

- *Characterising the carbonate system in shallow coastal waters using autonomy and associated computational methods (as per BGC Argo) can lead to significant errors.*
  - Reliance on model outputs produced systematic offsets relative to direct measurements, with error magnitudes large enough to alter the direction of air-sea $CO_2$ flux estimates.
- *Sensor redundancy can improve data quality by providing a better means for sensor drift correction than traditional computational techniques.*
  - Redundancy between LOC pH and SeaFET pH sensors allowed cross-validations and drift adjustment, which offered a more reliable correction approach (using k0 adjustment) than climatological or neural-network models in a coastal ocean setting– especially supported by the pH sensors agreeing better with one another than with model outputs.
- *Total Alkalinity parameterisation using established regional algorithms can be of adequate quality for carbonate system characterisation when paired with measured pH from autonomous sensors*.
  - TA parameterisations allowed characterisation of the carbonate system, and matrix sensitivity analysis showed TA contributed little to flux variability relative to pH. While adequate for some applications, reliance on modelled TA remains a limitation, especially in regions where not possible.

Chapter 4

- *High resolution pH, TA, $pCO_2$, and DO observations can help disentangle dominant metabolic processes in a reef system*
  - High-frequency pH, TA, and DO resolved distinct diel patterns that distinguished photosynthesis-respiration signals (tight pH-DO covariation, low TA-DIC slope) from calcification-dissolution influences (often weaker pH-DO alignment and higher TA-DIC slope). Autonomous TA, pH, and $pCO_2$ sensors also provided an overdetermined carbonate system characterisation of the reef lagoon (but not fore reef), that allowed internal consistency checks and reduced uncertainty in derived variables. Agreement among independently measured parameters validated both sensor performance and robustness of carbonate system calculations, but most importantly confirmed the observed variable signals and relationships were real.

- *TA and pH sensor measurements will reveal the relative contribution of NCP and NCC to the reef's metabolic signal*
  - TA–DIC slopes (DIC derived from TA and pH sensor measurements) indicated that net community production accounted for ∼87% of lagoon metabolic processes, consistent with prior reef studies. Differences between lagoon and fore-reef signals further demonstrated the value of autonomous TA for resolving metabolic dynamics, since TA was not measured on the fore reef.
- *High-frequency autonomous observations will capture diel and seasonal variability in reef carbonate chemistry that would be otherwise unresolved by traditional sampling approaches.*
  - Multi-month autonomous measurements resolved large diel pH and DO cycles in the lagoon, seasonal shifts across the reef, and site-specific differences that likely would have been missed with discrete sampling alone. However it can not be stated for certain the discrete sampling would have missed it because no discrete sampling took place, a major limitation of this chapter.
- *The relative contributions of NCP and NCC to the reef's metabolic signal will be related to the benthic community composition of the reef.*
  - The lagoon, dominated by turf algae, exhibited strong diel pH-DO covariation consistent with photosynthesis–respiration, while the fore reef (composed of more coral cover and than the lagoon and no algal cover) displayed weaker correlations indicative of stronger influence of calcification-dissolution than the lagoon. Analysis of the TA–DIC relationship further confirmed that net community production dominated lagoon variability, whereas higher calcifier abundance on the fore reef offers an explanation (in the absence of TA observations) for weaker pH-DO correlations.

## 5.4 Closing Statement

The ocean's role in the global carbon cycle is too important to remain under-observed. This thesis has demonstrated how autonomous technologies can transform ocean carbon understanding and observational efforts. These contributions arrive at a moment when climate-critical decisions demand robust, high-resolution, science-backed data from the ocean. The challenge of observing the marine carbonate system is substantial, but so too is the potential for use of cutting-edge autonomous technologies, like the ones presented in this thesis.

# Appendix A

# Supporting Information for Chapter 2

**Emily M. Hammermeister**, Stathys Papadimitriou, Martin Arundell, Jake Ludgate, Allison Schaap, Matthew C. Mowlem, Sara E. Fowell, Edward Chaney, and Socratis Loucaides *Environmental Science & Technology* 2025 59 (14), 7129-7144, https://doi.org/10.1021/acs.est.4c10139

### Summary

This supporting information contains six figures and one table that support Chapter 2: *New capability in autonomous ocean carbon observations using the Autosub Long-Range AUV equipped with novel pH and Total Alkalinity sensors*. The figures provide additional detail on sensor–CTD intercomparison, including concept visualisation (Figure A.1), spatial contour plots (Figures A.2 and A.3), deployment pH–oxygen relationship (Figure A.3), and residual analyses for both the shelf and deep transects(Figures A.5 and A.6). Table A.1 summarizes the uncertainty values applied in CO2SYS error propagation and combined standard uncertainty calculations defined in the main text of Chapter 2.

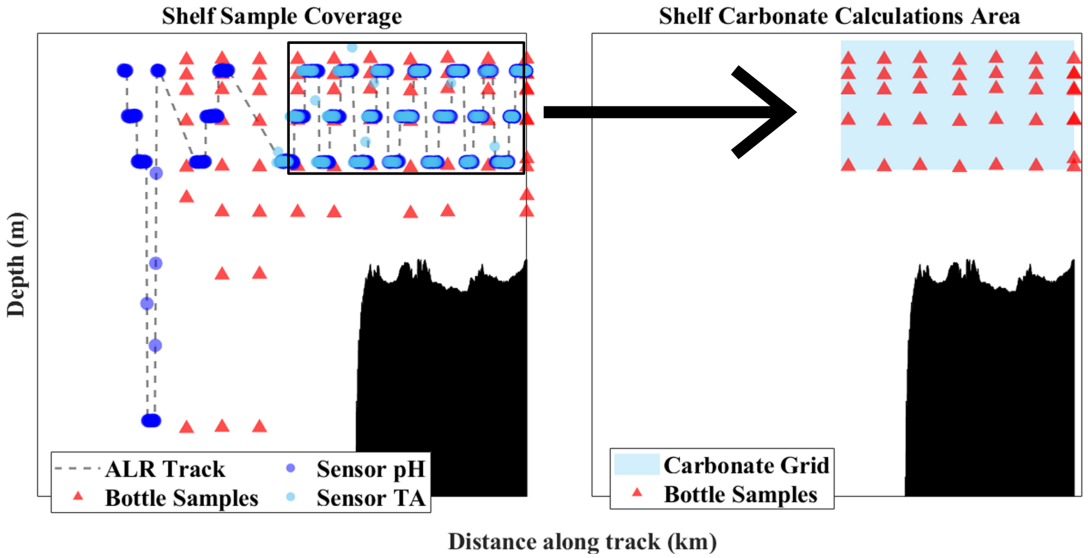


FIGURE A.1: Visual representation of "standardised" grid of $pH_{T\text{-}ALR}$ and $TA_{ALR}$ interpolated data coverage (light blue, right) is used for CO2SYS computation.

TABLE A.1: Uncertainty values for each input parameter used for error propagation calculations using CO2SYS *errors.m* routine and standard combined uncertainty calculations used in Equation 2.3 in Chapter 2. Uncertainties for parameters determined from technology manufacturers specifications as outlined in main text of Chapter 2

| **Input Parameter** | **Sensors onboard ALR** | **Discrete Bottled Samples** |
|---|---|---|
| $u_{TA}$ ($\mu$mol kg$^{-1}$) | 7 | 3 |
| $u_{pH}$ (pH units) | 0.010 | 0.005 |
| $u_{DIC}$ ($\mu$mol kg$^{-1}$) | n/a | 6 |
| $u_{Temperature}$ ($^{\circ}$C) | 0.002 | 0.001 |
| $u_{Salinity}$ | 0.003 | 0.003 |

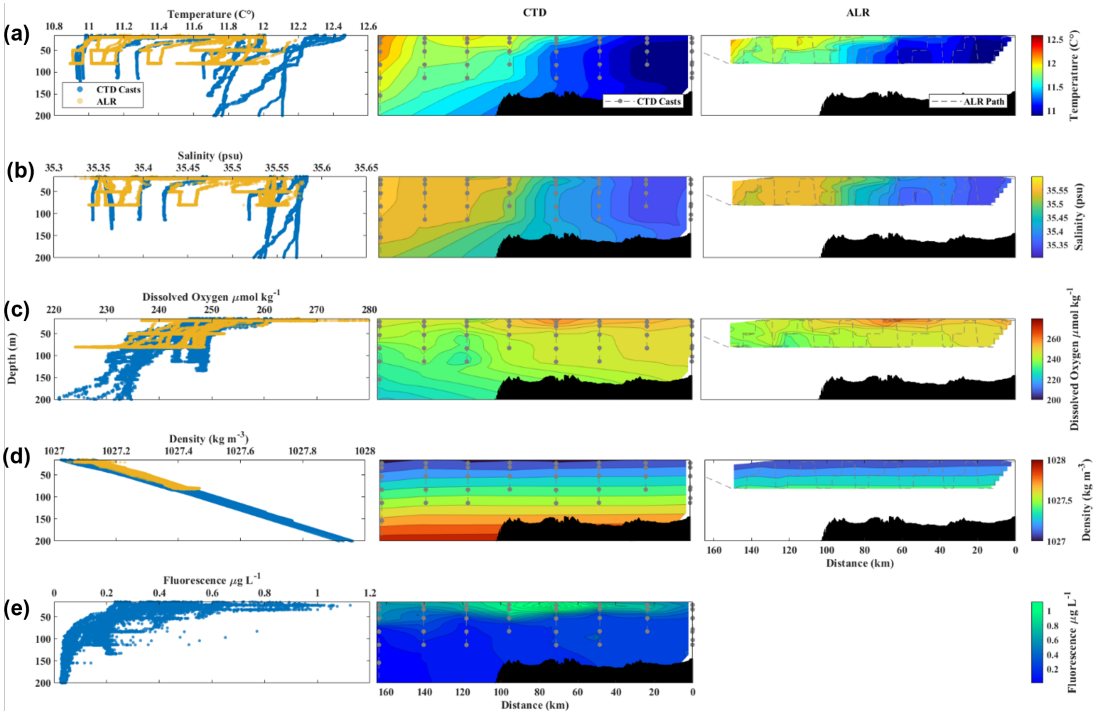


FIGURE A.2: Comparative profiles and spatial contour maps of parameters measured by CTD casts and ALR across the Shelf transect. Each row corresponds to a different parameter: (a) Temperature (°C) profiles with depth. The left panel shows CTD casts (blue) and ALR data (orange). The middle panel shows a contour plot of the CTD data, and the right panel shows a contour plot of the ALR data. Contour lines and their colour are defined by the parameter shown with depth along distance of Shelf Transect. The grey circles in the middle plots indicate CTD bottle locations and while the dashed grey lines in the right plots represent the ALR path. (b) Salinity (PSU) profiles and contours with the same format as in (a). (c) Dissolved oxygen ($\mu$mol kg$^{-1}$) profiles and contours with the same format as in (a). (d) Density (kg m$^{-3}$) profiles with the same format as in (a). (e) Fluorescence ($\mu$g L$^{-1}$) profiles with the same format as in (a). There was no fluorometer onboard the ALR which is why there is no depth profile or contour map in row (e) with ALR data. The ALR contour maps in the third column of rows a-d do not go to the same depth as the CTD contour maps in the second column because the ALR's maximum depth measuring these parameters in the shelf transect was 80 m.

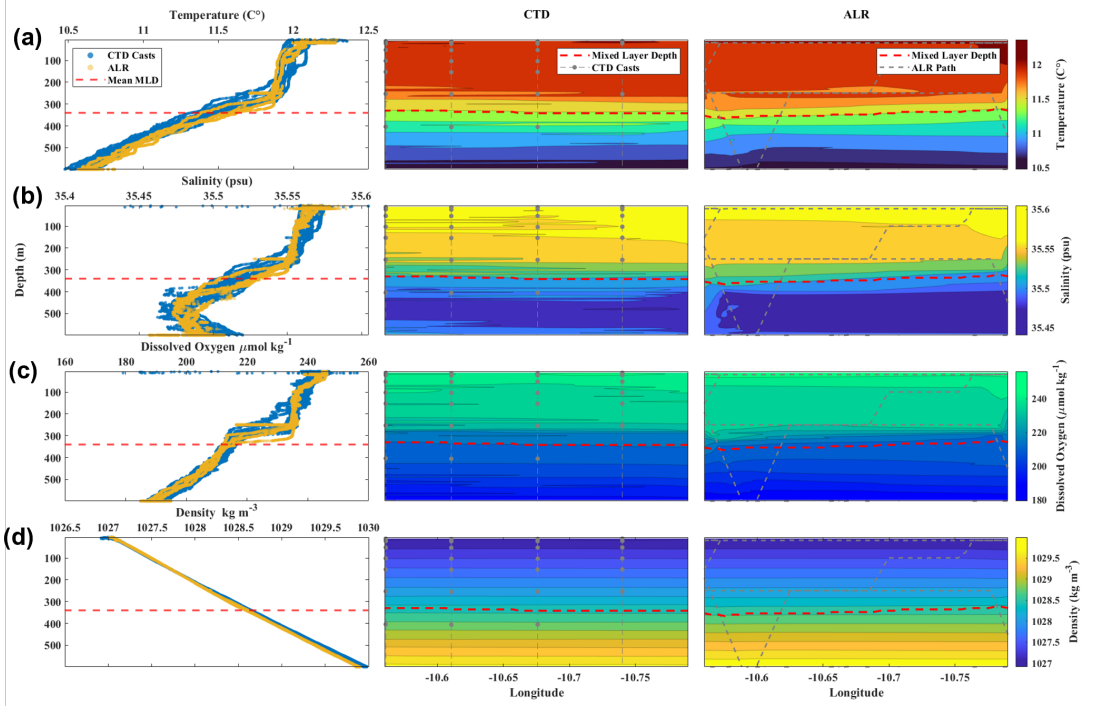


FIGURE A.3: Comparative profiles and spatial contour maps of parameters measured by CTD casts and ALR across the Deep Transect. The depth profiles on the leftmost plots for all rows a-d show CTD casts (blue) and ALR data (orange) of respective parameters plotted against depth. The red dashed line in all subplots represent the mean Mixed Layer Depth (MLD). The grey circles in the middle plots indicate CTD bottle locations and while the dashed grey lines in the right plots represent the ALR path. Contour lines and their colour are defined by the parameter shown with depth along longitude transect. Each row corresponds to a different parameter: (a) Temperature (°C) profiles with depth. The middle panel shows a contour plot of the CTD data, and the right panel shows a contour plot of the ALR data. (b) Salinity (PSU) depth profiles and contour maps with the same format as in (a). (c) Dissolved oxygen ($\mu$mol kg$^{-1}$) depth profiles and contour maps with the same format as in (a). (d) Density (kg m$^{-3}$) depth profiles and contour maps with the same format as in (a).

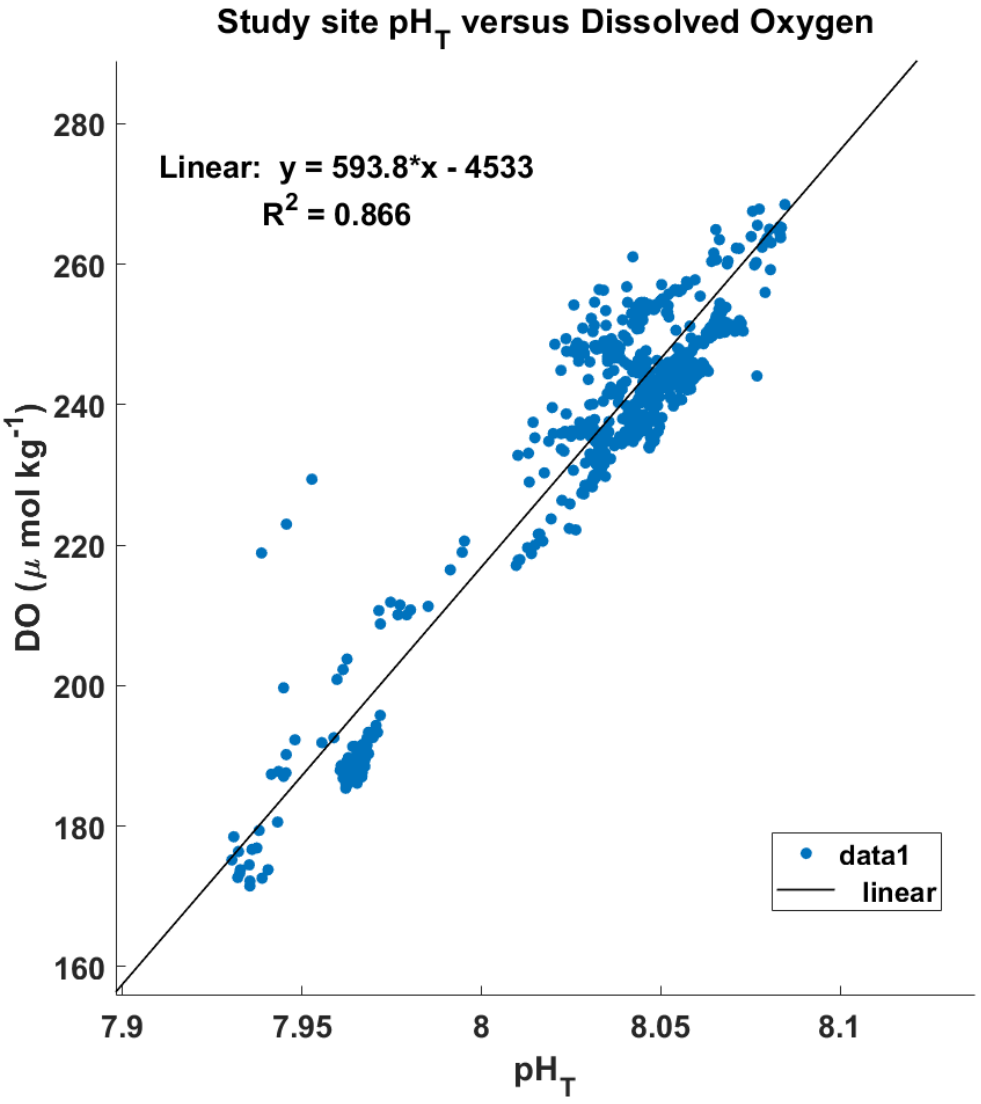


FIGURE A.4: All CTD and ALR from both ST and DT measured data of $pH_T$ (x-axis) plotted against Dissolved Oxygen (DO) (y-axis) to reveal a strong positive linear relationship where ($R^2 = 0.866$, $p < 0.05$, $n = 950$).

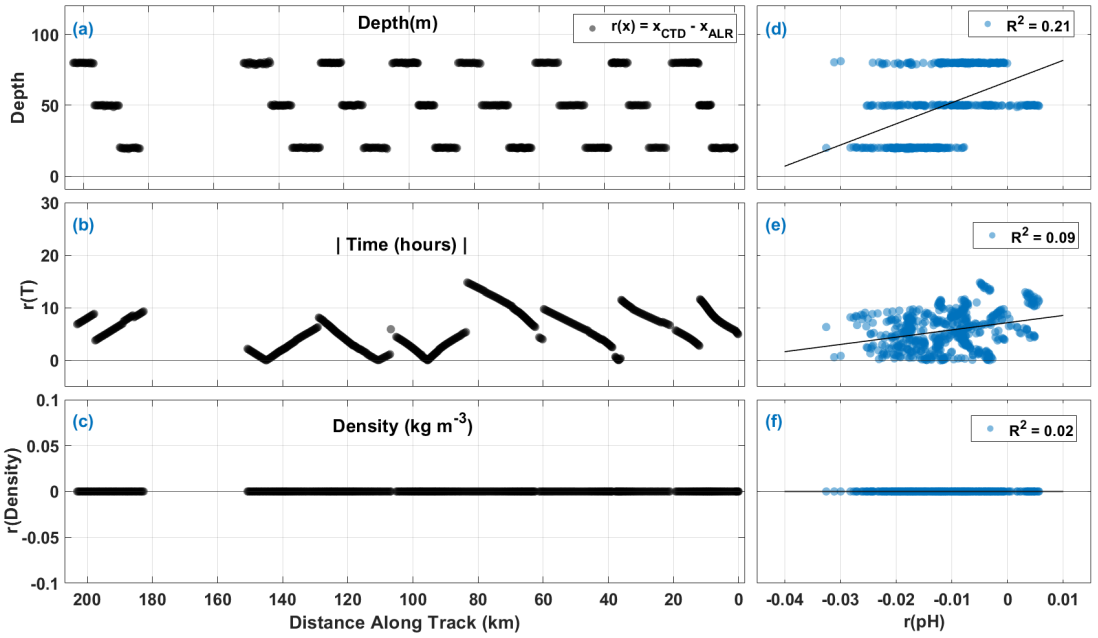


FIGURE A.5: Comparison of depth (a,d), time between CTD and ALR measurements r(Time) (b,e), and density residuals r(Density) (c,f) with respect to transect distance (x-axis in a–c) and $pH_T$ residuals (x-axis in d–f) in the Shelf Transect.

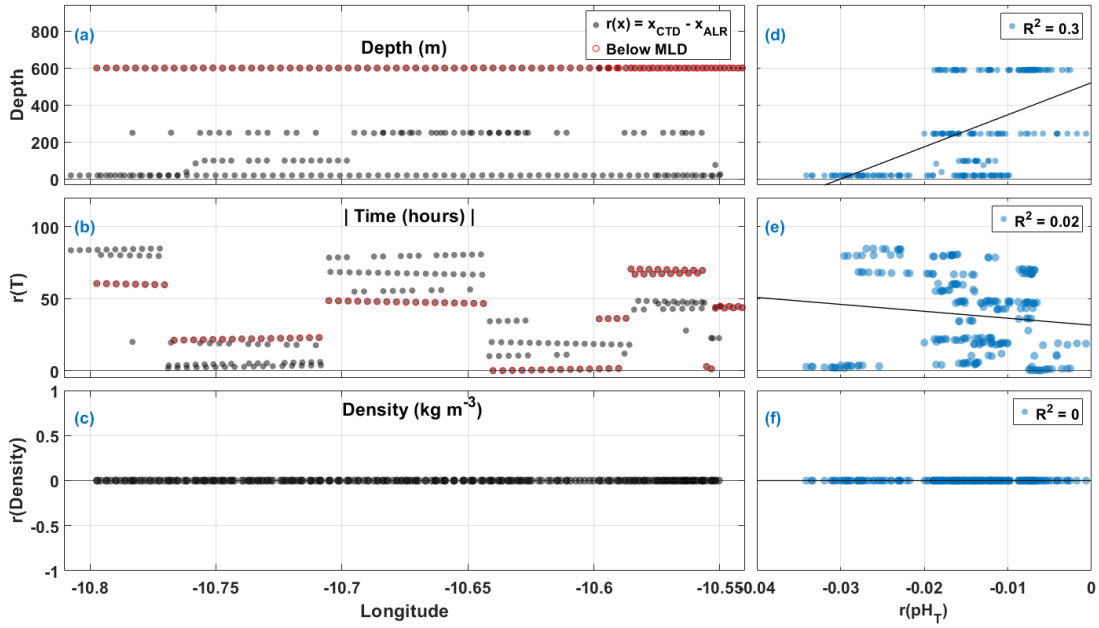


FIGURE A.6: Comparison of depth (a,d), time between CTD and ALR measurements r(Time) (b,e), and density residuals r(Density) (c,f) with respect to longitude (x-axis in a–c) and $pH_T$ residuals (x-axis in d–f) in the Deep Transect. In (a,b) residuals below the MLD (<345 m) are outlined in red.

# Appendix B

# Supporting Information for Chapter 3

Supporting Information for:
**Coastal Marine Carbon and Air-Sea Fluxes Quantified from pH Sensors on an Extended AUV Deployment**

**Emily M. Hammermeister**, Cathy Wimart-Rousseau, Stathys Papadimitriou, Pablo Trucco-Pignata, Edward Chaney, Robert Templeton, Alexander B. Phillips, and Socratis Loucaides

**Contents of this file:**

Text B1 to B2 (containing Equations B.1–B.5)
Table B.1
Figures B.1 to B.6

**Introduction**

This supporting information provides details on the calculations used for pH determination by each sensor, and the calibration coefficients for the SeaFET pH sensor (Table B.1. Figures B.1 and B.2 included in this supporting information show the interpolation of atmospheric carbon dioxide and wind speeds used in the main article. Figures B.3 and B.4 provide further pH comparisons between sensor determinations and model estimates. Figures B.5 and B.6are the calculated values from each matrix analysis performed.

## Text B1. Lab-On-Chip pH Sensor Calculations

The Lab-On-Chip (LOC) pH sensor measures $pH_T$ photometrically (using meta-Cresol Purple (mCP) indicator dye as stated in main text) at the temperature within the optical cell ($t_m$) measured from the internal thermistors within the sensor according to Liu et al. (2010) to get $pH_{T,m}$:

$$pH_{T,m} = -\log(K_2 e_2) + \log\left(\frac{R - e_1}{1 - R\frac{e_3}{e_2}}\right) \tag{B.1}$$

Where

- $K_2$ is the second stochiometric (concentration-based) equilibrium dissociation constant of mCP.
- $e_1$, $e_2$, and $e_3$ are molar extinctions coefficient ratios of mCP.
- $R$ is the conventional ratio of Absorbances ($A_\lambda$) at the absorbance maximum wavelengths ($\lambda$), 434 and 578 nm of the protonated and deprotonated mCP species respectively. Therefore $R = A_{578} \ / \ A_{434}$.

The *in situ* $pH_T$ is then derived from $pH_{T,m}$ using the linear temperature factor from Millero (1995) as follows:

$$in\ situ\ \ pH_T = pH_{T,m} - 0.01582(T - t_m) \tag{B.2}$$

Full details of the LOC pH sensor hardware configuration, calibration, and validation procedures are outlines in Yin et al. (2021).

## Text B2. SeaFET pH Sensor Calculations and Calibration

The $pH_T$ determination protocol for the Deep SeaFet V2 uses the following equations and coefficients as outlined in Sea-Bird Scientific Application Note 99 *Calculating pH from ISFET pH Sensors* (Sea-Bird Scientific, 2024).

$$pH_{CELL} = \frac{V_{REF} - k_0 - k_2 \times t - f(P)}{S_{nernst}} + \log\left(Cl_T\right) + 2 \times \log\left(\gamma_{\pm\ HCl}\right)_{T\&P} - \log\left(1 + \frac{S_T}{K_{S,\ T\&P}}\right) - \log\left(\frac{1000 - (1.005 \times S)}{1000}\right) \tag{B.3}$$

Where:

$$S_{nernst} = \frac{R \times T \times \ln(10)}{F} \tag{B.4}$$

Where:

- R is the universal gas constant (8.3144621 J/Kmol)
- t is the temperature in °C
- T is the temperature in K
- S is the Salinity in psu
- P is the pressure in dbar
- F is the Faraday constant (96485.365 C/mol)
- The constants $k_0$ and $k_2$ are the cell standard potential offset and temperature slope respectively
- $f$(P) is the sensor pressure response function (6th order polynomial):

$$f(P) = f_1 P + f_2 P^2 + f_3 P^3 + f_4 P^4 + f_5 P^5 + f_6 P^6 \tag{B.5}$$

$k_0$, $k_2$ *f1, f2, f3, f4, f5, f6* are the calibration coefficients of the SeaFET pH sensor. The coefficients used in the LDPT deployment can be found in Table B.1.
The remaining variables required to determine $pH_T$ from the above equations are defined as follows:

- Total chloride in seawater ($Cl_T$) from Dickson et al. (2007).
- Partial Molal Volume of $HCl$ $\left(\overline{V}_{HCl}\right)$ from Millero (1983).
- Sample Ionic Strength ($I$) from Dickson et al. (2007).
- Debye-Huckel constant for activity of $HCl$ $\left(A_{DH}\right)$ from Khoo et al. (1977).
- Logarithm of $HCl$ activity coefficient as a function of temperature and pressure $\left(\log\left(\gamma_{HCl}\right)_{T\&P}\right)$ from s. Johnson et al. (2023).
- Total sulfate in seawater $\left(S_T\right)$ from Dickson et al. (2007)
- Acid dissociation constant of $HSO_4^-$ $\left(K_S\right)$ from Dickson et al. (2007)
- Partial Molal Volume of $HSO_4^-$ $\left(\overline{V}_S\right)$ from Millero (1983)
- Compressibility of $HSO_4^-$ $\left(\overline{K}_S\right)$ from Millero (1983)
- Acid dissociation content of $HSO_4^-$ $\left(K_{S,\,T\&P}\right)$ fromMillero (1982)

## Supporting Information Table

TABLE B.1: Calibration coefficients for SeaFET (s/n 0000100) used on the Long-Distance Proving Trial deployment.

| Coefficient | Value |
|---|---|
| $f1$ | 1.626200e-5 |
| $f2$ | -9.490701e-9 |
| $f3$ | -1.092300e-11 |
| $f4$ | 1.814700e-14 |
| $f5$ | -8.782701e-18 |
| $f6$ | 1.44900e-21 |
| $k0$ | -1.424676 |
| $k2$ | -1.124320e-3 |

# Supporting Information Figures

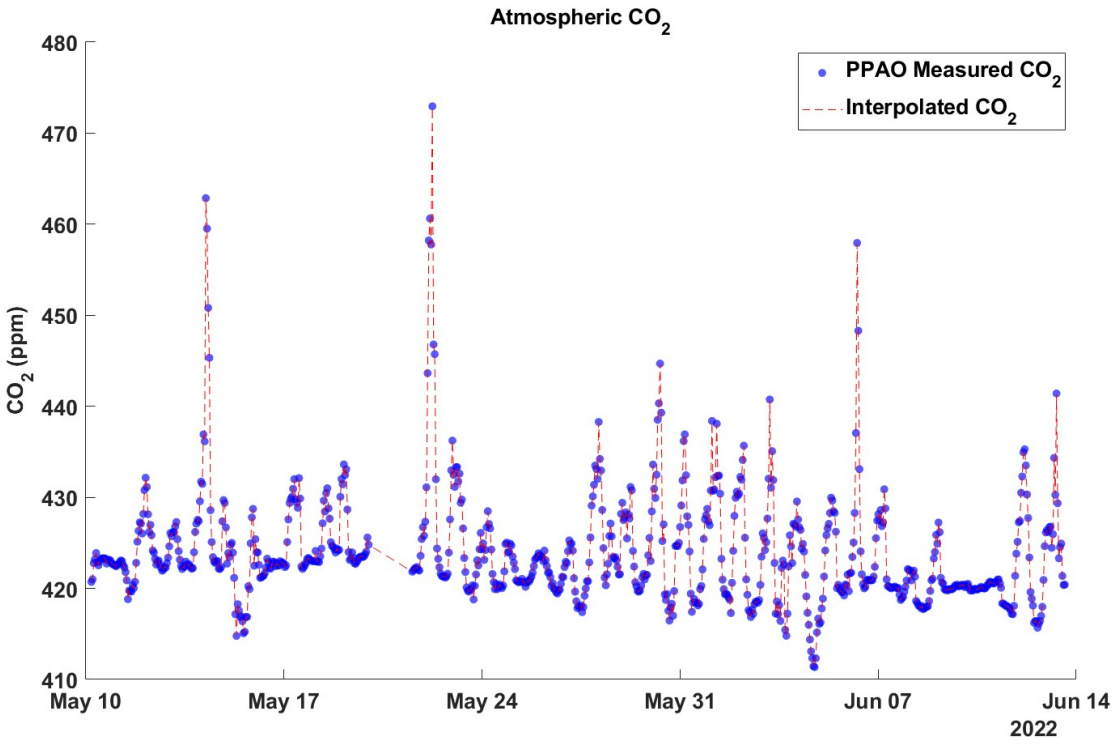


FIGURE B.1: Time series of atmospheric $CO_2$ interpolation.

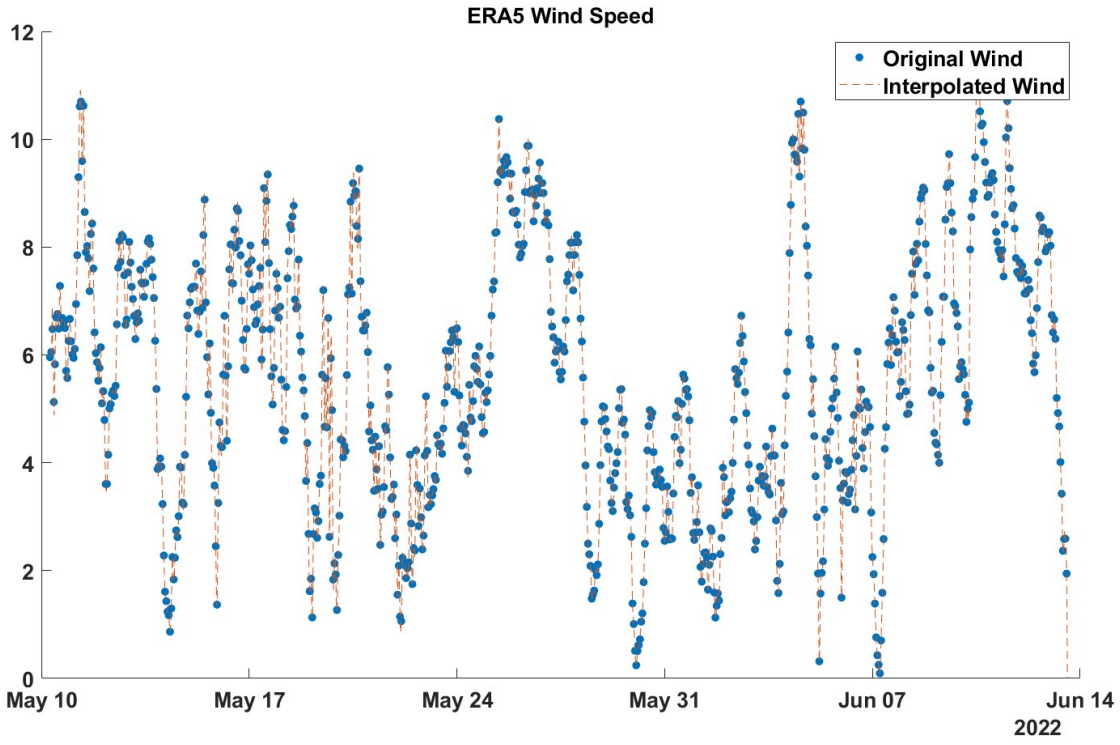


FIGURE B.2: Time series of wind speed interpolation.

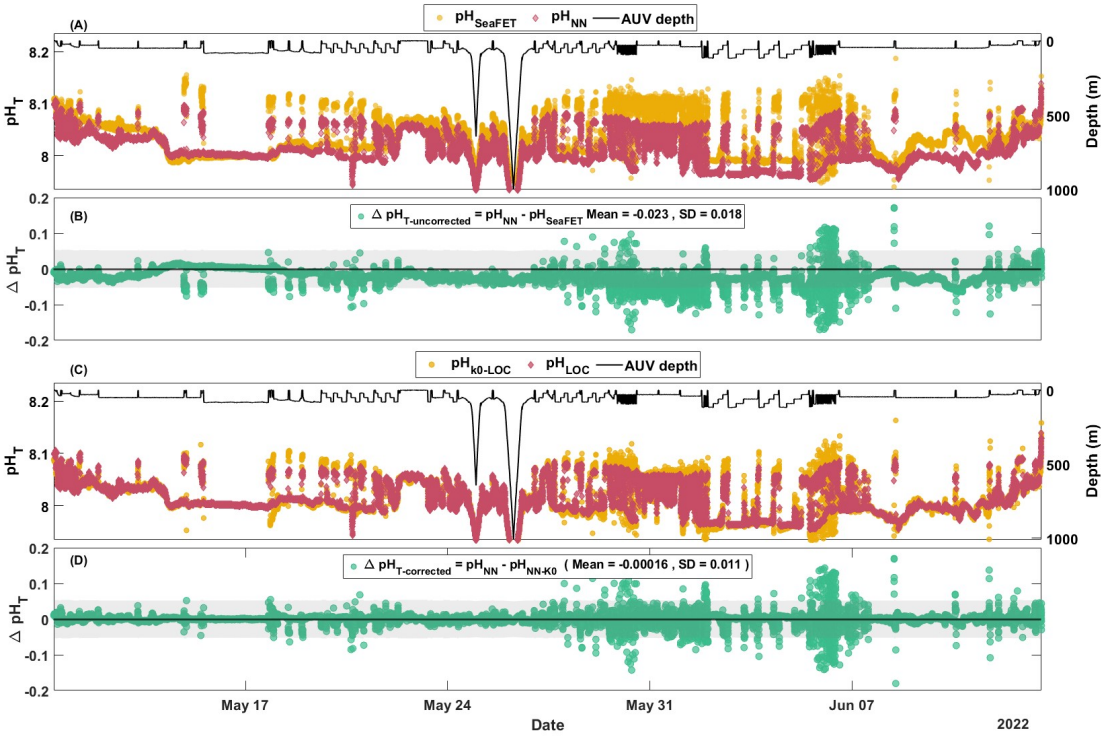


FIGURE B.3: Time series comparison of $pH_T$ measurements and offsets between SeaFET pH sensor and ESPER-NN pH estimates before and after k0 correction. (A) In situ uncorrected $pH_T$ data from the SeaFET sensor (yellow) and $pH_{NN}$ estimates (red diamonds) shown alongside transiting depth of the ALR (black line). (B) Uncorrected pH difference ($\Delta\, pH_{T-uncorrected} = pH_{NN} - pH_{SeaFET}$), with a mean offset of -0.023 and standard deviation of 0.018. (C) SeaFET sensor $pH_T$ corrected to ESPER-NN pH estimates using k0 adjustment (yellow), and same original $pH_{NN}$ routine estimates (red diamonds). (D) Resulting corrected offset ($\Delta\, pH_{T-uncorrected} = pH_{NN} - pH_{k0-NN}$), with mean offset of -0.00016 and standard deviation of 0.011. Shaded gray regions in (B) and (D) span $\pm$ 0.052 pH units (on average), representing combined uncertainty between the SeaFET pH sensor and the NN estimates

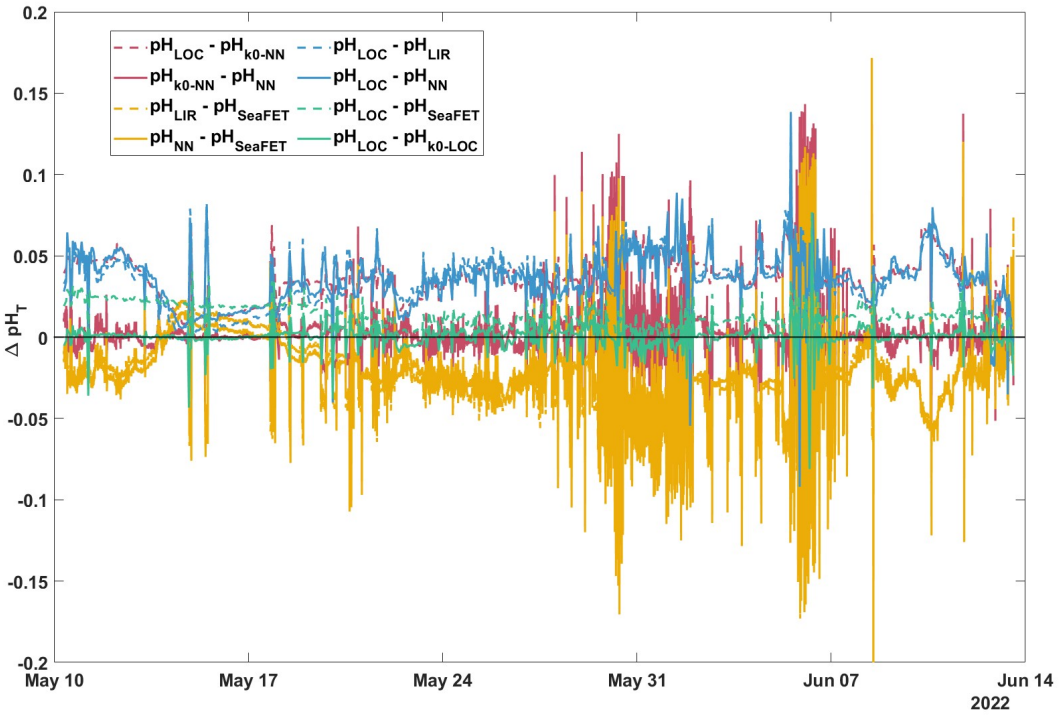


FIGURE B.4: Time series comparison of pH difference ($\Delta pH_T$, y-axis) between different pH sensor measurements and estimation methods from May 10 to June 14, 2022. $\Delta pH_T$ is calculated as pairwise differences between pH inputs, including: (1) SeaFET sensor pH ($ppH_{SeaFET}$), (2) LOC sensor pH ($pH_{LOC}$), (3) Seafet sensor pH corrected to LOC using the k0 adjustment ($pH_{k0–LOC}$), (4)/(5) ESPER routine pH estimates using a neural network ($pH_{NN}$) and linear regression ($pH_{LIR}$), and (5) SeaFET sensor pH corrected to $pH_{NN}$ using the k0 adjustment ($pH_{k0–nn}$). Each color represents a different comparison combination, as described in the legend. The black horizontal line is where $\Delta pH_T$ = 0, representing a perfect agreement between comparison combinations. The figure highlights the temporal variability and performance differences (noise) among sensor measurements, correction approaches, and reference methods

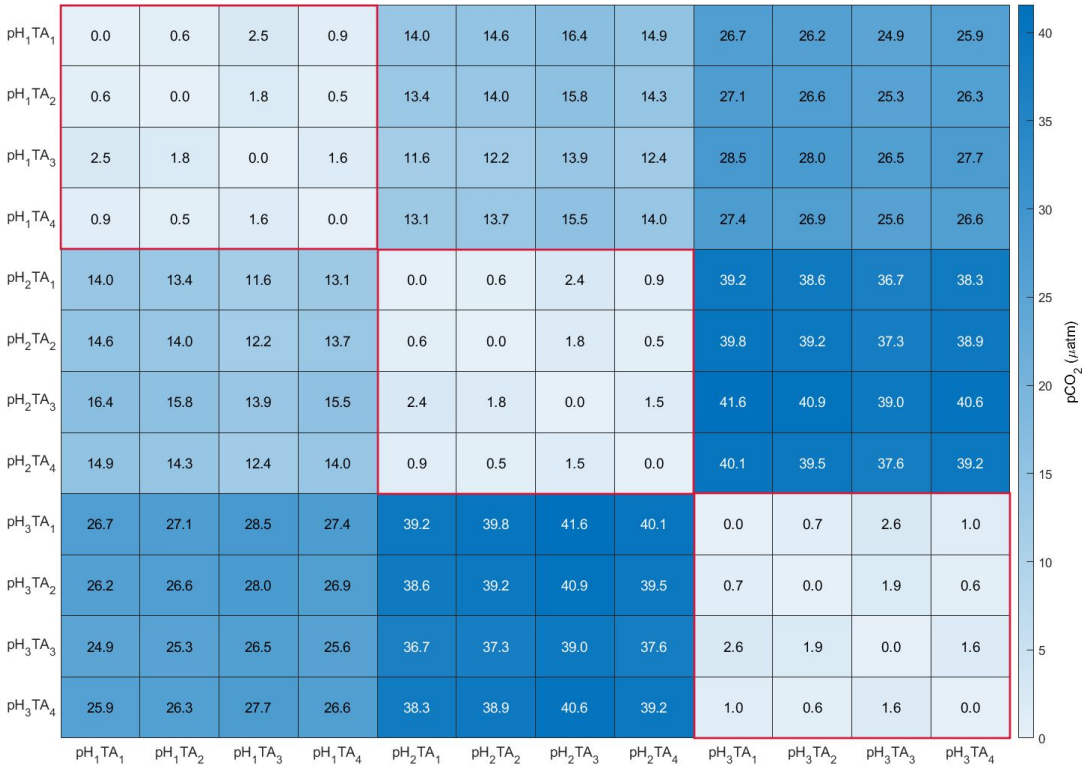


FIGURE B.5: Matrix analysis of mean $pCO_2$ differences between each set of input pairs ($pH_{1–3}$ and $TA_{1–4}$, defined in Table 3.2 of Chapter 3 main text). Color of each cell indicates the magnitude of each difference (ranging 0–42 $\mu$atm

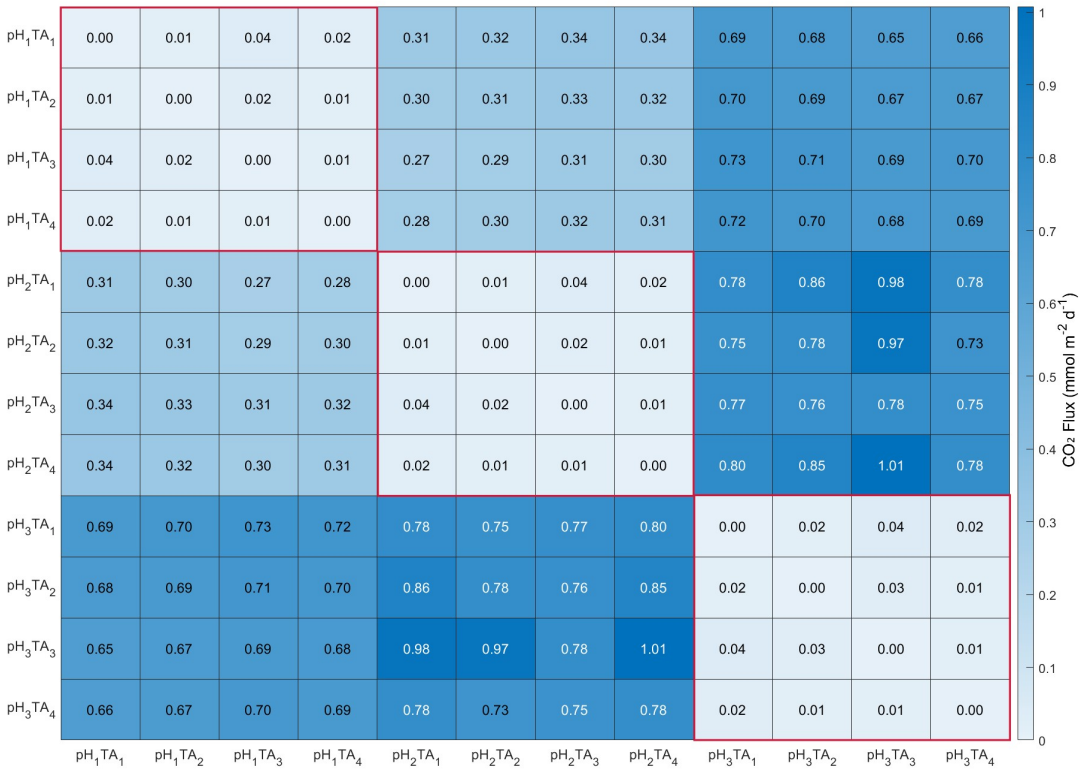


FIGURE B.6: Matrix analysis of $CO_2$ flux median differences between each set of input pairs ($pH_{1–3}$ and $TA_{1–4}$, defined in Table 3.2 of Chapter 3 main text). The color of each cell indicates the magnitude of each difference (ranging 0–1.1 mmol $m^{-2}$ $d^{-1}$

# Data Availability

*All data collected for this thesis is freely available online:*

**Emily M. Hammermeister**, Stathys Papadimitriou, Martin Arundell, Jake Ludgate, Allison Schaap, Matthew C. Mowlem, Sara E. Fowell, Edward Chaney, and Socratis Loucaides. New capability in autonomous ocean carbon observations using the autosub long-range auv equipped with novel ph and total alkalinity sensors. - March 2023. University of Southampton Data Repository doi:10.5258/SOTON/D3436 [Dataset] http://eprints.soton.ac.uk/id/eprint/499565

**Emily M. Hammermeister**, Cathy Wimart-Rousseau, Stathys Papadimitriou, Pablo Trucco-Pignata, Edward Chaney, Robert Templeton, Alexander B. Phillips, and Socratis Loucaides. Coastal Marine Carbon and Air-Sea Fluxes Quantified from pH Sensors on an Extended AUV Deployment. - March 2023 University of Southampton Data Repository doi: 10.5258/SOTON/D3716 [Dataset] https://eprints.soton.ac.uk/508509/

**Emily M. Hammermeister**, Sarah E. Cryer, Vincent Saderne, Chiara Pisapia, Stathys Papadimitriou, Sara E. Fowell, Jake Ludgate, Allison Schaap Socratis Loucaides and Maggie D. Johnson. Metabolic Dynamics of an Offshore Coral Reef in the Red Sea: Observations from Autonomous Sensors. University of Southampton Data Repository doi: 10.5258/SOTON/D3691 [Dataset] https://eprints.soton.ac.uk/508508/

# References

Isaac Amidror. Scattered data interpolation methods for electronic imaging systems: a survey. Journal of Electronic Imaging, 11:157–176, 4 2002. . URL https://doi.org/10.1117/1.1455013.

Laurence A Anderson. On the hydrogen and oxygen content of marine phytoplankton. Deep Sea Research Part I: Oceanographic Research Papers, 42: 1675–1680, 1995. ISSN 0967-0637. . URL https://www.sciencedirect.com/science/article/pii/096706379500072E.

Andreas J. Andersson and Dwight Gledhill. Ocean acidification and coral reefs: Effects on breakdown, dissolution, and net ecosystem calcification. Annual Review of Marine Science, 5:321–348, 1 2013. ISSN 19411405. . URL https://www.annualreviews.org/content/journals/10.1146/annurev-marine-121211-172241.

A. T. Archibald, B. Sinha, M. R. Russo, E. Matthews, F. A. Squires, N. L. Abraham, S. J.-B. Bauguitte, T. J. Bannan, T. G. Bell, D. Berry, L. J. Carpenter, H. Coe, A. Coward, P. Edwards, D. Feltham, D. Heard, J. Hopkins, J. Keeble, E. C. Kent, B. A. King, I. R. Lawrence, J. Lee, C. R. Macintosh, A. Megann, B. I. Moat, K. Read, C. Reed, M. J. Roberts, R. Schiemann, D. Schroeder, T. J. Smyth, L. Temple, N. Thamban, L. Whalley, S. Williams, H. Wu, and M. Yang. Data supporting the north atlantic climate system integrated study (ACSIS) programme, including atmospheric composition; oceanographic and sea-ice observations (2016–2022); and output from ocean, atmosphere, land, and sea-ice models (1950–2050). Earth System Science Data, 17(1):135–164, 2025. . URL https://essd.copernicus.org/articles/17/135/2025/.

P.A. Arias, N. Bellouin, E. Coppola, R.G. Jones, G. Krinner, J. Marotzke, V. Naik, M.D. Palmer, G.-K. Plattner, J. Rogelj, M. Rojas, J. Sillmann, T. Storelvmo, P.W. Thorne, B. Trewin, K. Achuta Rao, B. Adhikary, R.P. Allan, K. Armour, G. Bala, R. Barimalala, S. Berger, J.G. Canadell, C. Cassou, A. Cherchi, W. Collins, W.D. Collins, S.L. Connors, S. Corti, F. Cruz, F.J. Dentener, C. Dereczynski, A. Di Luca, A. Diongue Niang, F.J. Doblas-Reyes, A. Dosio, H. Douville, F. Engelbrecht, V. Eyring, E. Fischer, P. Forster, B. Fox-Kemper, J.S. Fuglestvedt, J.C. Fyfe, N.P.

Gillett, L. Goldfarb, I. Gorodetskaya, J.M. Gutierrez, R. Hamdi, E. Hawkins, H.T. Hewitt, P. Hope, A.S. Islam, C. Jones, D.S. Kaufman, R.E. Kopp, Y. Kosaka, J. Kossin, S. Krakovska, J.-Y. Lee, J. Li, T. Mauritsen, T.K. Maycock, M. Meinshausen, S.-K. Min, P.M.S. Monteiro, T. Ngo-Duc, F. Otto, I. Pinto, A. Pirani, K. Raghavan, R. Ranasinghe, A.C. Ruane, L. Ruiz, J.-B. Sallée, B.H. Samset, S. Sathyendranath, S.I. Seneviratne, A.A. Sörensson, S. Szopa, I. Takayabu, A.-M. Tréguier, B. van den Hurk, R. Vautard, K. von Schuckmann, S. Zaehle, X. Zhang, and K. Zickfeld. Technical Summary, page 33144. Cambridge University Press, Cambridge, United Kingdom and New York, NY, USA, 2021. .

Dorothee C E Bakker, Benjamin Pfeil, Camilla S Landa, Nicolas Metzl, Kevin M O'brien, Are Olsen, Karl Smith, Cathy Cosca, Sumiko Harasawa, Stephen D Jones, Shin-Ichiro Nakaoka, Yukihiro Nojiri, Ute Schuster, Tobias Steinhoff, Colm Sweeney, Taro Takahashi, Bronte Tilbrook, Chisato Wada, Rik Wanninkhof, Simone R Alin, Carlos F Balestrini, Leticia Barbero, Nicholas R Bates, Alejandro A Bianchi, Frédéric Bonou, Jacqueline Boutin, Yann Bozec, Eugene F Burger, Wei-Jun Cai, Robert D Castle, Liqi Chen, Melissa Chierici, Kim Currie, Wiley Evans, Charles Featherstone, Richard A Feely, Agneta Fransson, Catherine Goyet, Naomi Greenwood, Luke Gregor, Steven Hankin, Nick J Hardman-Mountford, Jérôme Harlay, Judith Hauck, Mario Hoppema, Matthew P Humphreys, Christopher W Hunt, Betty Huss, J Severino, P Ibánhez, Truls Johannessen, Ralph Keeling, Vassilis Kitidis, Arne Körtzinger, Alex Kozyr, Evangelia Krasakopoulou, Akira Kuwata, Peter Landschützer, Siv K Lauvset, Nathalie Lefèvre, Claire Lo Monaco, Ansley Manke, Jeremy T Mathis, Liliane Merlivat, Frank J Millero, Pedro M S Monteiro, David R Munro, Akihiko Murata, Timothy Newberger, Abdirahman M Omar, Tsuneo Ono, Kristina Paterson, David Pearce, Denis Pierrot, Lisa L Robbins, Shu Saito, Joe Salisbury, Reiner Schlitzer, Bernd Schneider, Roland Schweitzer, Rainer Sieger, Ingunn Skjelvan, Kevin F Sullivan, Stewart C Sutherland, Adrienne J Sutton, Kazuaki Tadokoro, Maciej Telszewski, Matthias Tuma, Steven M A C Van Heuven, Doug Vandemark, Brian Ward, Andrew J Watson, and Suqing Xu. A multi-decade record of high-quality fCO 2 data in version 3 of the Surface Ocean CO 2 Atlas (SOCAT). Earth Syst. Sci. Data, 8:383–413, 2016. . URL www.earth-syst-sci-data.net/8/383/2016/.

Stephen Barker and Andy Ridgwell. Ocean acidifcation. Nature Education Knowledge, 3, 2012.

Alan Barton, Burke Hales, George G. Waldbusser, Chris Langdon, and Richard A. Feelyd. The pacific oyster, crassostrea gigas, shows negative correlation to naturally elevated carbon dioxide levels: Implications for near-term ocean acidification effects. Limnology and Oceanography, 57:698–710, 5 2012. ISSN 1939-5590. . URL https://onlinelibrary.wiley.com/doi/full/10.4319/lo.2012.57.3.0698https:

//onlinelibrary.wiley.com/doi/abs/10.4319/lo.2012.57.3.0698https://aslopubs.onlinelibrary.wiley.com/doi/10.4319/lo.2012.57.3.0698.

R. G. Bates. ph measurements in the marine environment. Pure and Applied Chemistry, 54(1):229–232, 1982. . URL https://doi.org/10.1351/pac198254010229.

Alexander D. Beaton, Jemma L. Wadham, Jon Hawkings, Elizabeth A. Bagshaw, Guillaume Lamarche-Gagnon, Matthew C. Mowlem, and Martyn Tranter. High-resolution in situ measurement of nitrate in runoff from the greenland ice sheet. Environmental Science and Technology, 51:12518–12527, 11 2017. ISSN 15205851. . URL https://pubs.acs.org/doi/abs/10.1021/acs.est.7b03121.

Alexander D. Beaton, Allison M. Schaap, Robin Pascal, Rudolf Hanz, Urska Martincic, Christopher L. Cardwell, Andrew Morris, Geraldine Clinton-Bailey, Kevin Saw, Susan E. Hartman, and Matthew C. Mowlem. Lab-on-chip for in situ analysis of nutrients in the deep sea. ACS Sensors, 7:89–98, 1 2022. ISSN 23793694. . URL /doi/pdf/10.1021/acssensors.1c01685?ref=article_openPDF.

Susan Becker, Michio Aoyama, E. Malcolm S. Woodward, Karel Bakker, Stephen Coverly, Claire Mahaffey, and Toste Tanhua. Go-ship repeat hydrography nutrient manual: The precise and accurate determination of dissolved inorganic nutrients in seawater, using continuous flow analysis methods. Frontiers in Marine Science, 7, 2020. ISSN 2296-7745. . URL https://www.frontiersin.org/journals/marine-science/articles/10.3389/fmars.2020.581790.

J. G. Bellingham. Platforms: Autonomous underwater vehicles, pages 159–169. Elsevier, 1 2009. ISBN 9780128130810. .

D R Bellwood, T P Hughes, C Folke, and M Nyström. Confronting the coral reef crisis. Nature, 429:827–833, 2004. ISSN 1476-4687. . URL https://doi.org/10.1038/nature02691.

W. M. Berelson, W. M. Balch, R. Najjar, R. A. Feely, C. Sabine, and K. Lee. Relating estimates of caco3 production, export, and dissolution in the water column to measurements of caco3 rain into sediment traps and dissolution on the sea floor: A revised global carbonate budget. Global Biogeochemical Cycles, 21:1024, 3 2007. ISSN 1944-9224. . URL /doi/pdf/10.1029/2006GB002803https://onlinelibrary.wiley.com/doi/abs/10.1029/2006GB002803https://agupubs.onlinelibrary.wiley.com/doi/10.1029/2006GB002803.

A.J. Birchill, G. Clinton-Bailey, R. Hanz, E. Mawji, T. Cariou, C. White, S.J. Ussher, P.J. Worsfold, E.P. Achterberg, and M. Mowlem. Realistic measurement uncertainties for marine macronutrient measurements conducted using gas segmented flow and lab-on-chip techniques. Talanta, 200:228–235, 2019. ISSN 0039-9140. . URL https://www.sciencedirect.com/science/article/pii/S0039914019302747.

Henry C Bittig, Arne Körtzinger, Craig Neill, Eikbert van Ooijen, Joshua N Plant, Johannes Hahn, Kenneth S Johnson, Bo Yang, and Steven R Emerson. Oxygen optode sensors: Principle, characterization, calibration, and application in the ocean. Frontiers in Marine Science, Volume 4 - 2017, 2018. ISSN 2296-7745. URL https://www.frontiersin.org/journals/marine-science/articles/10.3389/fmars.2017.00429.

Paul Blanchon. Geomorphic Zonation, pages 469–486. Springer Netherlands, 2011. ISBN 978-90-481-2639-2. . URL https://doi.org/10.1007/978-90-481-2639-2_33.

A V Borges, B Delille, and M Frankignoulle. Budgeting sinks and sources of co2 in the coastal ocean: Diversity of ecosystems counts. Geophysical Research Letters, 32, 7 2005. ISSN 0094-8276. . URL https://doi.org/10.1029/2005GL023053.

Alberto Vieira Borges and Michel Frankignoulle. Distribution of surface carbon dioxide and air-sea exchange in the english channel and adjacent areas. Journal of Geophysical Research: Oceans, 108:3140, 5 2003. ISSN 2156-2202. . URL https://onlinelibrary.wiley.com/doi/full/10.1029/2000JC000571https://onlinelibrary.wiley.com/doi/abs/10.1029/2000JC000571https://agupubs.onlinelibrary.wiley.com/doi/10.1029/2000JC000571.

Jabe A. Breland and Robert H. Byrne. Spectrophotometric procedures for determination of sea water alkalinity using bromocresol green. Deep Sea Research Part I: Oceanographic Research Papers, 40(3):629–641, 1993. ISSN 0967-0637. . URL https://www.sciencedirect.com/science/article/pii/096706379390149W.

Philip J. Bresnahan, Todd R. Martz, Yuichiro Takeshita, Kenneth S. Johnson, and Makaila LaShomb. Best practices for autonomous measurement of seawater ph with the honeywell durafet. Methods in Oceanography, 9:44–60, 4 2014. ISSN 22111220. .

Andrew W Bruckner. Life-saving products from coral reefs. Issues in Science and Technology, 18:39–44, 2002. ISSN 0748-5492.

Seth M. Bushinsky, Yuichiro Takeshita, and Nancy L. Williams. Observing changes in ocean carbonate chemistry: Our autonomous future, 2019. ISSN 21986061.

Robert Byrne. Sensors and systems for in situ observations of marine carbon dioxide system variables. 5 2010. .

Robert H. Byrne. Inorganic speciation of dissolved elements in seawater: the influence of ph on concentration ratios. Geochemical Transactions, 3:11, 12 2002. ISSN 1467-4866. . URL /pmc/articles/PMC1475612//pmc/articles/PMC1475612/?report=abstracthttps://www.ncbi.nlm.nih.gov/pmc/articles/PMC1475612/.

Robert H. Byrne. Measuring ocean acidification: New technology for a new era of ocean chemistry. Environmental Science and Technology, 48:5352–5360, 2014. ISSN 15205851. .

Wei Jun Cai. Estuarine and coastal ocean carbon paradox: Co 2 sinks or sites of terrestrial carbon incineration? Annual Review of Marine Science, 3:123–145, 1 2011. ISSN 19411405. . URL https://www.annualreviews.org/content/journals/10.1146/annurev-marine-120709-142723.

Wei-Jun Cai, Xinping Hu, Wei-Jen Huang, Li-Qing Jiang, Yongchen Wang, Tsung-Hung Peng, and Xin Zhang. Alkalinity distribution in the western north atlantic ocean margins. Journal of Geophysical Research: Oceans, 115, 8 2010. ISSN 0148-0227. . URL https://doi.org/10.1029/2009JC005482.

Ken Caldeira and Michael E Wickett. Anthropogenic carbon and ocean ph. Nature, 425:365, 2003. ISSN 1476-4687. . URL https://doi.org/10.1038/425365a.

Mitchell Call, Kai G. Schulz, Matheus C. Carvalho, Isaac R. Santos, and Damien T. Maher. Technical note: Coupling infrared gas analysis and cavity ring down spectroscopy for autonomous, high-temporal-resolution measurements of dic and amp;lt;iamp;gt;amp;lt;/iamp;gt;amp;lt;supamp;gt;13amp;lt;/supamp;gt;c–dic. Biogeosciences, 14:1305–1313, 3 2017. ISSN 1726-4189. . URL https://bg.copernicus.org/articles/14/1305/2017/.

Katherine Calvin, Dipak Dasgupta, Gerhard Krinner, Aditi Mukherji, Peter W Thorne, Christopher Trisos, José Romero, Paulina Aldunce, Ko Barrett, Gabriel Blanco, William W L Cheung, Sarah Connors, Fatima Denton, Aïda Diongue-Niang, David Dodman, Matthias Garschagen, Oliver Geden, Bronwyn Hayward, Christopher Jones, Frank Jotzo, Thelma Krug, Rodel Lasco, Yune-Yi Lee, Valérie Masson-Delmotte, Malte Meinshausen, Katja Mintenbeck, Abdalah Mokssit, Friederike E L Otto, Minal Pathak, Anna Pirani, Elvira Poloczanska, Hans-Otto Pörtner, Aromar Revi, Debra C Roberts, Joyashree Roy, Alex C Ruane, Jim Skea, Priyadarshi R Shukla, Raphael Slade, Aimée Slangen, Youba Sokona, Anna A Sörensson, Melinda Tignor, Detlef Van Vuuren, Yi-Ming Wei, Harald Winkler, Panmao Zhai, Zinta Zommers, Jean-Charles Hourcade, Francis X Johnson, Shonali Pachauri, Nicholas P Simpson, Chandni Singh, Adelle Thomas, Edmond Totin, Andrés Alegría, Kyle Armour, Birgit Bednar-Friedl, Kornelis Blok, Guéladio Cissé, Frank Dentener, Siri Eriksen, Erich Fischer, Gregory Garner, Céline Guivarch, Marjolijn Haasnoot, Gerrit Hansen, Mathias Hauser, Ed Hawkins, Tim Hermans, Robert Kopp, Noëmie Leprince-Ringuet, Jared Lewis, Debora Ley, Chloé Ludden, Leila Niamir, Zebedee Nicholls, Shreya Some, Sophie Szopa, Blair Trewin, Kaj-Ivar Van Der Wijst, Gundula Winter, Maximilian Witting, Arlene Birt, and Meeyoung Ha. Ipcc, 2023: Climate change 2023: Synthesis report. contribution of working groups i, ii and iii to the sixth assessment report of the intergovernmental panel on

climate change [core writing team, h. lee and j. romero (eds.)]. ipcc, geneva, switzerland., 2023. URL https://www.ipcc.ch/report/ar6/syr/.

Camila D.M. Campos and José A.F. Da Silva. Applications of autonomous microfluidic systems in environmental monitoring. RSC Advances, 3:18216–18227, 9 2013. ISSN 2046-2069. . URL https://pubs.rsc.org/en/content/articlehtml/2013/ra/c3ra41561ahttps://pubs.rsc.org/en/content/articlelanding/2013/ra/c3ra41561a.

James H. Carpenter. The chesapeake bay institute technique for the winkler dissolved oxygen method. Limnology and Oceanography, 10(1):141–143, 1965. . URL https://aslopubs.onlinelibrary.wiley.com/doi/abs/10.4319/lo.1965.10.1.0141.

B R Carter, R A Feely, N L Williams, A G Dickson, M B Fong, and Y Takeshita. Updated methods for global locally interpolated estimation of alkalinity, ph, and nitrate. Limnology and Oceanography: Methods, 16:119–131, 2 2018. ISSN 1541-5856. . URL https://doi.org/10.1002/lom3.10232.

Brendan R Carter, Henry C Bittig, Andrea J Fassbender, Jonathan D Sharp, Yuichiro Takeshita, Yuan-Yuan Xu, Marta Álvarez, Rik Wanninkhof, Richard A Feely, and Leticia Barbero. New and updated global empirical seawater property estimation routines. Limnology and Oceanography: Methods, 19:785–809, 12 2021. ISSN 1541-5856. . URL https://doi.org/10.1002/lom3.10461.

Brendan R. Carter, Jonathan D. Sharp, Andrew G. Dickson, Marta Álvarez, Michael B. Fong, Maribel I. García-Ibáñez, Ryan J. Woosley, Yuichiro Takeshita, Leticia Barbero, Robert H. Byrne, Wei Jun Cai, Melissa Chierici, Simon L. Clegg, Regina A. Easley, Andrea J. Fassbender, Kalla L. Fleger, Xinyu Li, Macarena Martín-Mayor, Katelyn M. Schockman, and Zhaohui Aleck Wang. Uncertainty sources for measurable ocean carbonate chemistry variables, 1 2023. ISSN 19395590.

Brendan R. Carter, Jonathan D. Sharp, Maribel I. García-Ibáñez, Ryan J. Woosley, Michael B. Fong, Marta Álvarez, Leticia Barbero, Simon L. Clegg, Regina Easley, Andrea J. Fassbender, Xinyu Li, Katelyn M. Schockman, and Zhaohui Aleck Wang. Random and systematic uncertainty in ship-based seawater carbonate chemistry observations. Limnology and Oceanography, 69:2473–2488, 10 2024. ISSN 1939-5590. . URL /doi/pdf/10.1002/lno.12674https://onlinelibrary.wiley.com/doi/abs/10.1002/lno.12674https://aslopubs.onlinelibrary.wiley.com/doi/10.1002/lno.12674.

Francisco P. Chavez, Jeff Sevadjian, Chris Wahl, Jules Friederich, and Gernot E. Friederich. Measurements of pco2 and ph from an autonomous surface vehicle in a coastal upwelling system. Deep Sea Research Part II: Topical Studies in Oceanography, 151:137–146, 5 2018. ISSN 0967-0645. . URL https://www.sciencedirect.com/science/article/pii/S0967064516302338?via=ihub.

C.-T. A. Chen, T.-H. Huang, Y.-C. Chen, Y. Bai, X. He, and Y. Kang. Air–sea exchanges of $co_2$ in the world's coastal seas. Biogeosciences, 10(10):6509–6544, 2013. . URL https://bg.copernicus.org/articles/10/6509/2013/.

Jennifer S Clarke, Eric P Achterberg, Douglas P Connelly, Ute Schuster, and Matthew Mowlem. Developments in marine pco2 measurement technology; towards sustained in situ observations. TrAC Trends in Analytical Chemistry, 88:53–61, 2017. ISSN 0165-9936. . URL https://www.sciencedirect.com/science/article/pii/S0165993616301868.

Hervé Claustre, Kenneth S. Johnson, and Yuichiro Takeshita. Observing the global ocean with biogeochemical-argo. Annual Review of Marine Science, 12:23–48, 1 2020. ISSN 19410611. . URL https://www.annualreviews.org/content/journals/10.1146/annurev-marine-010419-010956.

Stephanie Cohen, Thomas Krueger, and Maoz Fine. Measuring coral calcification under ocean acidification: methodological considerations for the 45 ca-uptake and total alkalinity anomaly technique. PeerJ, 2017:e3749, 9 2017. ISSN 21678359. . URL https://peerj.com/articles/3749.

Robert Costanza, Rudolf de Groot, Paul Sutton, Sander van der Ploeg, Sharolyn J. Anderson, Ida Kubiszewski, Stephen Farber, and R. Kerry Turner. Changes in the global value of ecosystem services. Global Environmental Change, 26:152–158, 2014. ISSN 0959-3780. . URL https://www.sciencedirect.com/science/article/pii/S0959378014000685.

Travis A Courtney, Tyler Cyronak, Alyssa J Griffin, and Andreas J Andersson. Implications of salinity normalization of seawater total alkalinity in coral reef metabolism studies. PLOS ONE, 16:e0261210–, 12 2022. URL https://doi.org/10.1371/journal.pone.0261210.

A. K. Covington, R. G. Bates, and R. A. Durst. Definition of ph scales, standard reference values, measurement of ph and related terminology (recommendations 1984). Pure and Applied Chemistry, 57(3):531–542, 1985. . URL https://doi.org/10.1351/pac198557030531.

Meghan F. Cronin, Nathan D. Anderson, Dongxiao Zhang, Patrick Berk, Samantha M. Wills, Yolande Serra, Catherine Kohlman, Adrienne J. Sutton, Makio C. Honda, Yoshimi Kawai, Jie Yang, Jim Thomson, Noah Lawrence-Slavas, Jack Reeves Eyre, and Christian Meinig. Pmel ocean climate stations as reference time series and research aggregate devices. Oceanography, 36:46–53, 10 2023. ISSN 10428275. .

Sarah Cryer, Filipa Carvalho, Terry Wood, James Asa Strong, Peter Brown, Socratis Loucaides, Arlene Young, Richard Sanders, and Claire Evans. Evaluating the sensor-equipped autonomous surface vehicle c-worker 4 as a tool for identifying

coastal ocean acidification and changes in carbonate chemistry. Journal of Marine Science and Engineering 2020, Vol. 8, Page 939, 8:939, 11 2020. ISSN 2077-1312. . URL https://www.mdpi.com/2077-1312/8/11/939/htmhttps://www.mdpi.com/2077-1312/8/11/939.

Sarah E. Cryer, Claire Evans, Sara E. Fowell, Gilbert Andrews, Peter Brown, Filipa Carvalho, Diana Degallerie, Jake Ludgate, Samir Rosado, Richard Sanders, James A. Strong, Derrick Theophille, Arlene Young, and Socratis Loucaides. Characterizing reef net metabolism via the diel co-variation of ph and dissolved oxygen from high resolution in situ sensors. Global Biogeochemical Cycles, 37:e2022GB007577, 9 2023. ISSN 1944-9224. . URL https://onlinelibrary.wiley.com/doi/full/10.1029/2022GB007577https://onlinelibrary.wiley.com/doi/abs/10.1029/2022GB007577https://agupubs.onlinelibrary.wiley.com/doi/10.1029/2022GB007577.

Charles Culberson, R M Pytkowicz, and J E Hawley. Seawater alkalinity determination by the ph method. Journal of Marine Research, 28, 1970. URL www.journalofmarineresearch.org.

T Cyronak, I R Santos, and B D Eyre. Permeable coral reef sediment dissolution driven by elevated pco2 and pore water advection. Geophysical Research Letters, 40: 4876–4881, 9 2013. ISSN 0094-8276. . URL https://doi.org/10.1002/grl.50948.

Tyler Cyronak and Bradley D Eyre. The synergistic effects of ocean acidification and organic metabolism on calcium carbonate (caco3) dissolution in coral reef sediments. Marine Chemistry, 183:1–12, 2016. ISSN 0304-4203. . URL https://www.sciencedirect.com/science/article/pii/S0304420316300391.

Tyler Cyronak, Andreas J Andersson, Chris Langdon, Rebecca Albright, Nicholas R Bates, Ken Caldeira, Renee Carlton, Jorge E Corredor, Rob B Dunbar, Ian Enochs, Jonathan Erez, Bradley D Eyre, Jean-Pierre Gattuso, Dwight Gledhill, Hajime Kayanne, David I Kline, David A Koweek, Coulson Lantz, Boaz Lazar, Derek Manzello, Ashly McMahon, Melissa Meléndez, Heather N Page, Isaac R Santos, Kai G Schulz, Emily Shaw, Jacob Silverman, Atsushi Suzuki, Lida Teneva, Atsushi Watanabe, and Shoji Yamamoto. Taking the metabolic pulse of the world's coral reefs. PLOS ONE, 13:e0190872–, 1 2018. URL https://doi.org/10.1371/journal.pone.0190872.

Tyler Cyronak, Yuichiro Takeshita, Travis A Courtney, Eric H DeCarlo, Bradley D Eyre, David I Kline, Todd Martz, Heather Page, Nichole N Price, Jennifer Smith, Laura Stoltenberg, Martin Tresguerres, and Andreas J Andersson. Diel temperature and ph variability scale with depth across diverse coral reef habitats. Limnology and Oceanography Letters, 5:193–203, 4 2020. ISSN 2378-2242. . URL https://doi.org/10.1002/lol2.10129.

K A Davis, S J Lentz, J Pineda, J T Farrar, V R Starczak, and J H Churchill. Observations of the thermal environment on red sea platform reefs: a heat budget analysis. Coral Reefs, 30:25–36, 2011. ISSN 0722-4028.

Kay L Davis, Andrew P Colefax, James P Tucker, Brendan P Kelaher, and Isaac R Santos. Global coral reef ecosystems exhibit declining calcification and increasing primary productivity. Communications Earth  Environment, 2:105, 2021. ISSN 2662-4435. . URL https://doi.org/10.1038/s43247-021-00168-w.

Clément de Boyer Montégut, Gurvan Madec, Albert S. Fischer, Alban Lazar, and Daniele Iudicone. Mixed layer depth over the global ocean: An examination of profile data and a profile-based climatology. Journal of Geophysical Research: Oceans, 109:1–20, 12 2004a. ISSN 21699291. .

Clément de Boyer Montégut, Gurvan Madec, Albert S. Fischer, Alban Lazar, and Daniele Iudicone. Mixed layer depth over the global ocean: An examination of profile data and a profile-based climatology. Journal of Geophysical Research: Oceans, 109:1–20, 12 2004b. ISSN 21699291. .

Manoela Romanó de Orte, David A. Koweek, Tyler Cyronak, Yuichiro Takeshita, Alyssa Griffin, Kennedy Wolfe, Alina Szmant, Robert Whitehead, Rebecca Albright, and Ken Caldeira. Unexpected role of communities colonizing dead coral substrate in the calcification of coral reefs. Limnology and Oceanography, 66:1793–1803, 5 2021. ISSN 1939-5590. . URL /doi/pdf/10.1002/lno.11722https://onlinelibrary.wiley.com/doi/abs/10.1002/lno.11722https://aslopubs.onlinelibrary.wiley.com/doi/10.1002/lno.11722.

M D DeGrandpre, T R Hammar, S P Smith, and F L Sayles. In situ measurements of seawater pco2. Limnology and oceanography, 40:969–975, 1995. ISSN 0024-3590.

Joseph D DiBattista, May B Roberts, Jessica Bouwmeester, Brian W Bowen, Darren J Coker, Diego F Lozano-Cortés, J Howard Choat, Michelle R Gaither, Jean-Paul A Hobbs, Maha T Khalil, Marc Kochzius, Robert F Myers, Gustav Paulay, Vanessa S N Robitzch, Pablo Saenz-Agudelo, Eva Salas, Tane H Sinclair-Taylor, Robert J Toonen, Mark W Westneat, Suzanne T Williams, and Michael L Berumen. A review of contemporary patterns of endemism for shallow water reef fauna in the red sea. Journal of Biogeography, 43:423–439, 3 2016. ISSN 0305-0270. . URL https://doi.org/10.1111/jbi.12649.

A. G. Dickson. An exact definition of total alkalinity and a procedure for the estimation of alkalinity and total inorganic carbon from titration data. Deep Sea Research Part A. Oceanographic Research Papers, 28:609–623, 6 1981. ISSN 0198-0149. . URL https://www.sciencedirect.com/science/article/pii/0198014981901217?via%3Dihub.

A. G. Dickson and F. J. Millero. A comparison of the equilibrium constants for the dissociation of carbonic acid in seawater media. Deep Sea Research Part A. Oceanographic Research Papers, 34:1733–1743, 10 1987. ISSN 0198-0149. .

A.G Dickson. ph scales and proton-transfer reactions in saline media such as sea water. Geochimica et Cosmochimica Acta, 48(11):2299–2308, 1984. ISSN 0016-7037. . URL https://www.sciencedirect.com/science/article/pii/0016703784902254.

AG Dickson and JP Riley. The effect of analytical error on the evaluation of the components of the aquatic carbon-dioxide system. Marine Chemistry, 6(1):77–85, 1978.

Andrew Dickson and Andrew G Dickson. The carbon dioxide system in seawater: Equilibrium chemistry and measurements estimation of uncertainty of seawater ph measurements view project acidification in eastern pacific view project the carbon dioxide system in seawater: equilibrium chemistry and measurements 1 introduction 1.1, 2010. URL https://www.researchgate.net/publication/284774361.

Andrew Dickson, Sabine Chris, and J R Christian. Guide to best practices for ocean co2 measurements. Guide to Best Practices for Ocean CO2 Measurements, 3, 6 2007.

Andrew G Dickson. Standard potential of the reaction: Agcl(s) + 12h2(g) = ag(s) + hcl(aq), and and the standard acidity constant of the ion hso4 in synthetic sea water from 273.15 to 318.15 k. The Journal of Chemical Thermodynamics, 22:113–127, 1990. ISSN 0021-9614. . URL https://www.sciencedirect.com/science/article/pii/002196149090074Z.

Andrew G. Dickson. The measurement of sea water ph. Marine Chemistry, 44(2): 131–142, 1993. ISSN 0304-4203. . URL https://www.sciencedirect.com/science/article/pii/030442039390198W. Marine Physical Chemistry - in memory of the contributions made to the field by Dr. Ricardo Pytkowicz.

Scott C. Doney, Victoria J. Fabry, Richard A. Feely, and Joan A. Kleypas. Ocean acidification: The other co2 problem, 2009. ISSN 19411405.

Scott C. Doney, D. Shallin Busch, Sarah R. Cooley, and Kristy J. Kroeker. The impacts of ocean acidification on marine ecosystems and reliant human communities. Annual Review of Environment and Resources, 45:83–112, 10 2020. ISSN 15435938. . URL https://www.annualreviews.org/content/journals/10.1146/annurev-environ-012320-083019.

Carlos M Duarte, Iris E Hendriks, Tommy S Moore, Ylva S Olsen, Alexandra Steckbauer, Laura Ramajo, Jacob Carstensen, Julie A Trotter, and Malcolm

McCulloch. Is ocean acidification an open-ocean syndrome? understanding anthropogenic impacts on seawater ph. Estuaries and Coasts, 36:221–236, 2013. ISSN 1559-2731. . URL https://doi.org/10.1007/s12237-013-9594-3.

J P D'Olivo and M T McCulloch. Response of coral calcification and calcifying fluid composition to thermally induced bleaching stress. Scientific Reports, 7:2207, 2017. ISSN 2045-2322. . URL https://doi.org/10.1038/s41598-017-02306-x.

Steven Emerson and John Hedges. Chemical Oceanography and the Marine Carbon Cycle. Cambridge University Press, 2008. ISBN 9780521833134. . URL https://www.cambridge.org/core/product/EA962F7A4363031C2CB89036CCEE65BE.

Jonathan Erez, Stéphanie Reynaud, Jacob Silverman, Kenneth Schneider, and Denis Allemand. Coral Calcification Under Ocean Acidification and Global Change, pages 151–176. Springer Netherlands, 2011. ISBN 978-94-007-0114-4. . URL https://doi.org/10.1007/978-94-007-0114-4_10.

Bradley D Eyre, Tyler Cyronak, Patrick Drupp, Eric Heinen De Carlo, Julian P Sachs, and Andreas J Andersson. Coral reefs will transition to net dissolving before end of century. Science, 359:908–911, 2 2018. . URL https://doi.org/10.1126/science.aao1118. doi: 10.1126/science.aao1118.

Laura J. Falkenberg, Richard G.J. Bellerby, Sean D. Connell, Lora E. Fleming, Bruce Maycock, Bayden D. Russell, Francis J. Sullivan, and Sam Dupont. Ocean acidification and human health. International Journal of Environmental Research and Public Health 2020, Vol. 17, Page 4563, 17:4563, 6 2020. ISSN 1660-4601. . URL https://www.mdpi.com/1660-4601/17/12/4563/htmhttps://www.mdpi.com/1660-4601/17/12/4563.

James L Falter, Ryan J Lowe, Zhenlin Zhang, and Malcolm McCulloch. Physical and biological controls on the carbonate chemistry of coral reef waters: Effects of metabolism, wave forcing, sea level, and geomorphology. PLOS ONE, 8:e53303–, 1 2013. URL https://doi.org/10.1371/journal.pone.0053303.

R.A. Feely, R.A. Feely, R.A. Feely, R.A. Feely, R.A. Feely, R.A. Feely, R.A. Feely, R.A. Feely, R.A. Feely, R.A. Feely, R.A. Feely, and R.A. Feely. An international observational network for ocean acidification. undefined, pages 304–318, 12 2010. .

Richard A. Feely, Christopher L. Sabine, Kitack Lee, Will Berelson, Joanie Kleypas, Victoria J. Fabry, and Frank J. Millero. Impact of anthropogenic co2 on the caco3 system in the oceans. Science, 305:362–366, 7 2004. ISSN 00368075. .

Richard A. Feely, Brendan R. Carter, Simone R. Alin, Dana Greeley, and Nina Bednaršek. The combined effects of ocean acidification and respiration on habitat suitability for marine calcifiers along the west coast of north america. Journal of Geophysical Research: Oceans, 129:e2023JC019892, 4 2024. ISSN 2169-9291. . URL

/doi/pdf/10.1029/2023JC019892https://onlinelibrary.wiley.com/doi/abs/10.1029/2023JC019892https://agupubs.onlinelibrary.wiley.com/doi/10.1029/2023JC019892.

M Fine, M Cinar, C R Voolstra, A Safa, B Rinkevich, D Laffoley, N Hilmi, and D Allemand. Coral reefs of the red sea — challenges and potential solutions. Regional Studies in Marine Science, 25:100498, 2019. ISSN 2352-4855. . URL https://www.sciencedirect.com/science/article/pii/S235248551830519X.

Michel Frankignoulle and Alberto V Borges. European continental shelf as a significant sink for atmospheric carbon dioxide. Global Biogeochemical Cycles, 15: 569–576, 9 2001. ISSN 0886-6236. . URL https://doi.org/10.1029/2000GB001307.

C A Frieder, S H Nam, T R Martz, and L A Levin. High temporal and spatial variability of dissolved oxygen and ph in a nearshore california kelp forest. Biogeosciences, 9:3917–3930, 10 2012. ISSN 1726-4189. . URL https://bg.copernicus.org/articles/9/3917/2012/https://bg.copernicus.org/articles/9/3917/2012/bg-9-3917-2012.pdf.

P Friedlingstein, M O'Sullivan, M W Jones, R M Andrew, D C E Bakker, J Hauck, P Landschützer, C Le Quéré, I T Luijkx, G P Peters, W Peters, J Pongratz, C Schwingshackl, S Sitch, J G Canadell, P Ciais, R B Jackson, S R Alin, P Anthoni, L Barbero, N R Bates, M Becker, N Bellouin, B Decharme, L Bopp, I B M Brasika, P Cadule, M A Chamberlain, N Chandra, T.-T.-T. Chau, F Chevallier, L P Chini, M Cronin, X Dou, K Enyo, W Evans, S Falk, R A Feely, L Feng, D J Ford, T Gasser, J Ghattas, T Gkritzalis, G Grassi, L Gregor, N Gruber, Ö Gürses, I Harris, M Hefner, J Heinke, R A Houghton, G C Hurtt, Y Iida, T Ilyina, A R Jacobson, A Jain, T Jarn{ı}ková, A Jersild, F Jiang, Z Jin, F Joos, E Kato, R F Keeling, D Kennedy, K Klein Goldewijk, J Knauer, J I Korsbakken, A Körtzinger, X Lan, N Lefèvre, H Li, J Liu, Z Liu, L Ma, G Marland, N Mayot, P C McGuire, G A McKinley, G Meyer, E J Morgan, D R Munro, S.-I. Nakaoka, Y Niwa, K M O'Brien, A Olsen, A M Omar, T Ono, M Paulsen, D Pierrot, K Pocock, B Poulter, C M Powis, G Rehder, L Resplandy, E Robertson, C Rödenbeck, T M Rosan, J Schwinger, R Séférian, T L Smallman, S M Smith, R Sospedra-Alfonso, Q Sun, A J Sutton, C Sweeney, S Takao, P P Tans, H Tian, B Tilbrook, H Tsujino, F Tubiello, G R van der Werf, E van Ooijen, R Wanninkhof, M Watanabe, C Wimart-Rousseau, D Yang, X Yang, W Yuan, X Yue, S Zaehle, J Zeng, and B Zheng. Global carbon budget 2023. Earth System Science Data, 15:5301–5369, 2023. . URL https://essd.copernicus.org/articles/15/5301/2023/.

P Friedlingstein, M O'Sullivan, M W Jones, R M Andrew, J Hauck, P Landschützer, C Le Quéré, H Li, I T Luijkx, A Olsen, G P Peters, W Peters, J Pongratz, C Schwingshackl, S Sitch, J G Canadell, P Ciais, R B Jackson, S R Alin, A Arneth, V Arora, N R Bates, M Becker, N Bellouin, C F Berghoff, H C Bittig, L Bopp,

P Cadule, K Campbell, M A Chamberlain, N Chandra, F Chevallier, L P Chini, T Colligan, J Decayeux, L M Djeutchouang, X Dou, C Duran Rojas, K Enyo, W Evans, A R Fay, R A Feely, D J Ford, A Foster, T Gasser, M Gehlen, T Gkritzalis, G Grassi, L Gregor, N Gruber, Ö Gürses, I Harris, M Hefner, J Heinke, G C Hurtt, Y Iida, T Ilyina, A R Jacobson, A K Jain, T Jarníková, A Jersild, F Jiang, Z Jin, E Kato, R F Keeling, K Klein Goldewijk, J Knauer, J I Korsbakken, X Lan, S K Lauvset, N Lefèvre, Z Liu, J Liu, L Ma, S Maksyutov, G Marland, N Mayot, P C McGuire, N Metzl, N M Monacci, E J Morgan, S.-I. Nakaoka, C Neill, Y Niwa, T Nützel, L Olivier, T Ono, P I Palmer, D Pierrot, Z Qin, L Resplandy, A Roobaert, T M Rosan, C Rödenbeck, J Schwinger, T L Smallman, S M Smith, R Sospedra-Alfonso, T Steinhoff, Q Sun, A J Sutton, R Séférian, S Takao, H Tatebe, H Tian, B Tilbrook, O Torres, E Tourigny, H Tsujino, F Tubiello, G van der Werf, R Wanninkhof, X Wang, D Yang, X Yang, Z Yu, W Yuan, X Yue, S Zaehle, N Zeng, and J Zeng. Global carbon budget 2024. Earth Syst. Sci. Data, 17:965–1039, 3 2025. ISSN 1866-3516. . URL https://essd.copernicus.org/articles/17/965/2025/https://essd.copernicus.org/articles/17/965/2025/essd-17-965-2025.pdf.

Pierre Friedlingstein, Matthew W Jones, Michael O'sullivan, Robbie M Andrew, Dorothee C E Bakker, Judith Hauck, Corinne Le Quéré, Glen P Peters, Wouter Peters, Julia Pongratz, Stephen Sitch, Josep G Canadell, Philippe Ciais, Rob B Jackson, Simone R Alin, Peter Anthoni, Nicholas R Bates, Meike Becker, Nicolas Bellouin, Laurent Bopp, Thi Tuyet, Trang Chau, Frédéric Chevallier, Louise P Chini, Margot Cronin, Kim I Currie, Bertrand Decharme, Laique M Djeutchouang, Xinyu Dou, Wiley Evans, Richard A Feely, Liang Feng, Thomas Gasser, Dennis Gilfillan, Thanos Gkritzalis, Giacomo Grassi, Luke Gregor, Nicolas Gruber, Özgür Gürses, Ian Harris, Richard A Houghton, George C Hurtt, Yosuke Iida, Tatiana Ilyina, Ingrid T Luijkx, Atul Jain, Steve D Jones, Etsushi Kato, Daniel Kennedy, Kees Klein Goldewijk, Jürgen Knauer, Jan Ivar Korsbakken, Arne Körtzinger, Peter Landschützer, Francesco Tubiello, Guido R Van Der Werf, Nicolas Vuichard, Chisato Wada, Rik Wanninkhof, Andrew J Watson, David Willis, Andrew J Wiltshire, Wenping Yuan, Chao Yue, Xu Yue, Sönke Zaehle, and Jiye Zeng. Global carbon budget 2021. Earth Syst. Sci. Data, 14:1917–2005, 2022. . URL https://doi.org/10.5194/essd-14-1917-2022.

R Gandoin and J Garza. Underestimation of strong wind speeds offshore in era5: evidence, discussion and correction. Wind Energ. Sci., 9:1727–1745, 8 2024. ISSN 2366-7451. . URL https://wes.copernicus.org/articles/9/1727/2024/https://wes.copernicus.org/articles/9/1727/2024/wes-9-1727-2024.pdf.

Andrew R. Gates, Susan E. Hartman, Jon Campbell, Christopher Cardwell, Jennifer M. Durden, Anita Flohr, Tammy Horton, Steven Lankester, Richard S. Lampitt, Charlotte Miskin-Hymas, Corinne Pebody, Nick Rundle, Amanda Serpell-Stevens, and Brian J. Bett. Porcupine abyssal plain sustained observatory monitors the

atmosphere to the seafloor on multidecadal timescales. Oceanography, 34:29, 12 2021. ISSN 10428275. .

J. P. Gattuso, M. Frankignoulle, and R. Wollast. Carbon and carbonate metabolism in coastal aquatic ecosystems. Annual Review of Ecology and Systematics, 29:405–434, 11 1998. ISSN 00664162. . URL https://www.annualreviews.org/content/journals/10.1146/annurev.ecolsys.29.1.405.

Jean-Pierre Gattuso and Lina Hansson. Ocean Acidifcation. Oxford University Press Inc., 2011. ISBN 9780199591091.

Jean-Pierre Gattuso, Denis Allemand, and MICHEL FRANKIGNOULLE. Photosynthesis and calcification at cellular, organismal and community levels in coral reefs: A review on interactions and control by carbonate chemistry. American Zoologist, 39, 2 1999. .

F Gazeau, L Urbini, T E Cox, S Alliouane, and J Gattuso. Comparison of the alkalinity and calcium anomaly techniques to estimate rates of net calcification. Marine Ecology Progress Series, 527:1–12, 2015. URL https://www.int-res.com/abstracts/meps/v527/meps11287. 10.3354/meps11287.

Felix Geißler, Eric P. Achterberg, Alexander D. Beaton, Mark J. Hopwood, Jennifer S. Clarke, André Mutzberg, Matt C. Mowlem, and Douglas P. Connelly. Evaluation of a ferrozine based autonomous in situ lab-on-chip analyzer for dissolved iron species in coastal waters. Frontiers in Marine Science, 4:283384, 10 2017. ISSN 22967745. . URL www.frontiersin.org.

Damià Gomis, Michael A Pedder, and Alvaro Viúdez. Recovering spatial features in the ocean: performance of isopycnal vs. isobaric analysis. Journal of Marine Systems, 13:205–224, 1997. ISSN 0924-7963. . URL https://www.sciencedirect.com/science/article/pii/S0924796396001169.

Catherine Goyet and Amy K Snover. High-accuracy measurements of total dissolved inorganic carbon in the ocean: comparison of alternate detection methods. Marine Chemistry, 44:235–242, 1993. ISSN 0304-4203. . URL https://www.sciencedirect.com/science/article/pii/0304420393902053.

Nicolas Gruber, Dorothee C.E. Bakker, Tim DeVries, Luke Gregor, Judith Hauck, Peter Landschützer, Galen A. McKinley, and Jens Daniel Müller. Trends and variability in the ocean carbon sink. Nature Reviews Earth and Environment, 4:119–134, 2 2023. ISSN 2662138X. . URL https://www.nature.com/articles/s43017-022-00381-x.

Per 0. J Hall and Robert C Aller. Rapid, small-volume, flow injection analysis for sco2, and nh4+ in marine and freshwaters. Limnology and Oceanography, 37:1113–1119, 7 1992. ISSN 0024-3590. . URL https://doi.org/10.4319/lo.1992.37.5.1113.

Emily M Hammermeister, Stathys Papadimitriou, Martin Arundell, Jake Ludgate, Allison Schaap, Matthew C Mowlem, Sara E Fowell, Edward Chaney, and Socratis Loucaides. New capability in autonomous ocean carbon observations using the autosub long-range auv equipped with novel ph and total alkalinity sensors. Environmental Science  Technology, 59:7129–7144, 4 2025. ISSN 0013-936X. . URL https://doi.org/10.1021/acs.est.4c10139. doi: 10.1021/acs.est.4c10139.

Frank R Hampel. The influence curve and its role in robust estimation. Journal of the American Statistical Association, 69:383–393, 6 1974. ISSN 0162-1459. . URL https://www.tandfonline.com/doi/abs/10.1080/01621459.1974.10482962. doi: 10.1080/01621459.1974.10482962.

S E Hartman, M P Humphreys, C Kivimäe, E M S Woodward, V Kitidis, T Mcgrath, D J Hydes, N Greenwood, T Hull, C Ostle, D J Pearce, D Sivyer, B M Stewart, P Walsham, S C Painter, E Mcgovern, C Harris, A Griffiths, A Smilenova, J Clarke, C Davis, R Sanders, and P Nightingale. Seasonality and spatial heterogeneity of the surface ocean carbonate system in the northwest european continental shelf. 2014. . URL https://doi.org/10.1016/j.pocean.2018.02.005.

Susan E Hartman, Brian J Bett, Jennifer M Durden, Stephanie A Henson, Morten Iversen, Rachel M Jeffreys, Tammy Horton, Richard Lampitt, and Andrew R Gates. Enduring science: Three decades of observing the northeast atlantic from the porcupine abyssal plain sustained observatory (pap-so). Progress in Oceanography, 191:102508, 2021. ISSN 0079-6611. . URL https://www.sciencedirect.com/science/article/pii/S0079661120302433.

Judith Hauck, Cara Nissen, Peter Landschützer, Christian Rödenbeck, Seth Bushinsky, and Are Olsen. Sparse observations induce large biases in estimates of the global ocean co2 sink: an ocean model subsampling experiment. Philosophical Transactions of the Royal Society A, 381, 6 2023. ISSN 1364503X. . URL https://royalsocietypublishing.org/doi/10.1098/rsta.2022.0063.

C Hauri, B Irving, D Hayes, E Abdi, J Kemme, N Kinski, and A M P McDonnell. Expanding seawater carbon dioxide and methane measuring capabilities with a seaglider. Ocean Sci., 20:1403–1421, 10 2024. ISSN 1812-0792. . URL https://os.copernicus.org/articles/20/1403/2024/https://os.copernicus.org/articles/20/1403/2024/os-20-1403-2024.pdf.

M P Hemming, J Kaiser, K J Heywood, D C E Bakker, J Boutin, K Shitashima, G Lee, O Legge, and R Onken. Measuring ph variability using an experimental sensor on an underwater glider. Ocean Sci., 13:427–442, 5 2017. ISSN 1812-0792. . URL https://os.copernicus.org/articles/13/427/2017/https://os.copernicus.org/articles/13/427/2017/os-13-427-2017.pdf.

Scott F Heron, Jeffrey A Maynard, Ruben van Hooidonk, and C Mark Eakin. Warming trends and bleaching stress of the world's coral reefs 1985–2012. Scientific Reports, 6:38402, 2016. ISSN 2045-2322. . URL https://doi.org/10.1038/srep38402.

Hans Hersbach, Bill Bell, Paul Berrisford, Shoji Hirahara, András Horányi, Joaquín Muñoz-Sabater, Julien Nicolas, Carole Peubey, Raluca Radu, Dinand Schepers, Adrian Simmons, Cornel Soci, Saleh Abdalla, Xavier Abellan, Gianpaolo Balsamo, Peter Bechtold, Gionata Biavati, Jean Bidlot, Massimo Bonavita, Giovanna De Chiara, Per Dahlgren, Dick Dee, Michail Diamantakis, Rossana Dragani, Johannes Flemming, Richard Forbes, Manuel Fuentes, Alan Geer, Leo Haimberger, Sean Healy, Robin J Hogan, Elías Hólm, Marta Janisková, Sarah Keeley, Patrick Laloyaux, Philippe Lopez, Cristina Lupu, Gabor Radnoti, Patricia de Rosnay, Iryna Rozum, Freja Vamborg, Sebastien Villaume, and Jean-Noël Thépaut. The era5 global reanalysis. Quarterly Journal of the Royal Meteorological Society, 146:1999–2049, 7 2020. ISSN 0035-9009. . URL https://doi.org/10.1002/qj.3803.

Colin Ho and Srikanth Saripalli. Where do you sample? - an autonomous underwater vehicle story. ROSE 2011 - IEEE International Symposium on Robotic and Sensors Environments, Proceedings, pages 119–124, 2011. . URL https://asu.pure.elsevier.com/en/publications/where-do-you-sample-an-autonomous-underwater-vehicle-story.

D T Ho, L Bopp, J B Palter, M C Long, P W Boyd, G Neukermans, and L T Bach. Monitoring, reporting, and verification for ocean alkalinity enhancement. State Planet, 2-oae2023:12, 11 2023. ISSN 2752-0706. . URL https://sp.copernicus.org/articles/2-oae2023/12/2023/https://sp.copernicus.org/articles/2-oae2023/12/2023/sp-2-oae2023-12-2023.pdf.

David T Ho and Julian J Schanze. Precipitation-induced reduction in surface ocean pco2: Observations from the eastern tropical pacific ocean. Geophysical Research Letters, 47:e2020GL088252, 8 2020. ISSN 0094-8276. . URL https://doi.org/10.1029/2020GL088252.

O Hoegh-Guldberg, P J Mumby, A J Hooten, R S Steneck, P Greenfield, E Gomez, C D Harvell, P F Sale, A J Edwards, K Caldeira, N Knowlton, C M Eakin, R Iglesias-Prieto, N Muthiga, R H Bradbury, A Dubi, and M E Hatziolos. Coral reefs under rapid climate change and ocean acidification. Science, 318:1737–1742, 12 2007. . URL https://doi.org/10.1126/science.1152509. doi: 10.1126/science.1152509.

Terence P Hughes, Maria J Rodrigues, David R Bellwood, Daniela Ceccarelli, Ove Hoegh-Guldberg, Laurence McCook, Natalie Moltschaniwskyj, Morgan S Pratchett, Robert S Steneck, and Bette Willis. Phase shifts, herbivory, and the resilience of coral reefs to climate change. Current Biology, 17:360–365, 2 2007. ISSN 0960-9822. . URL https://doi.org/10.1016/j.cub.2006.12.049. doi: 10.1016/j.cub.2006.12.049.

Terry P Hughes, Nicholas A J Graham, Jeremy B C Jackson, Peter J Mumby, and Robert S Steneck. Rising to the challenge of sustaining coral reef resilience. Trends in Ecology  Evolution, 25:633–642, 11 2010. ISSN 0169-5347. . URL https://doi.org/10.1016/j.tree.2010.07.011. doi: 10.1016/j.tree.2010.07.011.

Terry P Hughes, James T Kerry, Mariana Álvarez Noriega, Jorge G Álvarez Romero, Kristen D Anderson, Andrew H Baird, Russell C Babcock, Maria Beger, David R Bellwood, Ray Berkelmans, Tom C Bridge, Ian R Butler, Maria Byrne, Neal E Cantin, Steeve Comeau, Sean R Connolly, Graeme S Cumming, Steven J Dalton, Guillermo Diaz-Pulido, C Mark Eakin, Will F Figueira, James P Gilmour, Hugo B Harrison, Scott F Heron, Andrew S Hoey, Jean-Paul A Hobbs, Mia O Hoogenboom, Emma V Kennedy, Chao yang Kuo, Janice M Lough, Ryan J Lowe, Gang Liu, Malcolm T McCulloch, Hamish A Malcolm, Michael J McWilliam, John M Pandolfi, Rachel J Pears, Morgan S Pratchett, Verena Schoepf, Tristan Simpson, William J Skirving, Brigitte Sommer, Gergely Torda, David R Wachenfeld, Bette L Willis, and Shaun K Wilson. Global warming and recurrent mass bleaching of corals. Nature, 543: 373–377, 2017. ISSN 1476-4687. . URL https://doi.org/10.1038/nature21707.

Matthew P Humphreys, Eric P Achterberg, Joanne E Hopkins, Mohammed Z H Chowdhury, Alex M Griffiths, Susan E Hartman, Tom Hull, Angelina Smilenova, Juliane U Wihsgott, E Malcolm S Woodward, and C Mark Moore. Mechanisms for a nutrient-conserving carbon pump in a seasonally stratified, temperate continental shelf sea. Progress in Oceanography, 177:101961, 2019. ISSN 0079-6611. . URL https://www.sciencedirect.com/science/article/pii/S0079661117301374.

The Mathworks Inc. Matlab version: 24.2.0 (r2024b), 2024. URL https://www.mathworks.com.

IOC, SCOR, and IAPSO. The international thermodynamic equation of seawater – 2010: Calculation and use of thermodynamic properties, volume 56. Intergovernmental Oceanographic Commission, UNESCO, 2010.

IOCCP. Essential ocean variable (eov): Inorganic carbon background and justification, 2017.

M N Islam, B E Casareto, and Y Suzuki. Eutrophication Accelerates Carbonate Dissolution under High ¡i¿p¡/i¿CO¡sub¿2¡/sub¿ Condition in Coral Reef Ecosystem. Journal of Scientific Research, 8(3):427–438, 2016. ISSN 2070-0245, 2070-0237. . URL https://www.banglajol.info/index.php/JSR/article/view/27937.

JCGM, BIPM, IEC, IFCC, ILAC, ISO, IUPAC, IUPAP, and OIMIL. Evaluation of measurement data-guide to the expression of uncertainty in measurement. JCGM 100:2008, 2008. URL www.bipm.org.

Li-Qing Jiang, Brendan R Carter, Richard A Feely, Siv K Lauvset, and Are Olsen. Surface ocean ph and buffer capacity: past, present and future. Scientific Reports, 9:

18624, 2019. ISSN 2045-2322. . URL https://doi.org/10.1038/s41598-019-55039-4.

Li Qing Jiang, John Dunne, Brendan R. Carter, Jerry F. Tjiputra, Jens Terhaar, Jonathan D. Sharp, Are Olsen, Simone Alin, Dorothee C.E. Bakker, Richard A. Feely, Jean Pierre Gattuso, Patrick Hogan, Tatiana Ilyina, Nico Lange, Siv K. Lauvset, Ernie R. Lewis, Tomas Lovato, Julien Palmieri, Yeray Santana-Falcón, Jörg Schwinger, Roland Séférian, Gary Strand, Neil Swart, Toste Tanhua, Hiroyuki Tsujino, Rik Wanninkhof, Michio Watanabe, Akitomo Yamamoto, and Tilo Ziehn. Global surface ocean acidification indicators from 1750 to 2100. Journal of Advances in Modeling Earth Systems, 15:e2022MS003563, 3 2023. ISSN 1942-2466. . URL /doi/pdf/10.1029/2022MS003563https://onlinelibrary.wiley.com/doi/abs/10.1029/2022MS003563https://agupubs.onlinelibrary.wiley.com/doi/10.1029/2022MS003563.

Zong-Pei Jiang, Toby Tyrrell, David J Hydes, Minhan Dai, and Susan E Hartman. Variability of alkalinity and the alkalinity-salinity relationship in the tropical and subtropical surface ocean. Global Biogeochemical Cycles, 28:729–742, 7 2014. ISSN 0886-6236. . URL https://doi.org/10.1002/2013GB004678.

Kenneth S Johnson, Hans W Jannasch, Luke J Coletti, Virginia A Elrod, Todd R Martz, Yuichiro Takeshita, Robert J Carlson, and James G Connery. Deep-sea durafet: A pressure tolerant ph sensor designed for global sensor networks. Analytical Chemistry, 88:3249–3256, 3 2016. ISSN 0003-2700. . URL https://doi.org/10.1021/acs.analchem.5b04653. doi: 10.1021/acs.analchem.5b04653.

Kenneth S Johnson, Joshua N Plant, Luke J Coletti, Hans W Jannasch, Carole M Sakamoto, Stephen C Riser, Dana D Swift, Nancy L Williams, Emmanuel Boss, Nils Haëntjens, Lynne D Talley, and Jorge L Sarmiento. Biogeochemical sensor performance in the soccom profiling float array. Journal of Geophysical Research: Oceans, 122:6416–6436, 8 2017. ISSN 2169-9275. . URL https://doi.org/10.1002/2017JC012838.

Ian Joint, Roland Wollast, Lei Chou, Sonia Batten, Marc Elskens, Elaine Edwards, Andrew Hirst, Peter Burkill, Stephen Groom, Stuart Gibb, Axel Miller, David Hydes, Frank Dehairs, Avan Antia, Raymond Barlow, Andrew Rees, Alan Pomroy, Uwe Brockmann, Denise Cummings, Richard Lampitt, Michèle Loijens, Fauzi Mantoura, Peter Miller, Thomas Raabe, Xose Alvarez-Salgado, Claire Stelfox, and James Woolfenden. Pelagic production at the celtic sea shelf break. Deep Sea Research Part II: Topical Studies in Oceanography, 48:3049–3081, 2001. ISSN 0967-0645. . URL https://www.sciencedirect.com/science/article/pii/S0967064501000327.

Jana C. Jokerst, Jason M. Emory, and Charles S. Henry. Advances in microfluidics for environmental analysis. Analyst, 137:24–34, 11 2011. ISSN 13645528. . URL https://pubs.rsc.org/en/content/articlehtml/2012/an/c1an15368dhttps://pubs.rsc.org/en/content/articlelanding/2012/an/c1an15368d.

L W Juranek, R A Feely, D Gilbert, H Freeland, and L A Miller. Real-time estimation of ph and aragonite saturation state from argo profiling floats: Prospects for an autonomous carbon observing strategy. Geophysical Research Letters, 38, 9 2011. ISSN 0094-8276. . URL https://doi.org/10.1029/2011GL048580.

Hajme Kayanne. Thirty years since the coral reef co¡sub¿2¡/sub¿ sink/source debate. Galaxea, Journal of Coral Reef Studies, 27:118–130, 2025. .

Charles D. Keeling, Robert B. Bacastow, Arnold E. Bainbridge, Carl A. Ekdahl, Peter R. Guenther, Lee S. Waterman, and John F. S. Chin. Atmospheric carbon dioxide variations at mauna loa observatory, hawaii. Tellus, 28:538–551, 12 1976. ISSN 2153-3490. . URL /doi/pdf/10.1111/j.2153-3490.1976.tb00701.xhttps://onlinelibrary.wiley.com/doi/abs/10.1111/j.2153-3490.1976.tb00701.xhttps://onlinelibrary.wiley.com/doi/10.1111/j.2153-3490.1976.tb00701.x.

Deborah S. Kelley, John R. Delaney, and Cabled Array Team. Nsf's cabled array: A wired tectonic plate and overlying ocean. In OCEANS 2016 MTS/IEEE Monterey, pages 1–10, 2016. .

S Khatiwala, T Tanhua, S Mikaloff Fletcher, M Gerber, S C Doney, H D Graven, N Gruber, G A McKinley, A Murata, A F Ríos, and C L Sabine. Global ocean storage of anthropogenic carbon. Biogeosciences, 10:2169–2191, 4 2013. ISSN 1726-4189. . URL https://bg.copernicus.org/articles/10/2169/2013/https://bg.copernicus.org/articles/10/2169/2013/bg-10-2169-2013.pdf.

K H Khoo, Richard W Ramette, Charles H Culberson, and Roger G Bates. Determination of hydrogen ion concentrations in seawater from 5 to 40.degree.c: standard potentials at salinities from 20 to 45 Analytical Chemistry, 49:29–34, 1 1977. ISSN 0003-2700. . URL https://doi.org/10.1021/ac50009a016. doi: 10.1021/ac50009a016.

R Killick, Fearnhead P., I A, and Eckley. Optimal detection of changepoints with a linear computational cost. Journal of the American Statistical Association, 107: 1590–1598, 12 2012. ISSN 0162-1459. . URL https://doi.org/10.1080/01621459.2012.737745. doi: 10.1080/01621459.2012.737745.

Vassilis Kitidis, Nicholas J Hardman-Mountford, Emmer Litt, Ian Brown, Denise Cummings, Sue Hartman, David Hydes, James R Fishwick, Carolyn Harris, Victor

Martinez-Vicente, E Malcolm, S Woodward, and Timothy J Smyth. Seasonal dynamics of the carbonate system in the western english channel. 2012. .

Joan A Kleypas, Robert W Buddemeier, David Archer, Jean-Pierre Gattuso, Chris Langdon, and Bradley N Opdyke. Geochemical consequences of increased atmospheric carbon dioxide on coral reefs. science, 284:118–120, 1999. ISSN 1095-9203.

Kristy J. Kroeker, Rebecca L. Kordas, Ryan Crim, Iris E. Hendriks, Laura Ramajo, Gerald S. Singh, Carlos M. Duarte, and Jean Pierre Gattuso. Impacts of ocean acidification on marine organisms: quantifying sensitivities and interaction with warming. Global change biology, 19:1884–1896, 6 2013. ISSN 1354-1013. . URL https://pubmed.ncbi.nlm.nih.gov/23505245/.

L Kwiatkowski, O Torres, L Bopp, O Aumont, M Chamberlain, J R Christian, J P Dunne, M Gehlen, T Ilyina, J G John, A Lenton, H Li, N S Lovenduski, J C Orr, J Palmieri, Y Santana-Falcón, J Schwinger, R Séférian, C A Stock, A Tagliabue, Y Takano, J Tjiputra, K Toyama, H Tsujino, M Watanabe, A Yamamoto, A Yool, and T Ziehn. Twenty-first century ocean warming, acidification, deoxygenation, and upper-ocean nutrient and primary production decline from cmip6 model projections. Biogeosciences, 17:3439–3470, 7 2020. ISSN 1726-4189. . URL https://bg.copernicus.org/articles/17/3439/2020/https://bg.copernicus.org/articles/17/3439/2020/bg-17-3439-2020.pdf.

Lester Kwiatkowski, Brian Gaylord, Tessa Hill, Jessica Hosfelt, Kristy J Kroeker, Yana Nebuchina, Aaron Ninokawa, Ann D Russell, Emily B Rivest, Marine Sesboüé, and Ken Caldeira. Nighttime dissolution in a temperate coastal ocean ecosystem increases under acidification. Scientific Reports, 6:22984, 2016. ISSN 2045-2322. . URL https://doi.org/10.1038/srep22984.

NOAA Global Monitoring Laboratory. Trends in co2 - noaa global monitoring laboratory. https://gml.noaa.gov/webdata/ccgg/trends/co2/co2_mm_mlo.txt, 2025. URL https://gml.noaa.gov/ccgg/trends/.

Chun-Ze Lai, Michael D DeGrandpre, and Reuben C Darlington. Autonomous optofluidic chemical analyzers for marine applications: Insights from the submersible autonomous moored instruments (sami) for ph and pco2. Frontiers in Marine Science, Volume 4 - 2017, 2018. ISSN 2296-7745. URL https://www.frontiersin.org/journals/marine-science/articles/10.3389/fmars.2017.00438.

R S Lampitt, D S M Billett, and A P Martin. The sustained observatory over the porcupine abyssal plain (pap): Insights from time series observations and process studies. Deep Sea Research Part II: Topical Studies in Oceanography, 57:1267–1271,

2010. ISSN 0967-0645. . URL https://www.sciencedirect.com/science/article/pii/S0967064510000330.

Xin Lan, Pieter Tans, Kirk Thoning, and NOAA Global Monitoring Laboratory. Trends in globally-averaged CO2 determined from NOAA global monitoring laboratory measurements, 2023.

C. Langdon. Determination of dissolved oxygen in seaweater by winkler titration using amperometric technique. in, the go-ship repeat hydrography manual: A collection of expert reports and guidelines. version 1,, 2010. URL https://repository.oceanbestpractices.org/handle/11329/380.

Goulven G Laruelle, Ronny Lauerwald, Benjamin Pfeil, and Pierre Regnier. Regionalized global budget of the co2 exchange at the air-water interface in continental shelf seas. Global biogeochemical cycles, 28:1199–1214, 2014. ISSN 0886-6236.

Goulven G Laruelle, Wei-Jun Cai, Xinping Hu, Nicolas Gruber, Fred T Mackenzie, and Pierre Regnier. Continental shelves as a variable but increasing global sink for atmospheric carbon dioxide. Nature Communications, 9:454, 2018. ISSN 2041-1723. . URL https://doi.org/10.1038/s41467-017-02738-z.

Hugo Ledoux, Christopher Gold, and Peter Fisher. An Efficient Natural Neighbour Interpolation Algorithm for Geoscientific Modelling, pages 97–108. 1 2005. ISBN 3-540-22610-9. .

By M Craig Lee, Michael DeGrandpre, John Guthrie, Victoria Hill, Ron Kwok, James Morison, Christopher J Cox, Hanumant Singh, Timothy P Stanton, and Jeremy Wilkinson. Emerging technologies and approaches for in situ, autonomous observing in the arctic. 35, 2022a.

Craig M. Lee, Michael Degrandpre, John Guthrie, Victoria Hill, Ron Kwok, James Morison, Christopher J. Cox, Hanumant Singh, Timothy P. Stanton, and Jeremy Wilkinson. Emerging technologies and approaches for in situ, autonomous observing in the arctic. Oceanography, 35, 2022b. ISSN 10428275. .

Kitack Lee, Lan T Tong, Frank J Millero, Christopher L Sabine, Andrew G Dickson, Catherine Goyet, Geun-Ha Park, Rik Wanninkhof, Richard A Feely, and Robert M Key. Global relationships of total alkalinity with salinity and temperature in surface waters of the world's oceans. Geophysical Research Letters, 33, 10 2006. ISSN 0094-8276. . URL https://doi.org/10.1029/2006GL027207.

Kitack Lee, Tae-Wook Kim, Robert H Byrne, Frank J Millero, Richard A Feely, and Yong-Ming Liu. The universal ratio of boron to chlorinity for the north pacific and north atlantic oceans. Geochimica et Cosmochimica Acta, 74:1801–1811, 2010. ISSN

0016-7037. . URL
https://www.sciencedirect.com/science/article/pii/S0016703709007789.

Sydney Levitus. Climatological atlas of the world ocean, volume 13. US Department of Commerce, National Oceanic and Atmospheric Administration, 1982.

E. R. Lewis and D. W. R. Wallace. Program developed for co2 system calculations. 1 1998. .

Xinyu Li, Maribel I. García-Ibáñez, Brendan R. Carter, Baoshan Chen, Qian Li, Regina A. Easley, and Wei Jun Cai. Purified meta-cresol purple dye perturbation: How it influences spectrophotometric ph measurements. Marine Chemistry, 225, 9 2020. ISSN 03044203. .

Hancong Liu, Sirish Shah, and Wei Jiang. On-line outlier detection and data cleaning. Computers Chemical Engineering, 28:1635–1647, 2004. ISSN 0098-1354. . URL
https://www.sciencedirect.com/science/article/pii/S0098135404000249.

K K Liu, L Atkinson, R Quiñones, and L Talaue-McManus. Carbon and Nutrient Fluxes in Continental Margins: A Global Synthesis. Springer Berlin Heidelberg, 2010. ISBN 9783540927358. URL
https://books.google.co.uk/books?id=tpfrKj4G3EUC.

Ryan Joseph Lowe, Xavier Pivan, James Falter, Graham Symonds, and Renee Gruber. Rising sea levels will reduce extreme temperature variations in tide-dominated reef habitats. Science Advances, 2, 8 2016. ISSN 23752548. . URL
https://pubmed.ncbi.nlm.nih.gov/27540589/.

M Susan Lozier, Michael S McCartney, and W Brechner Owens. Anomalous anomalies in averaged hydrographic data. Journal of Physical Oceanography, 24:2624–2638, 1994. . URL https://journals.ametsoc.org/view/journals/phoc/24/12/1520-0485_1994_024_2624_aaiahd_2_0_co_2.xml.

Timothy J Lueker, Andrew G Dickson, and Charles D Keeling. Ocean pco calculated from dissolved inorganic carbon, 2 alkalinity, and equations for k and k : validation based on 1 2 laboratory measurements of co in gas and seawater at 2 equilibrium, 2000. URL www.elsevier.nlrlocatermarchem.

Christian Lønborg, Moritz Müller, Edward C V Butler, Shan Jiang, Seng Keat Ooi, Dieu Huong Trinh, Pui Yee Wong, Suryati M Ali, Chun Cui, Wee Boon Siong, Erik S Yando, Daniel A Friess, Judith A Rosentreter, Bradley D Eyre, and Patrick Martin. Nutrient cycling in tropical and temperate coastal waters: Is latitude making a difference? Estuarine, Coastal and Shelf Science, 262:107571, 2021. ISSN 0272-7714. . URL
https://www.sciencedirect.com/science/article/pii/S0272771421004212.

Danling Ma, Luke Gregor, and Nicolas Gruber. Four decades of trends and drivers of global surface ocean acidification. Global Biogeochemical Cycles, 37: e2023GB007765, 7 2023. ISSN 1944-9224. . URL /doi/pdf/10.1029/2023GB007765https://onlinelibrary.wiley.com/doi/abs/10.1029/2023GB007765https://agupubs.onlinelibrary.wiley.com/doi/10.1029/2023GB007765.

A. Manz, N. Graber, and H. M. Widmer. Miniaturized total chemical analysis systems: A novel concept for chemical sensing. Sensors and Actuators B: Chemical, 1: 244–248, 1 1990. ISSN 0925-4005. .

P. Marrec, T. Cariou, E. Collin, A. Durand, M. Latimier, E. Macé, P. Morin, S. Raimund, M. Vernet, and Y. Bozec. Seasonal and latitudinal variability of the co2 system in the western english channel based on voluntary observing ship (vos) measurements. Marine Chemistry, 155:29–41, 2013. ISSN 0304-4203. .

P Marrec, T Cariou, E Macé, P Morin, L A Salt, M Vernet, B Taylor, K Paxman, and Y Bozec. Dynamics of air–sea co¡sub¿2¡/sub¿ fluxes in the northwestern european shelf based on voluntary observing ship and satellite observations. Biogeosciences, 12:5371–5391, 9 2015. ISSN 1726-4189. . URL https://bg.copernicus.org/articles/12/5371/2015/https://bg.copernicus.org/articles/12/5371/2015/bg-12-5371-2015.pdf.

Todd R Martz, James G Connery, and Kenneth S Johnson. Testing the honeywell durafet® for seawater ph applications. Limnology and Oceanography: Methods, 8: 172–184, 5 2010. ISSN 1541-5856. . URL https://doi.org/10.4319/lom.2010.8.172.

Todd R. Martz, Kendra L. Daly, Robert H. Byrne, Jonathon H. Stillman, and Daniela Turk. Technology for ocean acidification research: Needs and availability. Oceanography, 28:40–47, 6 2015. ISSN 10428275. .

Mark Maslin, Raina D. Ramnath, Gavin I. Welsh, and Sanjay M. Sisodiya. Understanding the health impacts of the climate crisis. Future Healthcare Journal, 12:100240, 3 2025. ISSN 2514-6645. . URL https://www.sciencedirect.com/science/article/pii/S2514664525000190.

T Mass, S Einbinder, E Brokovich, N Shashar, R Vago, J Erez, and Z Dubinsky. Photoacclimation of stylophora pistillata to light extremes: metabolism and calcification. Marine Ecology Progress Series, 334:93–102, 2007. URL https://www.int-res.com/abstracts/meps/v334/meps334093. 10.3354/meps334093.

Moritz Mathis, Fabrice Lacroix, Stefan Hagemann, David Marcolino Nielsen, Tatiana Ilyina, and Corinna Schrum. Enhanced co2 uptake of the coastal ocean is dominated

by biological carbon fixation. Nature Climate Change, 14:373–379, 2024. ISSN 1758-6798. . URL https://doi.org/10.1038/s41558-024-01956-w.

Tanya L Maurer, Joshua N Plant, and Kenneth S Johnson. Delayed-mode quality control of oxygen, nitrate, and ph data on soccom biogeochemical profiling floats. Frontiers in Marine Science, Volume 8 - 2021, 2021. ISSN 2296-7745. URL https://www.frontiersin.org/journals/marine-science/articles/10.3389/fmars.2021.683207.

Trevor J McDougall and Paul M Barker. Getting started with TEOS-10 and the Gibbs Seawater (GSW) Oceanographic Toolbox. Trevor J McDougall, 2011. ISBN 9780646556215.

Peter C. McIntosh. Oceanographic data interpolation: Objective analysis and splines. Journal of Geophysical Research: Oceans, 95:13529–13541, 8 1990. ISSN 0148-0227. .

Galen A McKinley, Darren J Pilcher, Amanda R Fay, Keith Lindsay, Matthew C Long, and Nicole S Lovenduski. Timescales for detection of trends in the ocean carbon sink. Nature, 530:469–472, 2016. ISSN 1476-4687. . URL https://doi.org/10.1038/nature16958.

K Mclaughlin, S B Weisberg, A G Dickson, G E Hofmann, J A Newton, D Aseltine-Neilson, A Barton, S Cudd, R A Feely, I W Jefferds, E B Jewett, T King, C J Langdon, S Mcafee, D Pleschner-Steele, and B Steele. Core principles of the california current acidification network: Linking chemistry, physics, and ecological effects. Oceanography, 28:160–169, 2015. . URL http://dx.doi.org/10.5670/oceanog.2015.39.DOIhttp://dx.doi.org/10.5670/oceanog.2015.39.

Ashly McMahon, Isaac R Santos, Kai G Schulz, Tyler Cyronak, and Damien T Maher. Determining coral reef calcification and primary production using automated alkalinity, ph and pco2 measurements at high temporal resolution. Estuarine, Coastal and Shelf Science, 209:80–88, 2018. ISSN 0272-7714. . URL https://www.sciencedirect.com/science/article/pii/S027277141730519X.

Metrohm. Metrohm knowledge base, 2022. URL https://guide.metrohm.com/w/en_US/show/f73646049f48526d0a0002025fb1335e_2_en_US.

Jack J. Middelburg, Karline Soetaert, and Mathilde Hagens. Ocean alkalinity, buffering and biogeochemical processes. Reviews of Geophysics, 58:e2019RG000681, 9 2020. ISSN 1944-9208. . URL /doi/pdf/10.1029/2019RG000681https://onlinelibrary.wiley.com/doi/abs/10.1029/2019RG000681https://agupubs.onlinelibrary.wiley.com/doi/10.1029/2019RG000681.

Frank J Millero. The effect of pressure on the solubility of minerals in water and seawater. Geochimica et Cosmochimica Acta, 46:11–22, 1982. ISSN 0016-7037. . URL https://www.sciencedirect.com/science/article/pii/0016703782902861.

Frank J Millero. The estimation of the pkha of acids in seawater using the pitzer equations. Geochimica et Cosmochimica Acta, 47:2121–2129, 1983. ISSN 0016-7037. . URL https://www.sciencedirect.com/science/article/pii/0016703783900376.

Frank J. Millero. Thermodynamics of the carbon dioxide system in the oceans. Geochimica et Cosmochimica Acta, 59:661–677, 1995. ISSN 00167037. .

Frank J. Millero. The marine inorganic carbon cycle. Chemical Reviews, 107:308–341, 2007. ISSN 00092665. . URL https://pubs.acs.org/doi/pdf/10.1021/cr0503557.

Frank J. Millero, Kitack Lee, and Mary Roche. Distribution of alkalinity in the surface waters of the major oceans. Marine Chemistry, 60:111–130, 2 1998. ISSN 0304-4203. .

O Moav-Barzel, J Erez, B Lazar, and J Silverman. Higher Nighttime Rates of CaCO3 Dissolution in the Nature Reserve Reef, Eilat, Israel in 2015–2016 Compared to 2000–2002. Journal of Geophysical Research: Biogeosciences, 128(1):e2021JG006763, 1 2023. ISSN 2169-8953. . URL https://doi.org/10.1029/2021JG006763.

Fredrik Moberg and Carl Folke. Ecological goods and services of coral reef ecosystems. Ecological economics, 29:215–233, 1999. ISSN 0921-8009.

Samuel A. Monk, Allison Schaap, Rudolf Hanz, Sergey M. Borisov, Socratis Loucaides, Martin Arundell, Stathys Papadimitriou, John Walk, Daisy Tong, James Wyatt, and Matthew Mowlem. Detecting and mapping a co2 plume with novel autonomous ph sensors on an underwater vehicle. International Journal of Greenhouse Gas Control, 112:103477, 12 2021. ISSN 1750-5836. .

Samuel Andrew Monk. Development of an autonomous dissolved inorganic carbon sensor for oceanic measurements. 2020.

Grigory Isayev Monterey and Sydney Levitus. Seasonal variability of mixed layer depth for the world ocean. NOAA atlas NESDIS, 14, 1997.

Sean Morgan, Sara Wong, Tyler Byrne, Adam Comeau, Brian Ward, Mark Barry, and Dariia Atamanchuk. Wave glider-based measurements and corrections of near-surface pco2 gradients in the coastal ocean. Global Biogeochemical Cycles, 39: e2024GB008396, 7 2025. ISSN 0886-6236. . URL https://doi.org/10.1029/2024GB008396.

Luke M Mosley, Shamus L G Husheer, and Keith A Hunter. Spectrophotometric ph measurement in estuaries using thymol blue and m-cresol purple. Marine Chemistry, 91:175–186, 2004. ISSN 0304-4203. . URL https://www.sciencedirect.com/science/article/pii/S0304420304001823.

Aurélie Moya, Sylvie Tambutté, Eric Tambutté, Didier Zoccola, Natacha Caminiti, and Denis Allemand. Study of calcification during a daily cycle of the coral stylophora

pistillata: implications forlight-enhanced calcification'. Journal of Experimental Biology, 209:3413–3419, 2006. ISSN 1477-9145.

Jens D Müller and Gregor Rehder. Metrology of pH measurements in brackish waters—part 2: Experimental characterization of purified meta-cresol purple for spectrophotometric pHT measurements. Frontiers in Marine Science, Volume 5 - 2018, 2018. ISSN 2296-7745. URL https://www.frontiersin.org/journals/marine-science/articles/10.3389/fmars.2018.00177.

Engineering National Academies of Sciences and Medicine. A Research Strategy for Ocean-based Carbon Dioxide Removal and Sequestration. The National Academies Press, Washington, DC, 2022. ISBN 978-0-309-08761-2. . URL https://nap.nationalacademies.org/catalog/26278/a-research-strategy-for-ocean-based-carbon-dioxide-removal-and-sequestration.

Münevver Nehir, Mario Esposito, Socratis Loucaides, and Eric P Achterberg. Field application of automated spectrophotometric analyzer for high-resolution in situ monitoring of ph in dynamic estuarine and coastal waters. Frontiers in Marine Science, 9, 2022. ISSN 2296-7745. URL https://www.frontiersin.org/journals/marine-science/articles/10.3389/fmars.2022.891876.

J.A. Newton, E.B. Jewett, B. Tilbrook, R. Bellerby, F. Chai, C.-T. A. Chen, S. Dupont, R. A. Feely, H. S. Findlay, L. Hansson, A.E.R. Hassoun, K. Isensee, S. Khokiattiwong, E. Mayorga, R.D. McIntosh, B. Pfeil, K. L. Schoo, N. Shaltout, and C. Vargas. Global ocean acidification observing network (goa-on) implementation strategy, 2019. Technical report, Global Ocean Acidification Observing Network (GOA-ON), 2019. URL www.goa-on.org.

Jan Newton, Richard Feely, Elizabeth Jewett, Phillip Williamson, and Jeremy Mathis. Global ocean acidification observing network: Requirements and governance plan, 2015. URL https://research-portal.uea.ac.uk/en/publications/global-ocean-acidification-observing-network-requirements-and-gov.

S Nickford, J B Palter, and L Mu. The importance of contemporaneous wind and pco2 measurements for regional air-sea co2 flux estimates. Journal of Geophysical Research: Oceans, 129:e2023JC020744, 6 2024. ISSN 2169-9275. . URL https://doi.org/10.1029/2023JC020744.

Devon Northcott, Jeff Sevadjian, Diego A. Sancho-Gallegos, Chris Wahl, Jules Friederich, and Francisco P. Chavez. Impacts of urban carbon dioxide emissions on sea-air flux and ocean acidification in nearshore waters. PLOS ONE, 14:e0214403, 3 2019. ISSN 1932-6203. . URL https://journals.plos.org/plosone/article?id=10.1371/journal.pone.0214403.

I R G Ogilvie, V J Sieben, C F A Floquet, R Zmijan, M C Mowlem, and H Morgan. Reduction of surface roughness for optical quality microfluidic devices in pmma

and coc. Journal of Micromechanics and Microengineering, 20(6):065016, may 2010. . URL https://doi.org/10.1088/0960-1317/20/6/065016.

A Olsen, R M Key, S van Heuven, S K Lauvset, A Velo, X Lin, C Schirnick, A Kozyr, T Tanhua, M Hoppema, S Jutterström, R Steinfeldt, E Jeansson, M Ishii, F F Pérez, and T Suzuki. The global ocean data analysis project version 2 (glodapv2) – an internally consistent data product for the world ocean. Earth Syst. Sci. Data, 8: 297–323, 8 2016. ISSN 1866-3516. . URL https://essd.copernicus.org/articles/8/297/2016/https://essd.copernicus.org/articles/8/297/2016/essd-8-297-2016.pdf.

J. C. Orr, J. M. Epitalon, and J. P. Gattuso. Comparison of ten packages that compute ocean carbonate chemistry. Biogeosciences, 12:1483–1510, 3 2015. ISSN 17264189. .

James C Orr, Victoria J Fabry, Olivier Aumont, Laurent Bopp, Scott C Doney, Richard A Feely, Anand Gnanadesikan, Nicolas Gruber, Akio Ishida, Fortunat Joos, Robert M Key, Keith Lindsay, Ernst Maier-Reimer, Richard Matear, Patrick Monfray, Anne Mouchet, Raymond G Najjar, Gian-Kasper Plattner, Keith B Rodgers, Christopher L Sabine, Jorge L Sarmiento, Reiner Schlitzer, Richard D Slater, Ian J Totterdell, Marie-France Weirig, Yasuhiro Yamanaka, and Andrew Yool. Anthropogenic ocean acidification over the twenty-first century and its impact on calcifying organisms. Nature, 437:681–686, 2005. ISSN 1476-4687. . URL https://doi.org/10.1038/nature04095.

James C. Orr, Jean Marie Epitalon, Andrew G. Dickson, and Jean Pierre Gattuso. Routine uncertainty propagation for the marine carbon dioxide system. Marine Chemistry, 207:84–107, 2018. ISSN 03044203. .

DW O'Sullivan and F J Millero. Continual measurement of the total inorganic carbon in surface seawater. Marine Chemistry, 60:75–83, 1998. ISSN 0304-4203. . URL https://www.sciencedirect.com/science/article/pii/S0304420397000790.

Sebastian Overmans and Susana Agustí. Latitudinal gradient of uv attenuation along the highly transparent red sea basin. Photochemistry and Photobiology, 95: 1267–1279, 9 2019. ISSN 0031-8655. . URL https://doi.org/10.1111/php.13112.

P Kilho Park. Oceanic co2 system: An evaluation of ten methods of investigation. Limnology and Oceanography, 14:179–186, 3 1969. ISSN 0024-3590. . URL https://doi.org/10.4319/lo.1969.14.2.0179.

Fiz F Perez and F Fraga. Association constant of fluoride and hydrogen ions in seawater. Marine Chemistry, 21:161–168, 1987. ISSN 0304-4203. . URL https://www.sciencedirect.com/science/article/pii/0304420387900363.

Chris T Perry, Lorenzo Alvarez-Filip, Nicholas A J Graham, Peter J Mumby, Shaun K Wilson, Paul S Kench, Derek P Manzello, Kyle M Morgan, Aimee B A Slangen,

Damian P Thomson, Fraser Januchowski-Hartley, Scott G Smithers, Robert S Steneck, Renee Carlton, Evan N Edinger, Ian C Enochs, Nuria Estrada-Saldívar, Michael D E Haywood, Graham Kolodziej, Gary N Murphy, Esmeralda Pérez-Cervantes, Adam Suchley, Lauren Valentino, Robert Boenish, Margaret Wilson, and Chancey Macdonald. Loss of coral reef growth capacity to track future increases in sea level. Nature, 558:396–400, 2018. ISSN 1476-4687. . URL https://doi.org/10.1038/s41586-018-0194-z.

Alexander B Phillips, Robert Templeton, Daniel Roper, Richard Morrison, Miles Pebody, Philip M Bagley, Rachel Marlow, Ed Chaney, James Burris, Alberto Consensi, Davide Fenucci, Francesco Fanelli, Achille Martin, Georgios Salavasidis, Owain Jones, Ashley Morris, Catherine A Harris, Alvaro Lorenzo, and Maaten Furlong. Autosub long range 1500: A continuous 2000 km field trial. Ocean Engineering, 280:114626, 2023. ISSN 0029-8018. . URL https://www.sciencedirect.com/science/article/pii/S0029801823010107.

D. D. Pickup, D. C. E. Bakker, K. J. Heywood, F. Glassup, E. Hammermeister, S. E. Stammerjohn, G. A. Lee, S. Loucaides, B. Y. Queste, B. G. M. Webber, and P. L. Yager. Cold lenses in the amundsen sea: Impacts of sea ice formation on subsurface ph and carbon. EGUsphere, 2025:1–23, 2025. . URL https://egusphere.copernicus.org/preprints/2025/egusphere-2025-2441/.

N J Pilcher. Corals and Human Disturbance, pages 671–677. Academic Press, 2001. ISBN 978-0-12-374473-9. . URL https://www.sciencedirect.com/science/article/pii/B9780123744739004896.

Chiara Pisapia, Eric Jeremy Hochberg, and Robert Carpenter. Multi-decadal change in reef-scale production and calcification associated with recent disturbances on a lizard island reef flat. Frontiers in Marine Science, 6:462771, 9 2019. ISSN 22967745. . URL www.frontiersin.org.

Plymouth Marine Laboratory and M. Yang. Penlee point atmospheric observatory: Meteorological and chemical observations 2014–present, 2017. URL https://catalogue.ceda.ac.uk/uuid/8f1ff8ea77534e08b03983685990a9b0. Accessed: November 7, 2024.

Luca Possenti, Matthew P. Humphreys, Dorothee C. E. Bakker, Marcos Cobas-García, Liam Fernand, Gareth A. Lee, Francesco Pallottino, Socratis Loucaides, Matt Charles Mowlem, and Jan Kaiser. Air-sea gas fluxes and remineralization from a novel combination of ph and o2 sensors on a glider. Frontiers in Marine Science, 8, 2021. ISSN 2296-7745. .

Elimar Precht and Markus Huettel. Advective pore-water exchange driven by surface gravity waves and its ecological implications. Limnology and Oceanography, 48:

1674–1684, 7 2003. ISSN 0024-3590. . URL https://doi.org/10.4319/lo.2003.48.4.1674.

PMEL Carbon Program. Hawaii carbon dioxide time-series, 2024. URL https://www.pmel.noaa.gov/co2/file/Hawaii%20Carbon%20Dioxide%20Time-Series.

Li Qiu, Quanlong Li, Dongxing Yuan, Jinshun Chen, Jiezhen Xie, Kunshan Jiang, Liguo Guo, Guibin Zhong, Bo Yang, and Eric P Achterberg. High-precision in situ total alkalinity analyzer capable of month-long observations in seawaters. ACS Sensors, 8:2702–2712, 7 2023. . URL https://doi.org/10.1021/acssensors.3c00552. doi: 10.1021/acssensors.3c00552.

Corinne Le Quéré, Michael R Raupach, Josep G Canadell, Gregg Marland, Laurent Bopp, Philippe Ciais, Thomas J Conway, Scott C Doney, Richard A Feely, Pru Foster, Pierre Friedlingstein, Kevin Gurney, Richard A Houghton, Joanna I House, Chris Huntingford, Peter E Levy, Mark R Lomas, Joseph Majkut, Nicolas Metzl, Jean P Ometto, Glen P Peters, I Colin Prentice, James T Randerson, Steven W Running, Jorge L Sarmiento, Ute Schuster, Stephen Sitch, Taro Takahashi, Nicolas Viovy, Guido R van der Werf, and F Ian Woodward. Trends in the sources and sinks of carbon dioxide. Nature Geoscience, 2:831–836, 2009a. ISSN 1752-0908. . URL https://doi.org/10.1038/ngeo689.

Corinne Le Quéré, Michael R Raupach, Josep G Canadell, Gregg Marland, Laurent Bopp, Philippe Ciais, Thomas J Conway, Scott C Doney, Richard A Feely, Pru Foster, Pierre Friedlingstein, Kevin Gurney, Richard A Houghton, Joanna I House, Chris Huntingford, Peter E Levy, Mark R Lomas, Joseph Majkut, Nicolas Metzl, Jean P Ometto, Glen P Peters, I Colin Prentice, James T Randerson, Steven W Running, Jorge L Sarmiento, Ute Schuster, Stephen Sitch, Taro Takahashi, Nicolas Viovy, Guido R van der Werf, and F Ian Woodward. Trends in the sources and sinks of carbon dioxide. Nature Geoscience, 2:831–836, 2009b. ISSN 1752-0908. . URL https://doi.org/10.1038/ngeo689.

Lorenza Raimondi, John Brian Robin Matthews, Dariia Atamanchuk, Kumiko Azetsu-Scott, and Douglas W R Wallace. The internal consistency of the marine carbon dioxide system for high latitude shipboard and in situ monitoring. Marine Chemistry, 213:49–70, 2019. ISSN 0304-4203. . URL https://www.sciencedirect.com/science/article/pii/S0304420318301671.

Alexandra M F Rao, Lubos Polerecky, Danny Ionescu, Filip J R Meysman, and Dirk de Beer. The influence of pore-water advection, benthic photosynthesis, and respiration on calcium carbonate dynamics in reef sands. Limnology and Oceanography, 57:809–825, 5 2012. ISSN 0024-3590. . URL https://doi.org/10.4319/lo.2012.57.3.0809.

Marjorie L Reaka-Kudla. The global biodiversity of coral reefs: a comparison with rain forests. Biodiversity II: Understanding and protecting our biological resources, 2: 551, 1997.

Pierre Regnier, Pierre Friedlingstein, Philippe Ciais, Fred T Mackenzie, Nicolas Gruber, Ivan A Janssens, Goulven G Laruelle, Ronny Lauerwald, Sebastiaan Luyssaert, Andreas J Andersson, Sandra Arndt, Carol Arnosti, Alberto V Borges, Andrew W Dale, Angela Gallego-Sala, Yves Goddéris, Nicolas Goossens, Jens Hartmann, Christoph Heinze, Tatiana Ilyina, Fortunat Joos, Douglas E LaRowe, Jens Leifeld, Filip J R Meysman, Guy Munhoven, Peter A Raymond, Renato Spahni, Parvadha Suntharalingam, and Martin Thullner. Anthropogenic perturbation of the carbon fluxes from land to ocean. Nature Geoscience, 6:597–607, 2013. ISSN 1752-0908. . URL https://doi.org/10.1038/ngeo1830.

Walter A Rich, Susana Carvalho, and Michael L Berumen. Coral bleaching due to cold stress on a central red sea reef flat. Ecology and Evolution, 12:e9450, 10 2022. ISSN 2045-7758. . URL https://doi.org/10.1002/ece3.9450.

K R Ridgway, J R Dunn, and J L Wilkin. Ocean interpolation by four-dimensional weighted least squares—application to the waters around australasia. Journal of Atmospheric and Oceanic Technology, 19:1357–1375, 2002. . URL https://journals.ametsoc.org/view/journals/atot/19/9/1520-0426_2002_019_1357_oibfdw_2_0_co_2.xml.

C. Roder, M. L. Berumen, J. Bouwmeester, E. Papathanassiou, A. Al-Suwailem, and C. R. Voolstra. First biological measurements of deep-sea corals from the red sea. Scientific Reports, 3:1–10, 10 2013. ISSN 20452322. . URL https://www.nature.com/articles/srep02802.

Dean Roemmich, Matthew H Alford, Hervé Claustre, Kenneth Johnson, Brian King, James Moum, Peter Oke, W Brechner Owens, Sylvie Pouliquen, Sarah Purkey, Megan Scanderbeg, Toshio Suga, Susan Wijffels, Nathalie Zilberman, Dorothee Bakker, Molly Baringer, Mathieu Belbeoch, Henry C Bittig, Emmanuel Boss, Paulo Calil, Fiona Carse, Thierry Carval, Fei Chai, Diarmuid Ó Conchubhair, Fabrizio d'Ortenzio, Giorgio Dall'Olmo, Damien Desbruyeres, Katja Fennel, Ilker Fer, Raffaele Ferrari, Gael Forget, Howard Freeland, Tetsuichi Fujiki, Marion Gehlen, Blair Greenan, Robert Hallberg, Toshiyuki Hibiya, Shigeki Hosoda, Steven Jayne, Markus Jochum, Gregory C Johnson, KiRyong Kang, Nicolas Kolodziejczyk, Arne Körtzinger, Pierre-Yves Le Traon, Yueng-Djern Lenn, Guillaume Maze, Kjell Arne Mork, Tamaryn Morris, Takeyoshi Nagai, Jonathan Nash, Alberto Naveira Garabato, Are Olsen, Rama Rao Pattabhi, Satya Prakash, Stephen Riser, Catherine Schmechtig, Claudia Schmid, Emily Shroyer, Andreas Sterl, Philip Sutton, Lynne Talley, Toste Tanhua, Virginie Thierry, Sandy Thomalla, John Toole, Ariel Troisi, Thomas W Trull, Jon Turton, Pedro Joaquin Velez-Belchi, Waldemar Walczowski,

Haili Wang, Rik Wanninkhof, Amy F Waterhouse, Stephanie Waterman, Andrew Watson, Cara Wilson, Annie P S Wong, Jianping Xu, and Ichiro Yasuda. On the future of argo: A global, full-depth, multi-disciplinary array. Frontiers in Marine Science, Volume 6 - 2019, 2019. ISSN 2296-7745. URL https://www.frontiersin.org/journals/marine-science/articles/10.3389/fmars.2019.00439.

A Roik, T Röthig, C Pogoreutz, V Saderne, and C R Voolstra. Coral reef carbonate budgets and ecological drivers in the central red sea – a naturally high temperature and high total alkalinity environment. Biogeosciences, 15:6277–6296, 10 2018. ISSN 1726-4189. . URL https://bg.copernicus.org/articles/15/6277/2018/https://bg.copernicus.org/articles/15/6277/2018/bg-15-6277-2018.pdf.

Anna Roik, Till Röthig, Cornelia Roder, Maren Ziegler, Stephan G. Kremb, and Christian R. Voolstra. Year-long monitoring of physico-chemical and biological variables provide a comparative baseline of coral reef functioning in the central red sea. PLOS ONE, 11:e0163939, 11 2016. ISSN 1932-6203. . URL https://journals.plos.org/plosone/article?id=10.1371/journal.pone.0163939.

Alizée Roobaert, Goulven G Laruelle, Peter Landschützer, Nicolas Gruber, Lei Chou, and Pierre Regnier. The spatiotemporal dynamics of the sources and sinks of co2 in the global coastal ocean. Global Biogeochemical Cycles, 33:1693–1714, 12 2019. ISSN 0886-6236. . URL https://doi.org/10.1029/2019GB006239.

Mario Roos-Hoefgeest Toribio, Alejandro Garnung Menéndez, Sara Roos-Hoefgeest Toribio, and Ignacio Álvarez García. A Novel Approach to Speed Up Hampel Filter for Outlier Detection. Sensors (Basel, Switzerland), 25(11):3319, 6 2025. ISSN 14248220. . URL https://pmc.ncbi.nlm.nih.gov/articles/PMC12157161/.

Daniel Roper, Catherine A. Harris, Georgios Salavasidis, Miles Pebody, Robert Templeton, Thomas Prampart, Matthew Kingsland, Richard Morrison, Maaten Furlong, Alexander B. Phillips, and Stephen McPhail. Autosub long range 6000: A multiple-month endurance auv for deep-ocean monitoring and survey. IEEE Journal of Oceanic Engineering, 46:1179–1191, 10 2021. ISSN 15581691. .

Florian Roth, Nils RAdecker, Susana Carvalho, Carlos M. Duarte, Vincent Saderne, Andrea Anton, Luis Silva, Maria Ll Calleja, XosÉ Anxelu G. MorÁn, Christian R. Voolstra, Benjamin Kürten, Burton H. Jones, and Christian Wild. High summer temperatures amplify functional differences between coral- and algae-dominated reef communities. Ecology, 102:e03226, 2 2020. ISSN 19399170. . URL https://pmc.ncbi.nlm.nih.gov/articles/PMC7900985/.

Florian Roth, Yusuf C El-Khaled, Denis B Karcher, Nils Rädecker, Susana Carvalho, Carlos M Duarte, Luis Silva, Maria Ll. Calleja, Xosé Anxelu G Morán, Burton H Jones, Christian R Voolstra, and Christian Wild. Nutrient pollution enhances

productivity and framework dissolution in algae- but not in coral-dominated reef communities. Marine Pollution Bulletin, 168:112444, 2021. ISSN 0025-326X. . URL https://www.sciencedirect.com/science/article/pii/S0025326X21004781.

Rob Rowan. Review—diversity and ecology of zooxanthellae on coral reefs. Journal of Phycology, 34:407–417, 6 1998. ISSN 0022-3646. . URL https://doi.org/10.1046/j.1529-8817.1998.340407.x.

Victoire Rérolle, Diana Ruiz-Pino, Mehrad Rafizadeh, Socratis Loucaides, Stathys Papadimitriou, Matthew Mowlem, and Jianfang Chen. Measuring ph in the arctic ocean: Colorimetric method or seafet? Methods in Oceanography, 17:32–49, 2016. ISSN 2211-1220. . URL https://www.sciencedirect.com/science/article/pii/S2211122015300244.

Victoire M C Rérolle, Cedric F A Floquet, Matt C Mowlem, Douglas P Connelly, Eric P Achterberg, and Richard R G J Bellerby. Seawater-pH measurements for ocean-acidification observations. TrAC Trends in Analytical Chemistry, 40:146–157, 2012. ISSN 0165-9936. . URL https://www.sciencedirect.com/science/article/pii/S0165993612002427.

Victoire M.C. Rérolle, Cedric F.A. Floquet, Andy J.K. Harris, Matt C. Mowlem, Richard R.G.J. Bellerby, and Eric P. Achterberg. Development of a colorimetric microfluidic ph sensor for autonomous seawater measurements. Analytica Chimica Acta, 786:124–131, 7 2013. ISSN 00032670. . URL https://pubmed.ncbi.nlm.nih.gov/23790301/.

Kenneth s. Johnson, Joshua n. Plant, Tanya l. Maurer, and Yuichihiro Takeshita. Processing bgc-argo ph data at the dac level, 2023. URL https://doi.org/10.13155/57195.

Grace K. Saba, Elizabeth Wright-Fairbanks, Travis N. Miles, Baoshan Chen, Wei Jun Cai, Kui Wang, Andrew H. Barnard, Charles W. Branham, and Clayton P. Jones. Developing a profiling glider ph sensor for high resolution coastal ocean acidification monitoring. undefined, 1 2018. .

Grace K Saba, Elizabeth Wright-Fairbanks, Baoshan Chen, Wei-Jun Cai, Andrew H Barnard, Clayton P Jones, Charles W Branham, Kui Wang, and Travis Miles. The development and validation of a profiling glider deep isfet-based ph sensor for high resolution observations of coastal and ocean acidification. Frontiers in Marine Science, 6, 2019. ISSN 2296-7745. URL https://www.frontiersin.org/journals/marine-science/articles/10.3389/fmars.2019.00664.

Christopher Sabine, Adrienne Sutton, Kelly McCabe, Noah Lawrence-Slavas, Simone Alin, Richard Feely, Richard Jenkins, Stacy Maenner, Christian Meinig, Jesse Thomas, ERIK VAN Ooijen, Abe Passmore, and Bronte Tilbrook. Evaluation of a

new carbon dioxide system for autonomous surface vehicles. undefined, 37: 1305–1317, 2020. ISSN 15200426. .

Vincent Saderne, Kimberlee Baldry, Andrea Anton, Susana Agustí, and Carlos M Duarte. Characterization of the co2 system in a coral reef, a seagrass meadow, and a mangrove forest in the central red sea. Journal of Geophysical Research: Oceans, 124:7513–7528, 11 2019. ISSN 2169-9275. . URL https://doi.org/10.1029/2019JC015266.

Malcolm Sambridge, Jean Braun, and Herbert McQueen. Geophysical parametrization and interpolation of irregular data using natural neighbours. Geophysical Journal International, 122:837–857, 12 1995. ISSN 0956-540X. . URL https://doi.org/10.1111/j.1365-246X.1995.tb06841.x.

Raphaëlle Sauzède, Henry C Bittig, Hervé Claustre, Orens Pasqueron de Fommervault, Jean-Pierre Gattuso, Louis Legendre, and Kenneth S Johnson. Estimates of water-column nutrient concentrations and carbonate system parameters in the global ocean: A novel approach based on neural networks. Frontiers in Marine Science, Volume 4 - 2017, 2017. ISSN 2296-7745. URL https://www.frontiersin.org/journals/marine-science/articles/10.3389/fmars.2017.00128.

F. L. Sayles and Calvert Eck. An autonomous instrument for time series analysis of tco2 from oceanographic moorings. Deep-Sea Research Part I: Oceanographic Research Papers, 56:1590–1603, 9 2009. ISSN 09670637. .

Allison Schaap, Dirk Koopmans, Moritz Holtappels, Marius Dewar, Martin Arundell, Stathys Papadimitriou, Rudolf Hanz, Samuel Monk, Matthew Mowlem, and Socratis Loucaides. Quantification of a subsea co2 release with lab-on-chip sensors measuring benthic gradients. International Journal of Greenhouse Gas Control, 110: 103427, 9 2021a. ISSN 1750-5836. .

Allison Schaap, Dirk Koopmans, Moritz Holtappels, Marius Dewar, Martin Arundell, Stathys Papadimitriou, Rudolf Hanz, Samuel Monk, Matthew Mowlem, and Socratis Loucaides. Quantification of a subsea CO2 release with lab-on-chip sensors measuring benthic gradients. International Journal of Greenhouse Gas Control, 110: 103427, 9 2021b. ISSN 1750-5836. .

Allison Schaap, Stathys Papadimitriou, Edward Mawji, John Walk, Emily Hammermeister, Matthew Mowlem, and Socratis Loucaides. Autonomous sensor for in situ measurements of total alkalinity in the ocean. ACS Sensors, 10:795–803, 2 2025. . URL https://doi.org/10.1021/acssensors.4c02349. doi: 10.1021/acssensors.4c02349.

Verena Schoepf, Andréa G Grottoli, Stephen J Levas, Matthew D Aschaffenburg, Justin H Baumann, Yohei Matsui, and Mark E Warner. Annual coral bleaching and

the long-term recovery capacity of coral. Proceedings of the Royal Society B: Biological Sciences, 282:20151887, 11 2015. . URL https://doi.org/10.1098/rspb.2015.1887. doi: 10.1098/rspb.2015.1887.

U Schuster, G A McKinley, N Bates, F Chevallier, S C Doney, A R Fay, M González-Dávila, N Gruber, S Jones, J Krijnen, P Landschützer, N Lefèvre, M Manizza, J Mathis, N Metzl, A Olsen, A F Rios, C Rödenbeck, J M Santana-Casiano, T Takahashi, R Wanninkhof, and A J Watson. An assessment of the atlantic and arctic sea–air co¡sub¿2¡/sub¿ fluxes, 1990–2009. Biogeosciences, 10: 607–627, 1 2013. ISSN 1726-4189. . URL https://bg.copernicus.org/articles/10/607/2013/https://bg.copernicus.org/articles/10/607/2013/bg-10-607-2013.pdf.

Sea-Bird Scientific. ECO Triplet-w | Sea-Bird Scientific - Overview | Sea-Bird, June 2023. URL https://www.seabird.com/eco-triplet-w/product?id=60762467721. ECO Triplet-w User Manual PDF download.

Sea-Bird Scientific. Calculating pH from ISFET pH sensors. Technical Report Application Note 99, Sea-Bird Scientific, March 2024. URL https://www.seabird.com/asset-get.download.jsa?id=54676777052. Accessed: 2025-03-04.

Sea-Bird Scientific. SeaFET™ V2 Ocean pH Sensor Datasheet and User Manual. Sea-Bird Scientific, May 2025. Datasheet (May 2025) and User Manual (rev E, July 2024).

Isabel Seguro, Alina D Marca, Suzanne J Painting, Jamie D Shutler, David J Suggett, and Jan Kaiser. High-resolution net and gross biological production during a celtic sea spring bloom. Progress in Oceanography, 177:101885, 2019. ISSN 0079-6611. . URL https://www.sciencedirect.com/science/article/pii/S0079661117300812.

Matthew P Seidel, Michael D DeGrandpre, and Andrew G Dickson. A sensor for in situ indicator-based measurements of seawater ph. Marine Chemistry, 109:18–28, 2008. ISSN 0304-4203. . URL https://www.sciencedirect.com/science/article/pii/S0304420307002782.

Hawai'i Ocean Time series (HOT). Hot surface seawater $co_2$ and ph data at station aloha. https://hahana.soest.hawaii.edu/hot/hotco2/HOT_surface_CO2.txt, 2025.

K E F Shamberger, R A Feely, C L Sabine, M J Atkinson, E H Decarlo, F T Mackenzie, P S Drupp, and D A Butterfield. Calcification and organic production on a hawaiian coral reef. 2011. . URL www.pmel.noaa.gov/co2.

Qipei Shangguan, Adam Prody, Taylor S Wirth, Ellen M Briggs, Todd R Martz, and Michael D DeGrandpre. An inter-comparison of autonomous in situ instruments for ocean co2 measurements under laboratory-controlled conditions. Marine Chemistry, 240:104085, 2022. ISSN 0304-4203. . URL https://www.sciencedirect.com/science/article/pii/S0304420322000020.

Jonathan D Sharp and Robert H Byrne. Technical note: Excess alkalinity in carbonate system reference materials. Marine Chemistry, 233:103965, 2021. ISSN 0304-4203. . URL https://www.sciencedirect.com/science/article/pii/S0304420321000505.

Jonathan D Sharp, Denis Pierrot, Matthew P Humphreys, Jean-Marie Epitalon, James C Orr, Ernie R Lewis, and Douglas W R Wallace. Co2sysv3 for matlab. 6 2023a. . URL https://zenodo.org/record/7552554.

Jonathan D. Sharp, Denis Pierrot, Matthew P. Humphreys, Jean-Marie Epitalon, James C. Orr, Ernie R. Lewis, and Douglas W.R. Wallace. Co2sysv3 for matlab, January 2023b. URL https://doi.org/10.5281/zenodo.7552554.

Emily C Shaw, Stuart R Phinn, Bronte Tilbrook, and Andy Steven. Comparability of slack water and lagrangian flow respirometry methods for community metabolic measurements. PLOS ONE, 9:e112161–, 11 2014. URL https://doi.org/10.1371/journal.pone.0112161.

Robin Sibson. A brief description of natural neighbour interpolation. Interpreting multivariate data, pages 21–36, 1981.

Jacob Silverman, Boaz Lazar, and Jonathan Erez. Effect of aragonite saturation, temperature, and nutrients on the community calcification rate of a coral reef. Journal of Geophysical Research: Oceans, 112, 5 2007. ISSN 0148-0227. . URL https://doi.org/10.1029/2006JC003770.

Bernadette M. Sloyan, Rik Wanninkhof, Martin Kramp, Gregory C. Johnson, Lynne D. Talley, Toste Tanhua, Elaine McDonagh, Caroline Cusack, Eleanor O'Rourke, Evin McGovern, Katsuro Katsumata, Steve Diggs, Julia Hummon, Masao Ishii, Kumiko Azetsu-Scott, Emmanuel Boss, Isabelle Ansorge, Fiz F. Perez, Herlé Mercier, Michael J. M. Williams, Leif Anderson, Jae Hak Lee, Akihiko Murata, Shinya Kouketsu, Emil Jeansson, Mario Hoppema, and Edmo Campos. The global ocean ship-based hydrographic investigations program (go-ship): A platform for integrated multidisciplinary ocean science. Frontiers in Marine Science, 6, 2019. ISSN 2296-7745. . URL https://www.frontiersin.org/journals/marine-science/articles/10.3389/fmars.2019.00445.

Jennifer E Smith, Rusty Brainard, Amanda Carter, Saray Grillo, Clinton Edwards, Jill Harris, Levi Lewis, David Obura, Forest Rohwer, Enric Sala, Peter S Vroom, and

Stuart Sandin. Re-evaluating the health of coral reef communities: baselines and evidence for human impacts across the central pacific. Proceedings of the Royal Society B: Biological Sciences, 283:20151985, 1 2016. . URL https://doi.org/10.1098/rspb.2015.1985. doi: 10.1098/rspb.2015.1985.

S V Smith. Carbon dioxide dynamics: A record of organic carbon production, respiration, and calcification in the eniwetok reef flat community. Limnology and Oceanography, 18:106–120, 1 1973. ISSN 0024-3590. . URL https://doi.org/10.4319/lo.1973.18.1.0106.

Colin Sonnichsen, Dariia Atamanchuk, Andre Hendricks, Sean Morgan, James Smith, Iain Grundke, Edward Luy, and Vincent Joseph Sieben. An automated microfluidic analyzer for in situ monitoring of total alkalinity. ACS Sensors, 8:344–352, 1 2023. . URL https://doi.org/10.1021/acssensors.2c02343. doi: 10.1021/acssensors.2c02343.

Reggie S Spaulding, Michael D DeGrandpre, James C Beck, Robert D Hart, Brittany Peterson, Eric H De Carlo, Patrick S Drupp, and Terry R Hammar. Autonomous in situ measurements of seawater alkalinity. Environmental Science  Technology, 48: 9573–9581, 8 2014. ISSN 0013-936X. . URL https://doi.org/10.1021/es501615x. doi: 10.1021/es501615x.

Zvi Steiner, Alexandra V Turchyn, Eyal Harpaz, and Jacob Silverman. Water chemistry reveals a significant decline in coral calcification rates in the southern red sea. Nature Communications, 9:3615, 2018. ISSN 2041-1723. . URL https://doi.org/10.1038/s41467-018-06030-6.

Laura Stoltenberg, Kai G Schulz, Coulson A Lantz, Tyler Cyronak, and Bradley D Eyre. Late afternoon seasonal transition to dissolution in a coral reef: An early warning of a net dissolving ecosystem? Geophysical Research Letters, 48:e2020GL090811, 3 2021. ISSN 0094-8276. . URL https://doi.org/10.1029/2020GL090811.

Werner Stumm and James J Morgan. Aquatic Chemistry. John Wiley  Sons, third edition, 1996. ISBN 9780471511854.

William G Sunda and Alfred K Hanson. Measurement of free cupric ion concentration in seawater by a ligand competition technique involving copper sorption onto c 1 8 sep-pak cartridges', 1987.

A. J. Sutton, C. L. Sabine, S. Maenner-Jones, N. Lawrence-Slavas, C. Meinig, R. A. Feely, J. T. Mathis, S. Musielewicz, R. Bott, P. D. McLain, H. J. Fought, and A. Kozyr. A high-frequency atmospheric and seawater pco2 data set from 14 open-ocean sites using a moored autonomous system. Earth System Science Data, 6:353–366, 11 2014. ISSN 18663516. .

A J Sutton, N L Williams, and B Tilbrook. Constraining southern ocean co2 flux uncertainty using uncrewed surface vehicle observations. Geophysical Research Letters, 48:e2020GL091748, 2 2021. ISSN 0094-8276. . URL https://doi.org/10.1029/2020GL091748.

Adrienne J. Sutton and Christopher L. Sabine. Emerging applications of longstanding autonomous ocean carbon observations. Oceanography, 36:148–155, 10 2023. ISSN 10428275. .

A Suzuki, Toru Nakamori, and H Kayanne. The mechanism of production enhancement in coral reef carbonate systems: model and empirical results. Sedimentary Geology, 99:259–280, 1995. ISSN 0037-0738.

Taro Takahashi, S C Sutherland, D W Chipman, J G Goddard, Cheng Ho, Timothy Newberger, Colm Sweeney, and D R Munro. Climatological distributions of ph, pco2, total co2, alkalinity, and caco3 saturation in the global surface ocean, and temporal changes at selected locations. Marine Chemistry, 164:95–125, 2014. ISSN 0304-4203. . URL https://www.sciencedirect.com/science/article/pii/S0304420314001042.

Yuichiro Takeshita, Tyler Cyronak, Todd R Martz, Theodor Kindeberg, and Andreas J Andersson. Coral reef carbonate chemistry variability at different functional scales. Frontiers in Marine Science, Volume 5 - 2018, 2018. ISSN 2296-7745. URL https://www.frontiersin.org/journals/marine-science/articles/10.3389/fmars.2018.00175.

Yuichiro Takeshita, Brent D Jones, Kenneth S Johnson, Francisco P Chavez, Daniel L Rudnick, Marguerite Blum, Kyle Conner, Scott Jensen, Jacqueline S Long, Thom Maughan, Keaton L Mertz, Jeffrey T Sherman, and Joseph K Warren. Accurate ph and o2 measurements from spray underwater gliders. Journal of Atmospheric and Oceanic Technology, 38:181–195, 2021. . URL https://journals.ametsoc.org/view/journals/atot/38/2/jtech-d-20-0095.1.xml.

Toste Tanhua, Andrea McCurdy, Albert Fischer, Ward Appeltans, Nicholas Bax, Kim Currie, Brad Deyoung, Daniel Dunn, Emma Heslop, Linda K. Glover, John Gunn, Katherine Hill, Masao Ishii, David Legler, Eric Lindstrom, Patricia Miloslavich, Tim Moltmann, Glenn Nolan, Artur Palacz, Samantha Simmons, Bernadette Sloyan, Leslie M. Smith, Neville Smith, Maciej Telszewski, Martin Visbeck, and John Wilkin. What we have learned from the framework for ocean observing: Evolution of the global ocean observing system. Frontiers in Marine Science, 6:436048, 8 2019. ISSN 22967745. .

Pieter Tans. An accounting of the observed increase in oceanic and atmospheric co2 and the outlook for the future. undefined, 22:26–35, 2009. ISSN 10428275. .

Bronte Tilbrook, Elizabeth B. Jewett, Michael D. DeGrandpre, Jose Martin Hernandez-Ayon, Richard A. Feely, Dwight K. Gledhill, Lina Hansson, Kirsten Isensee, Meredith L. Kurz, Janet A. Newton, Samantha A. Siedlecki, Fei Chai, Sam Dupont, Michelle Graco, Eva Calvo, Dana Greeley, Lydia Kapsenberg, Marine Lebrec, Carles Pelejero, Katherina L. Schoo, and Maciej Telszewski. An enhanced ocean acidification observing network: From people to technology to data synthesis and information exchange. Frontiers in Marine Science, 6:436026, 6 2019. ISSN 22967745. . URL www.frontiersin.org.

E A Titlyanov, T V Titlyanova, K Yamazato, and R van Woesik. Photo-acclimation dynamics of the coral stylophora pistillata to low and extremely low light. Journal of Experimental Marine Biology and Ecology, 263:211–225, 2001. ISSN 0022-0981. . URL https://www.sciencedirect.com/science/article/pii/S0022098101003094.

John Trowbridge, Robert Weller, Deborah Kelley, Edward Dever, Albert Plueddemann, John A Barth, and Orest Kawka. The Ocean Observatories Initiative. Frontiers in Marine Science, Volume 6 - 2019, 2019. ISSN 2296-7745. URL https://www.frontiersin.org/journals/marine-science/articles/10.3389/fmars.2019.00074.

UNESCO-IOC. Ocean decade progress report 2023–2024. Technical Report 53, UNESCO, Paris, 2025.

Steven van Heuven, Denis Pierrot, James Rae, Ernie Lewis, and D W R Wallace. CO2SYS v 1.1, matlab program developed for CO2 system calculations, 5 2011a.

Steven van Heuven, Denis Pierrot, James Rae, Ernie Lewis, and D W R Wallace. Co2sys v 1.1, matlab program developed for co2 system calculations, 5 2011b.

van Rein. Marine monitoring platform guidelines autonomous underwater vehicles for use in marine benthic monitoring. 2018. ISSN 2517-7605.

N von Oppeln-Bronikowski, B de Young, D Atamanchuk, and D Wallace. Glider-based observations of co2 in the labrador sea. Ocean Sci., 17:1–16, 1 2021. ISSN 1812-0792. . URL https://os.copernicus.org/articles/17/1/2021/https://os.copernicus.org/articles/17/1/2021/os-17-1-2021.pdf.

Daniel Wagner, Alan M Friedlander, Richard L Pyle, Cassandra M Brooks, Kristina M Gjerde, and T 'Aulani Wilhelm. Coral reefs of the high seas: Hidden biodiversity hotspots in need of protection. Frontiers in Marine Science, Volume 7 - 2020, 2020. ISSN 2296-7745. URL https://www.frontiersin.org/journals/marine-science/articles/10.3389/fmars.2020.567428.

S L Wakelin, J T Holt, J C Blackford, J I Allen, M Butenschön, and Y Artioli. Modeling the carbon fluxes of the northwest european continental shelf: Validation and

budgets. Journal of Geophysical Research: Oceans, 117, 5 2012. ISSN 0148-0227. . URL https://doi.org/10.1029/2011JC007402.

X J Wang, M Behrenfeld, R Le Borgne, R Murtugudde, and E Boss. Regulation of phytoplankton carbon to chlorophyll ratio by light, nutrients and temperature in the equatorial pacific ocean: a basin-scale model. Biogeosciences, 6:391–404, 3 2009. ISSN 1726-4189. . URL https://bg.copernicus.org/articles/6/391/2009/https://bg.copernicus.org/articles/6/391/2009/bg-6-391-2009.pdf.

Yixin Wang, Matthew R Mazloff, Ariane Verdy, Ivana Cerovecki, Malika Kheireddine, Patrick Naylor, George Krokos, and Ibrahim Hoteit. Observations and biogeochemical modeling reveal chlorophyll diel cycle with near-sunset maxima in the red sea. Global Biogeochemical Cycles, 39:e2024GB008226, 2 2025. ISSN 0886-6236. . URL https://doi.org/10.1029/2024GB008226.

Zhaohui Aleck Wang, Gareth L. Lawson, Cynthia H. Pilskaln, and Amy E. Maas. Seasonal controls of aragonite saturation states in the gulf of maine. Journal of Geophysical Research: Oceans, 122:372–389, 1 2017. ISSN 2169-9291. . URL https://onlinelibrary.wiley.com/doi/full/10.1002/2016JC012373https://onlinelibrary.wiley.com/doi/abs/10.1002/2016JC012373https://agupubs.onlinelibrary.wiley.com/doi/10.1002/2016JC012373.

R Wanninkhof, G.-H. Park, T Takahashi, C Sweeney, R Feely, Y Nojiri, N Gruber, S C Doney, G A McKinley, A Lenton, C Le Quéré, C Heinze, J Schwinger, H Graven, and S Khatiwala. Global ocean carbon uptake: magnitude, variability and trends. Biogeosciences, 10:1983–2000, 6 2013. ISSN 1726-4189. . URL https://bg.copernicus.org/articles/10/1983/2013/https://bg.copernicus.org/articles/10/1983/2013/bg-10-1983-2013.pdf.

R Wanninkhof, D Pierrot, K Sullivan, L Barbero, and J Triñanes. A 17-year dataset of surface water fugacity of co2 along with calculated ph, aragonite saturation state and air–sea co2 fluxes in the northern caribbean sea. Earth Syst. Sci. Data, 12: 1489–1509, 7 2020. ISSN 1866-3516. . URL https://essd.copernicus.org/articles/12/1489/2020/https://essd.copernicus.org/articles/12/1489/2020/essd-12-1489-2020.pdf.

Rik Wanninkhof. Relationship between wind speed and gas exchange over the ocean revisited. Limnology and Oceanography: Methods, 12:351–362, 6 2014. ISSN 1541-5856. . URL https://doi.org/10.4319/lom.2014.12.351.

R F Weiss. Carbon dioxide in water and seawater: the solubility of a non-ideal gas. Marine Chemistry, 2:203–215, 1974. ISSN 0304-4203. . URL https://www.sciencedirect.com/science/article/pii/0304420374900152.

Christopher Whitt, Jay Pearlman, Brian Polagye, Frank Caimi, Frank Muller-Karger, Andrea Copping, Heather Spence, Shyam Madhusudhana, William Kirkwood, Ludovic Grosjean, Bilal Muhammad Fiaz, Satinder Singh, Sikandra Singh, Dana Manalang, Ananya Sen Gupta, Alain Maguer, Justin J.H. Buck, Andreas Marouchos, Malayath Aravindakshan Atmanand, Ramasamy Venkatesan, Vedachalam Narayanaswamy, Pierre Testor, Elizabeth Douglas, Sebastien de Halleux, and Siri Jodha Khalsa. Future vision for autonomous ocean observations, 2020. ISSN 22967745.

N. L. Williams, L. W. Juranek, R. A. Feely, K. S. Johnson, J. L. Sarmiento, L. D. Talley, A. G. Dickson, A. R. Gray, R. Wanninkhof, J. L. Russell, S. C. Riser, and Y. Takeshita. Calculating surface ocean pco2 from biogeochemical argo floats equipped with ph: An uncertainty analysis. Global Biogeochemical Cycles, 31:591–604, 3 2017. ISSN 1944-9224. . URL https://onlinelibrary.wiley.com/doi/full/10.1002/2016GB005541https://onlinelibrary.wiley.com/doi/abs/10.1002/2016GB005541https://agupubs.onlinelibrary.wiley.com/doi/10.1002/2016GB005541.

Ludwig Wilhelm Winkler. Die bestimmung des im wasser gelösten sauerstoffes. Berichte der deutschen chemischen Gesellschaft, 21(2):2843–2854, 1888. . URL https://chemistry-europe.onlinelibrary.wiley.com/doi/abs/10.1002/cber.188802102122.

G Winters, S Beer, BB Zvi, I Brickner, and Y Loya. Spatial and temporal photoacclimation of stylophora pistillata: zooxanthella size, pigmentation, location and clade. Marine Ecology Progress Series, 384:107–119, 5 2009. ISSN 0171-8630. .

Dieter A. Wolf-Gladrow, Richard E. Zeebe, Christine Klaas, Arne Körtzinger, and Andrew G. Dickson. Total alkalinity: The explicit conservative expression and its application to biogeochemical processes. Marine Chemistry, 106(1-2 SPEC. ISS.): 287–300, 2007a. ISSN 03044203. .

Dieter A. Wolf-Gladrow, Richard E. Zeebe, Christine Klaas, Arne Körtzinger, and Andrew G. Dickson. Total alkalinity: The explicit conservative expression and its application to biogeochemical processes. Marine Chemistry, 106(1):287–300, 2007b. ISSN 0304-4203. . URL https://www.sciencedirect.com/science/article/pii/S0304420307000047. Special issue: Dedicated to the memory of Professor Roland Wollast.

George Wolff. Sarmiento, j. l. gruber, n. 2006. ocean biogeochemical dynamics.xiii + 503 pp. princeton, woodstock: Princeton university press. price £48.95 (hard covers). 0 691 01707 7. Geological Magazine, 144:1034–1034, 11 2007. ISSN 0016-7568. .

M Yang, T G Bell, I J Brown, J R Fishwick, V Kitidis, P D Nightingale, A P Rees, and T J Smyth. Insights from year-long measurements of air–water ch4 and co2 exchange in

a coastal environment. Biogeosciences, 16:961–978, 3 2019. ISSN 1726-4189. . URL https://bg.copernicus.org/articles/16/961/2019/https://bg.copernicus.org/articles/16/961/2019/bg-16-961-2019.pdf.

W. Yao, T. M. Morganti, J. Wu, M. Borchers, A. Anschütz, L. K. Bednarz, K. A. Bhaumik, M. Böttcher, K. Burkhard, T. Cabus, A. S. Chua, I. Diercks, M. Esposito, M. Fink, M. Fouqueray, F. Gasanzade, S. Geilert, J. Hauck, F. Havermann, I. Hellige, S. Hoog, M. Jürchott, H. T. Kalapurakkal, J. Kemper, I. Kremin, I. Lange, J. M. Lencina-Avila, M. Liadova, F. Liu, S. Mathesius, N. Mehendale, T. Nagwekar, M. Philippi, G. L.N. Luz, M. Ramasamy, F. Stahl, L. Tank, M. E. Vorrath, L. Westmark, H. W. Wey, R. Wollnik, M. Wölfelschneider, W. Bach, K. Bischof, M. Boersma, U. Daewel, M. Fernández-Méndez, J. K. Geuer, D. P. Keller, A. Kopf, C. Merk, N. Moosdorf, N. Oppelt, A. Oschlies, J. Pongratz, A. Proelss, G. J. Rehder, L. Rüpke, N. Szarka, D. Thraen, K. Wallmann, and N. Mengis. Exploring site-specific carbon dioxide removal options with storage or sequestration in the marine environment – the 10 mt co2 yr1 removal challenge for germany. Earth's Future, 13:e2024EF004902, 4 2025. ISSN 2328-4277. . URL /doi/pdf/10.1029/2024EF004902https://onlinelibrary.wiley.com/doi/abs/10.1029/2024EF004902https://agupubs.onlinelibrary.wiley.com/doi/10.1029/2024EF004902.

Kiley L Yeakel, Andreas J Andersson, Nicholas R Bates, Timothy J Noyes, Andrew Collins, and Rebecca Garley. Shifts in coral reef biogeochemistry and resulting acidification linked to offshore productivity. Proceedings of the National Academy of Sciences, 112:14512–14517, 11 2015. . URL https://doi.org/10.1073/pnas.1507021112. doi: 10.1073/pnas.1507021112.

Tianya Yin, Stathys Papadimitriou, Victoire M C Rérolle, Martin Arundell, Christopher L Cardwell, John Walk, Martin R Palmer, Sara E Fowell, Allison Schaap, Matthew C Mowlem, and Socratis Loucaides. A novel lab-on-chip spectrophotometric ph sensor for autonomous in situ seawater measurements to 6000 m depth on stationary and moving observing platforms. Environmental Science  Technology, 55:14968–14978, 11 2021. ISSN 0013-936X. . URL https://doi.org/10.1021/acs.est.1c03517. doi: 10.1021/acs.est.1c03517.

Richard E. Zeebe. History of seawater carbonate chemistry, atmospheric co2, and ocean acidification. http://dx.doi.org/10.1146/annurev-earth-042711-105521, 40: 141–165, 5 2012. ISSN 00846597. . URL https://www.annualreviews.org/doi/abs/10.1146/annurev-earth-042711-105521.

Richard E Zeebe and Dieter Wolf-Gladrow. CO2 in seawater: equilibrium, kinetics, isotopes, volume 65. Gulf Professional Publishing, 2001. ISBN 0444509461.

Zhenlin Zhang, James Falter, Ryan Lowe, Greg Ivey, and Malcolm McCulloch. Atmospheric forcing intensifies the effects of regional ocean warming on reef-scale

temperature anomalies during a coral bleaching event. Journal of Geophysical Research: Oceans, 118:4600–4616, 9 2013. ISSN 2169-9275. . URL https://doi.org/10.1002/jgrc.20338.

Òscar Guadayol, Nyssa J Silbiger, Megan J Donahue, and Florence I M Thomas. Patterns in temporal variability of temperature, oxygen and ph along an environmental gradient in a coral reef. PLOS ONE, 9:e85213–, 1 2014. URL https://doi.org/10.1371/journal.pone.0085213.